Towards High Solar to Fuel Efficiency: From Photonic Design, Interface Study, to Device Integration

Thesis by

Wen-Hui (Sophia) Cheng

In Partial Fulfillment of the Requirements for the Degree of
Doctor of Philosophy

CALIFORNIA INSTITUTE OF TECHNOLOGY
Pasadena, California

2020
(Defended April 20, 2020)

Wen-Hui (Sophia) Cheng
ORCID: 0000-0003-3233-4606

ACKNOWLEDGEMENTS

First of all, I want to share my immense gratitude to my advisor, Prof. Harry Atwater, for being supportive and always inspiring me with his passion toward research and science. Also, I would like to thank my committee members, Dr. Frances Houle, Prof. Bill Johnson, and Prof. Bill Goddard, for helpful suggestions to improve the thesis and set my vision. In memory to Prof. Hans Joachim (Achim) Lewerenz, it was great honor to work with him. Prof. Thomas Hannappel and Dr. Bruce Brunschwig, I appreciate their guidance and kind support when I needed.

Special thanks to Dr. Katherine Fountaine, for being my mentor when I first joined the group, I have learned a lot from her in both science and life. Special shout-out to Dr. Matthias Richter, for being one of the best cooperators and friends, I won't be able to break through all these records without his support, also want to thank him for introducing me the power of synchrotron work. Dr. Sisir Yalamanchili and Dr. Erik Verlage, thank them for involving me in the TiO_2 project, I am glad that we finally have it work out. Thanks to Prof. Rengui Li, our photocatalysis work is not included in this thesis, but I look forward to the fruitful outcome.

Other cooperators who either help me with my project or give me chance to learn from their works including: Prof. Frank Dimroth, Prof. Nate Lewis, Prof. Yun-Jung Lu, Prof. Pin Chieh Wu, Prof. Rebecca Saive, Prof. Dieter Schmeißer, Prof. Giulia Tabliabue, Prof. Joeseph DuChene, Dr. Chengxiang Xiang, Dr. Ian Sullivan, Dr. David Larson, Dr. Colton Bukowsky, Dr. Matthias May, Dr. Jens Ohlmann, Dr. David Lackner, Dr. Michael Kelzenberg, Dr. Michael Lichterman, Dr. Ethan Crumlin, Dr. Walter Drisdell, Dr. Yi-Rung Lin, Dr. Ibadillah Digdaya, Philip Jahelka, Paul Kempler, Alex Welch, Madeline Meier, and Azhar Carim. Thank them all.

I also want to take this chance to thank the best admin team ever, Christy Jenstad, Jennifer Blankenship, Tiffany Kimoto, Kam flower, Mabel Chik, Jonathan Gross, Lyann Lau, Elizabeth Jennings, Mabby Howard, and Tiffani Walker. Thank KNI heroes for maintaining the best cleanroom for research, Guy DeRose, Melissa Melendes, Nils Asplund, Nathan Lee, Bert Mendoza, Steven Martinez, Alex Wertheim, and Matthew Hunt. I am also grateful to Ali Ghaffari for technical support and providing teaching opportunity in APh109.

The whole Ateam is just wonderful, I wouldn't enjoy the past six years as much without everyone in the group. Girls' night in Amigo, summer softball game, group retreat, and Christmas party are all unforgettable memories. Thank the midnight team, Souvik, Joeson, Wei-Hsiang, Yao-Wei, and Pin Chieh, for rescuing me from problems when it was late in the night. Thank Phil for his patient and effort as the amazing IT personnel. Also thank Rebecca for always trying to involve people for different activities and caring our safety. Photocatalysis subgroup (Alex, Lucy, Aiden, Rengui, Giulia, Joe, Eowyn, Yi-Rung, and Chuen-Yo) are being the great team for all the valuable discussion.

JCAP as a friendly hub has the best research environment, but also being a nice place for food and alcohol gathering. Special thanks to Azhar for inviting me to his well-planned parties. Additional note to Kevin, thank him for his help with everything. The best "Dim Sum" group (Anya, Yury the strong, Ruzan, Jonathan, Yuri the beautiful, Ghazaleh, Amir, Giulia, Pablo, Benji, Kelly, Nina, and Pilar), "Craft and Tea" group (Wei-Lin, Yu-Xian, Michelle, Claire, Marianna, Samuel, Xiaomei, and Shiori), Materials Science buddies (Daryl, Harpreet, Wei-Lin, Louis, Jin, Max, Mike, Xiaolin, Jong Hun, and Danielle), thank them for all the fun time together. I would also like to thank my surf student Andrea Perry for trusting me and giving me the chance to be an independent mentor.

Association of Caltech Taiwanese (especially Sandy, Xavier, Hsiao-Yi, Ting, Louis, Jake, Hunter, Allen, Yu-Li, Lucas, I-Hui, Yen-Yung, and Tina), thank them for their company that I feel not lonely even away from home. Gathering events for Lunar New Year, dragon boat festival, moon festival, and birthday parties are wonderful moment to be remembered, and I hope all these tradition can be continued. Friends in Taiwan (especially Jian-Yang, Scott, Yi-Ting, Jerry, Yi-Shan, Peka, Windy, Shiue-Lan, Pin Chieh, Yuri, Hsiu-Ming, Chuen-Yo, Rita, Gloria, Batista, Xuan, Rex, Yun-Man, Ching, Yun, Jiao-Yu, Jay, Ming, Young, and Tzu-Chieh), even I didn't get to see them often, I know they are always there when I need. Special thanks to my master advisor, Prof. Jen-Sue Chen, for her emotional support.

Lastly, I want to thank all my family members, I wouldn't be able to go these far and finish one of the most important challenge in my life without their love and encouragement. I feel really lucky to get all the help and support during my journey in Caltech, and it would for sure

become the powerful fuels for my future. Please forgive me if I missed any of your name in the list of acknowledgment, I indeed appreciate whoever interacted with me and made me a better person. I love you all.

ABSTRACT

Efficient unassisted solar fuel generation, a pathway to storable renewable energy in the form of chemical bonds, requires optimization of a photoelectrochemical device based on photonic design and interface study. We first focused on enhancing absorption via nanophotonic design of light absorbers. Near-unity, broadband absorption in sparse InP nanowire arrays with multi-radii and tapered nanowire array designs are simulated and experimentally demonstrated. Later, a few strategies are introduced to achieved high solar-to-fuel efficiency.

Optically, photoelectrochemical device would require the catalyst ensembles to be highly transparent. We report a record solar-to-hydrogen efficiency by integrating Rh nanoparticle catalysts onto photocathodes with minimal parasitic absorption and reflection losses in the visible range. The other two light management strategies have been developed and experimentally verified to create highly active and effectively transparent catalyst structures: i) arrays of mesophotonic dielectric cone structures that serve as tapered waveguide light couplers to efficiently guide incident light through apertures in an opaque catalyst into the light absorber, and ii) an effectively transparent catalyst consisting of arrays of micron-scale triangular cross-sectional metal grid fingers, which are capable of redirecting the incoming light to the open areas of the PEC cell without shadow loss.

The electronic properties of the surface films exposed to the electrolyte are also critical. The anatase TiO_2 protection layer on the photocathode creates a favorable internal band alignment for hydrogen evolution, promoting the transport of the excess electrons and inhibiting voltage drops. The interfacial conduction mechanism between the defected TiO_2 and metal catalysts is investigated. A combinatorial approach of electrochemistry, X-ray photoelectron spectroscopy, and resonant X-ray spectroscopy reveals the correlation between the interfacial quasi-metal phase with TiO_2 properties. By careful control of gas diffusion electrode assembling to maintain appropriate wetted catalyst interface, another record solar-to-CO efficiency with extended stability can be realized.

PUBLISHED CONTENT AND CONTRIBUTIONS

Portions of this thesis have been drawn from the following publications:

Katherine T. Fountaine, **Wen-Hui Cheng**, Colton R. Bukowsky, and Harry A. Atwater, *Near-unity unselective absorption in sparse InP nanowire arrays.* ACS Photonics, 3 (10), 1826-1832, (**2016**). DOI: 10.1021/acsphotonics.6b00341

Contribution: fabrication and data collection.

Wen-Hui Cheng, Matthias H. Richter, Matthias M. May, Jens Ohlmann, David Lackner, Frank Dimroth, Thomas Hannappel, Harry A. Atwater, and Hans-Joachim Lewerenz, *Monolithic photoelectrochemical device for direct water splitting with 19% efficiency*. ACS Energy Letters 3 (8), 1795-1800, (**2018**). DOI: 10.1021/acsenergylett.8b00920

Contribution: conception and design, fabrication and data collection, simulation and analysis, manuscript writing, and revision.

Wen-Hui Cheng, Matthias H. Richter, Ian Sullivan, David M. Larson, Chengxiang Xiang, Bruce Brunschwig, Harry A. Atwater, *CO_2 reduction to CO with 19% efficiency in a solar-drive gas diffusion electrode flow cell under outdoor solar illumination.* ACS Energy Letters *5* (2), 470-476, (**2020**). DOI: 10.1021/acsenergylett.9b02576

Contribution: conception and design, fabrication and data collection, manuscript writing and revision.

Sisir Yalamanchili[*], Erik Verlage[*], **Wen-Hui Cheng**[*], Katherine T. Fountaine, Philip R. Jahelka, Paul A. Kempler, Rebecca Saive, Nathan S. Lewis, Harry A. Atwater, *High broadband light transmission for solar fuels production using dielectric optical waveguides in TiO_2 nanocone arrays.* Nano Letters 20 (1), 502-508, (**2020**). DOI: 10.1021/acs.nanolett.9b04225 ([*]equal contribution)

Contribution: fabrication and data collection, simulation and analysis, manuscript writing, and revision.

Wen-Hui Cheng, Matthias H. Richter, Michael Kelzenberg, Sisir Yalamanchili, Phillip R. Jahelka, Pin Chieh Wu, Rebecca Saive, Bruce S. Brunschwig, Thomas Hannappel, and Harry A. Atwater. *Incorporating effective transparent catalysts for photoelectrochemical application.* (Manuscript in preparation)

Contribution: conception and design, fabrication and data collection, simulation and analysis, manuscript writing, and revision.

Matthias H. Richter*, **Wen-Hui Cheng***, Michael F. Lichterman, Ethan J. Crumlin, Walter Drisdell, Harry A. Atwater, Dieter Schmeißer, Nathan S. Lewis, and Bruce S. Brunschwig, *Interaction of metal catalyst thin films with ALD titanium dioxide.* (Manuscript in preparation) (*equal contribution)

Contribution: fabrication, data collection, and manuscript writing.

TABLE OF CONTENTS

LIST OF FIGURES

LIST OF TABLES

CHAPTER 1
Introduction of Solar Fuels

1.1 Fundamentals of Photoelectrochemistry

To achieve a sustainable future with a carbon neutral environment, the world's reliance on renewable energy has dramatically increased. Solar photovoltaic and wind energy conversion are rapidly growing sources of low-carbon electric power due to the size of the resource and its wide geographical deployment potential.[1] However, intermittency of the solar and wind resources over wide time scales ranging from minutes to months means solar electricity is not a dispatchable power source. Thus, efficient and inexpensive approaches for energy storage are needed for wide penetration of renewable energy into the power grid.[2] While electrical energy storage in batteries may be important for short-term storage and grid power management, seasonal energy storage is unlikely to rely on batteries. Transformation of solar energy into chemical bonds provides a long-term energy storage strategy that opens a path for the synthesis of fuels and chemicals.[3] One approach to chemical energy storage is via solar-driven fuels generation, where i) photovoltaics supply carbon free electricity to the grid that is used to generate fuels by chemical reaction at high current densities;[56] ii) photovoltaics are used to directly drive electrolysis at low current densities,[4] or iii) an integrated photoelectrochemical device that performs unassisted direct fuels production.[5,6]

Photoelectrochemical (PEC) devices integrate multiple functional materials and couple various PEC processes to produce fuels from sunlight and water. Figure 1.1 illustrates key photoelectrochemical processes in a typical device. First, the incident sunlight is absorbed by the semiconductor materials. Any materials or components in the optical pathway between the sun and the semiconductors could potentially modulate and alter the light absorption. Therefore, understanding light-matter interaction in the PEC system becomes an important objective. Second, the absorbed photons in the semiconductor material generate energetic electrons and holes, which then transport to electrocatalysts via interfacial charge transfer. Third, the electrocatalysts perform the chemical reaction, in which products are produced simultaneously at the catalytic sites. For example, the two half reactions involved in the water splitting process are shown below:

Half reaction at cathode (reduction): $2H^+ + 2e^- \rightarrow H_2$ (E = 0 V vs RHE)

Half reaction at anode (oxidation): $H_2O + 2h^+ \rightarrow \frac{1}{2}O_2 + 2H^+$ (E = 1.23 V vs RHE)

Net Reaction: $H_2O \rightarrow H_2 + \frac{1}{2}O_2$

Where RHE is the reversible hydrogen electrode potential. Other cathode reactions include but not limit to CO_2 reduction reaction (CO_2RR):

$CO_2 + 2H^+ + 2e^- \rightarrow CO + H_2O$ (E = -0.11 V vs RHE)

$CO_2 + 2H^+ + 2e^- \rightarrow HCOOH$ (E = -0.17 V vs RHE)

$CO_2 + 8H^+ + 8e^- \rightarrow CH_4 + 2H_2O$ (E = 0.17 V vs RHE)

$2CO_2 + 8H^+ + 8e^- \rightarrow CH_3COOH + 2H_2O$ (E = 0.13 V vs RHE)

$2CO_2 + 12H^+ + 12e^- \rightarrow C_2H_4 + 4H_2O$ (E = 0.08 V vs RHE)

$2CO_2 + 12H^+ + 12e^- \rightarrow C_2H_5OH + 3H_2O$ (E = 0.08 V vs RHE)

$3CO_2 + 18H^+ + 18e^- \rightarrow C_3H_8O + 5H_2O$ (E = 0.1 V vs RHE)

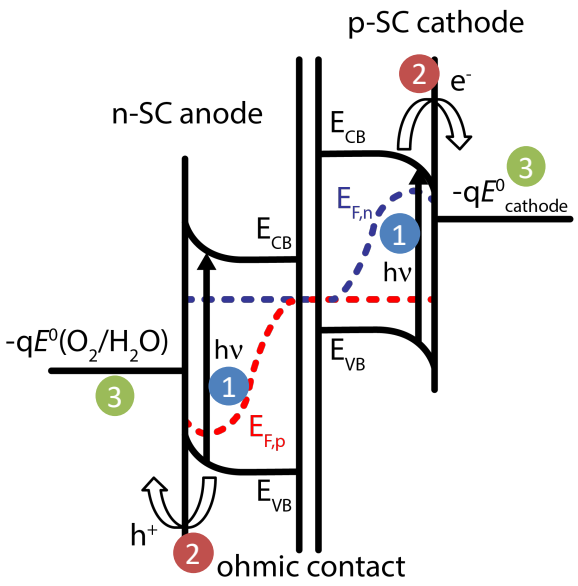

Figure 1.1: *Schematic illustrations of the general operating principles for PEC device.*

In the meantime, ionic transport between the cathode and anode chamber and product separation are required to maintain the efficient and safe operation of the cell. Note that all these

processes need to be fully coupled to produce a single rate of reaction for cathode and anode reaction in the PEC device. To overcome the thermodynamic potential (ΔU_{rxn}) , the difference between the anode oxygen evolution (1.23 V vs. RHE) and cathode reduction reaction, the total voltage (Fermi level splitting) of cathode and anode needs to be large enough to sustain the full reaction. For example, ΔU_{rxn} = 1.23V for H_2/O_2, 1.34V for CO/O_2. As illustrated in Figure 1.1, by employing semiconductor/electrolyte junctions, the conduction band edge (E_{CB}) of the cathode should be positioned at a higher energy level than the cathode reaction, while the valence band edge (E_{VB}) of the anode should be positioned at lower energy level than the anode reaction. [7,8] In addition, solid-state, buried junctions using traditional photovoltaic materials, such as Si, GaAs, etc., are often used to circumvent the stringent requirements for the band edge positions and to achieve high efficiency solar to fuel performances. [5,9,10]

1.2 Photoelectrochemical Device

Four general types of PEC water-splitting device architectures, as shown in **Figure 1.2**, have been modeled and experimentally demonstrated in the laboratory scale. [11] Type 1 and Type 2 device indicates a system where the catalyst on a light absorber is in the form of particles suspended in the electrolyte. Either a single-chamber device (Type 1), in which hydrogen and oxygen co-evolve where product separation would be necessary afterward, or dual-chamber device (Type 2), in which a bridge or membrane for ion transport is required in the Z scheme reaction, has been proposed and studied for particle-based systems. While the Type 1 and Type 2 device architecture shows great promise in many technoeconomic analyses (TEA), the solar-to-fuel (STF) conversion efficiency is currently limited to <2%. [12,13] Type 3 and Type 4 devices indicate systems where catalyst coated planar semiconductor materials and membrane separators are configured to maximize the light absorption and to minimize the transport loss in the device. Even though all architectures can operate under un-concentrated sunlight or sunlight with low concentrations, e.g., ~10x concentration, Type 4 indicates a PEC couple with a solar concentrator specifically.

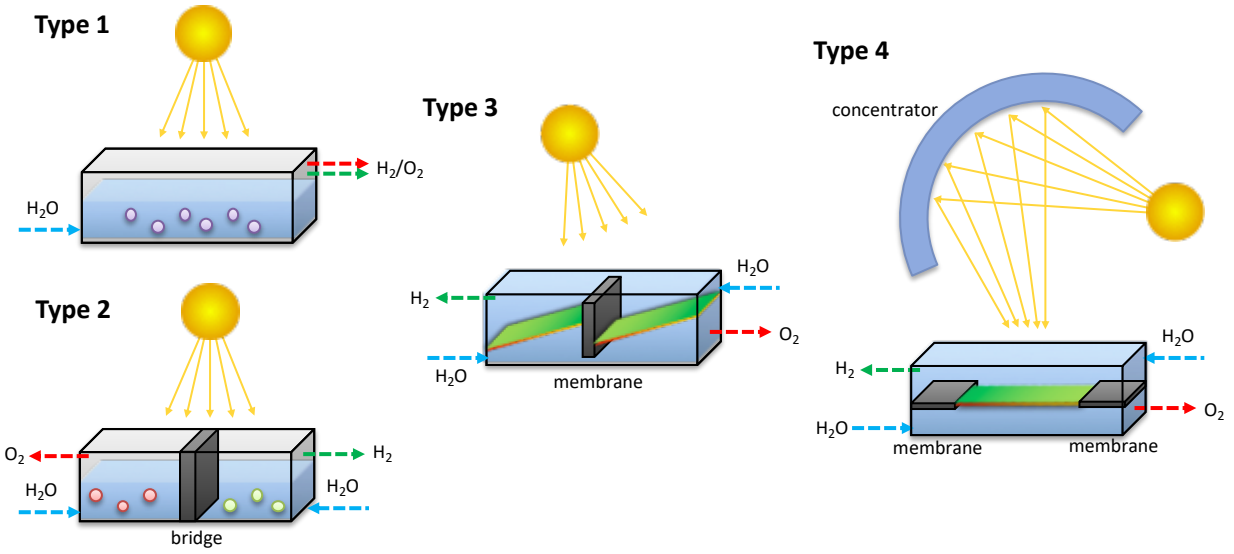

Figure 1.2: *Schematic illustrations of device architectures for Type 1 and Type 2 particle based PEC device, Tpye 3 and Type 4 planar catalyst coated semiconductor PEC device.*

1.3 Solar-to-Fuel Efficiency

Among various performance metrics, the solar-to-fuel (STF) conversion efficiency is one of the most important parameters in determining the levelized fuel production cost. [11] In particular, high STF conversion efficiency levitates the land requirements for a given capacity of fuel production and lowers the balance of system cost. We calculated the solar to fuel efficiency (η_{STF}) using equation below.

$$\eta_{STF} = \frac{P_{out}}{P_{in}} = \frac{I_{op} \cdot \Delta U_{rxn} \cdot f_{FE}}{P_{light} \cdot A_{PV}} = \frac{J_{catalyst} \cdot \Delta U_{rxn} \cdot f_{FE} \cdot A_{catalyst}}{P_{light} \cdot A_{PV}} = \frac{J_{PV} \cdot \Delta U_{rxn} \cdot f_{FE}}{P_{light}} \qquad \text{(Equation 1.1)}$$

Where P_{in} is input power, P_{out} is output power, $I_{op} = J_{catalyst} \cdot A_{catalyst} = J_{PV} \cdot A_{PV}$, I_{op} is the operation current of the system, $J_{catalyst}$ and $A_{catalyst}$ are the current density and area of the catalyst, J_{PV} and A_{PV} are the current density and area of PV, ΔU_{rxn} is the thermodynamic potential difference between the oxygen evolution half reaction (OER) and the cathode reduction reaction, f_{FE} is the reaction Faradaic efficiency, and P_{light} is the incident light irradiance ($mW \cdot cm^{-2}$) on the photovoltaic.

The energy efficiency for the cell (η_{cell}) was defined as follows:

$$\eta_{cell} = \frac{\mathrm{P}_{out}}{\mathrm{P}_{in}} = \frac{\Delta U_{\mathrm{rxn}} \cdot J_{\mathrm{catalyst}} \cdot A_{\mathrm{catalyst}} \cdot f_{FE}}{U_{cell} \cdot J_{\mathrm{PV}} \cdot A_{\mathrm{PV}}} = \frac{\Delta U_{\mathrm{rxn}} \cdot f_{FE}}{U_{cell}} \qquad \text{(Equation 1.2)}$$

Where U_{cell} is the total operating voltage of the cell.

For the integrated photoelectrochemical device, the catalyst and light absorber are coupled together. The solar fuel generator efficiency η_{STH} is given by:

$$\eta_{STH} = \frac{J_{PEC} \cdot \Delta U_{rxn} \cdot f_{FE}}{P_{light}} \qquad \text{(Equation 1.3)}$$

Where J_{PEC} is the PEC operating current density at 0 V vs counter electrode potential.

1.4 Thesis Outline

This thesis provides the research pathways to achieve a high efficiency solar fuel device from a better understanding of light matter interaction to carrier transport dynamic through device level integration. Below is the brief overview of each chapter in this thesis:

Chapter 2 focused on enhancing absorption via nanophotonic design of III-V based light absorber. Both multi-radii and tapered nanowire arrays are introduced and experimentally evaluated.

Chapter 3 realized high solar-to-H_2 efficiency in PEC devices, consisting of a III-V based tandem light absorber and RuO_x/Rh NP catalysts for OER and HER. Minimizing parasitic light absorption and reflection losses with favorable band alignment further reduces the efficiency gap to the theoretical limit.

Chapter 4 developed a solar-driven CO_2 reduction device using a gas diffusion electrode (GDE) with Ag nanoparticle catalyst directly powered by a III-V based triple junction solar cell. Device geometry was studied to extend the operation stability.

Chapter 5 demonstrated light management strategies to create highly active and effectively transparent catalyst structures with high index TiO_2 nanocones. It allowed incident broadband illumination couples to multiple waveguide modes, reducing interactions of the light with the metal catalysts.

Chapter 6 introduced another approach with an effectively transparent catalyst consisting of arrays of micron-scale triangular cross-sectional metal grid fingers. It redirected the incoming light to the open areas of the PEC cell to reduce the overall shadow loss.

Chapter 7 investigated the interfacial conduction mechanism between the TiO_2 protection layer and metal catalysts with a combinatorial approach of electrochemistry, XPS, resPEX, and RiXS.

Chapter 8 summarized the main outcome and contribution of this thesis.

CHAPTER 2
Broadband Adsorption InP NW

2.1 Introduction

Design of "perfect" absorbers and emitters is of considerable current interest and research in the nanophotonics and metamaterials fields. [14-16] Perfect absorbers and emitters can find applications in numerous fields across the electromagnetic spectrum, including light and thermal sources, [17-19] sensing, [20,21] and energy conversion. [18,22,23] Two types of near-unity or "perfect" absorption are straightforward to achieve: (1) a wavelength-sized resonator can be used for selective "perfect" absorption — absorption at a single frequency, polarization and incidence angle, [24-27] and (2) an optically thick layer of lossy material can be used for unselective, "perfect" absorption — absorption over a large range of frequencies, angles, and polarizations. [28] However, many applications would benefit from a more comprehensive ability to tailor perfect absorber characteristics, such as achieving directional, spectrally broadband thermal emission of infrared radiation sources [17,29] and broadband, angle-insensitive thin film perfect absorbers for high efficiency, lightweight photovoltaics. [28,30,31] To this end, recent work in the field has focused on the realization of selective perfect absorbers that are extremely thin, [14,26,32] actively tunable, [33,34] and wavelength, angle, or polarization-insensitive, [16,35,36] as well as unselective perfect absorbers with small form factors that are insensitive to angle, wavelength, or polarization. [22,23]

In this work, we focus on the design and fabrication of unselective perfect absorbers with small form factors using semiconductor nanowire arrays. Specifically, we examine sparse arrays of InP nanowires fabricated using a top-down lithographic pattern and etch procedures, followed by embedding in polydimethylsiloxane (PDMS) and mechanical removal from the substrate. These sparse arrays of vertically-oriented, semiconductor nanowires represent a promising approach to flexible, lightweight, high efficiency, and low-cost optoelectronic devices in sensing and energy applications, such as photodetectors, [37-39] bolometers, [40,41] solar cells, [23,42-44] and photoelectrochemical devices. [45,46] Currently in the photovoltaics field, the greatest challenge for use of III-V absorbers and cells is reducing cost/Watt. [47] Therefore, it is highly desirable to develop fabrication methods that reduce or eliminate costs associated with epitaxial growth and consumption of III-V compound semiconductor substrates. The wire-array fabrication process

described herein holds considerable promise for achieving these goals because many layers can be fabricated from a single compound semiconductor substrate. InP is of particular interest for wire array photovoltaics, and more broadly, InP has garnered much interest for nanowire-based optoelectronic devices due to its direct bandgap and low intrinsic surface recombination velocity, [48] which is critical to high performance in high surface area devices.

In recent years, the optical properties of semiconductor nanowire arrays have been the subject of great interest and intensive research. [49-52] Even at very low area fill fractions, semiconductor nanowire arrays exhibit strong optical absorption due to robust coupling into the waveguide modes of individual nanowires. [23,53] These arrays of essentially independent optical antennas have an optical response that is polarization-independent and angle-insensitive. [45] In a standard nanowire array with a uniform wire radius, strong absorption is observed over a relatively narrow spectral region in which end-mediated coupling into guided modes is favorable. [45,54] Array geometry, [55-57] nanowire shape, [23,58-60] and order[61,62] have previously been shown both experimentally and theoretically to control the spectral position of this region by others. In previous work, [23] we theoretically studied different nanowire motifs within sparse arrays and, by optical design of the waveguide modes, achieved broadband absorption enhancements for constant material usage. Specifically, we optimized arrays with multiple nanowire radii and tapered nanowires and predicted > 90 % broadband absorption (Vis-NIR) in 150 nm planar equivalence. Herein, we validate those predictions and experimentally demonstrate broadband, polarization-independent, angle-insensitive, near-unity (> 90 %) absorption in sparse arrays of InP nanowires.

2.2 Experimental and Numerical Method

InP nanowire arrays were fabricated top-down from InP wafers (2'' AXT, n-type, sulfur-doped, (100) orientation), using inductively coupled plasma reactive ion etching (ICP-RIE). Wafers were cleaned via sequential sonication for 10 min in water, IPA, acetone, and water. A piranha clean step was omitted because of the existence of the native InP_xO_y facilitated adhesion of the hard mask layers.

Two different hard masks were used in this work: SiO_2 and Cr. The SiO_2 mask was approximately 400 nm thick and deposited via RF sputtering (SiO_2 target, 3 mTorr Ar atmosphere,

200 W forward power). The pattern was defined in the mask via a direct electron beam lithography written into negative tone, MaN-2403 resist, followed by a pseudo-Bosch etching step (5 mTorr, 1000 W ICP forward power, 25 W RF forward power, 10°C, 26 sccm SF_6, 35 sccm C_4F_8) to transfer the pattern from the resist into the SiO_2. For the Cr hard mask, the pattern was defined via direct electron beam lithography written into a bilayer of positive tone resist (PMMA495-A4/PMMA95-A4), followed by electron beam deposition of a 50 nm Cr layer (0.5 $A \cdot s^{-1}$,10^{-6} Torr) and lift-off of the resist.

A $Cl_2/H_2/CH_4$ etch (4 mTorr, 2200 W ICP forward power, 200 W RF forward power, 28 sccm H_2, 32 sccm Cl_2) was used to transfer the pattern into the InP for the creation of nanowire arrays. The table temperature was set to 60°C and no thermal contact between the sample and the carrier wafer was omitted to achieve etch temperatures of ~300°C to ensure sufficient volatility of the In etch products. Because CH_4 provides sidewall passivation, its flow was varied between 24 and 30 sccm to control the degree of sidewall taper from normal taper to inverse taper, respectively.

To exfoliate the nanowire arrays from the InP substrate, the samples were covered with a thick layer of 10:1 PDMS solution, degassed for 20 min, baked overnight at 80°C, and mechanically peeled-off the substrate after cooling. All SEM images were taken on wafer, prior to embedding in PDMS. All experimental optical spectra were obtained using a Fianium laser as a tunable source and a home-built integrating sphere setup with silicon photodiode detectors. [63] Reflection and transmission spectra (when relevant) are composed of 276 points, spaced linearly in wavelength from 450 to 1000 nm. Absorption was calculated from 1-R-T.

Full-field, 3D simulations were performed using Lumerical FDTD, a commercial electromagnetics software package. At normal incidence, the infinite periodicity of the nanowire arrays was rendered using periodic boundary conditions and, at non-normal incidence, Bloch boundary conditions to enforce phase continuity. Symmetric boundary conditions were applied when relevant to reduce computation time. In the axial direction, perfectly matched layers were used to emulate infinite space above and below the array. All nanowire structures were modeled using Palik data for InP, Ag, Cr, and SiO_2, and ellipsometric data for PDMS. Image analysis of SEM images was used to determine the nanowire dimensions for simulation. The top-down fabrication process resulted in significant geometric variation within a single array; therefore, in

order to capture the optical behavior of the arrays, multiple array geometries were simulated. Three representative geometries were chosen for each sample, and results contain each of these three spectra as well as their average. Figure 2.1 displays the two geometries that were used to render the fabricated nanowires in simulation.

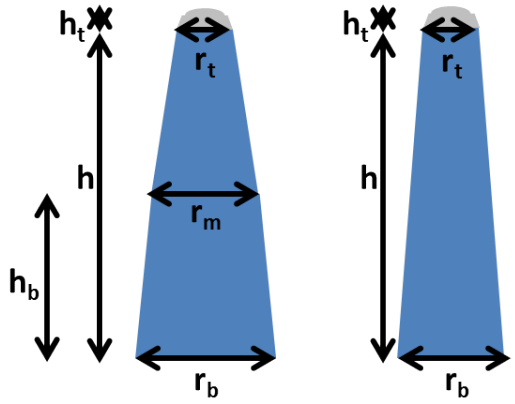

Figure 2.1: *Schematic of two different nanowire geometries used in simulation.*

The remaining SiO_2 and Cr masks were modeled as truncated cones with the bottom radius matching the top radius of the nanowire and a top radius of 10 nm. A finer mesh was used around the nanowire, with a mesh cell width of one tenth the smallest radius.

All simulations used a single wavelength, polarized infinite plane wave source, and each spectrum is composed of 276*n* simulations, spaced linearly in wavelength from 450 to 1000 nm, where *n* is the number of polarizations necessary to capture the unpolarized optical response of the array. Planar power monitors were used to extract the array absorption and also to distinguish between absorption in the InP and the other materials.

2.3 Results and Discussion

In this section, we begin with a brief discussion of InP nanowire array design. Next, we validate our experimental and theoretical methods via a uniform InP nanowire array. Subsequently, we prove that nanowire taper induces peak broadening, and multiple wire radii generate multiple

peaks via characterization of very sparse InP nanowire arrays. Finally, we demonstrate near-unity broadband absorption in sparse arrays of tapered and multi-radii InP nanowire arrays.

As previously stated, vertically-oriented semiconductor nanowires act as cylindrical dielectric waveguides with high absorption loss. In sparse arrays, the nanowires are essentially non-interacting and, thus, their optical behavior is well-described by traditional waveguide theory. [64] The nanowires exhibit a primary absorption peak, which is due to end-mediated coupling into the HE_{11} waveguide mode; the spectral region of strong coupling occurs in the moderately guided portion of the HE_{11} modal dispersion. [53] The dominant role of the waveguide modes in the absorption enhancement translates to a strong correlation between nanowire radius and the spectral region of absorption enhancement, and is used herein to guide the design of InP nanowire arrays. A radius range of 40 to 100 nm is needed to observe absorption enhancement in the visible up to the band edge of InP (450-925 nm).

Initially, we examine a uniform nanowire array (r = 90 nm, h = 1.2 μm, a = 750 nm) to validate our theoretical framework as well as our experimental and simulation methods. The three different geometries used are summarized in Table 2.1. The variable labels correspond to Figure 2.1. The fill fractions, ff, and effective InP thicknesses, t_{eff}, are also calculated and included in the table. This array, shown as the inset to Figure 2.2(d), has a fill fraction of 4.5% and a planar equivalent thickness of ~54 nm. Figure 2.2(a) displays the absorption (blue), reflection (green), and transmission (red) spectra for the array, after it was embedded in PDMS and peeled off of the substrate; Figure 2.2(b) displays reflection spectra for the array in three different configurations – on substrate, embedded in PDMS and on the substrate, and embedded in PDMS and peeled off of the substrate. These experimental spectra give the expected results – we observe low reflectivity for the array in all cases and a primary absorption peak around 850 nm, corresponding to coupling into the HE_{11} waveguide mode. Figure 2.2(c-d) displays the corresponding simulated spectra, with thick solid lines representing the average of three slightly different nanowire dimensions (thin, dashed, dotted lines). We found good agreement between experiment and simulation.

Table 2.1: *Summary of array geometries used in simulation of Figure 2.2(c). UR indicates uniform radii.*

	r_b (nm)	r_m (nm)	r_t (nm)	h (μm)	h_b (μm)	h_t (μm)	a (μm)	ff	t_{eff} (nm)
UR-1	90	87.5	90					0.044	69
UR-2	90	90	95	1.578	1.214	0.122	0.75	0.046	72
UR-3	85	85	90					0.041	65

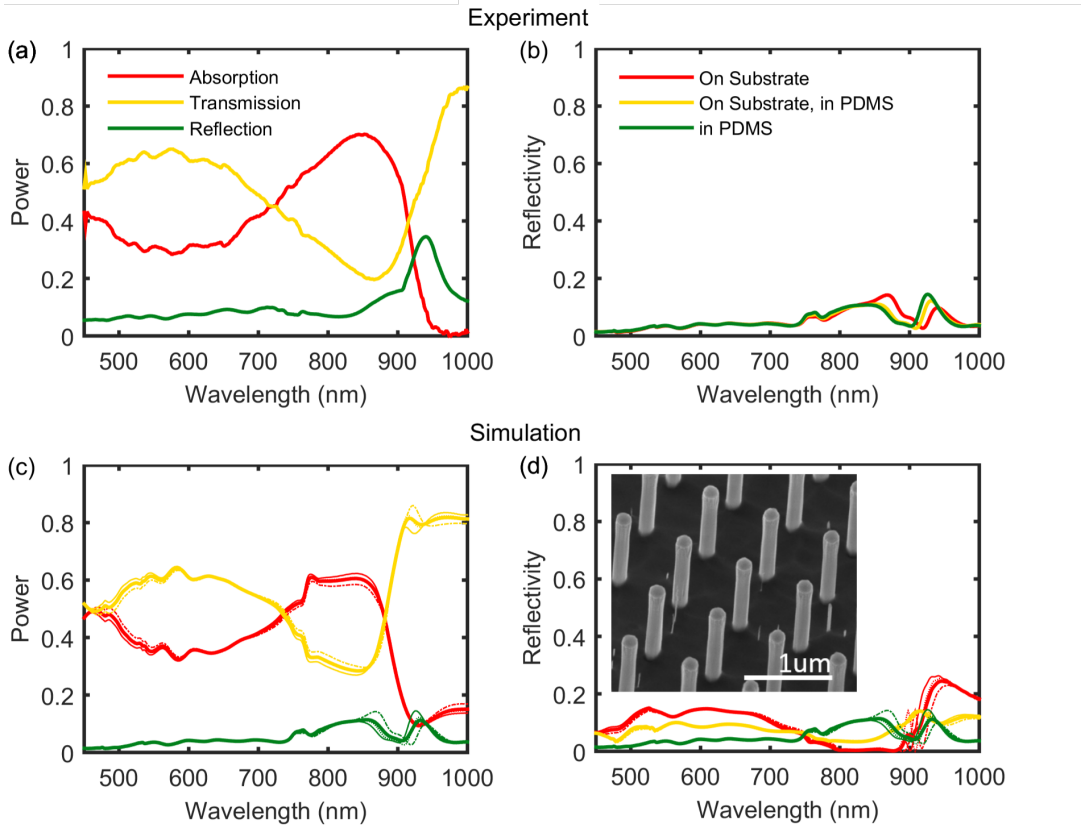

Figure 2.2: *Characterization of uniform radius array. (a) Absorption, reflection, and transmission spectra for the PDMS-embedded array shown as inset of (d), measured using an integrating sphere; (b) Reflection spectra for the array shown as inset of (d) in multiple configurations; (c,d) Simulated spectra corresponding to the experimental results in (a,b) with solid thick lines representing an*

average of three slight geometric variations (thin, dashed, dotted); inset of (d) is scanning electron micrograph of the uniform radius array; see Table 2.1 for array dimensions used in simulation.

The initial broadband absorber arrays presented herein were designed with the intention of demonstrating that tapered nanowires broaden the primary HE_{11} absorption peak and that multiple radii in a single array generate multiple absorption peaks. Therefore, sparse arrays of short nanowires were fabricated, and the multi-radii sub-cell consisted of only two different radii. The sparseness of these arrays results in more well-defined peak features, which is particularly essential to the distinction of multiple peaks in the multi-radii arrays that might otherwise blend into one extended peak due to experimental variation in the fabricated dimensions.

Figure 2.3(a-c) displays SEM images of the sparse (a = 750nm), uniform, tapered, and multi-radii arrays, which have fill fractions (planar equivalent thicknesses) of 4.5% (54 nm), 2.7% (29 nm), and 2.1% (33 nm), respectively. The fill fractions and planar equivalent thicknesses were determined from image analysis, and the precise dimensions used in simulation are listed in Table 2.2. Figure 2.3(d-e) displays the experimental and simulated absorption spectra for these arrays, demonstrating good qualitative agreement between simulation and experiment. The absorption spectrum of the tapered nanowire array (green) exhibits a broadened absorption peak in comparison to that of the uniform array (blue) and the absorption spectrum of the multi-radii nanowire array (red) exhibits two peaks, corresponding to the HE_{11} waveguide modes of the two different nanowire radii. It is important to note that while the uniform array may appear to be outperforming the tapered and multi-radii array designs in terms of integrated absorption, it is only because the uniform array contains nearly twice the amount of InP.

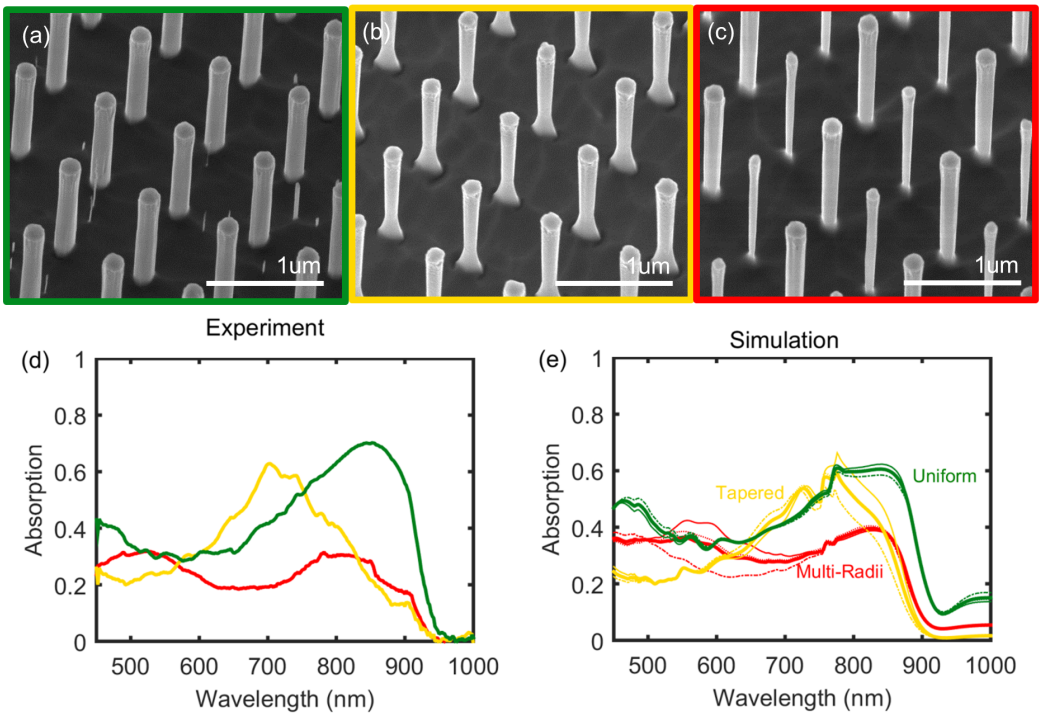

Figure 2.3: *Comparison of uniform, tapered, and multi-radii arrays. (a,b,c) Scanning electron micrographs of the uniform, tapered, and multi-radii array, respectively; (d) Absorption spectra for the PDMS-embedded arrays shown in (a,b,c), measured using an integrating sphere; (e) Simulated absorption spectra corresponding to the experimental results in (d) with solid thick lines representing an average of three slight geometric variations (thin, dashed, dotted); see Table 2.2 for array dimensions used in simulation. Colors are coordinated throughout the figure.*

Table 2.2: *Summary of array geometries used in simulation of Figure 2.3(e). UR indicates uniform radii. T indicates tapered. MR indicates multi-radii.*

	r_b (nm)	r_m (nm)	r_t (nm)	h (μm)	h_b (μm)	h_t (μm)	a (μm)	ff	t_{eff} (nm)
UR-1	90	87.5	90					0.044	69
UR-2	90	90	95	1.578	1.214	0.122	0.75	0.046	72
UR-3	85	85	90					0.041	65
T-1	57.5		75					0.025	27
T-2	60	-	77.5	1.08	-	0.12	0.75	0.027	29
T-3	62.5		80					0.029	31
MR-1	{72.5,37.5}	{82.5,50}	{92.5,57.5}					0.024	38
MR-2	{75,30}	{80,45)	{92.5,57.5}	1.587	{1.247, 1.304}	0.113	0.75	0.022	35
MR-3	{75,42.5}	{80,50}	{90,60}					0.024	38

To achieve near-unity broadband absorption, slightly denser arrays of taller nanowires were fabricated for both the tapered nanowire and multi-radii nanowire motifs. Additionally, the multi-radii array consisted of a 4 wire sub-cell (2x2) to distribute the strong in-coupling region of the HE_{11} mode more evenly across the visible spectrum.

Figure 2.4 contains the results for an exemplary tapered nanowire array, with ~1.6 μm tall nanowires with radii ranging from 30 to 110 nm, spaced 450 nm apart (SEM image in the inset of Figure 2.4(a)). A detailed accounting of array dimensions are listed in Table 2.3. The experimentally-measured and simulated absorption spectra for the PDMS-embedded, tapered

nanowire array are displayed in Figure 2.4(a-b), respectively, as a function of incidence angle. The experimental data includes incidence angles from 0° to 30°, in 5° increments. The simulated data includes 0°, 10°, and 20° for three slight geometric variations (thin, dashed, dotted lines) and their averages (thick solid lines); the absorption of the planar equivalence (108 nm) is also overlaid for reference (black, dashed line). In all spectra, we find good qualitative agreement between simulation and experiment.

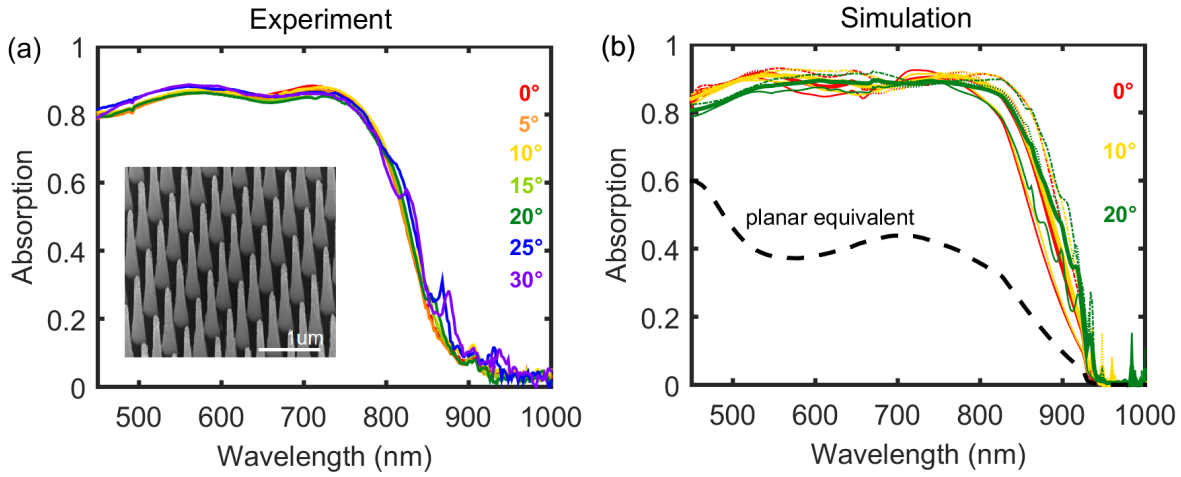

Figure 2.4: *Characterization of tapered array. (a) Absorption spectra at various incident angles for the PDMS-embedded array (SEM image shown as inset), measured using an integrating sphere; (b) Simulated spectra corresponding to the experimental results in (a) with solid thick lines representing an average of three slight geometric variations (thin, dashed, dotted), overlaid with the planar equivalent absorption spectra (108 nm thin film, black dashed); see Table 2.3 for array dimensions used in simulation.*

Table 2.3: *Summary of array geometries used in simulation of Figure 2.4(b). T indicates tapered.*

	r_b (nm)	r_m (nm)	r_t (nm)	h (μm)	h_b (μm)	h_t (μm)	a (μm)	ff	t_{eff} (nm)
T-4	100	50	32.5	1.55	0.775			0.057	91
T-5	107.5	52.5	35	1.6	0.8	0.05	0.45	0.067	107
T-6	112.5	57.5	37.5	1.65	0.825			0.078	125

The tapered array demonstrates angle-insensitive broadband absorption, approaching 90% absorption across the visible. The PDMS front surface results in approximately a 5% broadband reflectivity, and the remainder is transmission losses due to incomplete absorption. Compared to the planar equivalent thin film of 108 nm (black, dashed line in Figure 2.4(b)), the nanowire array exhibits broadband absorption enhancements across the visible spectrum. These absorption enhancements occur due to strong coupling into the HE_{11} waveguide mode, which has been engineered to occur over a broad spectral region via wire taper. Absorption drops off beyond 800 nm because there is insufficient wire length at the larger wire radii to observe significant absorption enhancements. Additionally, the noise in both the experimental and simulated spectra is attributed to residual pieces of the Cr etch mask.

Figure 2.5 displays the results for an exemplary multi-radii nanowire array, with ~ 1.75 μm tall nanowires with radii ranging from 35 to 115 nm, spaced 520 nm apart (shown as the inset of Figure 2.5(a)). A detailed account of array dimensions can be found in Table 2.4. The experimentally-measured and simulated absorption spectra for the PDMS-embedded, multi-radii nanowire array are displayed in Figure 2.5(a,c), respectively, as a function of incidence angle. To further push the array absorption towards near-unity, a silver back reflector was deposited to achieve 2-pass absorption, and the resulting experimental and simulated absorption spectra are shown in Figure 2.5(b,d). The experimental data includes incidence angles from 0° to 30°, in 5° increments. The simulated data includes 0°, 10°, and 20° for three slight geometric variations (thin,

dashed, dotted lines) and their averages (thick solid lines); the absorption of the planar equivalence (109 nm for single pass, 218 nm for 2-pass) is also overlaid for reference (black, dashed line). In all spectra, we find good qualitative agreement between simulation and experiment.

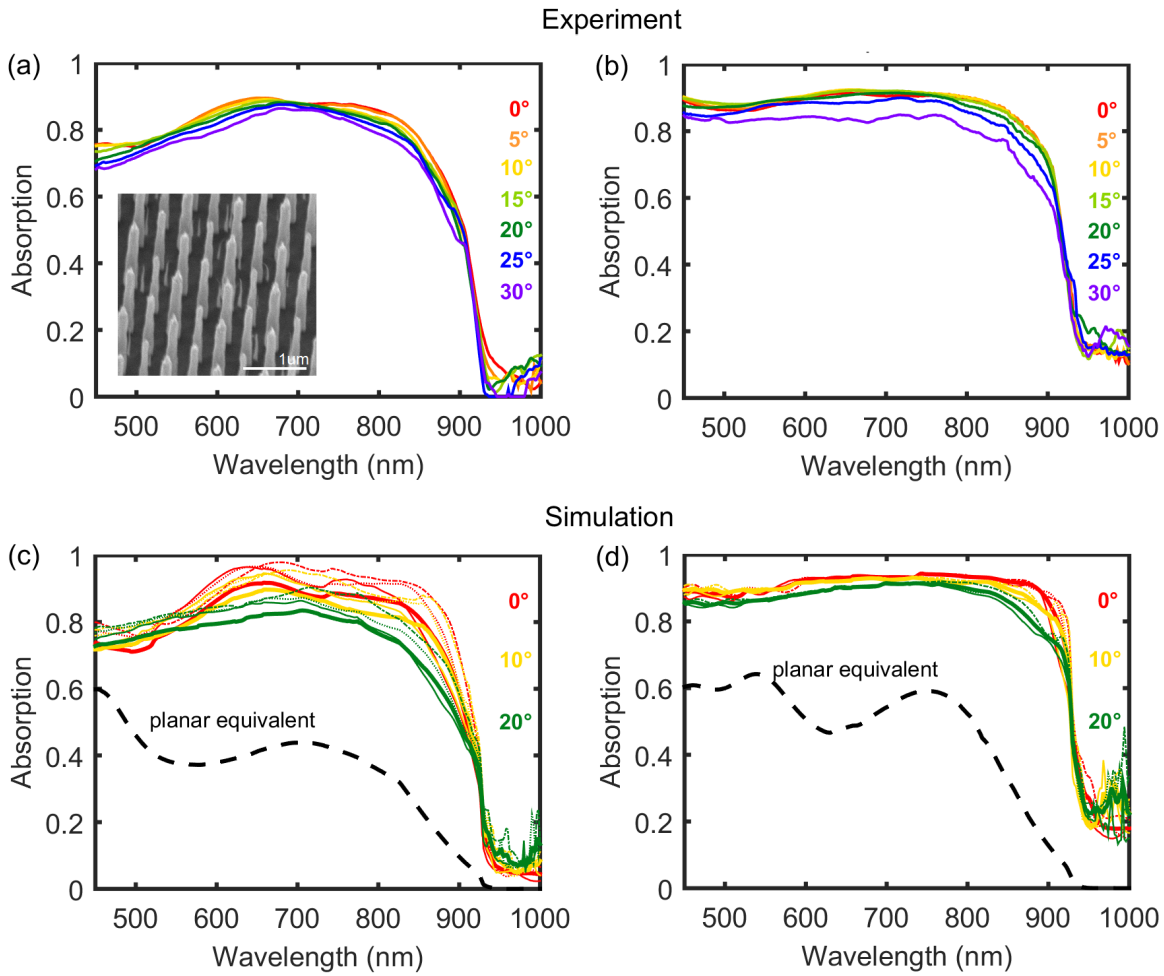

Figure 2.5: *Characterization of multi-radii array. (a,b) Absorption spectra at various incident angles for the PDMS-embedded array, shown as inset of (b), without and with a silver back reflector, respectively, measured using an integrating sphere; (c,d) Simulated spectra corresponding to the experimental results in (a,b) with solid thick lines representing an average of three slight geometric variations (thin, dashed, dotted), overlaid with the planar equivalent absorption spectra (109 and 218 nm thin films, black dashed); see Table 2.4 for array dimensions used in simulation.*

Table 2.4: *Summary of array geometries used in simulation of Figure 2.5(c,d). MR indicates multi-radii.*

	r_b (nm)	r_m (nm)	r_t (nm)	h (μm)	h_b (μm)	h_t (μm)	a (μm)	ff	t_{eff} (nm)
MR-4	{70,80, 87.5,110}		{35,42.5, 55,67.5}	1.7				0.058	98
MR-5	{70,82.5, 92.5,115}	-	{37.5,45, 60,72.5}	1.75	-	0.05	0.52	0.064	111
MR-6	{75,82.5, 97.5,115}		{42.5,50, 62.5,75}	1.8				0.068	122

The multi-radii array demonstrates angle-insensitive broadband absorption, approaching 90 % absorption in a single pass and exceeding 90% with a silver back reflector up to the band edge of InP ($\lambda \sim 925$ nm). Again, the PDMS front surface results in approximately a 5 % broadband reflectivity, which accounts for nearly all of the loss when the array has a back reflector. In the single pass case, the remainder is transmission losses due to incomplete absorption. Compared to the planar equivalent thin films (109 nm for single pass, 218 nm for double pass; black, dashed lines in Figure 2.5(b,d)), the nanowire array exhibits broadband absorption enhancements across the visible spectrum. These absorption enhancements occur due to strong coupling into the HE_{11} waveguide mode, which has been engineered to occur over a broad spectral region via multiple wire radii that span the appropriate range.

In the single pass case, absorption is slightly lower in the blue, exhibiting the inverse problem to the tapered array (absorption dropped off in the red); this discrepancy occurs for two reasons: (1) the radii range of the multi-radii array is slightly larger than the tapered array, resulting in a red-shift of the absorption, and (2) the largest wire radius of the sub-cell targets the red region of the spectrum, which is more effective than the very edge of the wire taper. In the double pass case, the absorption is nearly flat at > 90% absorption, up to the band edge of InP, but does not drop to zero beyond the band edge.

Figure 2.6 displays simulated absorption spectra for each material in the median tapered array. Note that a broadband source was used for this simulation, which requires a polynomial fit to the refractive index. InP absorption beyond the band edge is a result of fitting errors. Up to the band edge of InP ($\lambda \sim 925$nm), the majority of the absorption occurs in the InP nanowires, and absorption contributions from the silver and chromium are negligible. Beyond the band edge, significant absorption occurs in the silver layer. At the silver interface, the nanowire radius is at a maximum, and because the radius was designed to achieve field enhancements up to the band edge, there are still significant field enhancements at slightly longer wavelengths, which, in the absence of InP absorption, enhance absorption in the silver in this region. Conversely, the Cr mask absorbs minimally because it is adjacent to regions of small nanowire radius, corresponding to field enhancements at shorter wavelengths where InP is strongly absorbing. In multi-radii arrays, both the Cr and the Ag absorb significantly beyond the band edge because the largest radius nanowire enhances the field near both the Cr and the Ag.

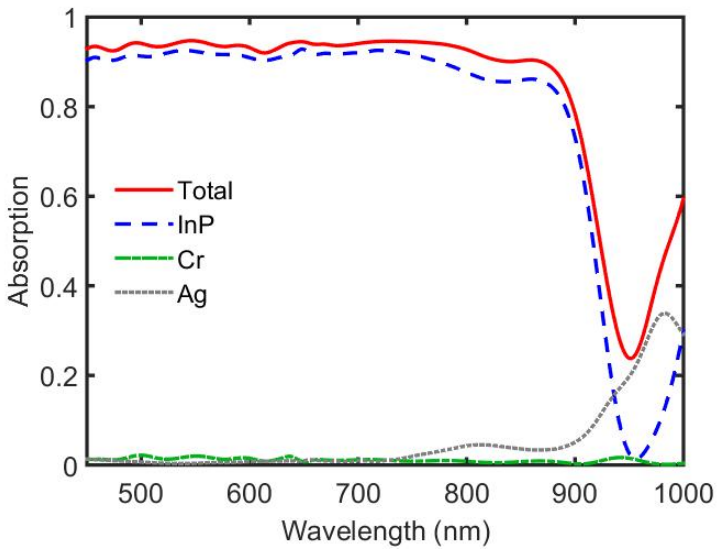

Figure 2.6: *Simulated absorption vs. wavelength of the median tapered array with a back reflector, separated by material.*

2.5 Conclusion and Outlook

In this work, we experimentally demonstrated near-unity, unselective absorption — absorption that is broadband, polarization-independent, and angle-insensitive — in sparse arrays of InP nanowire arrays, enabled by nanowire motif design. We explored two motifs — tapered nanowires and arrays of nanowires with varying radii — that aim to enhance absorption across a wide spectral range by optical design of the HE_{11} waveguide mode dispersion. Initially, we demonstrated that wire taper broadens the HE_{11} mode absorption peak and that incorporation of multiple wire radii results in multiple HE_{11} mode absorption peaks. Subsequently, we designed and fabricated sparse InP nanowire arrays using both wire taper and multiple wire radii that achieved near-unity, unselective absorption. Specifically, we achieved greater than 90% absorption up to the band edge of InP in a multi-radii nanowire array with a back reflector that contained approximately 100 nm planar equivalence of InP.

The cost of light absorbing material for high efficiency devices still creates big issues for real world application. Future direction involves developing large area nanowire arrays fabrication through a scalable, epitaxy-free fabrication method, for example, using nanoimprint lithography and wet etching. Polymer-embedded wires are removed from the bulk InP substrate by a mechanical method that facilitates extensive reuse of a single bulk InP wafer. The repeatable process of imprinting, etching, and peeling to obtain many nanowire arrays from one single wafer represents an economical manufacturing route for high efficiency III-V solar device. These semiconductor-based, spectrally, and angularly-unselective absorbers have great potential for flexible, high efficiency, and low-cost optoelectronic devices in energy and sensing applications.

CHAPTER 3
High Efficiency Solar to H_2 PEC Device

3.1 Introduction

Electrochemical water splitting was achieved by van Trostwijk and Deiman in 1789 and, about a decade later, by Nicholsen and Carlisle [65], whereas light-induced unassisted water splitting with rutile as a photoanode was reported in 1972, resulting in a small but measurable efficiency [54]. Efficient solar water splitting was first achieved using a dual junction tandem photoelectrode [66] under a light intensity equivalent to 11 suns.

In 2015, several devices with solar-to-hydrogen efficiency (STH) greater than 10 % at 1 sun illumination were reported [10], and in 2017 an efficiency of 16.2 % was achieved [5]. Overall, advances in solar water splitting [65] have led to a number of functional prototypes of photoelectrochemical and photoelectrosynthetic cells in recent years [58], featuring improved photoelectrode stability through the use of corrosion protection layers [67,68]. However, comparison of solar-to-hydrogen efficiencies realized so far with theoretical limiting efficiencies [69] shows considerable room for further improvement; at present, the highest efficiency systems reach about 2/3 of the theoretical limiting value for a given photoelectrode. To enable solar-to-hydrogen efficiencies approaching theoretical limits, the photovoltage has to be as large as possible, which requires a minimized photoelectrode dark current. This in turn dictates that the charge carrier recombination at interfaces must be prevented. To maximize the photocurrent, a reduction of the photoelectrode surface reflectivity under operating conditions is also required, as is mitigation of light absorption in the catalyst layer applied to the photoelectrode surface [70].

If one utilizes the band gap combination of a given tandem photoelectrode and the best reported exchange current densities for the HER and OER, omitting losses due to ERE and solution resistance, the realistic limiting STH efficiencies can be calculated [69]. For the tandem photoelectrode used here ($Ga_{0.41}In_{0.59}P/Ga_{0.89}In_{0.11}As$ with 1.78 eV and 1.26 eV), this value is 22.8 %. Approaching such limiting efficiencies provides a clear objective for a renewable fuels technology, since inclusion of hydrogen in the existing worldwide fuel generation infrastructure could enable direct and widespread application of renewable fuels in the transportation sector and for electricity generation [71].

Here, we demonstrate an approach to achieving efficiencies near the theoretical limits for the photoelectrode energy bandgaps employed. A key aspect of our approach is (i) the use of a crystalline anatase TiO_2 photocathode interfacial layer, deposited by atomic layer deposition (ALD), to facilitate reduced reflectivity and interface recombination velocity, and (ii) a size distribution and spatial arrangement of Rh catalyst nanoparticles tailored to achieve ultralow light attenuation. The crystalline anatase TiO_2 interlayer shows excellent energy band alignment with the tandem window layer and its interfacial ultrathin oxidized surface part and with the electrolyte. In addition, it serves as an efficient antireflection coating and as a support for the catalyst nanoparticles, with enhanced adhesion relative to III-V compound semiconductor surfaces.

3.2 Experimental Method

The dual-junction light absorber ($Ga_{0.41}In_{0.59}P/Ga_{0.89}In_{0.11}As$ with 1.78 eV and 1.26 eV) was grown by metal-organic vapor phase epitaxy in an Aixtron 2800-G4-TM reactor [72,73] on a 4'' p-GaAs (100) wafer with 6° offcut to [011] using a GaInAs metamorphic step-graded buffer layer to overcome the difference in lattice-constant between the substrate and the solar cell layers. The threading dislocation density after the metamorphic buffer is below $1x10^6$ cm^{-2}. Further details (layer composition and thickness) are given in the reference [72,73].

The native oxide on the back of the GaAs substrate was removed prior to metal ohmic contact deposition by (1) rinsing in acetone; (2) isopropanol; (3) 30 sec NH_4OH (10 %); (4) H_2O:N_2 and (5) drying in N_2. Immediately afterwards, 70 nm Pd, 70 nm Ti, and 200 nm Au were deposited by electron beam evaporation followed by rapid thermal annealing at 400 °C for 60 s under N_2 atmosphere [66]. Prior to the TiO_2 layer deposition, the front GaAs/GaInAs cap layer was removed in a chemical etch bath. The sample was (1) degreased by 15 s rinsing in 2-propanol, (2) 15 s in H_2O:N_2 followed by (3) a 60 s etch step in 25 % NH_4OH:30 % H_2O_2:H_2O (1:1:10), finishing with (4) a 20 s rinse in H_2O:N_2 and (5) drying under N_2 (Figure 3.1, step 1). Directly afterwards (a desiccator was used for sample transfer between systems), TiO_2 was deposited by atomic layer deposition (ALD) in an Ultratech Fiji F200/G2 ALD system using a titanium tetraisopropoxide (TTiP) precursor (STREM Chemical Inc.) and water as the oxidizer. The deposition temperature was set to 250 °C, and a total of 1500 ALD cycles were carried out (Figure 3.1, step 2). No high

temperature post annealing was required. Note that the edge of the sample had been carefully removed to prevent shunting of the front and back surfaces. Ag paste was applied to attach an ohmic contact to a coiled, tin-plated Cu wire which was then threaded through a glass tube. The sample was encapsulated and sealed to the glass tube using black epoxy (Electrolube ER2162). The exposed electrode surface area was precisely determined using an optical scanner and the open source software ImageJ. The steep edge of the high-viscosity epoxy was used as a borderline. Hence, the spill-out area (~20 µm, see reference [70]) was fully included in the area measurement. In this study the electrodes had different areas of 0.1 – 0.3 cm^2.

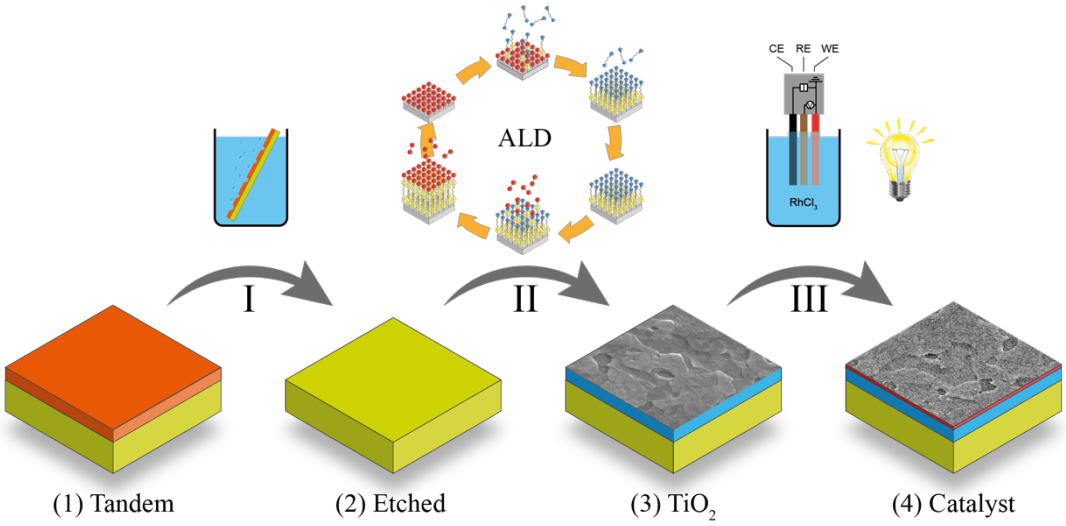

Figure 3.1: *Process flow for preparing the PEC device: (I) Chemical etching of the GaAs/GaInAs cap layer stopping at the AlInP window layer. (II) Deposition of the TiO_2 protection and antireflection coating with ALD. (III) Photoelectrochemical deposition of a closed layer of Rh nanoparticles onto the tandem.*

The Rh catalyst was photoeletrodeposited (Figure 3.1, step 3) in an aqueous solution of 0.5 mM Rh(III) chloride trihydrate (99.98%, Sigma Aldrich) + 0.5 M KCl (99.5%, Alfa Aesar) at +0.3 V vs. an SCE reference electrode under pulsed illumination. White light was provided by an Oriel Instruments Solar Simulator using a 1000 W Mercury-Xenon arc lamp. The frequency of the stroboscopic illumination resulted from the optical chopper frequency and the double structure of the chopper wheel.

Counter electrodes were prepared by sputtering ruthenium for 60 min on titanium foil (0.125 mm, 98 %, Sigma Aldrich) using an AJA sputtering system with a forward RF power of 200 W, 5 mTorr Ar atmosphere and a base pressure of $2x10^{-8}$ mTorr. Then, prepared electrodes were cut into 1 cm^2 pieces and attached with Ag paste to a tin-plated Cu wire which was then threaded through a glass tube. The counter electrode sample was encapsulated and sealed to the glass tube using black epoxy (Electrolube ER2162).

All photoelectrochemical measurements were performed using Biologic SP-200 potentiostats. 1 M $HClO_4$ was used as the electrolyte for pH 0 and 0.5 M KH_2PO_4/K_2HPO_4 phosphate buffer for pH 7. All electrolytes were purged with N_2 (4N) for minimum 1 h before usage. A saturated calomel electrode (SCE) was used as the reference electrode for three-electrode measurements. Custom-made three-necked cell Glass cells with a quartz window with a volume of 35 mL were used as the vessel for the experiments, allowing them to be easily cleaned in Aqua Regia. To avoid internal reflections in the cell, a black mask was directly attached in front of the quartz window so that only the sample itself was illuminated. The tandem device with areas ranging from 0.1 – 0.3 cm^2 was positioned 10 mm away from the quartz window with the counter electrode of a size of 0.6 cm^2 being placed in close vicinity to the working electrode. The photograph of the custom-built cell is shown in Figure 3.2. The electrolyte was vigorously agitated with a magnetic stir bar to minimize the diffusion losses. J-V measurements were performed with a scan velocity of 50 mV/s. To prevent the degradation from running at anodic condition where the dark current occurred, we only recorded J-V curves until 0 V vs. the counter electrode. Stability and efficiency tests were carried out in a two electrode configuration using a calibrated Class AAA AM1.5G solar spectrum provide by an ABET Technologies Sun 3000 Solar Simulator (Figure 3.3). The light intensity was set to 100 mW/cm^2 using a calibrated silicon reference solar cell.

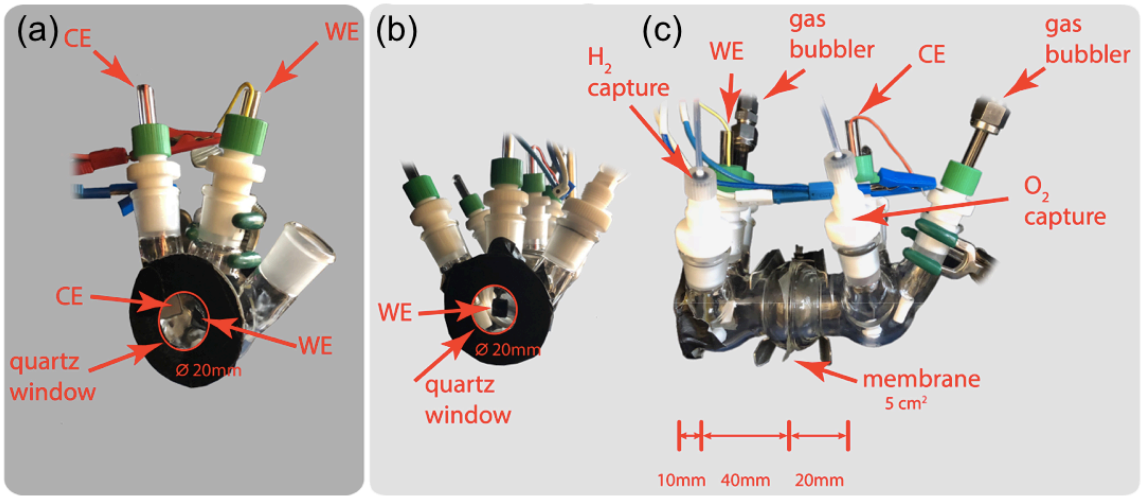

Figure 3.2: *(a) Cell used for high efficiency benchmarking with WE and CE in close vicinity. The distance WE to window is 10 mm and the distance WE to CE is < 10 mm. (b) Front view and (c) side view of the double glass cell used for gas collection. The distance WE to window is 10 mm, the distance WE to membrane is 40 mm and the distance membrane to CE is 20 mm. The membrane has an area of 5 cm². Each compartment has a gas bubbler for pre-saturation of the electrolyte with H_2/O_2 purging and gas outlets which are connected to inverted water filled burette for gas collection. For both cells (a) and (b/c) the quartz window is covered with black tape having an opening with ∅20 mm.*

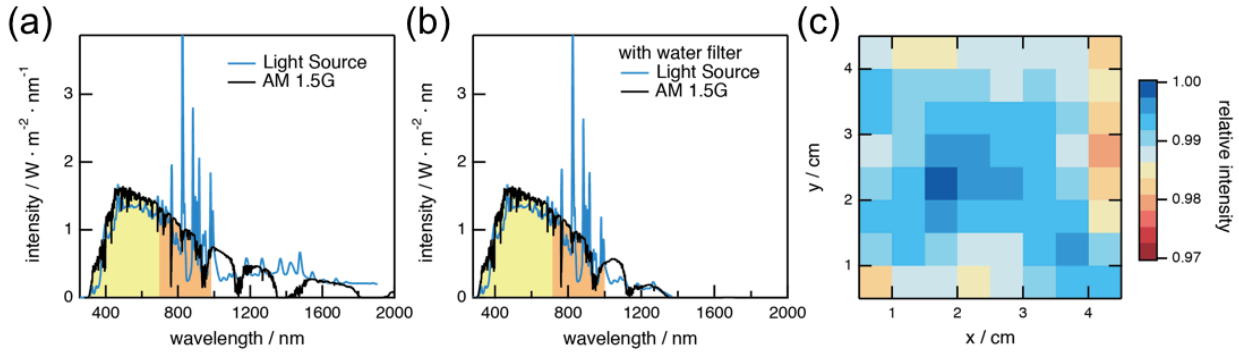

Figure 3.3: *(a) Light spectrum of the solar simulator (ABET Sun 3000 Solar Simulator) and AM1.5G spectrum. (b) Light spectrum of the solar simulator and AM1.5G with water filter. (c) Uniformity map of the solar simulator illumination area. The band gaps of the dual-junction light absorber are indicated in (a) and (b). (Yellow color for top cell and orange color for bottom cell.)*

External quantum efficiency (EQE) measurements were performed on fully processed tandem devices solely to calculate the spectral correction factor to account for the difference between artificial and solar illumination. Hence, to avoid hydrogen evolution and H_2 bubble formation during EQE measurements, a 50 mM methyl viologen hydrate (98%, ACROS Organics), dissolved in ultrapure water, was used as the electrolyte. For continuous light biasing of each individual tandem sub-cell during EQE measurements of the complementary sub-cell, a 780 nm high-power LED (Thorlabs M780L2) was used to bias the bottom cell and a 455 nm high-power LED (Thorlabs M455L2) was used to bias the top cell. Monochromatic illumination was delivered by an Oriel Solar Simulator with a 150 W Mercury-Xenon arc lamp attached to a Newport monochromator (1200 lines/mm). The monochromatic light was chopped at 10 Hz. The modulated photocurrent was amplified by an SRS model SR570 low noise current preamplifier. The current preamplifier was also used to supply a -1 V bias to the tandem working electrode to ensure measurement in the light limiting current regime. A coiled Pt wire was used as the counter electrode for this two-electrode measurement. The output from the preamplifier was then measured by a SRS model SR830 lock-in amplifier which was phase locked to the frequency of the optical chopper yielding the photocurrent for the individual sub-cell $J_{top/bottom}(\lambda)$.

To measure the absolute light intensity ($W \cdot nm^{-1} \cdot cm^{-2}$) as delivered by the monochromator, a certified calibrated silicon diode (biased at -1 V) was positioned in the light path inside the photoelectrochemical cell filled with the electrolyte (to exclude effects of the electrolyte and quartz window on the measured light intensity), and the photocurrent density was measured (the LEDs for light biasing of the tandem were switched off during this reference scan). The photocurrent density could then be converted to the light intensity $I(\lambda)$ by the known spectral response of the silicon diode. The EQE for each sub-cell is then given by

$$EQE_{top/bottom}(\lambda) = \frac{R_{top/bottom}(\lambda)}{\lambda} \cdot \frac{hc}{e} = \frac{J_{top/bottom}(\lambda)}{I(\lambda)} \cdot \frac{1}{\lambda} \cdot \frac{hc}{e} \text{(Equation 3.1)}$$

$J_{top/bottom}(\lambda)$ is the photocurrent density of the corresponding sub-cell in $A \cdot nm^{-1} \cdot cm^{-2}$, $I(\lambda)$ the light intensity delivered by the monochromator in $W \cdot nm^{-1} \cdot cm^{-2}$, λ is the wavelength in nm, h is the Planck constant, c is the speed of light in a vacuum, and e is the elementary charge. $R_{top/bottom}$ is the spectral response for each sub-cell.

To obtain the Faraday efficiency, hydrogen and oxygen gas collection were performed using a eudiometric gas collection setup. A SELEMINON ion exchange membrane with an area of 5 cm^2 in size was utilized to separate the cathode and anode chamber. Electrolytes were purged with ultrapure N_2 (4N), the cathode side was pre-sutured with H_2, and the anode side was pre-saturated with O_2 by means of H_2 and O_2 gas bubbling through a fine gas dispersion frit for an hour. Each side was sealed against the ambient but connected via a short thin tubing to an inverted water filled burette (purged and pre-saturated). The change in pressure in each burette upon H_2 and O_2 gas collection due to photoelectrochemical water splitting in the PEC cell was monitored by pressure transducers (EXTECH HD755). The change in pressure over time was then converted to a gas volume under consideration of the reduced pressure in the inverted burette. For constant temperature, $\Delta V_0 = \frac{P}{P_0} \cdot \Delta V$ with $P = (407.2 - h)$ and $P_0 = 407.2$, using inWC (inches of water column) as pressure units. $\frac{P}{P_0}$ is the volumetric correction factor necessary to account for reduced pressure in the inverted burette. The expected produced volume of hydrogen and oxygen gas for the cathodic and anodic reaction was calculated by the transferred electrical charge as measured by the potentiostat.

Optical measurements were performed to obtain reflectivity spectra for different surface layer stacks in air. A Cary 5000 UV/vis/NIR with an integrating sphere that includes a diffuse reflectivity measurement was used. For surface topography studies, a Bruker Dimension Icon AFM in Peakforce mode was used. Scanning electron microscopy images were obtained with a FEI Nova NanoSEM 450 microscope. XPS measurements were performed using a Kratos Axis Ultra and Surface Science M-Probe system with a base pressure of < $1x10^{-9}$ mTorr. A monochromatic AlKα (hK = 1486.69 eV) source with a power of 150 W was used for all measurements. He I ultraviolet photoelectron spectroscopy (UPS) was performed on the Kratos Axis Ultra system using a Helium gas discharge lamp.

3.3 Results and Discussion

We employed a dual-junction tandem photoelectrode where the high band gap subcell thickness had been increased for better current matching, and the transparency of the tunnel diode

was improved [70,72,73]. To further increase the STH efficiency, interfacial layers were designed to reduce charge carrier recombination and to increase optical light coupling into the photoelectrode absorber layers. The surface conditioning sequence resulted in etching of the GaAs cap layer by a NH_4OH-H_2O_2-H_2O solution, leaving an oxidized surface layer ($AlInPO_x$) on top of the n^+-doped AlInP window layer. A crystalline anatase TiO_2 film with an effective thickness of 30 nm was deposited to act as a corrosion protection layer and an antireflection coating, as well as serving as conducting substrate surface for photoelectrodeposition of Rh nanoparticle (NP) electrocatalysts. The Rh NPs exhibited large surface areas and thus high exchange current and, simultaneously, particularly low light attenuation. The photocathode device configuration employed is generally less prone to photodecomposition than photoanode devices, where charge carriers with high oxidation potential are present at the semiconductor surface.

Figure 3.4 shows a schematic of the resulting device: the photoelectrode consisting of GaInP and GaInAs subcells on a GaAs substrate, an anatase TiO_2 protective layer, the Rh NPs catalyst layer, and a sputtered RuO_2 counter electrode (OER) are depicted. Also depicted on the side of the layer structure is an energy band diagram under illumination where the quasi Fermi levels show the splitting for electrons, and holes necessary to achieve unassisted water splitting. Measurement of band gap, work function, and band bending are included in Figure 3.5 and Figure 3.6. The corresponding energy band relations can be inferred from surface characterization using ultraviolet and X-ray photoelectron spectroscopy. While the simplest approach to assessment of band alignment follows Anderson's idealized model [67] for planar contacts and does not consider energy band shifts due to surface and/or interface dipoles, this approach certainly does not apply here, as the junctions formed at the AlInP/oxide, oxide/TiO_2 and TiO_2/Rh/electrolyte interfaces are complex. Thus the energy band diagram of the heterojunction structure was inferred from ultraviolet and X-ray photoelectron spectroscopy measurements. It should be noted that equilibrium formation between small metallic catalyst nanoparticles and semiconductors appears to depend on the substrate doping level [10] and does obviously not follow a Schottky thermionic emission model, in particular in contact with an electrolyte [68,69]. In addition, metal work functions depend on NP size [70], so comparison of the energy levels of NP catalyst layers with planar thin films is notably challenging; therefore, only an estimate of the NP catalyst layer energy level can be given, supported by the device operating data. The resulting surface band alignment as

displayed in Figure 3.7 can be obtained after aligning the Fermi level of the solid state device to the hydrogen evolution potential (HER) at 4.6 eV. Due to the higher work function of 4.5 eV for TiO_2 than 4.1 eV for the tandem, a lower barrier from 0.5 eV to 0.1 eV for hydrogen evolution (HER) will be expected.

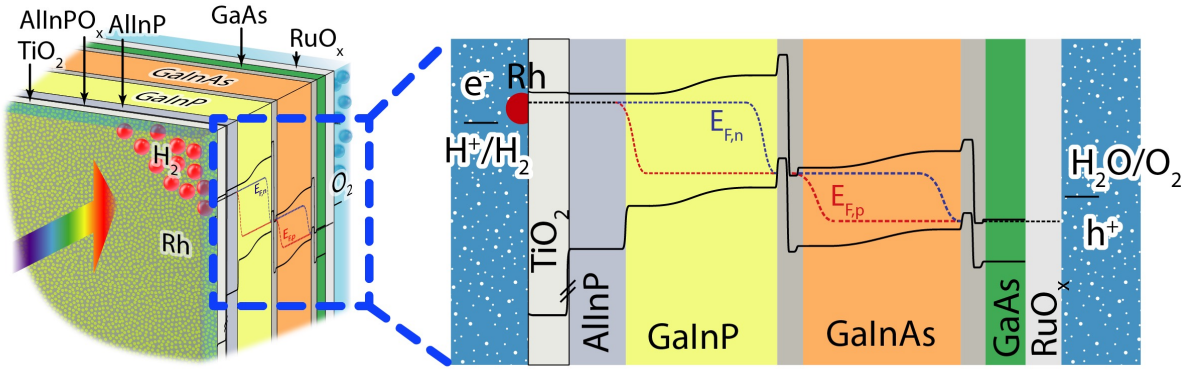

Figure 3.4: *Illustration of the photoelectrochemical water splitting device structure after functionalization with interfacial films and electrocatalysts. Band alignment at the operation point is depicted on the side and zoomed in to gain the visibility.*

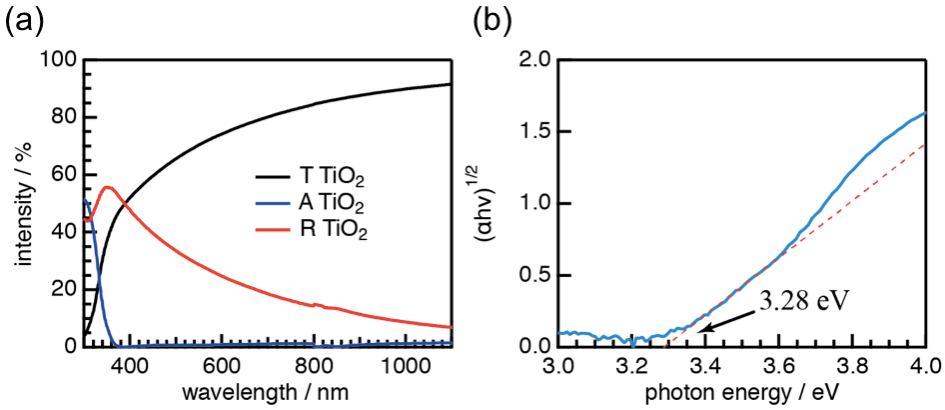

Figure 3.5: *(a) Optical properties (A: absorption, T: transmission, R: reflection) of TiO_2 (TTiP ALD) in air. (b) Tauc plot of ALD grown TiO_2. The intersection with the horizontal axis indicates an indirect optical gap around 3.3 eV.*

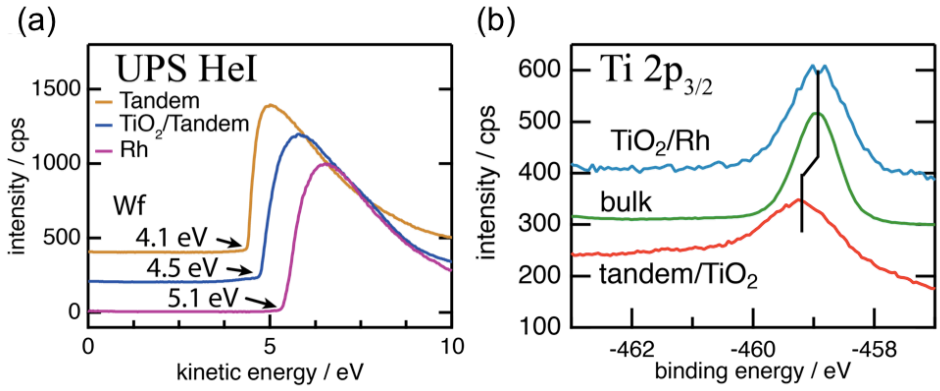

Figure 3.6: *(a) Work function measurements by UPS for the tandem, for TiO_2 on the tandem, and for Rh metal. The increase of work function from 4.1 eV to 4.5 eV was observed after applying TiO_2 protection layer on tandem. The Rh metal spectrum is measured on the foil as a reference instead of the photoelectrochemical deposited nanoparticles. (b) Core level shift of Ti $2p_{3/2}$ indicating ~0.3 eV downward band bending at the tandem/TiO_2 interface and nearly no band bending at the TiO_2/Rh interface. The tandem/TiO_2 sample was made with 40 ALD cycles TiO_2 on top of the tandem. The Rh has originally high metal work function of 5.1 eV but does not create band bending at the junction with TiO_2. This can be explained by the pinch-off effect when the metal NPs are small enough that the Fermi level would directly attach to the semiconductor Fermi level without creating a barrier* [71].

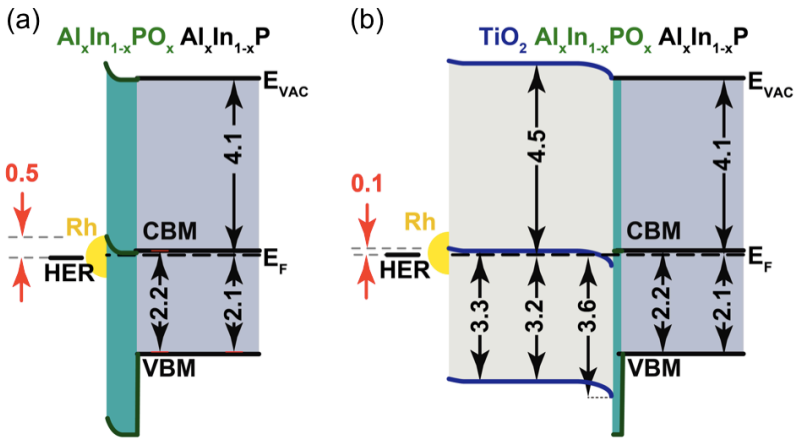

Figure 3.7: *Surface band alignment of the electrolyte interface layers (a) without and (b) with TiO_2.*

The surface of the crystalline TiO_2 film illustrated in Figure 3.8 indicates a continuous film with height variations, seen by AFM, that give it a flake-like appearance. The TiO_2 is then decorated with a uniformly dense layer of ca. 10 nm Rh nanoparticles. The catalyst distribution of the optimized devices is also shown in Figure 3.8. Figure 3.9 illustrates the protocol for pulsed photoelectrodeposition of Rh catalyst nanoparticles. The potential choices made are indicated by black dots; the best result was obtained for E = +0.3 V vs. SCE. Fine control of particle size smaller than 20 nm was achieved by careful adjustment of the electrode potential, enabling considerably higher catalyst loading compared to a dense film of equivalent catalyst loading deposited by conventional vapor phase or electrochemical reduction. This procedure facilitates photocathodes with high transparency catalysts, which maintain the high photocurrent densities and result in increased efficiency, which is determined from the relation

$\eta_{STH} = \frac{J_{op} \cdot \Delta U_{rxn} \cdot f_{FE}}{P_{in}}$ (Equation 3.2).

The solar fuel generator efficiency η_{STH} is given by the operating current at the counter electrode potential, the thermodynamic value for the reaction (ΔU_{rxn} = 1.23 V for water splitting under standard conditions), and by the reaction Faradaic efficiency f_{FE}, determined by gas product analysis measurements.

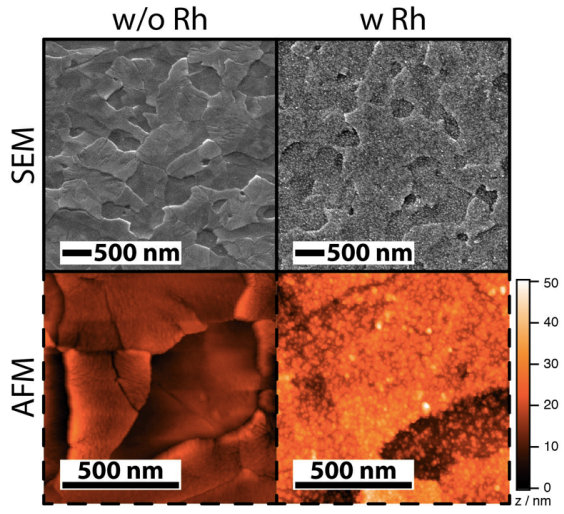

Figure 3.8: *SEM images and AFM microtopographs of the dual-junction PEC device with TiO_2 coating with and without Rh catalyst nanoparticles. The scale bar is 500 nm. The AFM images are*

scaled to the same 50 nm z-axis dynamic range. The surface roughness (RMS) is 3.6 nm without Rh and 6.3 nm with Rh.

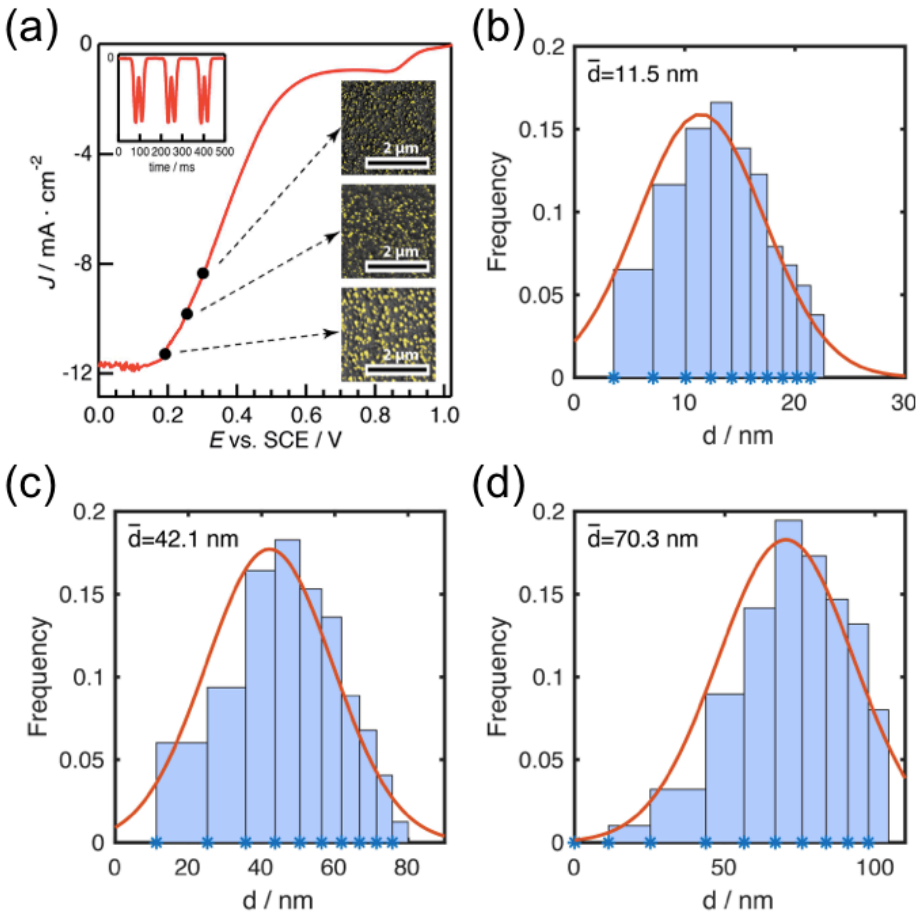

Figure 3.9: *(a) Fine control of particle size d ranging from 10 nm to 100 nm is achievable by appropriate adjustment of the potential during catalyst electrochemical deposition. Stroboscopic deposition under white light illumination as shown in the upper left insert. The three images on the right inset are SEM images with scale bar 2 µm. (b-d) Particle size histograms correspond to each SEM image depicted from top to bottom in (a) with the most frequent particle size indicated by* $\bar{d}$.

Electronically, the photoelectrode configuration used here facilitates alignment of the conduction bands of the AlInP window layer of the tandem photoelectrode to the indium oxide and indium phosphate layers (created by the cap layer etching process) and the anatase TiO_2 protection/antireflective layer. We note that photogenerated electrons, which are minority carriers in the main part of the tandem subcells, become majority carriers in the AlInP and TiO_2 layers, reducing recombination losses in carrier transport. In addition, the large valence band offset between AlInP and TiO_2 blocks interfacial hole transport, resulting in a small overall reverse saturation current, improving the photovoltage. This feature is important for achieving high STH efficiencies.

Amorphous defective TiO_2 coatings have been commonly applied using ALD with Tetrakis(dimethylamino)titanium (TDMAT) precursors to yield protected photoanodes, a concept designed to facilitate transport of holes through a defect band in the TiO_2 [68,74]. However, the dominant process that limits the photoelectrochemical performance of high-quality semiconductors is not transport but interface recombination. Thus, we instead utilize a defect band free, microcrystalline anatase phase TiO_2 coating formed by ALD with titanium tetraisopropoxide (TTiP) precursors as an electron-selective contact to protect the surface of photocathode from photocorrosion (Figure 3.10).

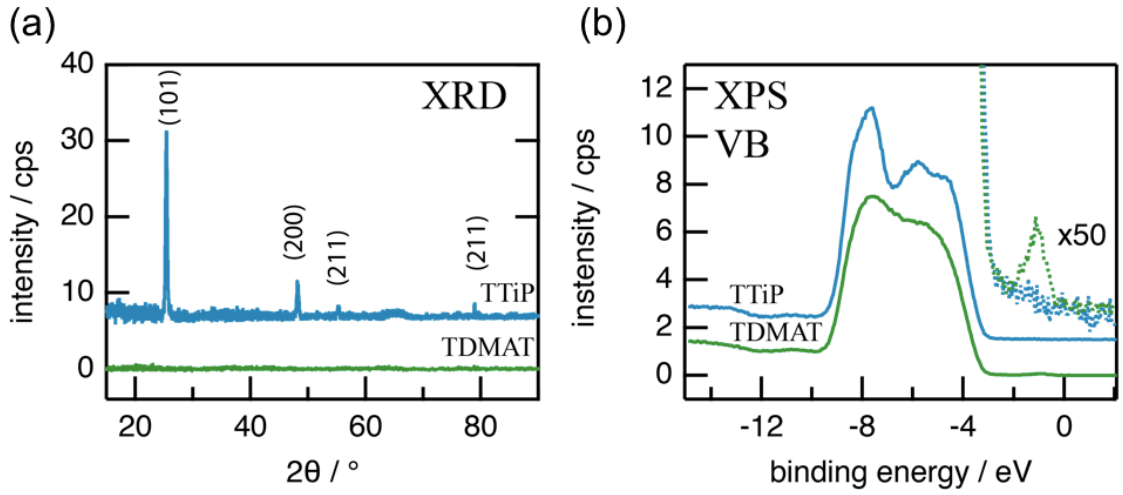

Figure 3.10: *(a) X-ray diffraction data of ALD deposited TiO_2 from TTiP or TDMAT precursor. The TTiP TiO_2 shows anatase crystalline phase while the TDMAT TiO_2 is amorphous. (b) XPS valance band spectra of TTiP and TDMAT TiO_2. A defect band in TDMAT TiO_2 can be observed*

at -1 eV which facilitates hole transport in photoanodes [74]. Instead, TTiP TiO_2 exhibits an XPS spectrum without a defect band and would be more suited to prevent recombination in photocathodes.

To assess the optimal thickness, we performed a series of optical reflectivity measurements on TiO_2 films deposited by atomic layer deposition (ALD) on the tandem photoelectrodes with various thicknesses in the range of interest. The results are shown in Figure 3.11(a). We find the 30nm thickness TiO_2 layer reported in the manuscript has the lowest reflection in the relevant spectral range. Figure 3.11(b) shows results of calculations using full wave electromagnetic simulations performed using finite-difference time-domain methods (Lumerical FDTD) assessing the effect of thickness variations on optical reflectivity similar to the experimental results. For the TiO_2, we find a very low reflectivity over a wide spectral range for a nominal thickness of 30 nm.

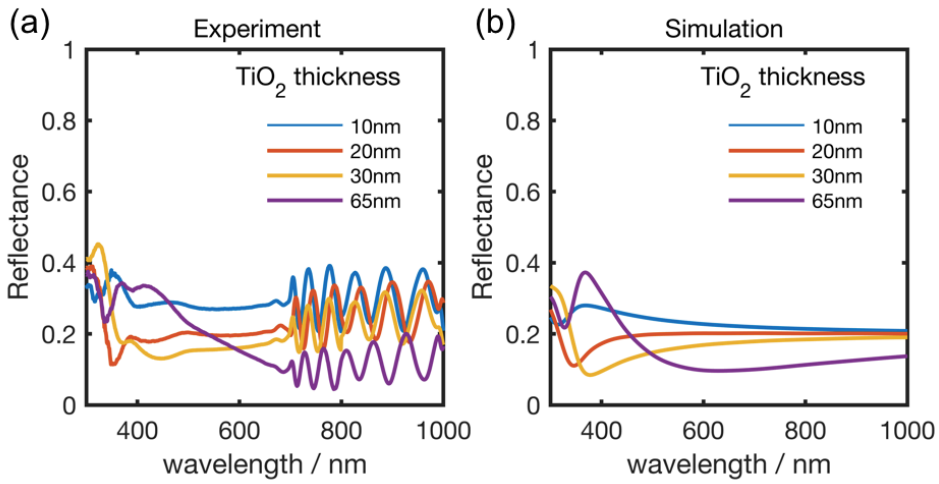

Figure 3.11: *(a) Reflectance, measured in air, of the dual-junction tandem solar cell with different thicknesses of the TiO_2 coating by changing the ALD deposited cycles. (b) Reflectance, simulated by Lumerical FDTD, with different thicknesses of TiO_2 for correlation with the experimental results.*

To optimize light coupling, we also carefully tailored the optical properties of the Rh nanoparticles to work in combination with an optimum TiO_2 thickness of 30nm, determining the reflectance, absorbance, and transmittance. To determine the influence of the Rh particle size on

reflectance, absorbance, and transmittance, we modeled three particle sizes using full wave electromagnetic simulations. The optical transmission modeling in Figure 3.12(b) shows that for a 10nm Rh particle size, an optimum is reached. We show that the transmittance and photoelectrode light coupling for the entire structure consisting of (tandem photoelectrode/30nm TiO_2/10nm Rh particles) is almost identical to a bare surface without Rh. Although a 40 nm Rh particle size shows lower reflectivity in the relevant spectral range in Figure 3.12(a), the Rh particle absorption increases substantially, resulting in an overall lowered transmittance into the cell, as seen in Figure 3.12(c). The transmittance is therefore reduced and fewer photons reach the photoactive part of the cell (see Figure 3.12(b)).

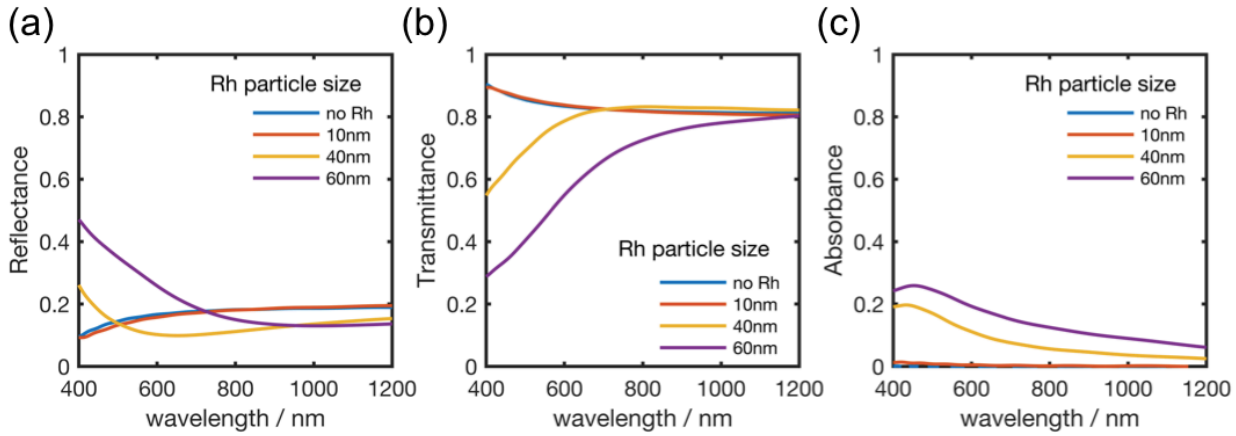

Figure 3.12: *FDTD simulated (a) reflectance, (b) transmittance, and (c) absorption defined as A = 1 - R - T of different Rh particle sizes on 30nmTiO2/AlInP (window layer of the tandem).*

A similar trend is observed in the experimental results shown in Figure 3.13. We measured the reflectance of samples with different particle size. The blue curve shows the reflectance of the tandem with a TiO_2 layer, but without Rh catalysts. The red curve shows the system with ~10nm Rh particles added, as used in our record device. As can be seen from the simulations in Figure 3.12(b), we expect the 10nm Rh particles to be effectively transparent. The yellow and purple curves show the reflectance with medium and large sized Rh particles, which would lead to a larger loss due to parasitic absorption and reflection.

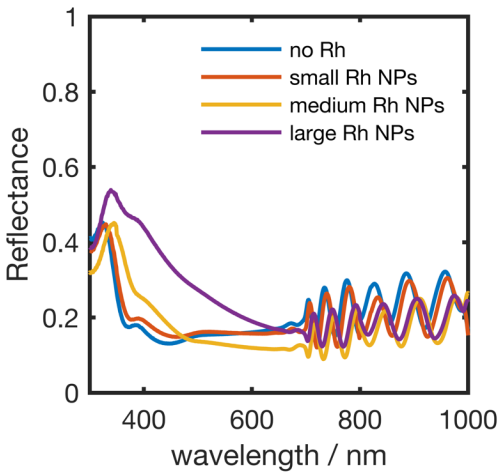

Figure 3.13: *Reflectance, measured in air, of samples with different Rh NPs size on the dual-junction tandem solar cell with 1500 ALD cycles TiO_2 corresponding to a layer thickness of 30 nm.*

The influence of the surface modifications on optical properties and on the photocurrent of the optimized device is shown in Figure 3.14. A reduction of the reflectivity by ~15 % is achieved by use of the TiO_2 interlayer (Figure 3.15) whereas the Rh NPs in Figure 3.14(a) show negligible additional absorption, which is attributed to the blue-shifted plasmonic resonance of the Rh nanoparticles. For particle sizes below 20 nm, a shift from the visible region into the ultraviolet one occurs, making the Rh layer almost fully transparent [75,76]. The output data shown in Figure 3.14(b) were obtained in an acidic electrolyte of pH 0. The corresponding photocurrent-voltage characteristics in acidic electrolyte demonstrate a pronounced increase in the current and, as expected, also a shift of the bend of the photocurrent characteristic towards more anodic potentials, thereby additionally increasing the photocurrent at the RuO_2 counter electrode (OER) potential. The result with incorporation of TiO_2 is a relative increase of 28 % of the tandem cell output. An STH efficiency of 19.3 % is obtained at 0 V, with an operating current of 15.7 mA/cm^2, assuming an initial Faradaic efficiency of unity, which is supported by the gas evolution measurements. These data represent a 20 % increase in efficiency above the previously reported one sun photoelectrosynthetic cell efficiency benchmark [5]. The high photocurrent at 0 V vs. RuO_2 indicates that electron transport is virtually uninhibited from the absorber layer through the indium and phosphorus oxide and TiO_2 interfacial layers to the electrolyte, matching well with the surface band alignment analysis.

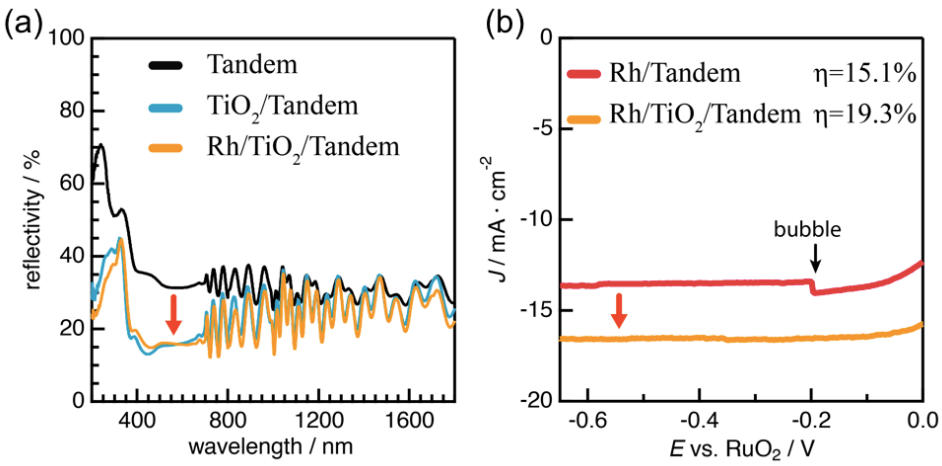

Figure 3.14: *Optoelectronic properties of the surface functionalized electrolyte / Rh / TiO_2 / oxide / AlInP - GaInP / GaInAs / GaAs water splitting device. (a) Reflectivity, measured in air, of the dual-junction tandem solar cell without ARC (black curve), secondly reflectivity obtained after TiO_2 coating (blue curve) and after photoelectrochemically deposited Rh NPs (yellow curve). Reflectivity is larger than under operation in the electrolyte due to the different refractive indices of air and water. (b) Comparison of the output characteristics of the tandem device after cap layer etching and of the fully surface functionalized photoelectrode. The orange arrows indicate the improvement after incorporation of the TiO_2 layer.*

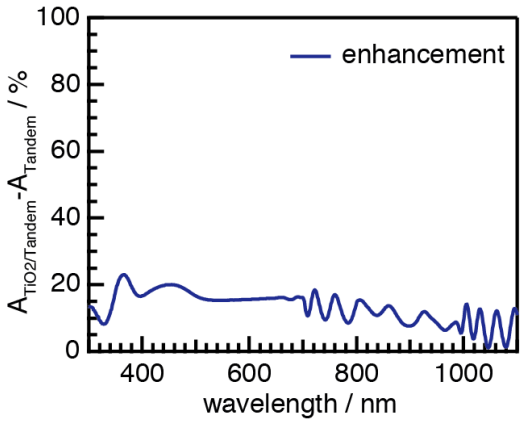

Figure 3.15: *The enhancement of absorption based on the reduction of the reflectivity for the PEC device due to employment of TiO_2 layer. (Absorption = 1-Reflection) The 15% average increase of absorption can directly contribute to the enhancement of photocurrent.*

The observed unassisted water splitting efficiencies critically depend on the experimental conditions. In order to consider the influence of the spectral mismatch of the irradiance between our solar simulator and the AM1.5G spectrum, a spectral correction factor (SCF) was calculated. It is based on the relative EQE of the device, the irradiance of the solar simulator $\{I_{meas}(\lambda)\}$ and the AM1.5G reference spectrum $\{I_{AM1.5G}(\lambda)\}$ (Figure 3.3(a)). The influence of the water filter $\{F_{water}(\lambda)\}$ on the spectra was considered for the calculations (Figure 3.3(b)). The index j denotes to the individual sub cell.

$$J_{AM1.5G} = J_{meas} \cdot \frac{\min_j \int_{280nm}^{1200nm} I_{AM1.5G}(\lambda) \cdot F_{water}(\lambda) \cdot EQE_{j,device}(\lambda) d\lambda}{\min_j \int_{280nm}^{1200nm} I_{meas}(\lambda) \cdot F_{water}(\lambda) \cdot EQE_{j,device}(\lambda) d\lambda} = J_{meas} \cdot SCF \quad \text{(Equation 3.3).}$$

For illumination under AM1.5G conditions, the AM1.5G ASTM G-173 reference spectrum was taken from the Renewable Resource Data Center (RReDC) of the National Renewable Energy Laboratory (NREL). Although the SCF is a simple correction between spectra, we still need to be careful to prevent artificial inflation or underestimation of efficiency. We note that the SCF will be unsuitable to apply with large deviation from 1 since the current correction will become unrealistic due to severe difference of overpotential and bubble formation.

To calculate the spectral correction factor (SCF) between solar simulator and the AM1.5G spectrum, the EQE measurements were performed in 50 mM methyl viologen where no bubble formation would deteriorate the accuracy. The bias light was 780 nm and 455 nm for the bottom and top sub-cell, respectively. The result is shown in Figure 3.16. To correct for nonparallel illumination in the solar simulator that results in focusing of the light by the quartz window, the beam divergence in each axis was experimentally determined, and a concentration ratio (CR) was calculated (Figure 3.17). The corrected photocurrent is given by $J_0 = \frac{J_{meas}}{CR}$. The total correction factor for each sample is then given by $J_{AM1.5G} = J_{meas} \cdot SCF/CR$, e.g. for the 19.3 % efficient cell reported in this study, the values are SCF = 1.024 and CR = 1.028.

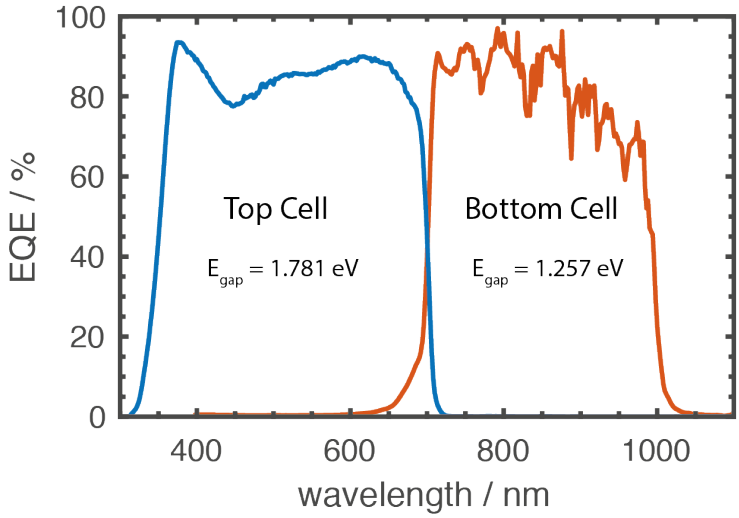

Figure 3.16: *Relative EQE of a fully processed PEC tandem device: the bandgap combination is determined to be around 1.78 eV for the top cell and 1.26 eV for the bottom cell.*

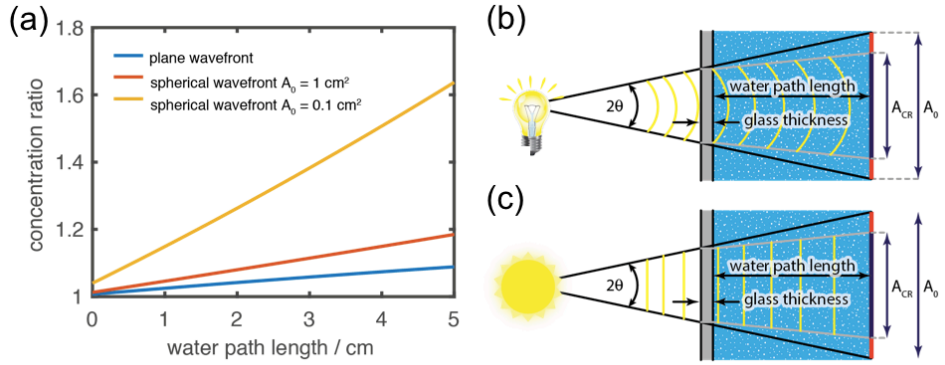

Figure 3.17: *(a) Calculated optical concentration ratio of the non-parallel light-beam of solar simulator illumination in PEC cells for plane wavefront and spherical wavefront as a function of water path length. (b) Illustration of the spherical wavefront case. The concentration ratio (CR = A0/ACR) depends on the exact sample area A0. (c) Illustration of the plane wavefront case. An opening aperture in front of the quartz window of the PEC cell with a diameter of 2 cm was used in this study. The beam divergence was experimentally determined to be Θ_V = 1.8 ° vertically and Θ_H = 2.5 ° horizontally by measuring the size increase of the light beam through a 2 cm aperture at specific distances (10 cm to 30 cm).*

For an evaluation of the influence of polarization losses including ohmic losses, diffusion losses, and kinetic losses [77], we simulated the maximum obtainable efficiencies in the detailed-balance scheme with the program YaSoFo [70]. Since the electrolyte was vigorously agitated and buffered, we are able to minimize the diffusion losses. Optical losses were assumed to be the cause for the difference in theoretical and practically obtained limiting photocurrents. In the simulation, these were taken into account by scaling the AM 1.5G spectrum with a constant factor of 0.89. The diode current-voltage curve (ideality factor n_i=1) intersected with the characteristics of the catalyst following a Tafel behavior described by exchange current density and Tafel slope under the assumption of an additional ohmic drop of 2 Ω. Fig. Figure 3.18(a) shows the maximum STH efficiency as a function of exchange current density and Tafel slope. We observe that in the regime of our OER catalyst (exchange current density of ~10^{-3} mA·cm^{-2} for RuO_2, Tafel slope for RuO_2 as 83 mV·dec^{-1} at pH 0 and 100 mV·dec^{-1} at pH 7, see Figure 3.19), the exchange current density and Tafel slope are still in the plateau of the maximum efficiency; the corresponding points are indicated in Figure 3.18(a). As our case catalysis is dominated by the OER, it is not an efficiency-limiting factor of our setup. We also show in Figure 3.18(b) the efficiency as a function of the ohmic drop. For this analysis, we fixed exchange current density and Tafel slope to typical values of IrO_2 and varied the ohmic resistivity. One notices that the efficiency only starts to drop at high values beyond 40 Ω, which is why the resistive overpotential is not limiting in our setup, either. Combining the ohmic loss that can be induced from the electrolyte (~4 Ω for pH 0 and ~15 Ω for pH 7), and interface loss from imperfect surface band alignment (~40 Ω without TiO_2 and ~6 Ω with TiO_2), our record device photocurrent is still located at the linear region which indicates that the optical losses are prevailing in our system. However, the system, in principle, reacts sensitively to the polarization losses, emphasizing the importance of judiciously combining interface and catalyst.

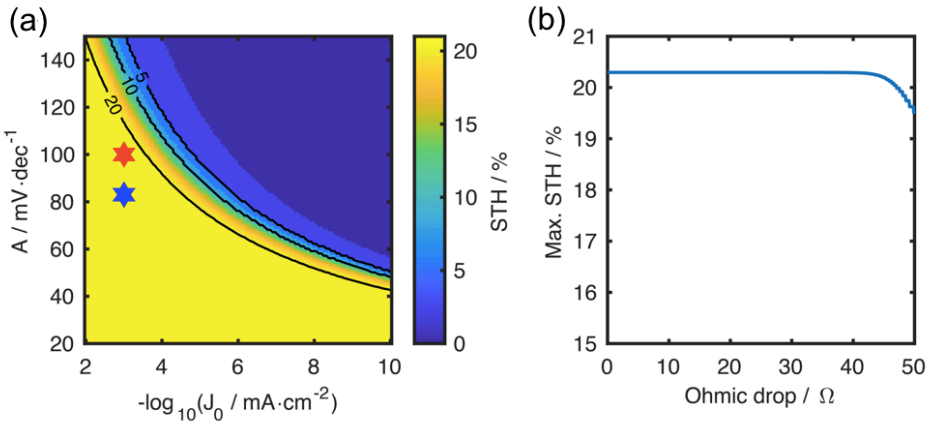

Figure 3.18: *Calculated maximum STH efficiency as function of (a) Tafel slope A and exchange current density J_0, (b) ohmic drop. Maximum obtainable efficiencies for the given tandem absorber are shown in the detailed-balance scheme as a function of the catalyst parameters and resistivity loss. The maximum photocurrent density was scaled to the experimentally determined current density under strong cathodic bias. The blue star indicates our device under pH 0 condition and the red star indicates our device under pH 7 condition.*

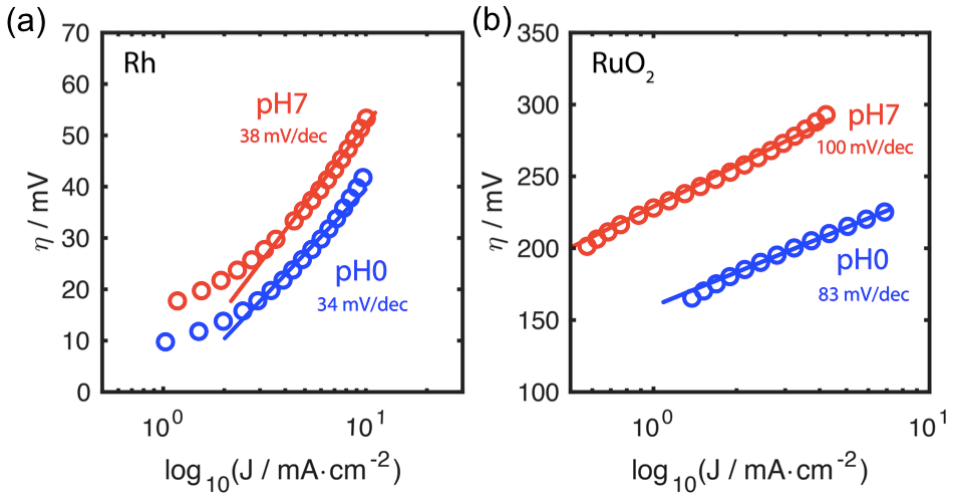

Figure 3.19: *Tafel plots of (a) Rh and (b) RuO_2 catalysts under pH 0 and pH 7 conditions. The Tafel slopes are 34, 38, 83, and 100 mV·dec^{-1} for Rh-pH_0, Rh-pH_7, RuO_2-pH0, and RuO_2-pH7 respectively.*

Figure 3.20 summarizes the main performance characteristics. Figure 3.20(a) illustrates the photocurrent-voltage characteristics under three conditions: i) at pH 0 with 19.3% STH, ii) at neutral pH with 18.5 % STH, and iii) using an anion exchange membrane (AEM) with an STH of 14.8 %. Figure 3.20(b) gives the unassisted two-electrode photocurrent density vs. time for the initial operation regime, showing that while the photocurrent density decreases with time for acidic pH, it remains more stable in neutral pH solutions. Chronoamperometric tests (at -0.4 V vs. counter electrode as shown in Figure 3.20(c) show that the device photocurrent density decreases in an acidic electrolyte to low values within 3 h. However, in neutral pH electrolyte, stability over 20 h was demonstrated, with the photocurrent density remaining at 83 % of its initial value. In both cases, for pH 0 and pH 7, near unity Faradaic efficiency is confirmed through the agreement between the expected (solid line) and measured gas volumes (symbols) in Figure 3.20(d). However, whereas the curves for pH 7 stay linear with a constant gas production rate for H_2/O_2, as expected from the stability measurements, the curves for pH 0 show a deviation from linearity due to the decreasing photocurrent.

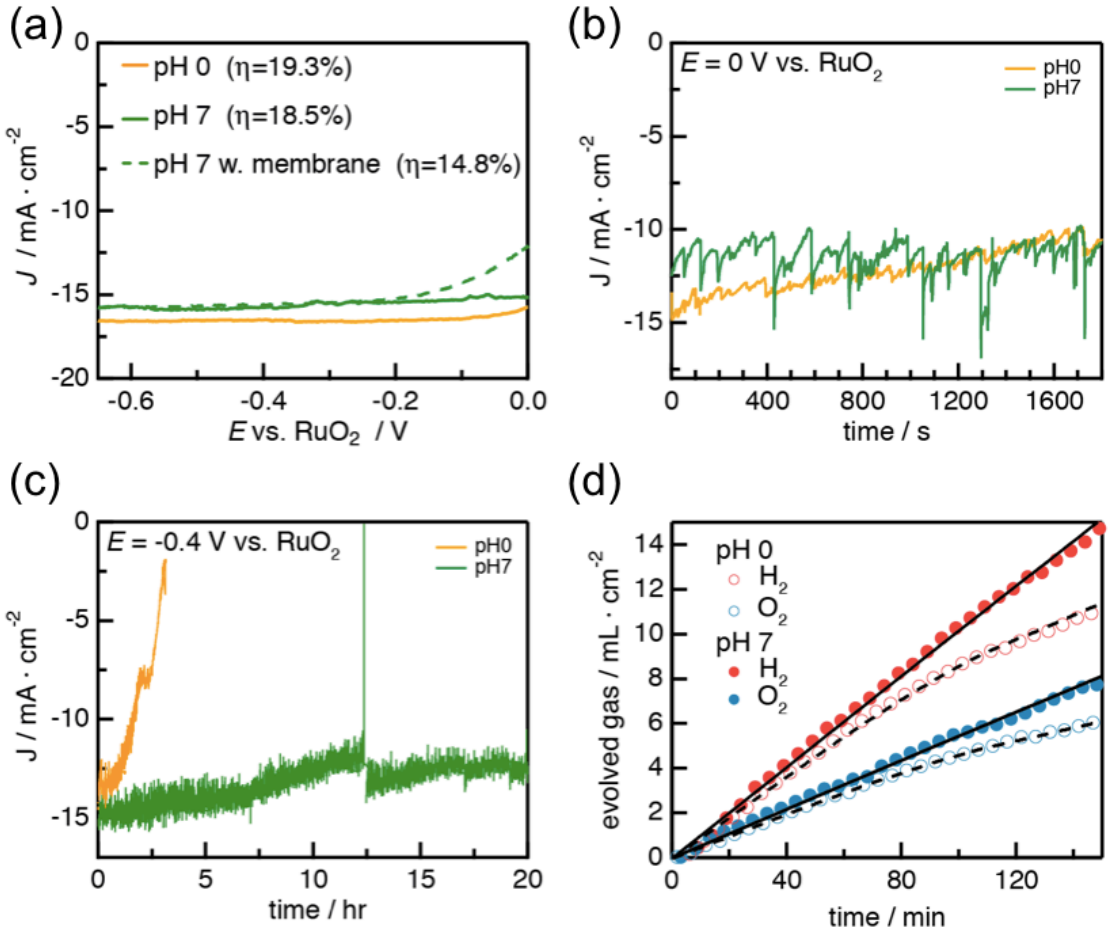

Figure 3.20: *Output characteristics of the RuO_2-Ge/GaInAs/GaInP/AlInP/anatase TiO_2/Rh-electrolyte dual junction tandem structure. (a) Photocurrent-voltage characteristics in acidic (pH 0), neutral (pH 7) electrolyte, and in neutral electrolyte including an AEM membrane. (b) Chronoamperometric data of the initial temporal regime. (c) Stability measurements at -0.4 V vs. RuO_2 counter electrode for acidic and neutral pH. (d) Hydrogen and oxygen gas collection for operation in acidic (open spheres) and neutral (full spheres) electrolyte. The measured gas volume for oxygen (blue symbols) and hydrogen (red symbols) is overlaid with the expected produced gas volume, as calculated from charge passed through the anode and cathode.*

Etching of TiO_2 is expected to occur at pH 0 but not at pH 7, as can be seen in the TiO_2 Pourbaix diagram in Figure 3.21. Corrosion reactions can degrade the junction photovoltage, as well as lead to undercutting and removal of catalyst particles, thus reducing the exchange current of the Rh NP arrangement and a slowing of the HER kinetics. The system reacts also sensitively

to series resistance changes, as illustrated by characteristics for devices employing an anion exchange membrane. The bend of the J-V curve is shifted to cathodic potentials. However, device operation at pH 7 still yields a high STH efficiency of 18.5 %, and the device appears to be stable for a more extended period in accordance with predictions of TiO_2 stability from thermodynamics. Even a slower reduction of the photocurrent is observed, we found that this photocurrent reduction could be partially reversed by emersion of the device from the electrolyte solution and applying a soft cleansing procedure. The observation that the photocurrent can be partially restored appears to rule out loss of Rh catalyst particles, or even partial removal of the anatase interfacial layer, as causes of photocurrent reduction.

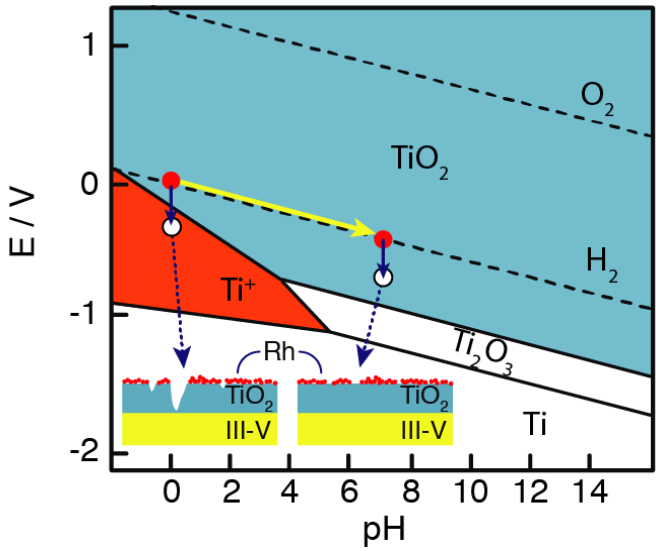

Figure 3.21: *Potential-pH equilibrium diagram for the system titanium-water system at 25 °C, adapted from ref.* [77]*. For pH 0, the stable region is small. Upon overpotential to hydrogen evolution, corrosion sets in, which ultimately leads to the degradation of the device and its efficiency.*

Increasing the efficiency of a photoelectrosynthetic device from already high values towards theoretical limits is especially challenging. We have used a series of surface conditioning steps that have a twofold function: light management was drastically improved, and the electronic properties were at least maintained. Compared to our earlier results [10], we see an increase in the available cell voltage that is related to the increase in photocurrent at the counter electrode operation potential. Junction formation between the etched AlInP layer, TiO_2 layer, and Rh NPs

suggests that the Fermi level alignment is nearly ideal. Using the parameters shown in Table 3.1, our photoelectrosynthetic device reaches 0.85 of the theoretical limiting efficiency. It should be noted that the theoretical efficiency determined from the data in Table 3.1 is based on the best presently known electrocatalysts, a unity photoelectrode radiative efficiency, and an absence of absorption losses [69]. Figure 3.22 shows a summary to date of selected STH efficiencies realized for monolithic integrated photoelectrosynthetic devices capable of unassisted water splitting. (The performance of each device are listed in Table 3.2.)

Table 3.1: Approaches to theoretical limitation of light-induced photoelectrochemical water splitting; ideal, only exchange current density limited and devices that are optically and electrochemically limited are displayed, respectively. For the used band gap combination and only catalytic exchange current density (J_{XC}) limitation, η_{theo} = 22.8 % at AM 1.5G irradiation.

	$J_{0,cathode}$ ($mAcm^{-2}$)	$J_{0,\ anode}$ ($mAcm^{-2}$)	f_{abs}	ERE	R_s (Ω)	R_{sh} (Ω)
ideal	∞	∞	1	1	0	∞
J_{XC} limited	1	10^{-3}	1	1	0	∞
J_{XC} and optically limited	1	10^{-3}	0.9	0.03	0	∞

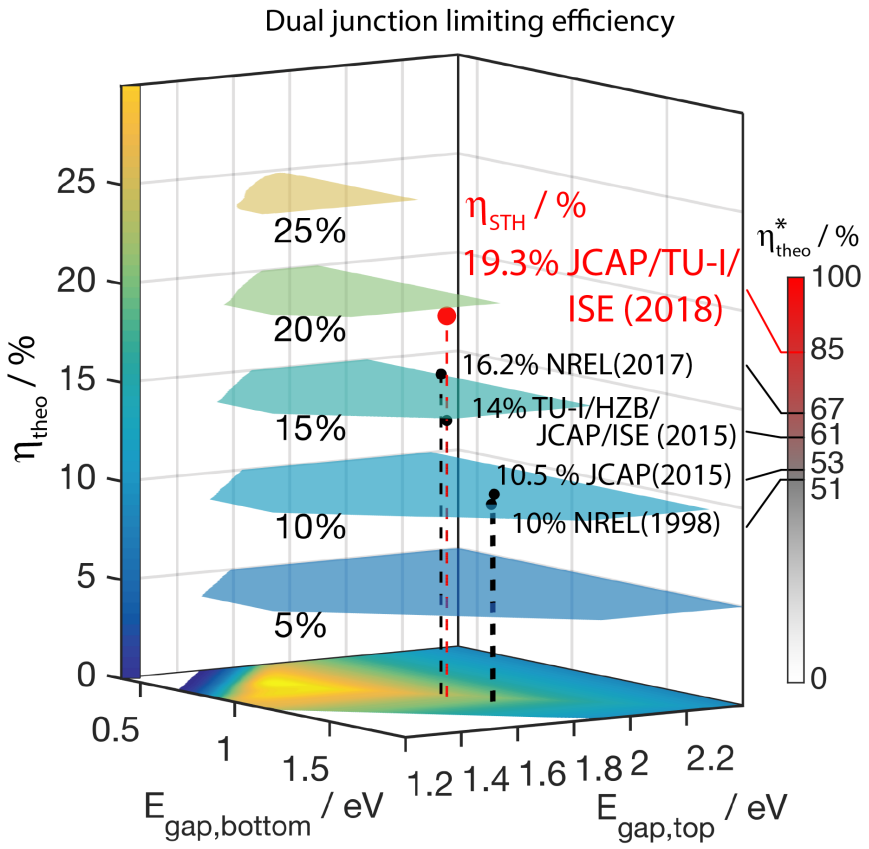

Figure 3.22: *Comparison of realized limiting STH efficiencies and historic development. The analysis refers to a theoretical benchmarking value η_{theo} and takes into account the top and bottom cell band gaps for the respective photolysis cells; also shown are the institutions of the contributing research teams. Abbreviations: NREL - National Renewable Energy Laboratory, USA; ISE - Institute for Solar Energy, Germany; JCAP - Joint Center for Artificial Photosynthesis, Caltech; TU-I - Ilmenau University of Technology, Germany; HZB - Helmholtz Zentrum Berlin, Germany. The bar chart on the right indicates the achieved efficiency with respect to the respective theoretical limit (η^*_{theo}).*

Table 3.2: *Reported STH benchmarks from literature with employed bandgaps, achieved STH efficiency (η_{STH}), theoretical limit for realistic water splitting (η_{theo}), and ratio of achieved STH to η_{theo} as η^{*}_{theo}.*

	Bandgaps	η_{STH} **(%)**	η_{theo} **(%)**	η^{*}_{theo} **(%)**	**Reference**
JCAP/TU-I/ISE	1.78/1.26	19.3	22.8	85	This work
NREL	1.8/1.2	16.2	24.2	67	[5]
TU-I/HZB/JCAP/ISE	1.78/1.26	14	22.8	61	[10]
JCAP	1.84/1.42	10.5	19.7	53	[78]
NREL	1.83/1.42	10	19.7	51	[5,66]

Compared to an earlier reported record photoelectrosynthetic cell with inverted metamorphic multi-junction semiconductor architecture [5], the tandem device employed in the present study has a less ideal bandgap combination of 1.78 V/1.26 V, compared to 1.8 V/1.2 V, which leads to the reduction of theoretical efficiency from 24.2 % to 22.8 %. However, due to better light management (antireflection layer, optimized catalyst loading, thinning, and transparency of the tunnel junction), a higher current density and higher STH efficiency of 19.3 % are observed. This efficiency corresponds to an enhancement from 67 % to 85 % of the ratio of achieved efficiency to theoretical efficiency for the employed bandgaps. The stability tests using a two-electrode configuration at 0 V vs. RuO_2 counter electrode to demonstrate unassisted water splitting for the two devices are shown in Figure 3.23(a). The result from ref. [5] was corrected by scaling the initial current density (including spectral calibration errors) to 13.17 mA/cm^2 calculated from their reported highest efficiency of 16.2%. At an acidic pH, our device current density drops from 15 mA/cm^2 to less than 5 mA/cm^2 within an hour. By contrast, for pH 7, the photocurrent density and device performance are more stable and show similar chronoamperometric performance to that reported in ref. [5]; our device is stable for the first 20 min, then the photocurrent density slowly decreases. The spikes in current density indicate the influence of bubble formation and subsequent detachment. The dynamics are different due to the change in the reduction mechanism (proton

reduction at pH 0, water reduction at pH 7) and the surface tension of the electrolyte. The surface tension of the phosphate buffer is higher than for acidic electrolyte (see Figure 3.24) and exhibits more severe bubble accumulation that induces greater photocurrent density fluctuations.

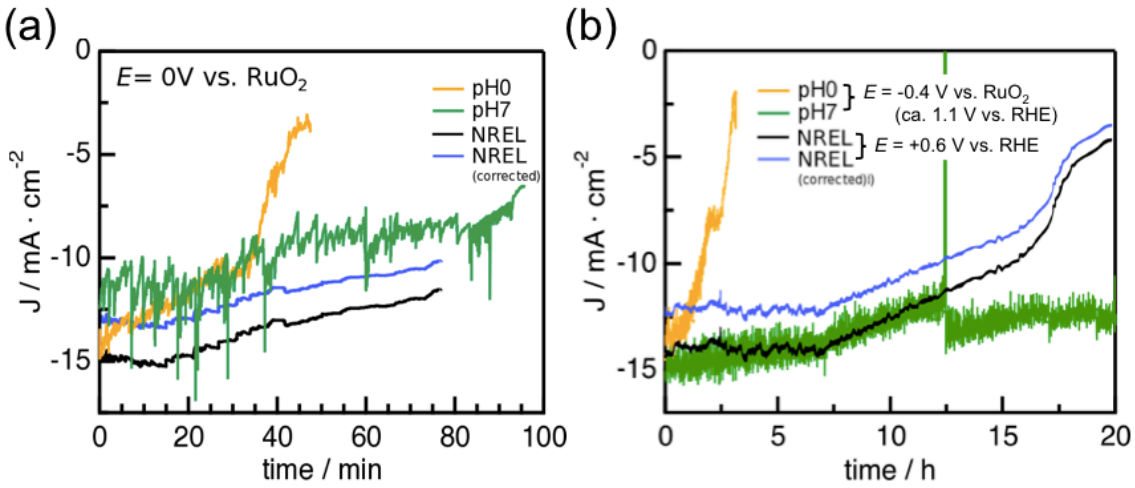

Figure 3.23: *(a) Stability measurements at 0 V vs. RuO_2 counter electrode for acidic and neutral pH. The result from ref. [5] are adapted and included for comparison as the black curve. (b) Chronoamperometric measurements at -0.4 V vs. RuO_2 counter electrode for acidic and neutral pH. The results from ref. [5] at 0.6 V vs. RHE are adapted and included for comparison in black. Currents rescaled based on the reported efficiency in ref. [5] are shown in blue.*

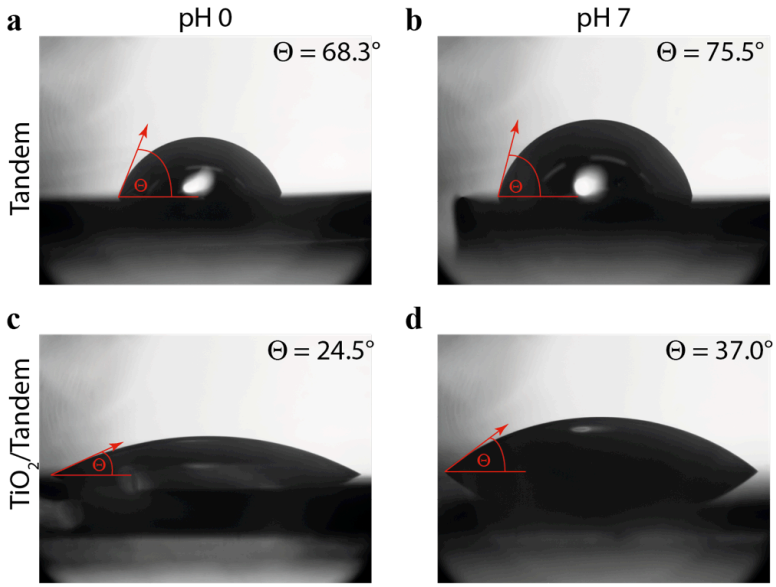

Figure 3.24: *Contact angle measurement for pH0 1 M $HClO_4$ (a, c) or pH7 0.5 M phosphate buffer (b, d) on the tandem (a, b) or on the TiO_2/tandem (c, d) sample. The image was analyzed with ImageJ with the help of the "Drop Analysis" plugin developed at the École polytechnique fédérale de Lausanne (EPFL) (http://bigwww.epfl.ch/demo/dropanalysis/). The larger contact angle of phosphate buffer indicates higher surface tension, which can lead to more severe bubble accumulation and larger photocurrent density fluctuations.*

It is well known that photoelectrochemical devices can be better stabilized in a three-electrode configuration at the RHE potential. We were also able to demonstrate long-term stability of 50 hrs under these conditions without the existence of a protection layer in an acidic environment (see Figure 3.25). However, these conditions are not comparable to operation at 0 V vs. CE in a two-electrode configuration, as operation at RHE potential diminishes the effect of corrosion. For comparison and to understand the intrinsic differences between operation at different pH conditions, chronoamperometric tests were conducted at -0.4 V vs. counter electrode (equivalent to approximately +1.1 V with respect to RHE (estimated to be 1.23 V plus catalysts overpotential minus 0.4 V) as shown in Figure 3.23(b). The stability data of the device reported in ref. [5], which was operated at +0.6 V vs. RHE with and without current rescaling, is included for comparison. It shows that the device photocurrent density decreases in acidic electrolyte to low values within 3 h. In neutral pH electrolyte, stability over 20 h was demonstrated, with the photocurrent density

remaining at 83 % of its initial value. At 12 h into the test, a diurnal cycle was simulated by emersion of the sample in the dark for a few minutes. This step resulted in a substantial current density enhancement. Overall, our device operated in neutral pH conditions shows similar stability characteristics compared to that reported in ref. [5], while exhibiting higher efficiency. Our device, operated in a biased two-electrode configuration exhibits an extended stability with respect to the three-electrode measurements reported in ref. [5]. We conducted XPS measurements to further understand the degradation mechanism.

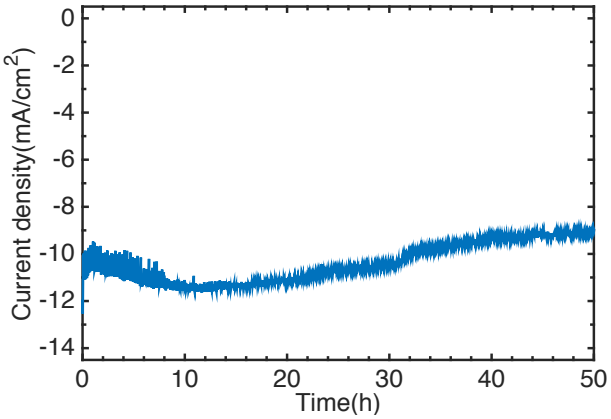

Figure 3.25: *Chronoamperometric measurements at 0 V vs. RHE for Rh/Tandem device without protection layer in acidic environment.*

X-ray photoelectron spectra of tandem samples after each step in the PEC device production process are shown in Figure 3.26. The tandem etched spectra show the exposed $AlInPO_x$ window layer. Upon deposition of TiO_2 with no visible In and P signal, we infer full coverage of the protection layer without pinhole formation. Photoelectrochemical deposited Rh with the similar intensity to the Rh film indicates a sufficient amount of catalysts. However, the small remaining Ti peaks present the existence of the TiO_2 exposed area. After photoelectrolysis in an acidic environment, the TiO_2 peak enhancement indicates more exposed areas upon local detachment of catalysts (see Figure 3.27). The maintained prominent Rh peak implies the loss of catalyst is not the limiting factor of degradation. Instead, the appearance of underlying In and PO_x peaks supports the scenario of tandem corrosion due to local TiO_2 etching. After operation in neutral pH, we observed the enhancement of the phosphate peak for the aged sample and reduction again after the

recovery as shown in Figure 3.28. Note that no In signal is detected in all samples, which indicates the source of phosphate species is the buffer electrolyte rather than tandem corrosion. We thus deduce that the current reduction during the stability test is mainly contributed by the poisoning of Rh catalysts by the phosphates group. The photoelectrode regeneration procedure results in a 50 % recovery of the photocurrent lost during the first 12 hrs, suggesting that the high porosity of the Rh NP layer inhibits full recovery by a short intermediate treatment. The residual loss remaining after dark recovery can be attributed to the PO_x groups still remaining on the surface. Employing a different electrolyte for pH 7 conditions might therefore benefit longterm activity of the device.

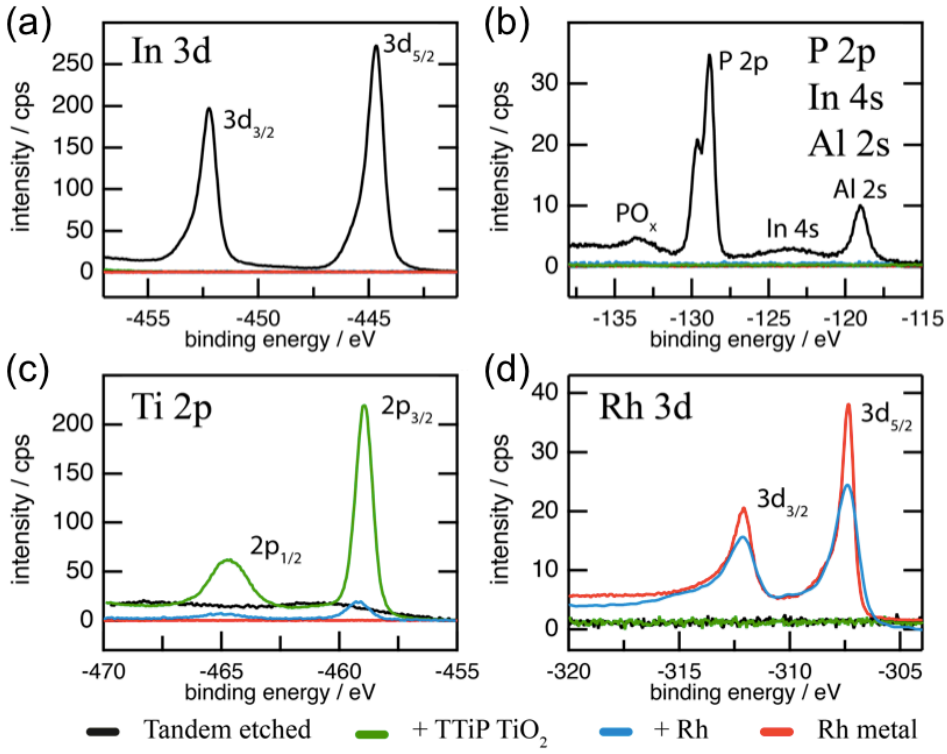

Figure 3.26: *X-ray photoelectron spectra of tandem samples after each step in the PEC device production process: after removing the GaAs/GaInAs cap layer by chemical etching (black curve, indicated as Tandem etched), after deposition of the TiO_2 layer by ALD (green curves, indicated as +TTiP TiO_2); and after photoelectrochemical deposition of Rh nanoparticle catalysts (blue curve, indicated as +Rh). As a reference, spectra of metallic Rh electrode are included (red curve,*

indicated as Rh metal). (a) In 3d core levels; (b) P 2p, In 4s and Al 2s core levels, the peak of PO_x is indicated; (c) Ti 2p core level; and (d) Rh 3d core level.

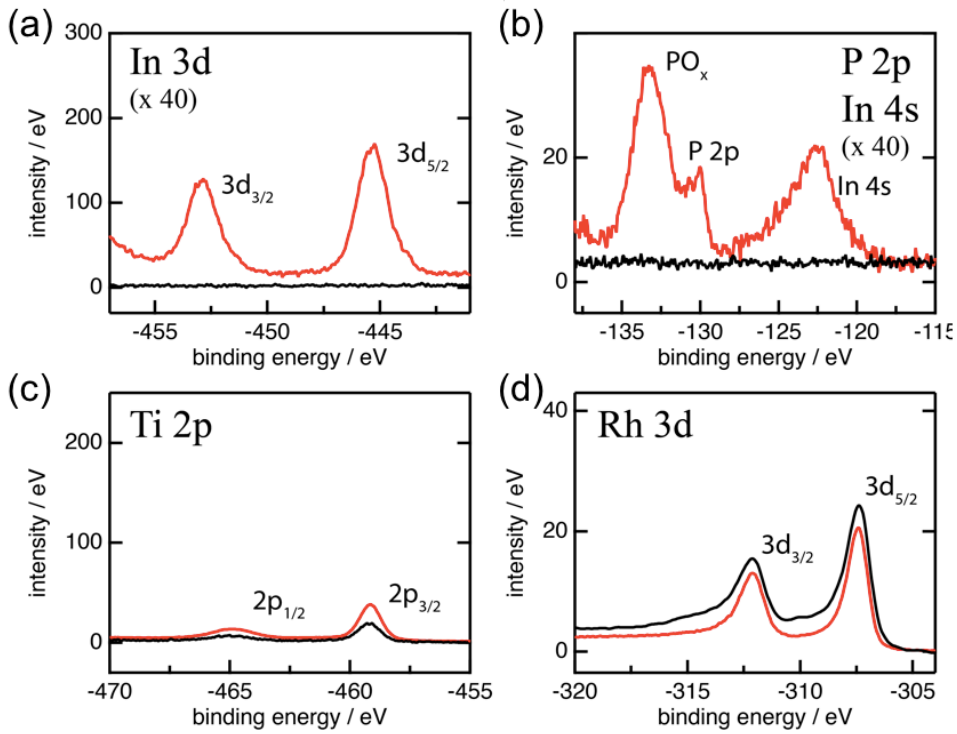

Figure 3.27: *X-ray photoelectron spectra of a pristine Rh/TiO_2/Tandem sample (black) and after degradation in acidic environment (red): (a) In 3d core levels; (b) P 2p and In 4s core levels, the peak of PO_x is indicated; (c) Ti 2p core level; and (d) Rh 3d core level.*

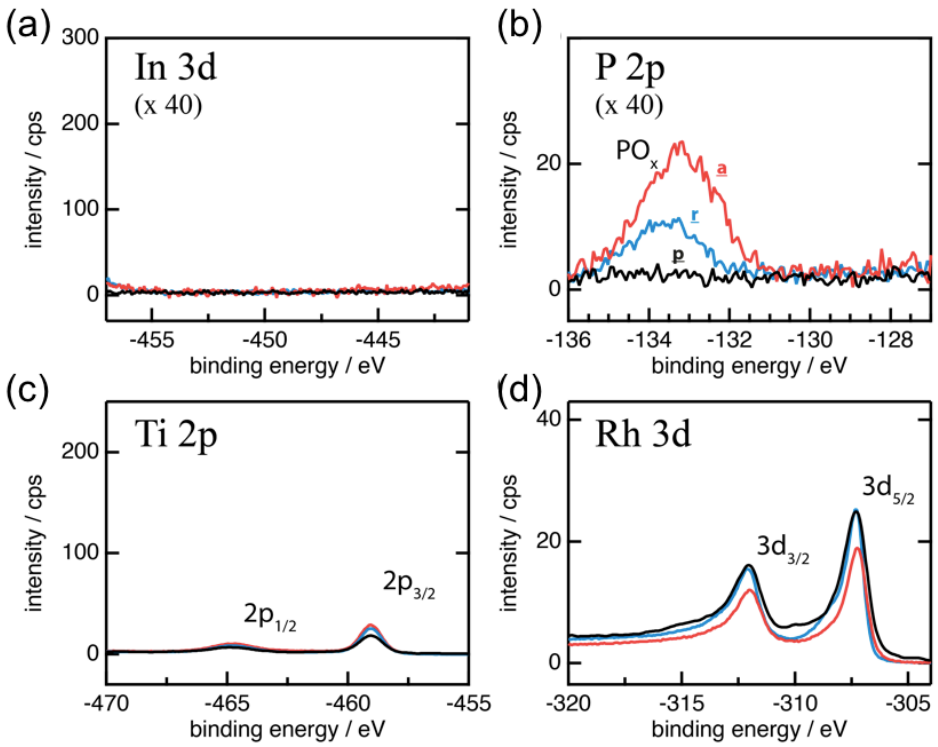

Figure 3.28: *X-ray photoelectron spectra for the study of Rh catalyst poisoning by PO_x groups in pH 7: (a) In 3d core levels; (b) P 2p core levels, the peak of PO_x is indicated; (c) Ti 2p core level; and (d) Rh 3d core level. The black curve indicates the pristine (p) sample before any photoelectrochemical measurement. The red curve indicates the aged (a) sample, which was taken out from the electrolyte under light illumination after operation. The blue curve indicates the recovered (r) sample, which was taken out from the electrolyte under dark condition to simulate the diurnal cycle.*

3.4 Conclusion and Outlook

Stability appears to remain an issue of this photocathode device configuration, but we have demonstrated high efficiency in neutral electrolytes, and that extended operation of photocathode devices becomes possible if one can control the Rh surface chemistry. The use of Rh NPs with tailored size and shape distributions enables ultralow absorption. The future design of even more optimized tandem photoelectrodes appears to be possible, enabling solar fuel generation (water splitting, as well as CO_2 or N_2 reduction) efficiencies to be even higher than reported here, for

example with STH champion device efficiencies of >20 % for integrated direct water photolysis being a realistic goal.

In PEC system, the cost of raw materials and system level deployment are critical issues for real world application. As a general guidance, STH efficiency of 15% and extended lifetime of 20 years would make PEC device a practical solution. Stability is currently the most important challenge to overcome. Although many demonstrations show the photoelectrochemical devices can be stable for long period of time at 0 V vs RHE potential, the device can barely survive at real operation conditions for a short time. New approaches and strategies of the protection scheme would need to be developed.

CHAPTER 4
High Efficiency Solar to CO PV-GDE Device

4.1 Introduction

Parallel to solar hydrogen generation approaches, pathways for solar-driven reduction of carbon dioxide to fuels have used i) direct electrolysis,[79] ii) photovoltaic directly driven electrolysis [80], and iii) integrated photoelectrochemical conversion.[81,82] Of particular interest is solar-driven reduction of carbon dioxide using a high efficiency photovoltaic (PV) device directly coupled to an electrochemical cell tailored for reduction of CO_2 to CO.[83] Mixtures of solar-generated CO and H_2,[84] could be used as syngas precursors in a future Fischer-Tropsch chemical synthesis process [85] to produce high molecular weight hydrocarbon fuels, or chemicals as products.[68] Carbon dioxide reduction to CO is generally more energy efficient and kinetically easier than direct reduction of CO_2 to multicarbon products.[83,86]

Among the most efficient heterogeneous solid state catalysts for CO_2 reduction to CO are gold,[87,88] silver,[89] WSe_2,[90] and MoS_2.[91] The use of high surface area morphology structures such as nanoparticles can improve catalytic activity.[92] Other factors that impact catalytic performance include catalyst morphology,[87] cations present in the electrolyte solution,[93] electrolyte concentration [94], and local pH.[95] The state-of-the-art CO_2 to CO conversion using a Au needle catalyst [94] showed an operating current of 15 $mA \cdot cm^{-2}$ and 95 % Faradic efficiency at -0.35 V vs. RHE. However, the current record efficiency device for solar conversion of CO_2 to CO using a solution-based electrochemical cell suffered from low current density (0.33 $mA \cdot cm^{-2}$ at -0.6 V vs. RHE) due to limited catalyst activity. This required the use of large-area electrodes to match the photovoltaic device area.[80] Table 4.1 shows overpotential and Faradic efficiency data at current densities close to 15 $mA \cdot cm^{-2}$ along with the electrolyte conditions and catalyst loading for various Ag and Au electrodes. The catalytic activities of the catalysts indicate that in many cases, nanoparticles of Ag have a similar activity to that of Au while costing significantly less.

Table 4.1: *Comparison of the CO_2 reduction performance of our Ag-NP catalyst with previously reported Ag and Au electrodes. (U as overpotential vs. $E^0_{CO/CO2}$ (-0.11 V vs. RHE), mass activity define as $\frac{J \cdot f_{FE}}{loading}$.)*

Catalysts	**Electrolyte**	**pH**	***U* (V) at ~15 mA·cm^{-2}**	**$f_{FE,CO}$ (%)**	**Loading (mg·cm^{-2})**	**Mass activity (mA·mg^{-1})**	**Ref.**
Nanoporous Au	CO_2-sat 0.2 M $KHCO_3$	6.8	1.24	N/A	0.39 (200 nm film)	N/A	[96]
Nanoporous Au	CO_2-sat 0.1 M $KHCO_3$	6.8	0.6	60	0.47 (eq. 240 nm film)	19.15	[87]
OD-Au	CO_2-sat 0.5 M $NaHCO_3$	7.2	0.39	100	193 (0.1 mm foil)	0.08	[88]
Au-NWs	CO_2-sat 0.5 M $KHCO_3$	7.2	0.32	90	4.43	3.05	[76]
Au nanoneedle	CO_2-sat 0.5 M $KHCO_3$	7.4	0.24	95	N/A	N/A	[94]
Bilayer Au/PE	CO_2-sat 0.5 M $KHCO_3$ flow cell	7.2	0.39	85	0.15	85	[97]
Au-NPs	2M KOH flow cell	13.77	0.2	70	0.18	58.33	[98]
Polycrystalline Ag	CO_2-sat 0.1 M $KHCO_3$	6.8	1.4	30	105 (0.1 mm foil)	0.04	[99]
Polycrystalline Ag	CO_2-sat 0.5 M $KHCO_3$	7.0	1.04	60	N/A (foil)	N/A	[100]
5 nm Ag/C	CO_2-sat 0.5 M $KHCO_3$	7.0	0.84	40	0.09	66.67	[100]
Ag-NPs	CO_2-sat 0.1 M $KHCO_3$	6.8	0.84	83	N/A	N/A	[101]
cysteamine-capped Ag-NPs	CO_2-sat 0.5 M $NaHCO_3$	7.2	0.69	66	0.08	123.75	[102]
Ag Nano-coarals	CO_2-sat 0.1 M $KHCO_3$	6.8	0.61	95	N/A (on foil)	N/A	[103]

Nanoporous Ag	CO_2-sat 0.5 M $KHCO_3$	7.2	0.49	92	40	0.35	[104]
Ag/PTFE	1 M $KHCO_3$ flow cell	8.5	0.64	70	0.52 (eq. 500 nm film)	20.19	[105]
Ag-NPs	1M KOH flow cell	14	0.39	95	1	14.25	[106]
Ag/PTFE	1M KOH flow cell	14	0.34	90	0.52 (eq. 500 nm film)	25.96	[105]
Ag-NPs	0.5M KOH flow cell	13.23	0.34	95	2	7.125	[107]
Ag-NPs	1M KOH flow cell	14	0.49	99	0.12	124	This work

Bulk aqueous electrolyte cells can exhibit high catalyst overpotentials due to the limited solubility of CO_2 (33.4 mM) in the electrolyte, a limited pH operating range of ~6 - 10, and slow ionic transport in the solution. In contrast, gas diffusion electrode (GDE) assemblies do not suffer these same restrictions.[97,107-111] In a GDE using 1 atm CO_2 vapor, CO_2 is transported in the vapor phase and reacts at a thin (<100 nm) solid-liquid-gas phase interface. In this configuration, liquid-state concentration and diffusion do not limit the conversion rate, resulting in lower overpotentials and higher current densities for CO_2 reduction.[108] Simulations have also shown that a cell using a thin (10 nm) layer of electrolyte on the catalysts (wetted catalyst) outperform cells with either a completely dry or a completely flooded catalyst configuration.[112] These insights have led to the development of gas diffusion electrodes[113] and membrane electrode assemblies (MEA) [114] with a humidified gas supply to facilitate ion conduction and water balance.

Although membrane electrode assemblies systems are more scalable, they often suffer from short-term stability due to salt precipitation or membrane dehydration at high current densities.[90] Hence, we chose to work with an aqueous GDE cell configuration. In this work, we employ a triple junction photovoltaic (PV) device directly coupled with a gas diffusion electrode (GDE) as the first demonstration of an electrolyte flow type PV-GDE reactor that provides both high selectivity and long-term stability. For a directly driven PV-GDE system, the power generated by the PV is directly supplied to the GDE. In our device, the areas of the PV photo-absorber (A_{PV}) and GDE (A_{GDE}) were both 0.31 cm^2. To match the lower current density of the PV cell with the operating

conditions of the anode, a relatively low catalyst loading of GDE was chosen. A Ag nanoparticle catalyst was used owing to its relatively high activity and relatively low cost.

4.2 Experimental Method

GDEs were prepared with diluted Ag-NPs (Sigma Aldrich 736481, particle diameter ≤50 nm, 30-35 wt. % in triethylene glycol monoethyl ether) by drop-casting on carbon paper (Sigracet 29 BC). 50 μL of Ag-NPs ink was diluted with 15 mL of methanol and sonicated prior to use. 200 μL of the diluted Ag-NPs were drop-casted on 25 mm by 25 mm size carbon paper (masked to A_{GDE} = 0.31 cm^2 later for operation). The GDE was baked at ~100 ˚C for 10 min on a hot plate to remove the remaining solvent and was post annealed at 200 ºC for 1 h in a muffle furnace in air. Surface chemical analysis was conducted using X-ray photoelectron spectroscopy (XPS) with the catalyst primarily in a metallic phase.

A PEEK compression cell (Figure 4.1, Figure 4.2) was used as the vessel for the measurement with anode and cathode chamber volumes of 2 mL. The anode and cathode electrode working areas were 0.31 cm^2, and the membrane area was 2.4 cm^2 as constrained by the design of the compression cell. 1 M potassium hydroxide (KOH) was used as the catholyte for experiments at pH 14, while 1 M potassium bicarbonate ($KHCO_3$) buffer was used for pH 8.5. The anolyte was 1 M KOH. The corresponding anion exchange membrane (AEM) was a Fumasep FAA-3-50 for alkaline environments and a Selemion AMV for neutral environments. The anode was a Pt foil under three-electrode operation, while for full cell operation in KOH electrolyte we used Ni foam to reduce the overpotential for oxygen evolution reaction. A leakless Ag/AgCl reference electrode was used for three-electrode measurements and to determine the GDE potential in the two-electrode measurements. All electrochemical measurements were performed using a Biologic VSP-300 potentiostat. Scan rates were set to 50 $mV \cdot s^{-1}$. A Keithley 2000 multimeter was used to record the cell voltage and a Keithley 2182A nanovoltmeter for recording the voltage between the cathode and reference electrode. Gas flow rates of the flow controller (Gas inlet) and flow meter (Gas outlet) were recorded by the external device inputs of the potentiostat. Gas was delivered to the GDE through an interdigitated electrode flow field against which the GDE is compressed to

maximize the interaction of CO_2 with the catalyst and gas utilization.[91] Current to the GDE was supplied through the interdigitated electrode to the Ag-NP/carbon paper substrate.

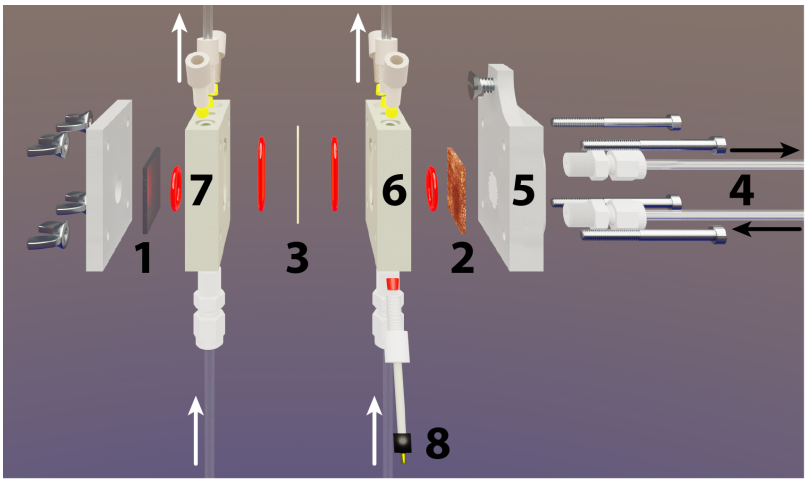

Figure 4.1: *Cell configuration composed of 1 NiO_x or Pt anode, 2 Ag-NPs on Sigracet 29BC carbon paper cathode, 3 anion exchange membrane, 4 CO_2 gas inlet and CO/CO_2 outlet, 5 Acrylic backplate, 6 catholyte chamber, 7 anolyte chamber, 8 reference electrode. Black arrows indicate the gas flow, and white arrows indicate the electrolyte flow. Note that the backplate, 5, is designed to use an interdigitated wire electrode flow field to enhance the interaction between gas and catalysts and improve CO_2 utilization (see also Figure 4.2).*

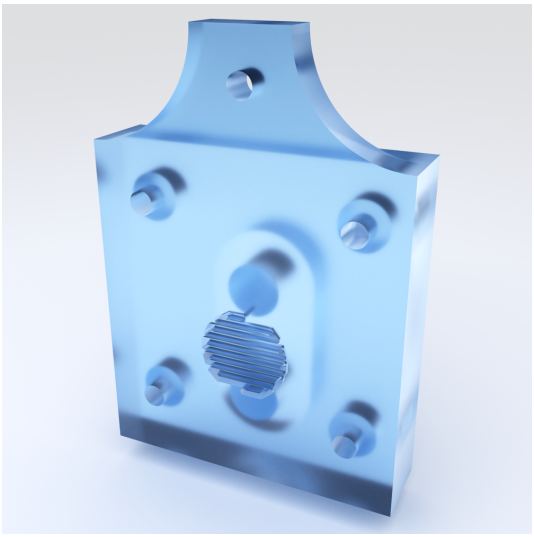

Figure 4.2: *Backplate as shown in Figure 4.1 item 5 with an interdigitated flow field.*

The electrochemical setup was operated in a continuous flow mode. Carbon dioxide was provided to the electrochemical cell and its flow rate was controlled with an Alicat flow controller. The carbon dioxide stream could be supplied either as dry gas or humidified CO_2 with a gas bubbler between the cell and flow controller. The exhaust gasses went through a liquid trap than an Alicat flow meter, and finally to a gas chromatograph (SRI-8610) using a Hayesep D column and a Molsieve 5A column with N_2 as the carrier gas. The gaseous products were detected using a thermal conductivity detector (TCD) and a flame ionization detector (FID) equipped with a methanizer. Quantitative analysis of gaseous products was based on calibration with several gas standards over many orders of magnitude in concentration.

The GaInP/GaInAs/Ge triple junction cell is commercially available from Spectrolab (C4MJ) with a geometric area of 0.31 cm^2. For illumination during laboratory tests, an Oriel Instruments 75 W Solar Simulator was used and matched with AM 1.5G. The response to natural sunlight of the triple junction at short circuit was calibrated by measuring the outdoor sunlight irradiance with a calibrated Si photodiode. The light intensity of the solar simulator was set to provide the same short circuit current from the GaInP/GaInAs/Ge triple junction cell as it would under AM 1.5G outdoor sunlight. While this is not expected to yield a simulated solar irradiance of 100 $mW \cdot cm^{-2}$ due to the different solar irradiance in the 800–1000 and 1150–1800 nm regions, it does produce a response of the triple junction PV that is the same as it would be in actual AM 1.5G sunlight.

For outdoor tests, the triple junction solar cell was mounted on a solar tracker, see illustration in Figure 4.3. An Arduino microcontroller was used to control the solar tracker and measure the sun light intensity through a calibrated (350 to 1100 nm, 1 cm^2) NIST traceable Si photodiode (Thorlabs FDS1010-CAL).

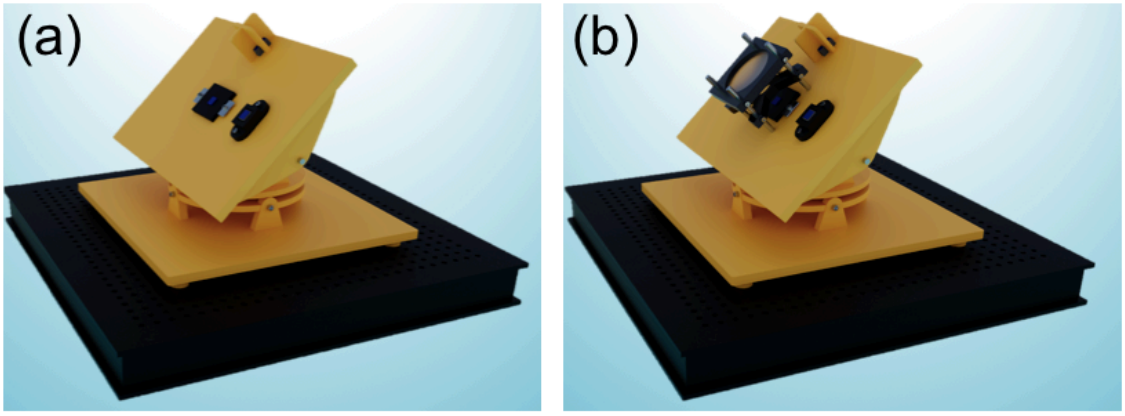

Figure 4.3 *(a) Illustration of the solar tracker. (b) With the addition of C = 3.25 Suns solar concentrator. The PV element is located in the left with a silicon reference photodiode mounted on the right. Above the PV element is the light-dependent resistor sensor array for determining and tracking the position of the sun. For concentrator operation, a Fresnel lens with 51 mm focal length was placed in front of the solar cell to provide a concentration of 3.25x.*

Kratos Axis Ultra was used to perform X-ray photoelectron spectroscopy (XPS) measurements with base pressure under $1x10^{-9}$ Torr. A monochromatic Al Kα ($\hbar\omega$ = 1486.69 eV) source with a power of 150 W was used for all measurements. A ramé-hart contact angle goniometer was used for surface angle measurement. The images were analyzed with ImageJ with the help of the Drop Analysis plugin developed at the École polytechnique fédérale de Lausanne (EPFL).

4.3 Results and Discussion

The gas diffusion electrode catalytic performance was evaluated with the compression flow cell. Dilute silver nanoparticles (Ag-NPs) with diameters of ≤50 nm were drop cast onto the microporous side of the GDE substrate (Sigracet 29BC). The loading of Ag-NPs in this work was measured to be 0.12 $mg \cdot cm^{-2}$. Scanning electron microscopy (SEM) images of the microporous layer with and without Ag-NPs are shown in Figure 4.4.

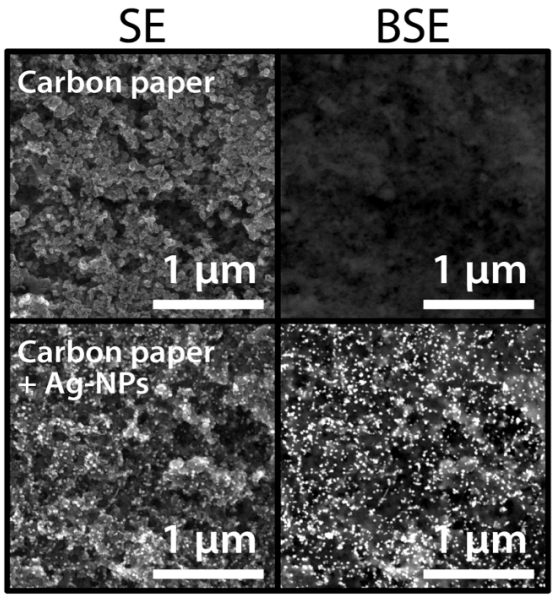

Figure 4.4: *Scanning electron microscopy images of carbon paper without (top) and with (bottom) Ag-NP catalyst, secondary electrons image (left row) backscattered electrons image (right row). (b)Illustration of the reverse-assembled GDE cathode cross-section with wetted catalyst and operation for CO_2 reduction.*

An issue for aqueous GDEs is flooding or saturation of the porous catalyst layer with electrolyte or water during operation. This results in a thick (>1 µm) electrolyte layer and a diffusion-limited supply of CO_2 to the electrode.[115] To maintain the catalyst in a wetted but not flooded condition that minimizes losses of CO_2 to the electrolyte and extends the operational lifetime, we assembled our aqueous GDE in a nontraditional manner with the catalyst coating of Ag-NPs facing away from the electrolyte and towards the CO_2 gas supply. We denoted this configuration as a *reverse-assembled* GDE. The microporous layer of the GDE was treated with polytetrafluoroethylene (PTFE), which helped to prevent flooding. Needle valves in the gas and liquid output streams allowed separation of the liquid and gas phases as well as control of the pressure difference between the aqueous electrolyte and the CO_2 stream. Contact angle analysis indicated that the Ag-NP coated surface was significantly less hydrophobic than the surface without Ag-NPs. Contact angle and optical microscope images of the GDE are shown in Figure 4.5.

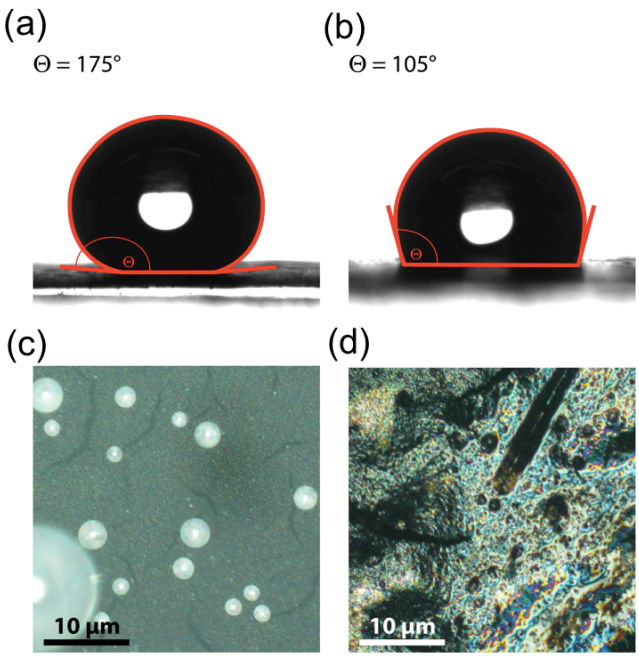

Figure 4.5: *Contact angle Θ measurement of water on (a) pristine Sigracet 29 BC carbon paper and (b) with Ag-NPs on Sigracet 29BC carbon paper after electrolysis. The contact angle is 175° for (a) and 105° for (b). Optical micrographs of water pushing through the back of the Sigracet 29 BC carbon paper (c) without Ag-NPs and (d) with Ag-NPs. The formation of small liquid bubbles is observed in (c) while a thin water layer is shown in (d) indicating the catalyst surface is wetted during operation as proposed.*

With both the gas inlet and outlet on the same side of the GDE, the device operates in a "flow-by" GDE configuration. The Ag-NP catalyst side of the electrode was facing the CO_2 gas channel as illustrated in Figure 4.6. This orientation of the Ag-NPs maintained a thin electrolyte layer on the catalyst and enhanced the rate of CO_2 reduction.[112] The turnover frequency of the Ag-NP catalyst for the *reverse-assembled* GDE at -0.6 V vs RHE was calculated as ~9×10^3 h^{-1}. Turnover frequency (TOF) was defined as the CO production rate (in moles cm^{-1} h^{-1}) divided by the number of moles of active site catalyst. Consider the 0.26 $mmol \cdot h^{-1} \cdot cm^{-2}$ (7.4 $mg \cdot h^{-1} \cdot cm^{-2}$) CO production rate per catalyst area at -0.6 V vs RHE. The total catalyst loading was 0.001 $mmol \cdot cm^{-2}$ (0.12 $mg \cdot cm^{-2}$) that gave a TOF based on the total amount of Ag-NPs as 260 h^{-1}. Since only the surface atoms of the nanoparticle can contribute to active sites, we estimate the fraction of surface atoms

of a 50 nm diameter Ag nanoparticle to be ~3 %, then the moles of active sites are ~3 × 10^{-5} mmol cm^{-2}, and the TOF based on the number of surface atoms is ~9 × 10^{3} h^{-1}.

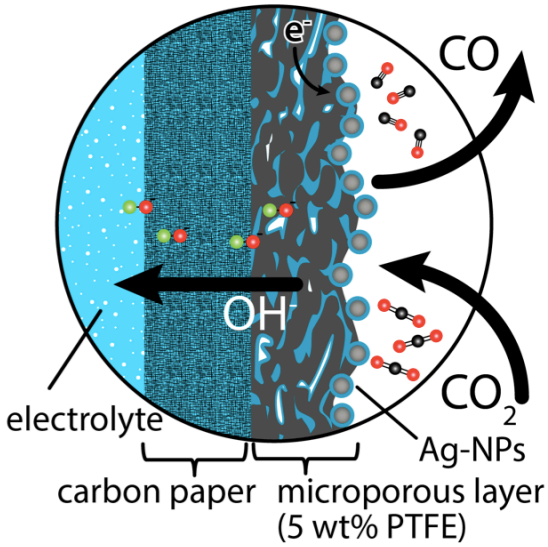

Figure 4.6: *Illustration of the reverse-assembled GDE cathode cross-section with wetted catalyst and operation for CO_2 reduction.*

The anode was made from either Pt or an electrochemically activated Ni foam for three- and two-electrode measurements, respectively. An aqueous catholyte of 1 M aqueous potassium bicarbonate ($KHCO_3$) or potassium hydroxide (KOH) was used under near neutral or basic conditions, respectively. In all cases, 1M KOH was the anolyte. The anion exchange membrane (AEM) was Selemion for neutral environment or Fumasep FAA-3-50 for alkaline environment. Electrolyte (500 ml) was continuously pumped through the cathode chamber in a closed loop at a rate of 2 mL/min. A change of pH (from 14 to 13.7) was observed for the 1 M KOH catholyte after 150 h of continuous operation, corresponding to irreversible loss of 0.25 mol KOH (50% of the electrolyte). The volume of the catholyte was 0.5 L 1 M KOH (0.5 mol KOH) with an initial pH of 14 which changed to 13.7 after 150 h of continuous operation. A pH of 13.7 is $10^{13.7-14}$M KOH = 0.5 M KOH which for 0.5 L is 0.25 mol KOH. The reaction of KOH and CO_2 is given:

$2KOH + CO_2 = K_2CO_3 + H_2O$ (Equation 4.1).

A loss of 0.25 mol KOH corresponds to a loss of 0.125 mol CO_2 and formation of an equal amount of (0.125 mol) K_2CO_3. The CO_2 flowrate during the experiment was 10 sccm, which over 150 h corresponds to 4.043 mol CO_2. The total percentage of CO_2 lost to KOH neutralization and carbonate formation is then $\frac{0.125}{4.043} = 0.031 \equiv 3.1\ \%$. Further improvement to reduce CO_2 loss or regenerate the electrolyte would be necessary for fully sustainable operation. The neutralized carbonate electrolyte can possibly be utilized in carbonate-to-syngas system to compensate the loss of CO_2 in a gas-fed MEA cell with bipolar membrane. [116]

Results from three-electrode measurements for *reverse-* and *standard-assembled* GDEs are shown in Figure 4.7(a-b), respectively, for 1 M $KHCO_3$ (bulk pH of 8.5) and 1 M KOH (bulk pH of 14). Current densities are substantially lower than earlier reported GDE devices due to the low catalyst loading used to match the current from the PV (current matching). For the *reverse-assembled* GDE, both the Faradaic efficiency ($f_{FE,CO}$) for CO and current density (J_{GDE}) increased with increasing potential with $f_{FE,CO}$ close to 100 % at -0.6 V vs. RHE in 1 M KOH. Similar trends of current density and Faradaic efficiency versus applied potential were found for the *standard-assembled* GDE.

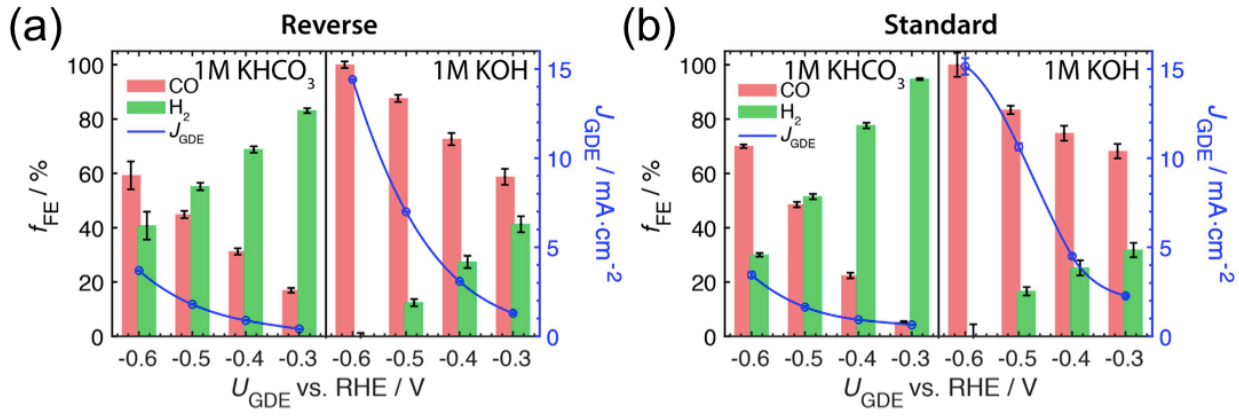

Figure 4.7: *Dark catalysis three-electrode measurement of Ag-NPs GDE. Faradaic efficiency versus GDE potential operated in 1 M KHCO3 (left half of graph) or 1 M KOH (right half of graph) of (a) the reserve-assembled Ag-NP GDE and (b) a standard-assembled Ag-NP GDE.*

To compare the activity of the Ag-NPs in different orientations and pH, overpotential analysis for CO_2 reduction to CO was preformed, Figure 4.8. The overpotential of the GDE is defined as the difference of applied potential to the thermodynamic potential of CO_2 to CO on the RHE scale (–0.11 V vs RHE). The comparable Tafel slopes (~0.23V/dec) in $KHCO_3$ and KOH for either orientation indicate a similar catalytic pathway regardless of the operating conditions. The Tafel behavior plotted with potentials vs NHE falls on a rough single line (Figure 4.9) and suggests that the rate-determining step for the reduction on our Ag-NP GDE is not proton limited. The achievable current density and Faradaic efficiency ($f_{FE,CO}$) for CO are higher in 1 M KOH than in 1M $KHCO_3$ at the same overpotential, likely due to a pH independent rate determining step. All subsequent measurements were, therefore, performed using 1 M KOH for the PV-GDE integrated device.

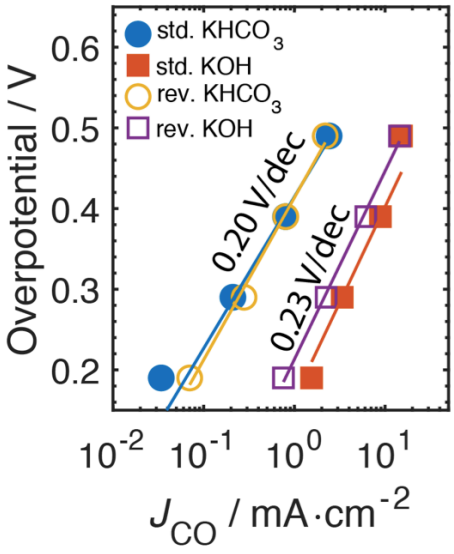

Figure 4.8: *Overpotential versus CO partial current of Ag-NPs GDE for CO_2 reduction to CO. Overpotential=*$\left|U_{GDE,RHE} + 0.11V\right|$, $J_{CO} \equiv J_{GDE} \times f_{FE,CO}$.

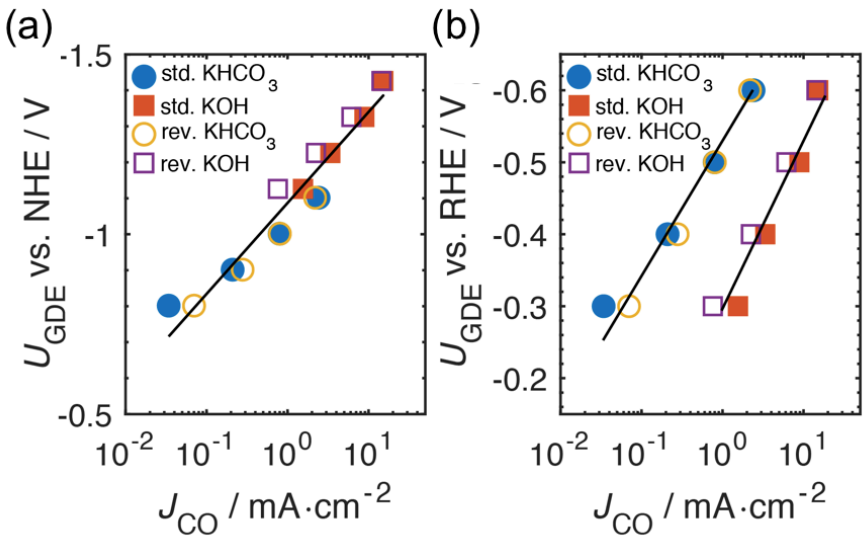

Figure 4.9: *(a) GDE potential vs. NHE, (b) GDE potential vs. RHE versus CO partial current of Ag-NP GDE (rev. indicating reserve-assembled, std. indicating standard-assembled) for CO_2 reduction to CO in 1 M $KHCO_3$ and 1 M KOH.*

Figure 4.10 shows the Faradic efficiency for CO vs. time at -0.6 V vs. RHE for the two GDE orientations in KOH. For the standard configuration, the $f_{FE,CO}$ decreasing to ~75% after 1 h and to 50 % after 2 h, while for the reverse configuration, the $f_{FE,CO}$ was ~97% for 3 h. Though similar in initial current density and $f_{FE,CO}$, the *standard assembly*, with the Ag-NP catalyst facing the electrolyte, became flooded during the first hour of operation resulting in a reduction of the Faradic efficiency. Surface chemical analysis was conducted using X-ray photoelectron spectroscopy (XPS) with the catalyst primarily in a metallic phase, see Figure 4.11. No obvious changes were observed other than the absorption of potassium after operation.

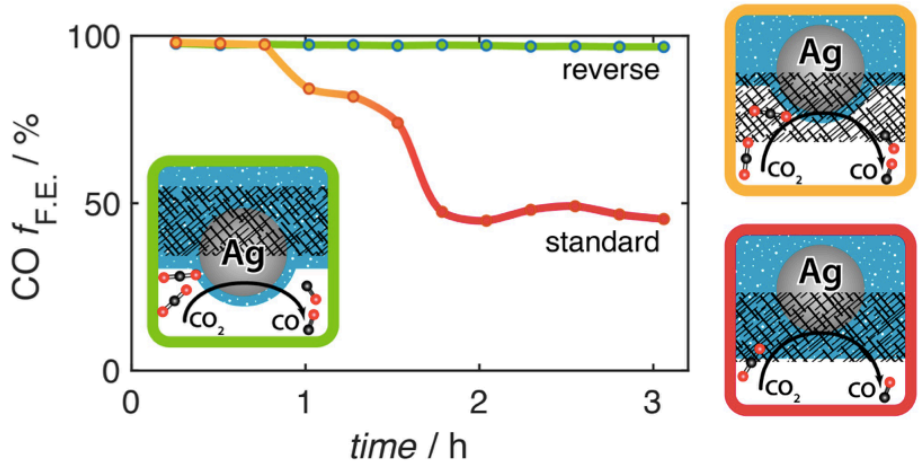

Figure 4.10: *Stability of reserve-assembled and standard-assembled Ag-NPs GDE operated at -0.6 V vs. RHE in 1 M KOH.*

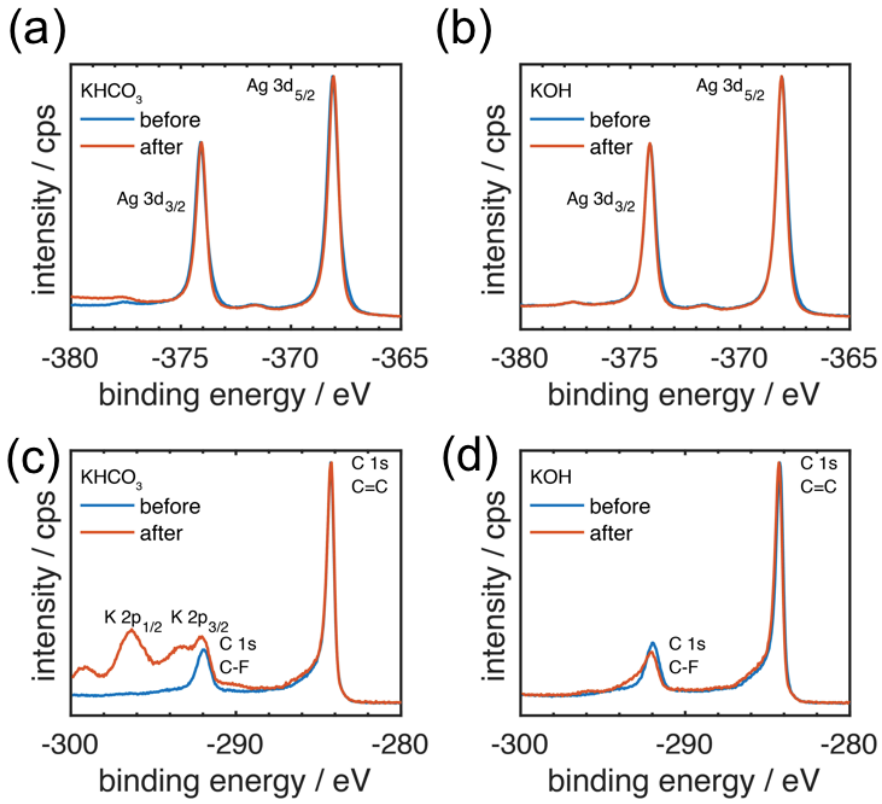

Figure 4.11: *Silver 3d (Ag 3d) and carbon 1s (C 1s) X-ray photoelectron spectra of Ag-NP GDE before/after electrocatalysis with an electrolyte of (a,c) 1 M KHCO3; (b,d) 1 M KOH.*

We performed two-electrode measurements for the GDE using an electrochemically activated nickel foam anode coupled to the GaInP/GaInAs/Ge triple junction cell. The solid-state J-V characteristic and performance parameters of the solar cell are shown in Figure 4.12. For illumination during laboratory tests, an Oriel Instruments 75 W Solar Simulator was used, the lamp spectrum matching with AM 1.5G is presented in Figure 4.13. The corresponding sub-cell currents with integration of external quantum efficiency and short circuit current over the two illumination spectra are shown in Table 4.2.

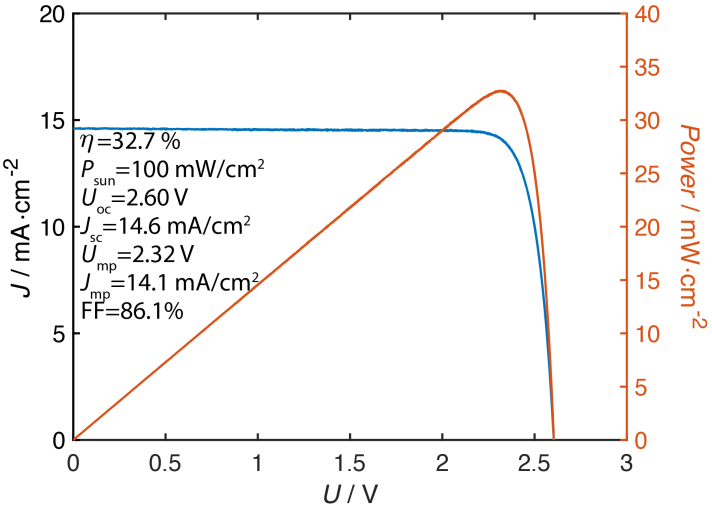

Figure 4.12: *J-V characteristic of the GaInP/GaInAs/Ge triple junction cell. U_{oc} is the open circuit voltage, J_{sc} the short circuit current, U_{mp}/J_{mp} the current and voltage at the maximum power point, and FF the fill factor.*

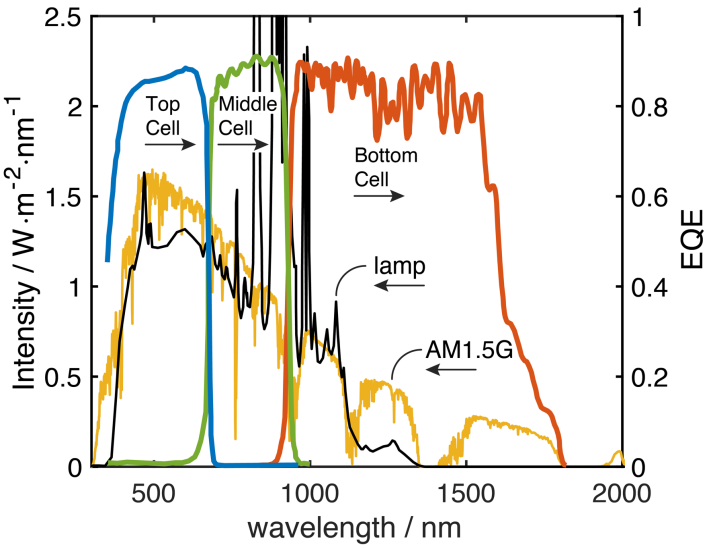

Figure 4.13: *Intensity (left axis) of AM 1.5G 1 sun reference spectrum (gold) and solar simulator spectrum (black), external quantum efficiency (right axis) of the GaInP/GaInAs/Ge (blue, green, red) triple junction cell.*

Table 4.2: *Currents calculated for the individual sub-cells of the of the GaInP/GaInAs/Ge triple junction PV cell under 1.5G 1 sun illumination assuming the standard reference sunlight spectrum (AM1.5G ASTM G-173 reference spectrum was taken from the Renewable Resource Data Center (RReDC) of the National Renewable Energy Laboratory (NREL)) or the solar simulator spectrum and measured short circuit photocurrent J_{sc} under respective 1 sun conditions.*

Illumination Source	J_{GaInP} **(mA·cm^{-2})**	J_{GaInAs} **(mA·cm^{-2})**	J_{Ge} **(mA·cm^{-2})**	J_{sc} **(mA·cm^{-2})**
AM 1.5G	15.56	14.83	18.53	14.6
Solar simulator	15.32	29.73	14.83	14.6

A schematic of the cell is shown in Figure 4.14(a) with 1M KOH as electrolyte using a Fumasep FAA-3-50 membrane. Both the cell potential (U_{cell}) and the cathode to reference electrode potential (U_{GDE}) were monitored during the operation. We calculated the solar to fuel efficiency (η_{STF}) for CO_2 reduction using equation below.

$$\eta_{STF} = \frac{\text{P}_{\text{out}}}{\text{P}_{\text{in}}} = \frac{J_{\text{GDE}} \cdot \Delta U_{\text{rxn}} \cdot f_{\text{FE,CO}} \cdot A_{\text{GDE}}}{P_{\text{light}} \cdot A_{\text{PV}}} = \frac{J \cdot \Delta U_{rxn} \cdot f_{FE,CO.}}{P_{light}} \quad \text{(Equation 4.2)}$$

Where ΔU_{rxn} is the thermodynamic potential difference between the oxygen evolution half reaction (OER) and the CO_2 reduction half reaction of 1.34 V, A is the area of the GDE or PV with $A_{\text{GDE}} = A_{\text{PV}} = 0.31$ cm^2, J (= $J_{\text{GDE}} = J_{\text{PV}}$) is the operation current density of the system, and P_{light} is the incident light irradiance (mW·cm^{-2}) on the photovoltaic. The energy efficiency for the GDE cell (η_{GDE}) was defined as follows:

$$\eta_{\text{GDE}} = \frac{\text{P}_{out}}{\text{P}_{in}} = \frac{\Delta U_{\text{rxn}} \cdot J_{\text{GDE}} \cdot A_{\text{GDE}} \cdot f_{FE,CO.}}{U_{cell} \cdot J_{\text{PV}} \cdot A_{\text{PV}}} = \frac{\Delta U_{\text{rxn}} \cdot f_{FE,CO.}}{U_{cell}} \text{(Equation 4.3)}$$

where $J_{\text{GDE}} \cdot A_{\text{GDE}} = J_{\text{PV}} \cdot A_{\text{PV}}$, and U_{cell} is the total operating voltage of the cell.

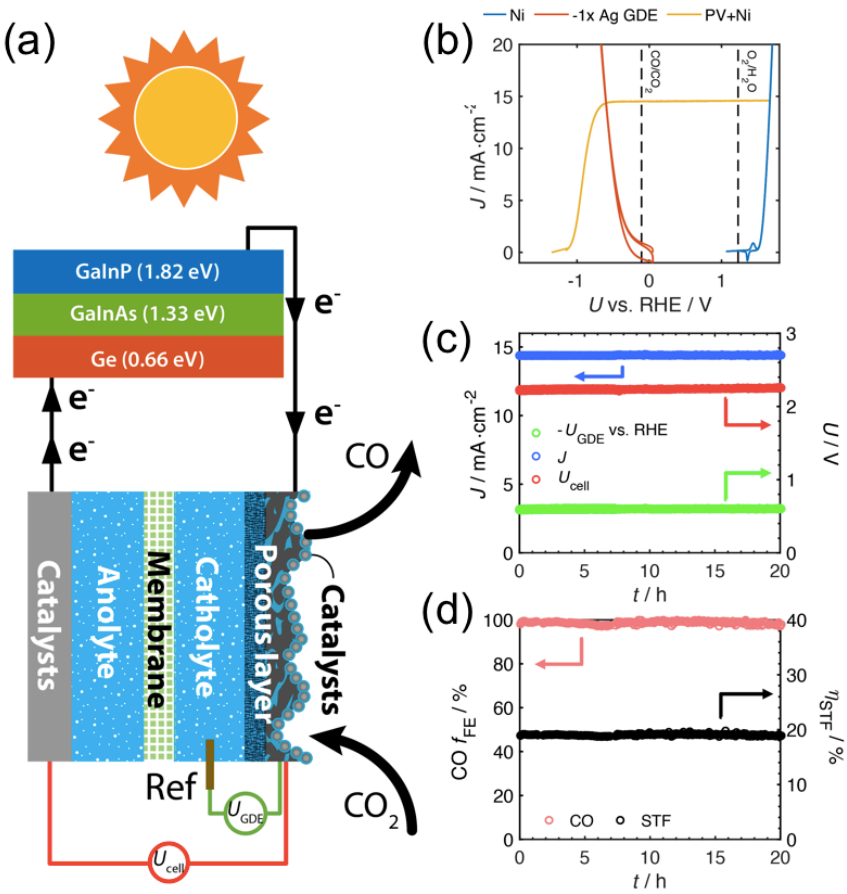

Figure 4.14: *Light driven PV-GDE measurement (A_{PV} = A_{GDE} = 0.31 cm^2). (a) Illustration of wire connection between the triple junction cell and GDE cell. (b) J-U characteristic of Ni anode, solar cell with Ni anode, and Ag-NP gas diffusion cathode under 1 Sun. (c) Current, GDE potential vs RHE, and cell voltage measurement over 20 h duration. (d) The corresponding CO Faradaic efficiency and solar to fuel efficiency over the same 20 h duration.*

To evaluate efficiency and stability, we measured cell parameters using simulated AM 1.5G sun illumination at 1 Sun in the laboratory, as shown in Figure 4.14(b-d). The blue curve in Figure 4.14(b) represents the performance of the electrochemically activated Ni foam anode alone, while the yellow curve indicates the behavior of PV plus anode. The red curve shows the catalytic current of the Ag-NPs GDE. The intersection between the red and yellow curves defines the operation point, located at -0.6 V vs. RHE and 14.4 $mA{\cdot}cm^{-2}$ with a cell voltage of 2.23 V. Figure 4.14(c-d) illustrates the cell performance over 20 hours with an average Faradic efficiency for CO of

99 ± 2 % and an average CO production rate of 2.3 mg/h. No degradation in performance was observed. From the experimental results, we calculated the average solar to CO efficiency for the 20 h operation as 19.1 ± 0.2 %, with an average energy efficiency η_{GDE} of 59.4 ± 0.6 %. The error bars were obtained as the variation within the 20 h of operation.

The solar to CO efficiency of 19.1 % represents a new record efficiency. A performance comparison with the current state-of-the-art PV-electrolyzer for CO_2 reduction to CO is shown in Table 4.3. The PV-GDE device had a CO production rate per projected cathode area 50 times higher than for the bulk electrolyte device (7.4 $mg \cdot h^{-1} \cdot cm^{-2}$ versus 0.145 $mg \cdot h^{-1} \cdot cm^{-2}$) with greatly improved stability (20 h with no degradation versus 15 % loss in 5 h).[80] A similar PV-GDE device operated under 3.25 Suns illumination with A_{GDE} = 1 cm^2, A_{PV} = 0.31 cm^2, (3.25 $\approx A_{GDE}/A_{PV}$) showed over 150 hours of stability, with an average Faradic efficiency of 96 ± 2 %, an average solar to CO efficiency of 18.9 ± 0.5 %, and an average energy efficiency η_{GDE} of 53.7 ± 1.2 %, as in Figure 4.15.

Table 4.3: *Comparison of the performance of the PV-GDE studied herein with the current state of the art PV-electrolyzer for CO_2 reduction to CO.*[80]

	Current record [80]	**This work**
Solar-to-CO (%)	13.4	**19.1**
PV size (cm^2)	0.563	0.31
Cathode / Anode	both SnO_2 / CuO	Ag GDE / Ni foil
Cathode & Anode size (cm^2)	20	0.31
Catholyte / Membrane / Anolyte	0.25 M CsOH / BPM / CO_2-sat 0.1 M $CsHCO_3$	1 M KOH /AEM / 1 M KOH
Operation current (mA)	6.6	4.5
$f_{FE,CO}$ (%)	86	99
CO production rate ($mg \cdot h^{-1} \cdot cm^{-2}$)	0.145	**7.4**
CO production rate outdoor (mg/day)	-	**15 (50 at 3.25 Suns)**
Stability (h)	5 (with 15% loss)	**20 (150 h at 3.25 Suns)**

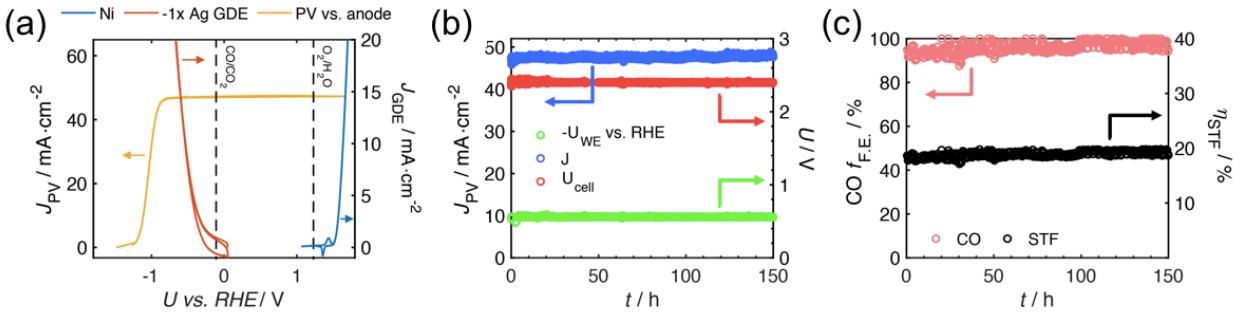

Figure 4.15: *Efficiency and stability assessment at a solar concentration 3.25 Suns. (C = 3.25, A_{GDE} = 1 cm^2, A_{PV} = 0.31 cm^2) (a) J-U characteristic of Ni anode, solar cell with Ni anode, and Ag-NP gas diffusion cathode under 3.25 Suns. (b) Current and cell voltage measurement over*

150 h duration. (c) The corresponding CO Faradaic efficiency and solar to fuel efficiency over the same 150 h duration.

Full day outdoor tests were conducted with online gas product analysis in order to obtain the solar to fuel efficiency over the entire day. The triple junction cell and a calibrated silicon photodiode were mounted on a solar tracker to maintain optimum orientation toward the Sun. Results are shown in Figure 4.16. The dips in sun intensity at 7:00am - 9:00am and 4:00 - 6:00 p.m. in the data were the result of trees blocking the sunlight. The system operated at a cell voltage of 2.20 V and GDE potential of -0.57 V vs. RHE under natural full sun illumination. A Faradaic efficiency of 96 ± 8 % and solar to fuel conversion efficiency of 18.7 ± 1.7 % was observed over an optimal 6 h period within the day. The diurnal-averaged solar to fuel conversion efficiency was 5.8 %. The CO production rate for one day under actual outdoor sun conditions was calculated to be 15 mg/day of CO. Another outdoor demonstration used a lens to concentrate the sunlight producing an irradiance of 3.25 Suns (C = 3.25, A_{GDE} = 1 cm^2, A_{PV} = 0.31 cm^2) with data included in Figure 4.17 with a CO generation rate of 50 mg/day. Using this calculated rate, a system scale up to 1 m^2 would result in a CO production rate of 0.5 kg/day.

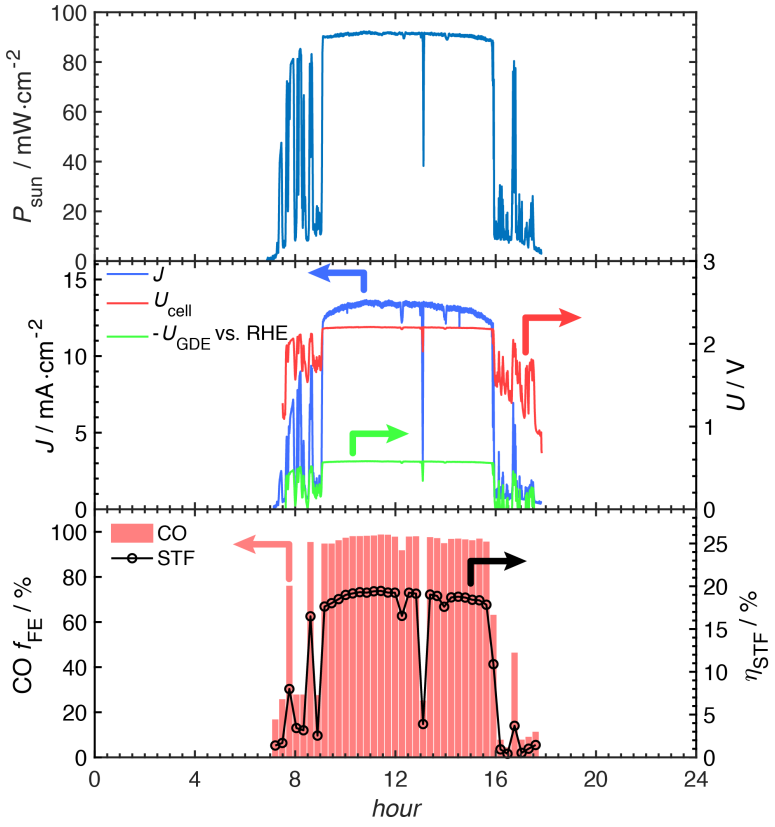

Figure 4.16: *Outdoor assessments of solar driven PV-GDE in Pasadena, CA (A_{PV} = A_{GDE} = 0.31 cm^2). The solar irradiance was monitored with a calibrated silicon photodiode. Operation current density J (= J_{GDE} = J_{PV}), cell voltage U_{cell}, GDE potential U_{GDE} vs. RHE, CO Faradaic efficiency $f_{FE,CO}$, and solar to fuel efficiency η_{STF} were recorded for a 24h day cycle.*

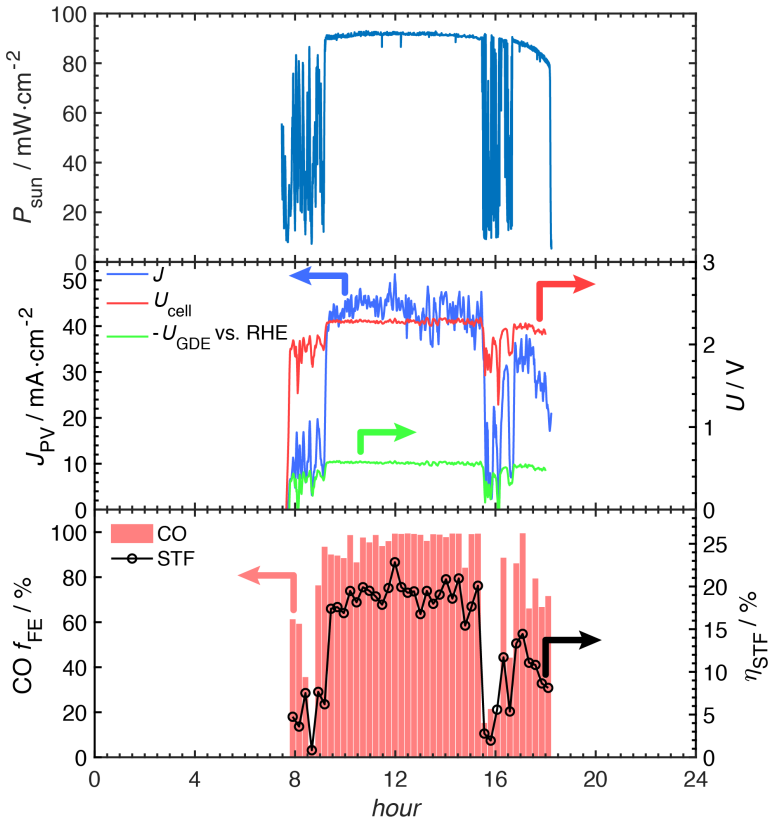

Figure 4.17: *Outdoor tests of solar-driven PV-GDE in Pasadena, CA. The solar irradiance was monitored with a calibrated silicon photodiode. PV operation current J_{PV}, cell voltage U_{cell}, working electrode potential U_{GDE}, CO Faradaic efficiency $f_{FE,CO}$, and solar to fuel efficiency η_{STF} were recorded for a 24h day cycle with 3.25x solar concentrator (C = 3.25, A_{GDE} = 1 cm^2, A_{PV} = 0.31 cm^2).*

The performance of our directly coupled PV-GDE device was compared to a DC-DC converter coupled PV and GDE with power-matching electronics. We simulate DC-DC converter output curves with the input of our solid-state PV curve as shown in Figure 4.18. Though the DC-DC converter can track the maximum power point (MPP) of the PV, a practical loss of 5-10 % is expected.[117] The operating point for the directly driven PV-GDE cell is U_{cell} = 2.23 V, J = 14.4 mA·cm^{-2} with a maximum efficiency of 19.3 %. With a 95 % efficient DC-DC converter, the operation point would be U_{cell} = 2.22 V, J = 13.8 mA·cm^{-2} with a maximum efficiency of 18.5 %. For a 90 % efficient DC-DC converter, the operation point would be U_{cell} = 2.20 V, J = 13.2 mA·cm^{-2} with a maximum efficiency of 17.7 %. The maximum efficiencies are calculated

assuming 100 % CO Faradic efficiency. The slightly higher efficiency of our directly driven PV-GDE device, compared to the same setup with integrated DC-DC converter and power matching electronics, reveals the potential of developing a directly coupled PV-GDE device with its reduced complexity. All the experimental results (including simulated/natural sun light, with/without concentrator) and calculated systems in this work are summarized in Table 4.4.

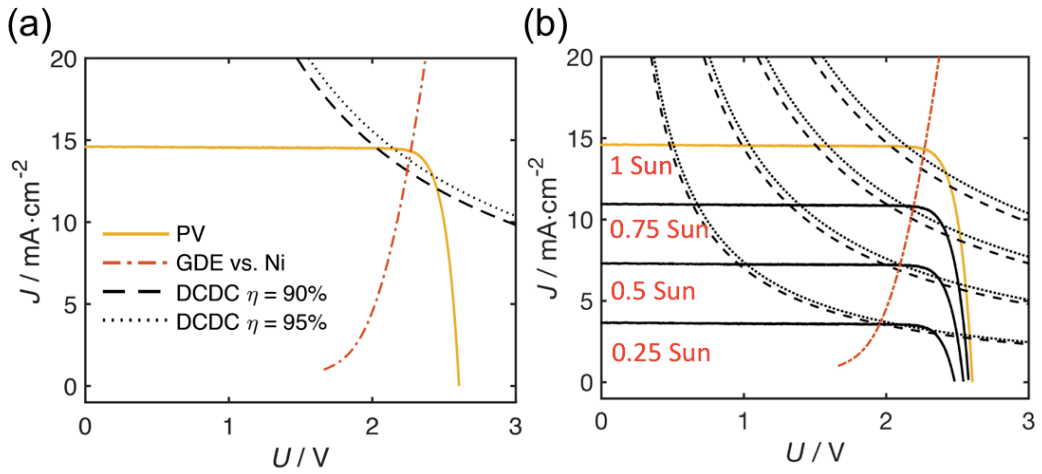

***Figure 4.18**: J-U characteristic of the GaInP/GaInAs/Ge triple junction cell under 1 Sun (yellow solid line) with combined load curve of Ni anode and Ag GDE cathode (red dot-dashed line) in addition to DC-DC converter output curves (solid PV curve as input) with converter efficiency of 90 % (black dashed line) and 95 % (black dotted line). The PV curves for lower illumination conditions are included on the right figure.*

Table 4.4: *Comparison of the PV-GDE performance studied herein with different measurement conditions and calculations.*

Irradiance ($mW \cdot cm^{-2}$)	**Source**	**A_{PV} (cm^2)**	**A_{GDE} (cm^2)**	**$f_{FE,CO}$ (%)**	**η_{GDE} (%)**	**η_{STF} (%)**	**J_{PV} ($mA \cdot cm^{-2}$)**	**U_{cell} (V)**	**Power ($mW \cdot cm^{-2}$)**
100	Simulated	0.31	0.31	99	59.4	19.1	14.4	2.23	32.1
325	Simulated	0.31	1	96	53.7	18.9	47.5	2.39	113.5
91	Natural	0.31	0.31	96	58.5	18.7	13.0	2.20	28.6
296	Natural	0.31	1	96	55.9	18.9	43.0	2.30	98.9
100	Calculated	0.31	0.31	100	60.0	19.3	14.4	2.23	32.1
100	Calculated	0.31	0.31	100	60.4	18.5	13.8	2.22	30.6
100	Calculated	0.31	0.31	100	60.9	17.7	13.2	2.20	29.0

4.4 Conclusion and Outlook

In summary, we have demonstrated a highly efficient solar-driven CO_2 reduction device for CO generation using a flow-by *reverse-assembled* gas diffusion electrode cell directly coupled to a triple junction solar cell. The *reverse-assembled* GDE is designed to minimize parasitic CO_2 losses, utilizing a high CO_2 concentration and low overpotential catalysts for the CO_2 reduction reaction. The Ag-NPs based catalysts exhibited near unity Faradic efficiency towards CO generation at approximately -0.6 V vs. RHE in 1 M KOH electrolyte. The PV-GDE system was evaluated under both laboratory AM 1.5G simulated solar irradiation and outdoor real sun conditions. Near-unity Faradic efficiency was observed for CO_2-to-CO conversion and an average solar-to-CO energy efficiency of 19.1 % was achieved with AM 1.5G illumination at 1 Sun, leading to over 50 times higher CO production rate per catalyst area than the current record

photovoltaic-driven electrolysis device. The GDE was demonstrated to be stable for over 150 hours without degradation, supporting our hypothesis that, by using a *reverse-assembled* GDE device configuration with the catalyst layer facing towards the CO_2 gas supply, we could extend the system operation time without suffering a transition from a wetted to a flooded gas diffusion layer. Under outdoor sun conditions, the PV-GDE system exhibited a solar to CO conversion efficiency of 18.7 % during noontime, and yielded a CO production rate of 15 $mg \cdot cm^{-2}$ per day. This *reverse-assembled* PV-GDE establishes a new efficiency record for directly solar-driven CO_2 reduction, and offers an example of a very high efficiency, stable device for solar CO_2 conversion.

Preventing CO_2 neutralization of the basic electrolyte for sustainable operation would be the practical direction to pursue. It is proven that by catalyst engineering, near unity Faradaic efficiency toward CO production under low overpotential in bicarbonate electrolyte can be achieved. Possible strategies involve introducing defects or surface ligand, facet or morphology control, oxidation state manipulation, and utilizing co-catalysts or alloy catalysts. Direct reduction from bicarbonate electrolyte eliminates the high energy input of normal CO_2 capture process, and can possibly enhance the CO_2 utilization rate.

CHAPTER 5
Broadband Transmission TiO_2 Nanocone

5.1 Introduction

High efficiency conversion of solar energy to electricity or fuels using photovoltaic (PV) [118-122] or photoelectrochemical (PEC) [65,69,123] cells requires optimization of the broadband absorption of sunlight. Anti-reflective coatings (ARCs) [124], surface textures, [125-128] and high-index light-trapping structures[129,130] are among the many strategies that have been shown to increase broadband absorption relative to unmodified planar light absorbers. PECs and multijunction PVs generally require front contacts and/or electrocatalytic films that substantially reflect or absorb light, thereby reducing their photocurrent densities. [131] In integrated PECs used to affect solar-driven water splitting or CO_2 reduction, [6,78,82] the front contact is made to an electrolyte, and a catalyst located in the optical path increases the efficiency of the cell by reducing the kinetic barrier for the electrochemical half-reaction occurring at the top contact. Depending on the orientation of the design, as well as the chemical inputs and desired products, the catalyst may be optically opaque (such as CoP for water reduction or Cu for CO_2 reduction) or may be electrochromic (such as $NiFeO_x$ for water oxidation). [132] Although an all-back-contact design[133,134] can prevent contact shading losses in crystalline Si solar cells, such a design is not compatible with all of the solid/liquid interfaces either with integrated PECs for highly efficient fuel production or with multijunction PV device structures. [135]

Nanostructuring the semiconductor is one approach that has been developed to enhance broadband absorption. Nanowires, [43,56,136] inverted pyramids, [137] nanodomes, [138] nanoshells, [139] nanopillars, [140,141] and nanocones[142] have been explored for use in many optoelectronic devices. For example, for wavelengths ranging between 400 – 1100 nm and angles-of-incidence between 0° – 50°, Si microcone arrays exhibit nearly perfect angularly and spectrally averaged reflectivity (< 1 %) as well as high (89.1 %) absorption. [143] In Chapter 2, we also demonstrate sparse arrays of InP nanocones exhibiting angle-insensitive, near-unity (>90%), broadband (450−900 nm) optical absorption. [144] Cones inherently possess a continuous range of radii that provides a range of waveguide modes accessible for coupling with incident light. [23] Hence, cones are intrinsically favorable structures for enabling enhanced broadband absorption.

Moreover, the radius at the base of the cone and the radius of any truncation can be chosen specifically to select a spectral range of interest.

Alternatively, broadband absorption can be enhanced by decorating the light-facing surface of the semiconductor with dielectric nanostructures, such as nanospheres, [145] that serve as waveguides. This approach requires a high-index dielectric that can be deposited on planar surfaces using scalable methods. For integrated PEC devices, the dielectric also must be stable in the chosen aqueous electrochemical environment. TiO_2 has been used in waveguides for near-visible and telecommunication wavelengths, [146-151] and has a higher index of refraction (n~ 2.5) than many other dielectric materials commonly used in solar photovoltaic devices, including SiO_2 (n = 1.5) and Al_2O_3 (n = 1.77). TiO_2 is relatively inert electrochemically and has a wide band gap that allows transmission of incident solar illumination, and has been utilized extensively as a protective coating in efficient PEC devices. [6,74,78,82,152-156] TiO_2 is therefore a promising candidate material for nanostructured waveguides in PEC devices.

Devices that make use of nanostructured surfaces nevertheless require front contacts, either to a conductor for PVs or to a catalyst for PECs, but the front contact can block light. In devices that require connections between external circuits and nanostructured optical surfaces, front contacts typically are formed by coating the surface with a transparent and conductive material, such as indium tin oxide (ITO). However, efficient integrated PECs for fuel production additionally require catalysts on at least one of the optical surfaces. Very high (> 90%) absorption and high front-surface conductivity have been demonstrated using both simulation and experiment in a device consisting of SiN_x-coated Si nanopillars protruding from a crystalline Si substrate coated with an opaque Au front-side contact that covered 65% of the Si surface. [141] Although the selective etching process used in this approach limits its applicability to a few specific interfaces such as Au/Si, this work shows that nanostructures can direct light around opaque metallic front contacts deposited onto the optical surfaces of PV devices, and suggests a strategy for guiding light around catalyst layers in PECs.

Considered together, the prior work in the areas of antireflective nanostructures and dielectric waveguides underscores the potential value and developmental feasibility of modular antireflective coatings that promote broadband absorption over a spectral range above the

photoelectrode bandgap without requiring modification of the underlying semiconductor or contact interfaces. Herein, we combine simulations and proof-of-concept experiments to evaluate and demonstrate light management by an array of TiO_2 nanocones placed on the surface of a p^+n-Si photoanode with a metallic Ni contact covering the exposed Si surface.

5.2 Numerical and Experimental Method

3D full-field electromagnetic wave finite-difference time-domain (FDTD) simulations of TiO_2 nanocone arrays with or without Ni films, with hexagonal arrays of holes on Si, were performed using a commercial software package, Lumerical FDTD. The nanocone arrays on Si were constructed using the 3D simulation region with periodic boundary conditions along the *x*- and *y*-axes, and infinite boundary conditions were rendered as perfectly matched layers along the *z*-axis. Palik materials data were used for Si and Ni. Material data from the Ioffe Institute and ellipsometry measurements (J.A. Woollam Co. model VASE) were both used for simulation of the optical properties of the TiO_2 nanocones. A plane-wave source of illumination was applied to simulate the steady-state behavior of TiO_2 nanocones with or without Ni arrays on the Si substrate. Broadband simulations were performed in the 400 – 1100 nm spectral range for two orthogonal polarizations. Transmission spectra for unpolarized light were obtained by averaging the transmission spectra for the two orthogonal polarizations. These transmission spectra, along with the standard AM 1.5G spectra, were used to calculate the fraction of the spectral photon flux that was transmitted into the Si. The expected light-limited photocurrent density ($J_{ph,max}$) can be estimated by integration of the transmitted spectral photon flux with the corresponding wavelength. Frequency-domain field and power monitors were applied in the simulation to produce the steady-state electric-field data for plots of electric-field profiles.

Czochralski-grown n-type Si wafers with <100> orientation and a resistivity of 0.1-1 ohm-cm (Addison Engineering Inc.) were cleaned via a modified RCA standard clean 1 (5:1:1 by volume of H_2O:NH_4OH:H_2O_2 at 70 °C), then 1 min immersions in 10% (v/v) HF, and followed by an RCA standard clean 2 (6:1:1 H_2O:HCl:H_2O_2 (v/v) at 70 °C). The cleaned n-Si samples were thermally doped with boron using a BN-975 (Saint-Gobain) wafer at 950 °C for 30 min to produce a p^+n-Si homojunction. The doped p^+n-Si samples were immersed in 10% (v/v) HF(aq) for 2 min,

oxidized in a tube furnace at 750 °C for 20 min, and then dipped in 10% (v/v) HF for 2 min to remove any defective layers on the Si surface.

A layer of SiO_2 (5 – 10 nm) was deposited onto the p^+n Si wafers via electron-beam evaporation, and 2.3 μm of TiO_2 was then deposited onto the samples via electron-beam evaporation. Electron-beam evaporation depletes the source of oxygen and results in TiO_2 with higher conductivity than perfectly stoichiometric TiO_2, so the deposition was performed in 3-4 steps, refilling the TiO_2 source between steps to maintain higher oxygen content in the film. The TiO_2-coated p^+n-Si samples were spin-coated at 4000 rpm for 60 s with 495 PMMA A4 and baked at 80 °C for 5 min, then spin-coated at 4000 rpm for 60 s with 950 PMMA A4 and baked again at 80 °C for 5 min to form a bilayer of positive tone resist to facilitate lift-off. The samples were patterned with a hexagonal array of 100 nm diameter circles on a 700 nm pitch, using direct electron-beam lithography (VISTEC electron-beam pattern generator (EBPG) 5000+) with an acceleration voltage of 100 keV and a current of 5 nA. After electron-beam writing, the pattern was developed in a 1:3 MIBK (methyl isobutyl ketone):isopropanol for 60 s at room temperature, resulting in a hexagonal array of 100 nm diameter holes with a 700 nm pitch in the PMMA layers. A 200 nm layer of Cr was evaporated over these samples (rate 1 $A \cdot s^{-1}$ at 10^{-6} Torr), and lift-off was performed in acetone, leaving a hexagonal array of Cr that served as a hard mask for TiO_2 dry etching. Dry etching was then conducted using an Oxford Instruments Plasma Lab System 100 ICP-RIE by using SF_6 / C_4F_8 etching chemistry, in which SF_6 was the etching gas and C_4F_8 was the passivating gas. Etching was performed at a capacitively coupled power of 150 W, an inductively coupled power of 2500 W, a SF_6 / C_4F_8 gas ratio of 23.5 sccm / 40 sccm, a chamber pressure of 7 mTorr, and a table temperature of 0 °C for 15 min.

Electrodes were prepared from the n^+p-Si samples with etched TiO_2 cones by first cleaving the samples to remove the edges, thus avoiding shorts due to doped layers. In-Ga eutectic was applied on the back side of the samples to form an ohmic contact to the p^+n-Si homojunction. Ag paste (Ted Pella) was used to attach a Sn-plated Cu wire to the In-Ga on the back side of the sample. The wire was run through a glass tube, and the samples were sealed to the glass tube using epoxy (Loctite 9460) and annealed at 80 °C for ~ 6 h. The active area of the electrodes was determined using a high-resolution image taken using a commercial scanner and image-processing software (ImageJ). Typical electrode areas were ~ 0.04 cm^2.

The samples were then dipped in buffered HF (40% NH_4F to 49% HF volume ratio 6:1) for 10 s to remove the remaining SiO_2 between the TiO_2 cones and to fully remove the Cr mask. The Ni layer was subsequently electrodeposited on the areas of the surface of the p^+n-Si between the TiO_2 nanocones using a commercially available Ni plating solution (Clean Earth Nickel Mirror, Grobet USA) at a potential of -0.956 V vs Ag /AgCl (using a Biologic SP-200 potentiostat) until ~ 300 mC cm^{-2} of cathodic charge was passed. An illustration of the process flow for fabrication of the desired structures is shown in Figure 5.1.

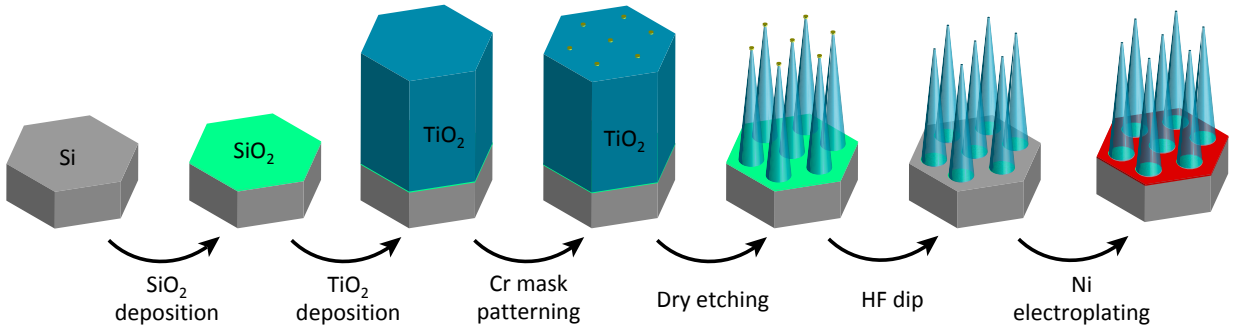

Figure 5.1: *Process flow diagram for fabrication of Si photoanodes with TiO_2 nanocones and Ni catalysts.*

An array of holes in a Ni layer on p+n-Si was fabricated as a comparing sample. Electron-beam evaporation was used to deposit a layer of Ni on p^+n-Si samples. The samples were then covered with ZEP 520A by spin-coating at 4000 rpm for 60 s and were baked at 180 °C for 3 min. A hexagonal array of circles 500 nm in diameter with a 700 nm pitch was written onto the samples by direct electron-beam lithography using an acceleration voltage of 100 keV and a current of 50 nA. The pattern was then developed by immersing the samples in a ZED N50 solution for 90 s. The patterned resist was used as a mask for ICP-RIE etching of the Ni film. Etching was performed using the following parameters: 4 mTorr, 600 W ICP forward power, 150 W RF forward power, 20 °C, 30 sccm Ar. The final removal of ZEP 520A was performed using remover PG.

A three-necked glass cell with a quartz window was used as a vessel for the photoelectrochemical oxygen-evolution reaction (OER). The OER was performed in aqueous 1.0 M KOH (Sigma-Aldrich) using a three-electrode setup, with a saturated calomel electrode (SCE) as the reference electrode, a carbon electrode as the counter electrode, and the p^+n-Si sample with

TiO_2 cones and Ni as the working electrode. Measurements were conducted under simulated sunlight (Oriel Instruments Solar Simulator equipped with a 1000 W Mercury Xenon lamp calibrated to 100 mW cm^{-2} (AM1.5) illumination using a Si photodiode). For current-density versus voltage (*J-V*) measurements, the voltage was swept at a scan rate of 50 mV s^{-1} from -0.5 V to 1.5 V vs SCE.

5.3 Results and Discussion

Figure 5.2 shows schematics for three device configurations that were compared using simulations to understand the optical properties of TiO_2 nanocones. In the first configuration, Figure 5.2(a), TiO_2 nanocones with a height of 2300 nm and a base radius of 250 nm were placed on the Si substrate in a 2D hexagonal array with a 700 nm pitch. This arrangement left 54% of the Si surface uncovered by TiO_2 nanocones. In the second configuration, Figure 5.2(b), 50 nm of Ni covered the area of Si that remained exposed in the first configuration. The third configuration, Figure 5.2(c) was the same as the second, but the TiO_2 nanocones were removed, leaving a hexagonal array of circles of exposed Si in the Ni layer.

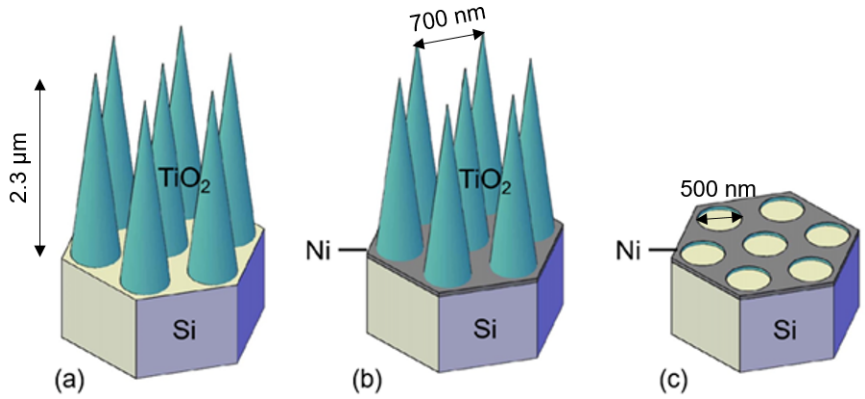

Figure 5.2: *Schematics of the three configurations that were simulated. (a) TiO_2 nanocones on Si substrate; (b) Ni between the TiO_2 nanocones on Si substrate; (c) Ni hole arrays on Si substrate.*

Figure 5.3 compares the simulated transmission, absorption, and reflection spectra for the TiO_2 and Ni components of the three structures, either in air (n = 1.0) or in water (n = 1.33). Figure

5.3 (a,d) shows that the TiO_2 nanocones neither absorb nor reflect substantially in the 400 – 1100 nm spectral range, with the nanocones allowing transmission of 97.5% of the total incident photons in air or 96.9% in water. The planar TiO_2 film simulations, with higher reflection losses, are shown in Figure 5.4, leading to transmission of 74.7% in air and 84% in water. When 50 nm of Ni was added into the spaces between the nanocones, the simulated transmitted photon flux was reduced to 86.2% in air or 84.7% in water (Figure 5.3(b,e)). The minima in transmission primarily result from absorption by Ni, and the wavelengths of the minima shift depending on the index of refraction of the surrounding environment.

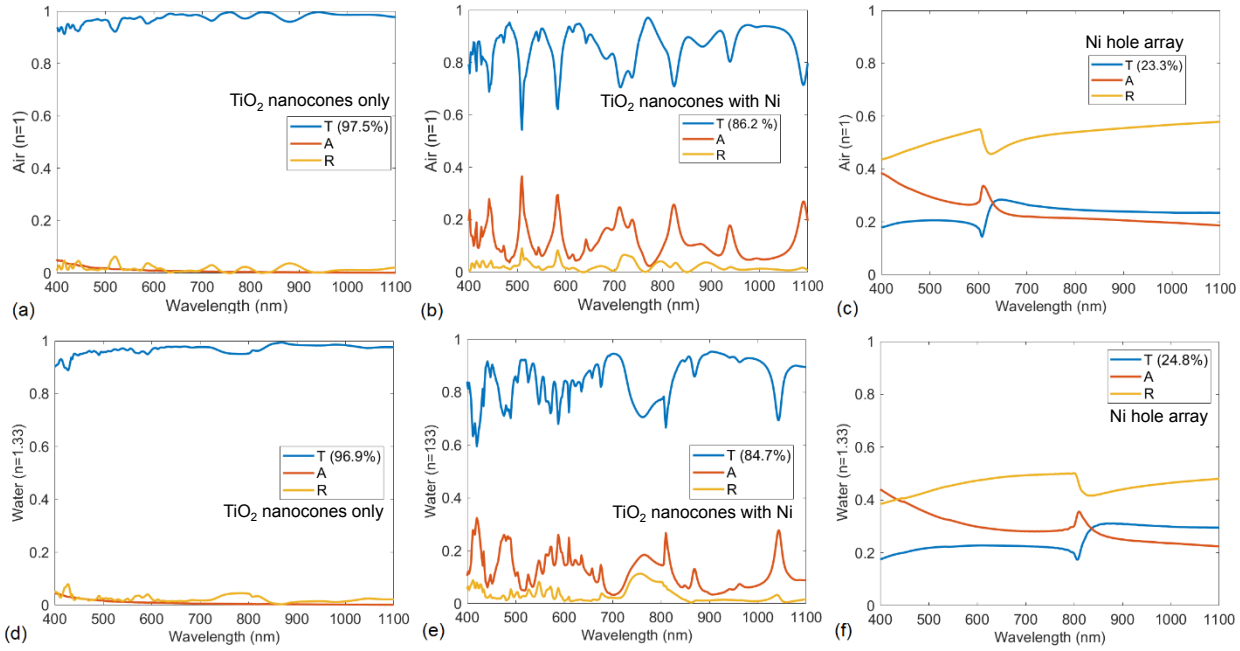

Figure 5.3: *Simulated transmission (T), absorption (A), and reflection (R) spectra of the three configurations of the TiO_2 nanocone array and Ni layer in Figure 5.2. (a), (b), and (c) plot the spectra in air for an array of TiO_2 cones, a TiO_2 cone array with Ni, and a Ni hole array, respectively. (d), (e), and (f) plot the same structures but in water. The optical effects of the Si substrate are not shown.*

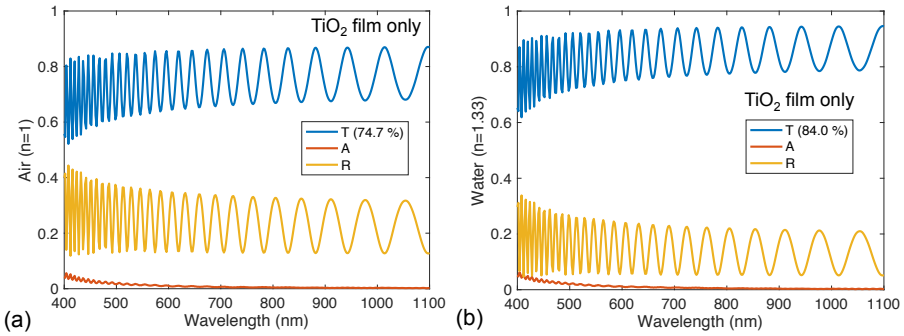

Figure 5.4: *Simulated transmission (T), absorption (A), and reflection (R) spectra of the TiO_2 film with thickness of 2.3 µm. (a) plot the spectra in air (b) plot the spectra in water.*

When the TiO_2 nanocones were removed from the simulation, leaving just the hexagonal array of circular holes in a 50 nm layer of Ni that covered 54% of the optical plane, the transmitted photon fluxes were reduced to 23.3% in air or 24.8% in water, with reflection and parasitic absorption accounting for ≥ 75% of the optical losses (Figure 5.3(c,f)). The size and pitch of the holes in the Ni layer were particularly unfavorable for transmission of light through the Ni layer in the absence of the TiO_2 cones, because over a large fraction of the incident solar spectrum, the diameter of the holes was less than the wavelength of the incident light. In the specific configuration shown in Figure 5.2(b), the TiO_2 nanocones minimized the interaction between the light and the Ni layer, enabling > 3 times the amount of light to be transmitted than for the Ni hole array that did not also contain the TiO_2 cones. For the TiO_2 nanocone array with Ni, the simulated transmission at the minima was ≥ 60%, Figure 5.3(b,e), whereas for the Ni hole array without TiO_2 nanocones, the simulated transmission of was 20-30%, Figure 5.3(c,f)). The simulations thus indicated that incident light is expected to couple efficiently to the TiO_2 nanocones that guide the light around the Ni layer.

Figure 5.5 plots the transmitted photon flux for each structure along with the Air Mass (AM) 1.5G solar spectrum. Using the transmitted spectral photon flux, the maximum photocurrent densities, $J_{ph,max}$, in air estimated from the simulations for a Si solar cell covered by either the TiO_2 nanocone array, the TiO_2 nanocone array with Ni or the Ni hole array were $J_{ph,max}$ = 42.9 mA cm^{-2}, 37.9 mA cm^{-2}, and 10.9 mA cm^{-2} respectively. In water, the corresponding estimated simulated

maximum photocurrent densities were $J_{ph,max}$ = 41.8 mA cm^{-2}, 36.5 mA cm^{-2}, and 10.7 mA cm^{-2}, respectively.

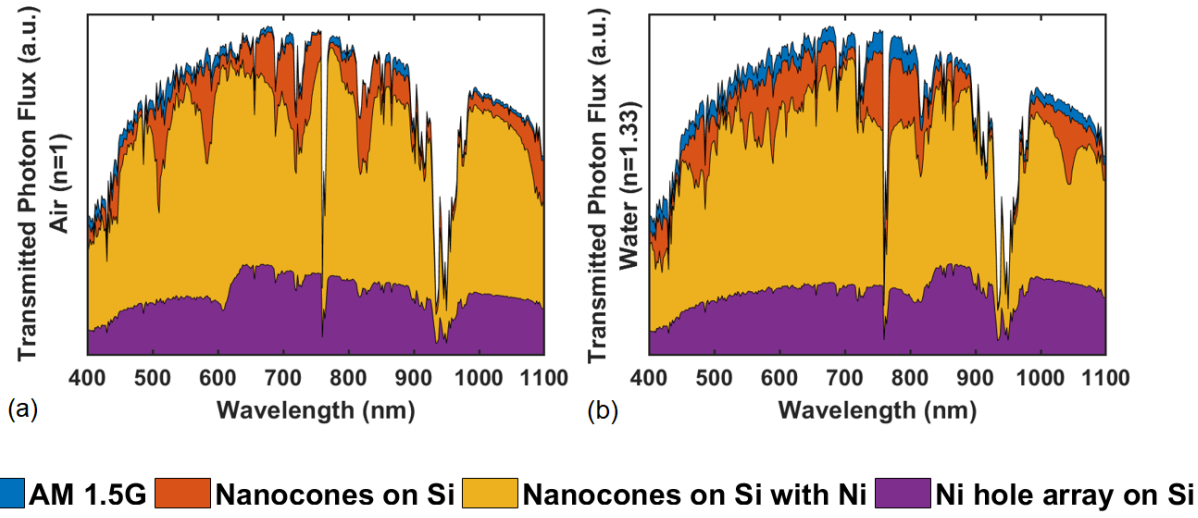

Figure 5.5: *Area plot of simulated transmitted spectral photon flux in air and water for the three structures in Figure 1. Blue represents the AM 1.5G spectral photon flux. Orange, yellow, and purple depict the transmitted spectral photon flux into Si for: nanocones on Si, nanocones with Ni on Si, and Ni hole array on Si, respectively.*

Figure 5.6 shows the simulated profiles of the electric field along the central cross section of a nanocone. Figure 5.6(c-f) shows the field profiles for wavelengths of 484 nm, 552 nm, 628 nm, and 770 nm, respectively, which correspond to the maxima in the transmission spectra shown in Figure 5.3(b). The electric field was predominantly confined to the waveguide modes in the nanocone, with strong coupling of incident light occurring at different radii for the different wavelengths, as expected for a conical nanostructure. [23,143,144] In the simulation, the light propagated through the nanocone and was transmitted into the Si substrate, where the field intensity decreased due to absorption by the Si. Figure 5.6(g-j) shows the field profiles for wavelengths of 442 nm, 584 nm, 738 nm, and 940 nm, respectively, which correspond to the minima in the transmission spectra shown in Figure 5.3(b). Compared to the field profiles shown in Figure 5.6(c-f), the profiles in Figure 5.6(g-j) showed an increased intensity of the electric field in the space adjacent to the nanocone. The corresponding plots for transmitted light intensities $|E|^2$

versus Y(μm) at the interfaces of Si/Ni (indicated as on Si) and Ni/air (indicated as on Ni) are shown in Figure 5.7.

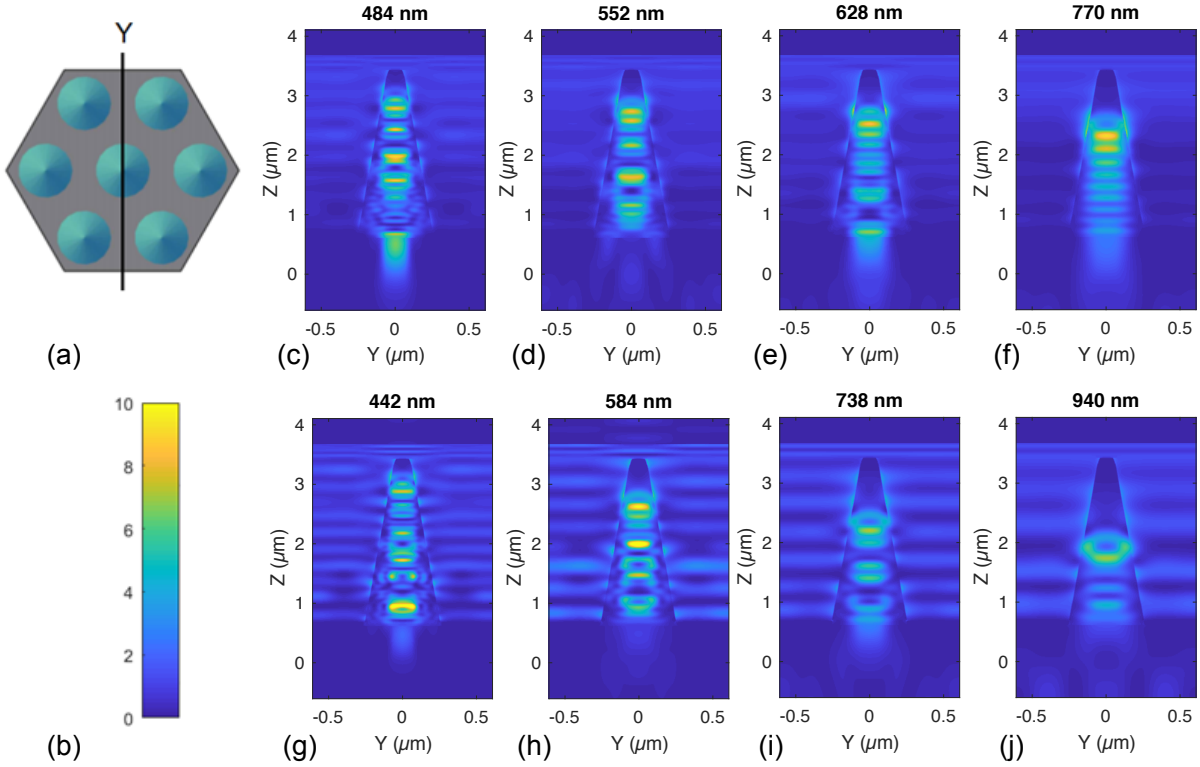

Figure 5.6: *Simulated electric field profiles along the cross section of a TiO_2 nanocone on a Si substrate. (a) Cross section and (b) scale for the relative electric field intensity for the profile plots. (c-f) Profiles for wavelengths of 484 nm, 552 nm, 628 nm, and 770 nm, respectively, which correspond to the maxima in the transmission spectra shown in Figure 5.3(b). (g-j) Profiles for wavelengths of 442 nm, 584 nm, 738 nm, and 940 nm, respectively, which correspond to minima in the transmission spectrum in Figure 5.3(b).*

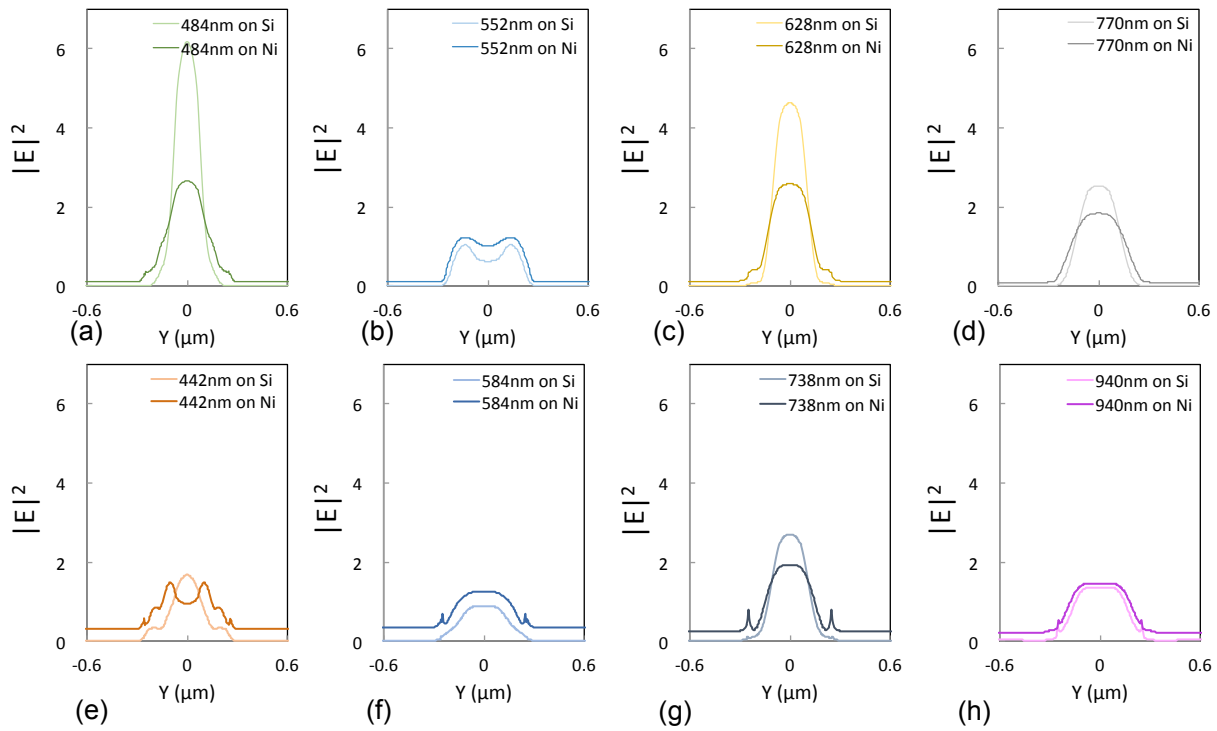

Figure 5.7: *Transmitted light intensities $|E|^2$ versus Y(μm) at interfaces of Si/Ni (indicated as on Si) and Ni/air (indicated as on Ni). (a-d) Profiles for wavelengths of 484 nm, 552 nm, 628 nm, and 770 nm, respectively, which correspond to the maxima in the transmission spectra shown in Figure 5.3(b). (e-h) Profiles for wavelengths of 442 nm, 584 nm, 738 nm, and 940 nm, respectively, which correspond to minima in the transmission spectrum in Figure 5.3(b).*

Depending on the dimensions of the nanocones and the background index of refraction, simulations indicated that the electric fields associated with some wavelengths of light were highly confined inside the TiO_2 nanocone, while the electric fields associated with other wavelengths were only partially confined. Simulation results with varying dimensions of cones are presented in Figure 5.8. In contrast, the optical absorption in the Ni was enhanced for the wavelengths of light that were not completely confined within the nanocones. The wavelength-dependent variation in the confinement of the electric field within TiO_2 nanocones cannot be explained using effective medium theory. Instead, wave-optic simulations showed that the nanocones acted as antennae for the incoming radiation, coupling the light to waveguide modes, and providing a route for the light to reach the underlying Si substrate even though 54 % of the surface was covered by Ni.

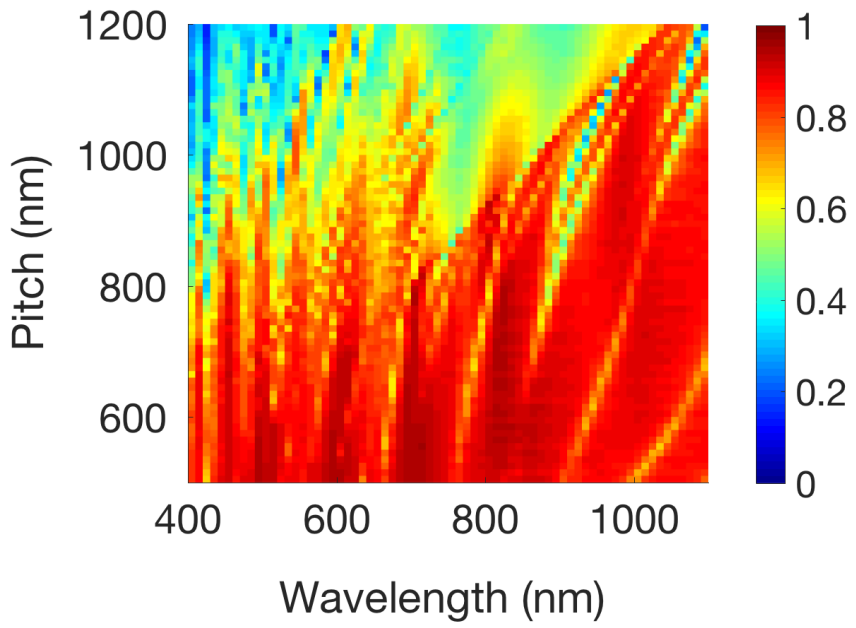

Figure 5.8: *Dimension variation effect of Ni film on transmission to Si through TiO_2 nanocone waveguides in air. Hexagonal array (variant pitches) of 2.5 μm tall cones with a 200 nm base radius and a 50 nm tip with a 200 nm radius Ni hole array.*

The optimal structures revealed by simulation were fabricated and investigated in detail. To experimentally demonstrate the enhancement in photocurrent density obtainable by utilizing TiO_2 nanocone arrays, planar p^+n Si homojunction photoanodes were prepared by doping n-type Si with boron (B). Briefly, electron-beam evaporation was used to deposit 5 - 10 nm of SiO_2 over the Si photoanodes, prior to deposition of 2.3 μm of TiO_2. Electron-beam evaporation depletes the TiO_2 source of oxygen and thus increases the conductivity of the resulting films, so the 5 – 10 nm thick SiO_2 was deliberately incorporated to electrically isolate the TiO_2 from making an electrical contact to the highly doped p^+-Si surface, while minimally affecting the optical behavior.

Figure 5.9 shows scanning-electron micrographs (SEMs), before and after electrodeposition of Ni, for samples of dry-etched TiO_2 nancone arrays on planar p^+n-Si substrates. The EDS mappings are included in Figure 5.10. The TiO_2 nanocones were ~ 2.3 μm tall and had base radii of ~ 250 nm. Discontinuities in the taper of the nanocones were evident, particularly near the vertex of each cone. The radii at the vertices of the nanocones were < 50 nm. Figure 5.9(b,d) show that the Ni predominantly deposited onto the Si surface in the spaces between the TiO_2 nanocones, as

expected because the insulating 5-10 nm layer of SiO_2 beneath the base of the cones should prevent electrodeposition onto the TiO_2. The Ni layer was ~ 70 nm thick as estimated based on the charge passed during electrodeposition. The SEM image of a 50 nm thick Ni hole array fabricated via electron-beam patterning and dry etching is shown in Figure 5.11.

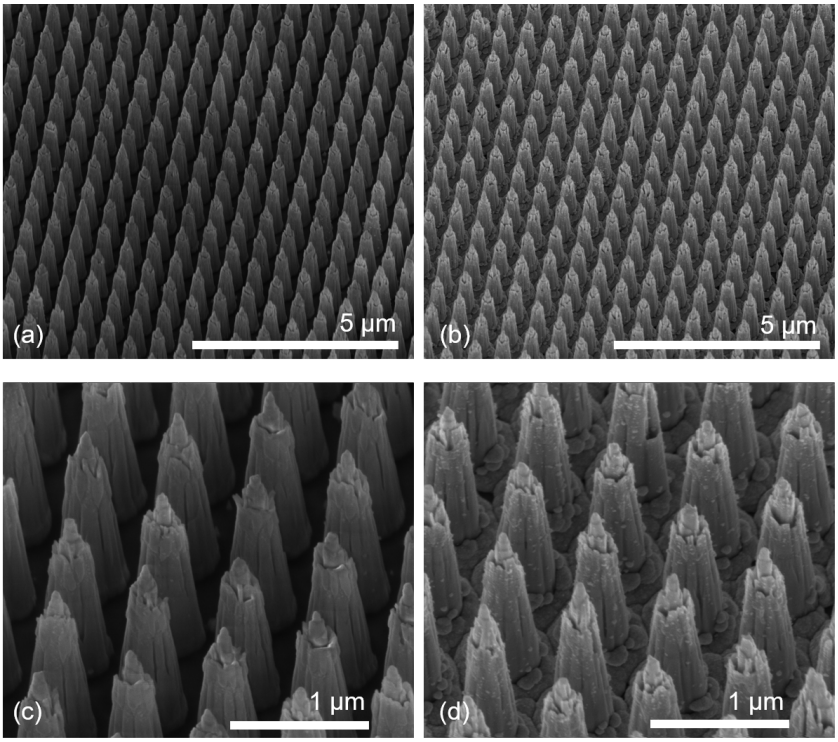

Figure 5.9: *Scanning-electron micrographs of dry-etched TiO_2 nanocones on p^+n-Si substrates before (a,c) and after (b,d) electrodeposition of Ni.*

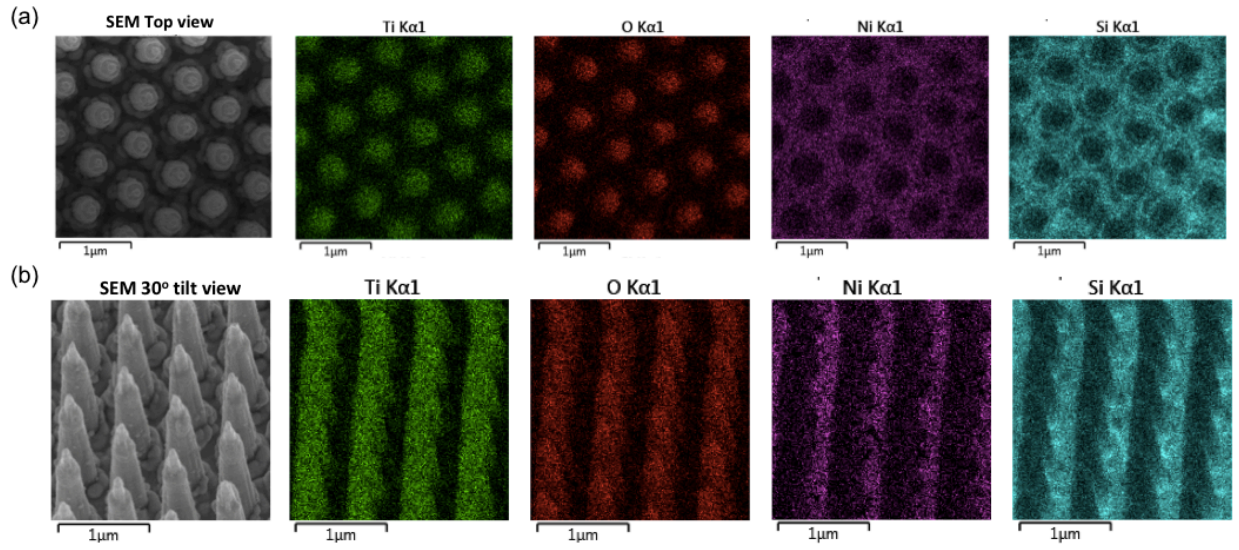

Figure 5.10: *EDS mappings of elements Ti, O, Ni, Si (a) with top view (b) with 30° tilt view of the Ni/TiO_2 nanocones/p^+n-Si sample.*

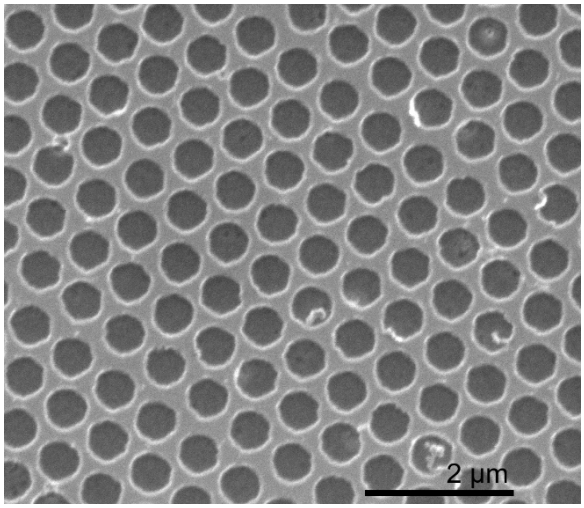

Figure 5.11: *SEM image of the Ni hole array fabricated via electron-beam patterning and dry etching of a 50 nm thick Ni layer. The average diameter of the holes was ~ 500 nm.*

Figure 5.12 compares the real component of the complex refractive index measured by ellipsometry for the electron-beam-evaporated amorphous TiO_2 used to make nanocones in this work relative to the real component of the index of refraction of ideal rutile TiO_2 tabulated in

standard reference data. [157] The real component of the refractive index for the electron-beam-evaporated TiO_2 was substantially lower (n = 2.05 – 2.3) than for the standard value (n = 2.7 – 3.3), presumably due to oxygen depletion during evaporation and the amorphous phase of the TiO_2 film.

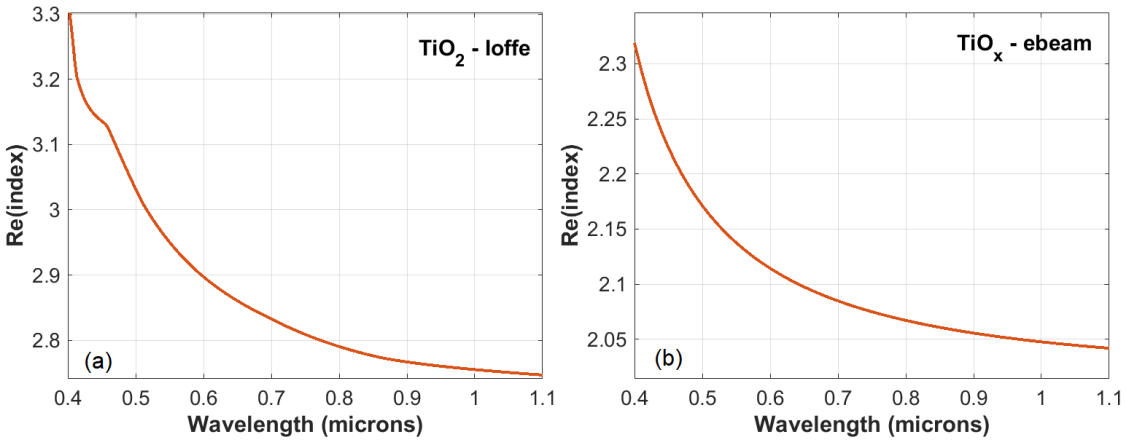

Figure 5.12: *Real component of the refractive index for (a) an ideal rutile TiO_2 standard, and (b) measured for a sample of electron-beam-evaporated amorphous TiO_2.*

Figure 5.13(a) shows the reflection, transmission, and absorption spectra calculated for TiO_2 nanocones with 50 nm Ni using the experimentally measured refractive index data for electron-beam-evaporated TiO_2, while Figure 5.13(b) shows the simulated transmitted photon flux along with the AM 1.5G spectrum. The estimated attainable photocurrent density calculated from these revised simulations for a Si solar cell covered with the TiO_2 nanocone array and Ni was $J_{ph,max}$ = 29.8 mA cm^{-2}, after correcting for losses due to reflection at the air/glass/water interfaces that are unavoidable in an electrochemical cell configuration. This estimated maximum photocurrent density ($J_{ph,max}$ = 29.8 mA cm^{-2}) was substantially lower than the current density that could be obtained with ideal TiO_2 ($J_{ph,max}$ = 36.5 mA cm^{-2}), but is still larger than the value expected for a bare, planar Si surface ($J_{ph,max}$ ~ 28 mA cm^{-2}).

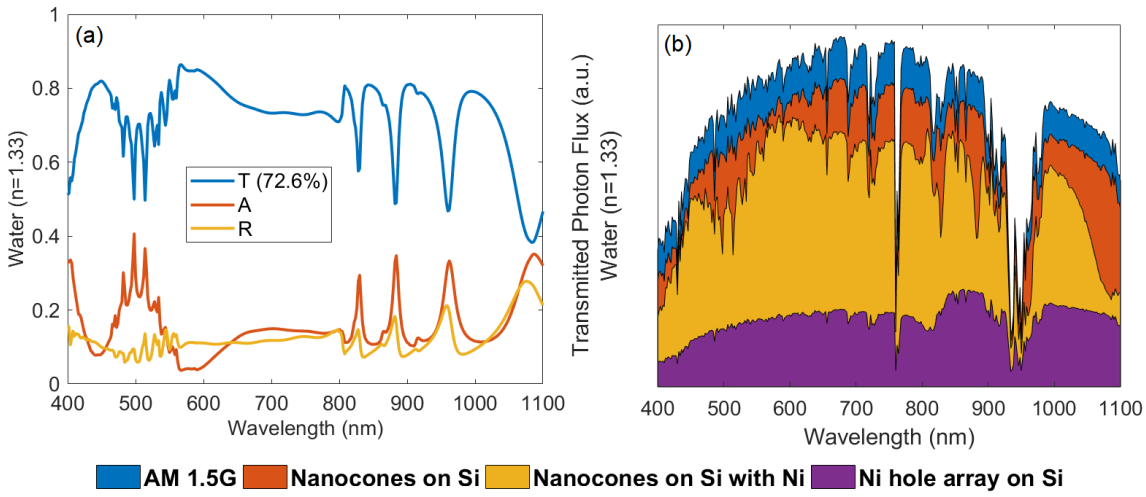

Figure 5.13: *Transmission (T), absorption (A), and reflection (R) plots for Si with TiO_2 nanocones and 50 nm thick Ni calculated with evaporated TiO_2 refractive index data are shown in (a). (b) shows the area plot overlapped over the AM 1.5G spectrum for the three different cases, as shown in Figure 5.2, using the refractive index data for amorphous TiO_2 deposited by e-beam evaporation.*

Figure 5.14 compares simulated and experimentally measured reflectance spectra for a TiO_2 nanocone array on Si, a TiO_2 nanocone array with Ni on Si, and for a 50 nm layer of Ni with an array of holes. The experimental and theoretical spectra are in good mutual agreement, with certain differences readily ascribed to technical differences between the simulation and experimental conditions. For example, the simulations were performed using a coherent illumination source, whereas experimental measurements were not. Moreover, the simulations used smoothly tapering nanocones and a flat layer of Ni, whereas the samples did not have either smoothly tapering cones or a perfectly flat Ni layer (Figure 5.9).

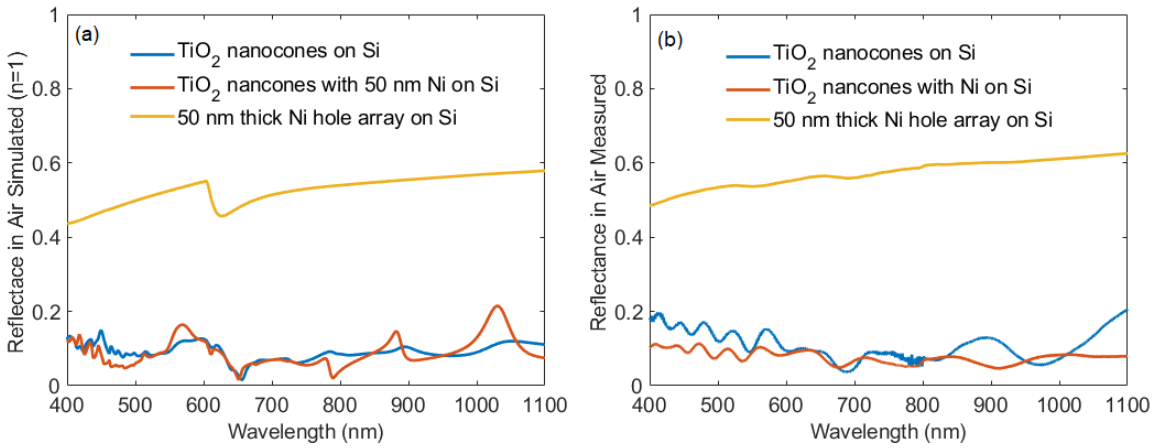

Figure 5.14: *Reflection spectra (a) simulated and (b) measured for samples consisting of an array of TiO_2 nanocones on Si (blue), an array of TiO_2 nanocones with Ni on Si (red), an array of holes in a Ni layer on Si (yellow).*

Figure 5.15 shows the current density versus potential behavior, in the dark and under 100 mW cm^{-2} of simulated AM1.5 illumination, respectively, while in contact with 1.0 M KOH(aq), for a photoanode made from a p^+n-Si substrate covered with an array of TiO_2 nanocones and a layer of Ni (Figure 5.9(b,d)). The light-limited photocurrent density, obtained by subtracting the current density measured in the dark at ~ 1 V vs the saturated calomel electrode (SCE) from the current density measured in the light at the same potential, was ~ $J_{ph,max}$ = 28 mA cm^{-2}, and matched well with the value estimated ($J_{ph,max}$ = 29.8 mA cm^{-2}) from the simulations. The current density at the formal potential for water oxidation, $E°'(O_2/H_2O)$, was 2 - 7 mA cm^{-2}. The observed light-limited photocurrent density was comparable to the photocurrent density normally measured for a bare planar Si surface, consistent with the TiO_2 nanocones serving as antireflective structures that can couple to incoming light to enable transmission of light into the Si substrate even when ~ 54 % of the Si surface was covered with ~70 nm of Ni.

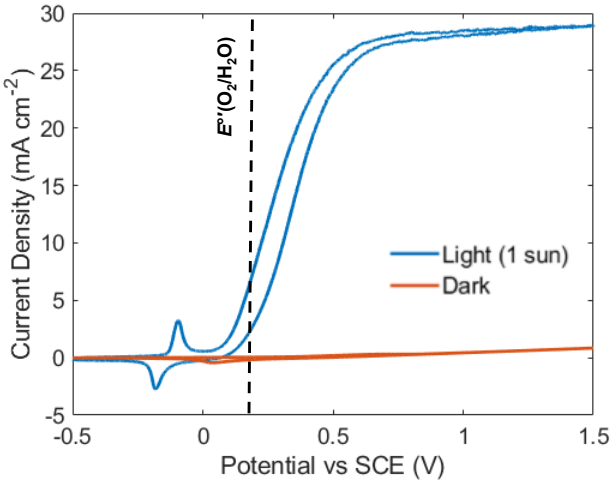

Figure 5.15: *Current-density versus potential behavior, in the dark and under 100 mW cm^{-2} of simulated AM1.5 solar illumination, respectively, for a p$^+$n-Si sample covered by an array of TiO$_2$ nanocones and 300 mC cm^{-2} of electrodeposited Ni while in contact with 1.0 M KOH(aq). The scan rate was 50 mV s^{-1}.*

Si photoanodes with a uniform 2 nm layer of Ni have been reported previously to exhibit a light-limited photocurrent density of $J_{ph,max}$ ~55 mA cm^{-2} under ~2.25 Suns equivalent of illumination, whereas increasing the Ni thickness to 20 nm reduced $J_{ph,max}$ to ~32 mA cm^{-2}. [158] These results translate at 1 Sun intensity into $J_{ph,max}$ < 25 mA cm^{-2} for 2 nm Ni and < 15 mA cm^{-2} with 20 nm Ni, whereas for comparison, the p$^+$n-Si photoanodes investigated herein exhibited $J_{ph,max}$ ~ 28 mA cm^{-2}. Although thick Ni catalysts are not required to lower the overpotential for water oxidation, [159] the use of thick electrocatalyst layers can minimize performance degradation associated with catalyst detachment.

A wide range of alternate approaches to efficient photoelectrode performance have been demonstrated, especially when active catalysts for the desired water-splitting half-reactions are used. [132] For example, p$^+$n-Si(111) photoanodes decorated with 15nm thick Ni islands that covered 18% of the photoelectrode surface have demonstrated a light-limited current density of 20.4 mA cm^{-2}. [159] Modeling has shown that the optimal efficiency of a water-splitting system using a light-facing photocathode patterned with Pt islands covering 5% of the optical plane closely approaches that of a system using a photocathode patterned with a hypothetical transparent catalyst with the

same activity as Pt. [160] Furthermore, photoanodes do not require reflective metallic catalyst coatings; indeed, p^+n-Si(100) photoanodes coated with 75 nm of sputtered NiO_x have been shown to be stable for 1200 h of continuous oxygen evolution in contact with 1.0 M KOH(aq) and exhibit a light-limited photocurrent density > 30 mA cm^{-2}. The TiO_2 nanocone array structure can effectively optimize light transmission and catalysis simultaneously in a variety of possible materials systems, and would be especially beneficial for chemical reactions that require very high mass loadings of catalysts, such as O_2 evolution or CO_2 reduction using earth-abundant electrocatalyst materials.

5.4 Conclusion and Outlook

Dielectric nanocone arrays provide an additional option to a growing toolbox of strategies for directing broadband light around opaque top contacts to PV or PEC cells. The approach ought to be generally applicable for any combination of semiconductor and metal, and in principle is scalable; however, arbitrary combinations of semiconductors and metals may not be compatible with electrodeposition of the metal onto the semiconductor as used in the fabrication process described herein. Furthermore, the fabrication process developed herein for a proof-of-concept experimental demonstration of a device that makes use of a TiO_2 nanocone array for light management was complex relative to other known options for light management, such as antireflective catalyst coatings or deposition of a controlled density and diameter of catalyst islands. The value of the dielectric nanocone approach to light management can be increased by developing a simplified fabrication process and by developing synthetic methods that yield TiO_2 nanocones with a refractive index that approaches the index for ideal TiO_2. Modeling and simulation efforts that compare attainable efficiencies for application-specific devices across relevant light-management strategies will prove valuable for identifying the strategies that are most promising for a given application.

CHAPTER 6
Effectively Transparent Catalysts for PEC Device

6.1 Introduction

Direct solar-to-fuel generation using a photocathode-based PEC cell requires a light absorber which can provide the photovoltage necessary to overcome the thermodynamic potential (1.23V for H_2/O_2, 1.33V for CO/O_2) as well as the catalyst overpotentials for both cathode and anode reactions. To realize high solar-to-fuel efficiency, it is necessary to maintain a catalytic current density close to the light limiting photocurrent density for a solar-driven light absorber, which can be fulfilled when catalyst ensembles are highly transparent. In Chapter 3, we have successfully achieved a record for solar-to-hydrogen PEC conversion efficiency of 19.3% (under simulated sunlight) in acid electrolytes by integrating Rh nanoparticle catalysts onto photocathodes with minimal parasitic absorption and reflection losses in the visible range. However, for CO_2 reduction, a different approach is required, given the opaque nature and limited activity of most CO_2R catalysts. The complexity of the CO_2R kinetic landscape makes it harder to control than the competing HER at lower overpotentials. A large geometric filling fraction of opaque electrocatalysts on the electrode surface and therefore a high active catalyst area will help to enhance the catalytic activity and reduce the overpotential. Thus, strategies for design and fabrication of front illuminated photocathode PECs need to be developed.

Earlier demonstration on Si photocathode using metal catalyst hole arrays as the catalyst still block the majority of light[96], and it would be even sensitive to apply such approach on tandem or triple junction solar cells since the current matching between each subcell is so critical that broadband transmission through catalysts layer is necessary. The earlier work with catalysts loading on high aspect ratio wire to prevent light blocking effect is promising[161,162], nevertheless, is only suitable for single junction cells and can't be applied as a general approach. Here, we propose to use light management strategies to create highly active and effectively transparent catalyst (ETC) structures for photocathodic CO_2 reduction. An effectively transparent catalyst consisting of arrays of micron-scale triangular cross-sectional metal grid fingers is capable of redirecting the incoming light to the open areas of the PEC cell without shadow loss. Broadband

high transmission in the visible range enables the high photocurrent, further realizing renewable fuel production from sunlight.

6.2 Numerical and Experimental Method

All of the simulation spectra and field distributions are carried out by solving the Maxwell equation with the commercial COMSOL Multiphysics software based on the finite element method (FEM). The triangular metal grids were constructed using the 2D simulation with periodic boundary conditions along the *x*-axis, and infinite boundary conditions were rendered as perfectly matched layers (PMLs) along the *y*-axis. Figure 6.1 displays the geometry parameters that were used in simulation. Coverage is defined as width (w) divided by pitch (p), and height is indicated as h. A plane-wave source of illumination in the wavelength range from 350 nm to 1350 nm was utilized. Spectra for unpolarized light were obtained by averaging the spectra for the two orthogonal polarizations. All materials refractive index were modeled using tabulated data provided in the software.

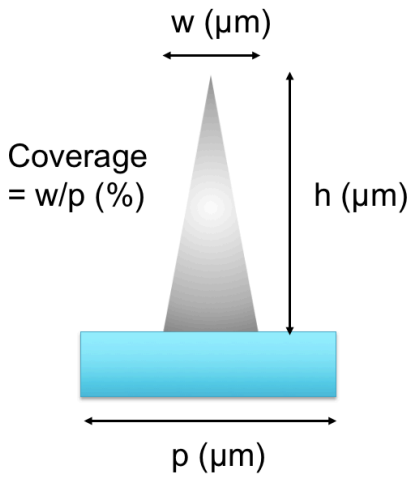

Figure 6.1: *Schematic of triangular metal gird geometries used in simulation.*

The GaInP/GaInAs/Ge triple junction cell from Spectrolab (C4MJ) and GaInP/GaAs/Si triple junction cell from ISE are considered in this study. For illumination during laboratory tests, an Oriel Instruments 75 W Solar Simulator was used and matched with AM 1.5G. The corresponding

sub-cell currents with integration of external quantum efficiency determined the expected short circuit current density under AM 1.5G illumination. The light intensity of the solar simulator was set to provide the expected short circuit current density from the specific triple junction cell. While this is not expected to yield a simulated solar irradiance of 100 $mW \cdot cm^{-2}$ due to the different solar irradiance in the 800–1000 and 1150–1800 nm regions, it does produce a response of the triple junction PV that is the same as it would be in actual AM 1.5G sunlight.

The fabrication processes of metal triangular grid on glass to be placed onto triple junction photocathode is illustrated in Figure 6.2. First, a master was fabricated on Si substrate using a two-photon lithography technique. Second, a PDMS stamp was formed with the lithography master. The PDMS stamp has an inverse structure to the lithography master. Next, the PDMS stamp was stamped onto a glass substrate to fill the metal ink where a pre-clean process of the glass substrate is preferred. The metal grid structures were printed onto the glass substrate after baking on a hot plate at ~100 °C for 10 min to remove the remaining solvent, then the PDMS stamp could be taken off. Afterward, the metal triangular grid on glass sample was post annealed at 200 °C for 1 h in a muffle furnace in air. Scanning electron microscope (SEM) images show the metal grids with a cross section of a triangle structure. Additional metal catalysts could be electrodeposited (Figure 6.3) in an aqueous solution at 0.1 mA for 2-4 min. A Cary 5000 UV/vis/NIR with integrating sphere was used to obtain reflection, transmission, and absorption spectra in air.

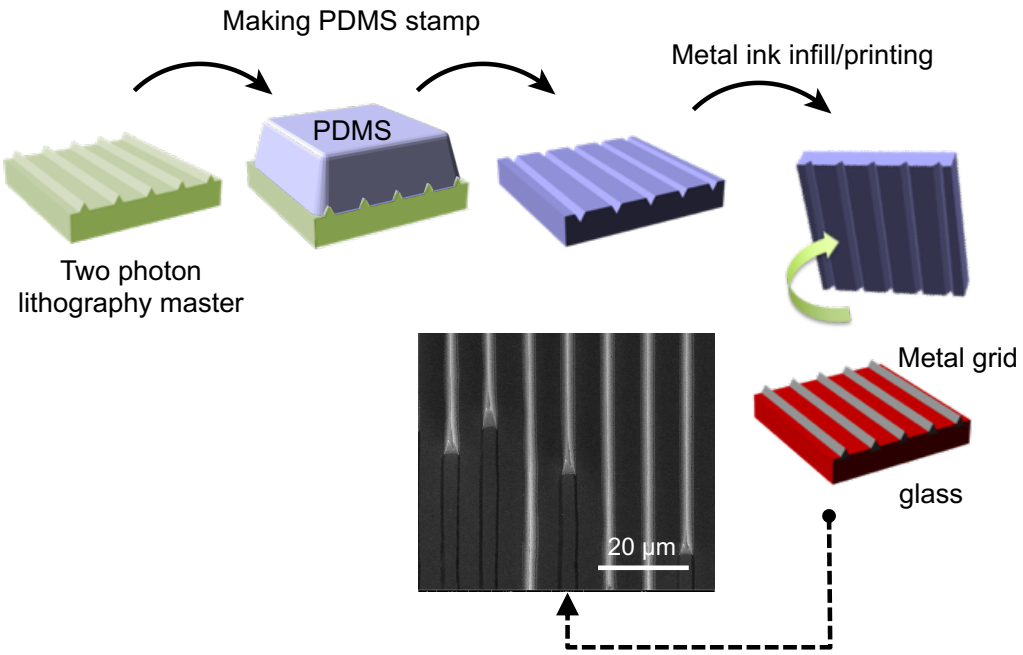

Figure 6.2: *Illustration of the fabrication process for metal catalyst triangles. SEM image shows an example of printed Ag metal triangle grid with 35% coverage.*

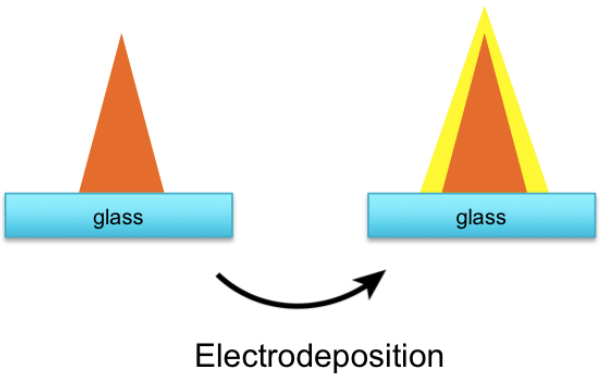

Figure 6.3: *Illustration of the metal deposition process on top of metal catalyst triangular grids.*

A modified PEEK compression cell (Figure 6.4) with lateral off-set between cathode and anode to allow illumination on the cathode was used as the vessel for the measurement. Anode chamber volumes is 2 mL, and cathode chamber volume is 4 mL. The anode and cathode electrode working areas were 6 cm^2 and 0.2 cm^2, and the membrane area was 2.4 cm^2. The activated NiO_x foam anode size is enlarged to reduce overpotential from OER, and can be folded to reduce the

geometric area. 100 mM potassium bicarbonate ($KHCO_3$) saturated with CO_2 was used as the electrolyte for experiments at pH 6.8. The anion exchange membrane (AEM) was chosen as Fumasep FAA-3-50 for lower resistance. A leakless Ag/AgCl reference electrode was used to determine the electrode potential versus RHE. All electrochemical measurements were performed using a Biologic VSP-300 potentiostat. Scan rates were set to 50 $mV \cdot s^{-1}$.

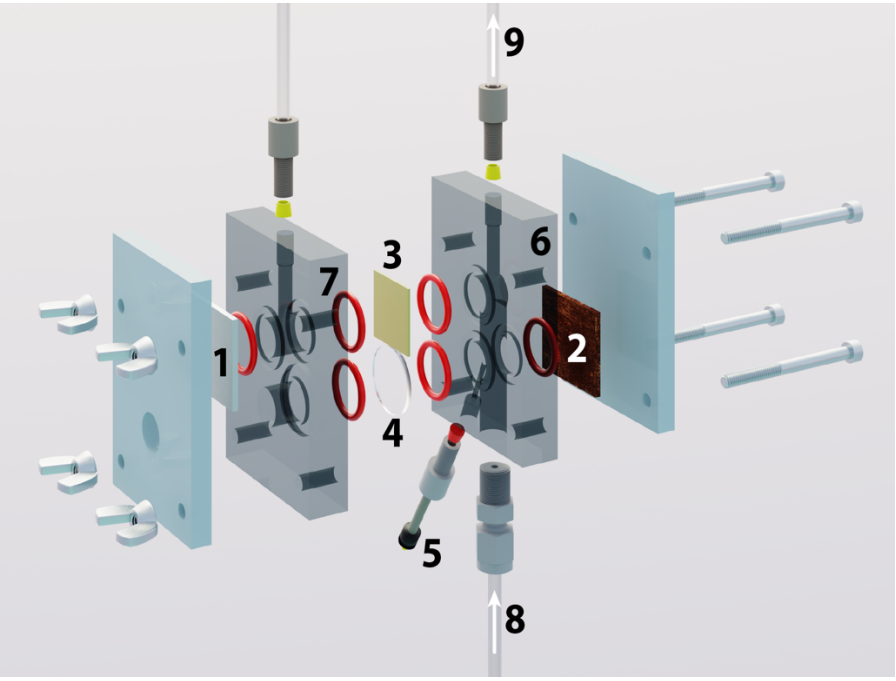

Figure 6.4: *Cell configuration composed of 1 NiO_x anode, 2 ETC-PEC assembled cathode, 3 anion exchange membrane, 4 quartz window, 5 reference electrode, 6 catholyte chamber, 7 anolyte chamber, 8 CO_2 gas inlet, and 9 gas product/CO_2 outlet. White arrows indicate the gas flow.*

The electrochemical setup was operated in a continuous flow mode. Humidified carbon dioxide was provided to the electrochemical cell and its flow rate was controlled with an Alicat flow controller. The exhaust gasses went through a mixing volumn, then an Alicat flow meter, and finally to a gas chromatograph (SRI-8610) using a Hayesep D column and a Molsieve 5A column with N_2 as the carrier gas. The gaseous products were detected using a thermal conductivity detector (TCD) and a flame ionization detector (FID) equipped with a methanizer. The high performance liquid chromatography (HPLC) is used to analyze liquid products after 1 h accumulation at each operation condition. Both anolyte and catholyte were sampled to capture

possible product cross-over. Quantitative analysis of gaseous/liquid products was based on calibration with several standards over many orders of magnitude in concentration.

6.3 Results and Discussion

PEC device with an effective transparent catalyst (ETC) is illustrated in Figure 6.5. It describes a schematic of light management implementing metal triangles on top of a semiconductor photoelectrochemical cell. The micro-scale triangle grid arrays can redirect light to photoabsorbing surfaces and reduce reflection loss that is normally expected from metal catalysts. Once light can be efficiently absorbed, electrons generated from the semiconductor PEC cell transfer to the metal triangle and initiate cathode reduction reaction. To catalyze CO_2 reduction reactions and generate CO and/or higher energy density hydrocarbon product, silver (Ag), gold (Au), and copper (Cu) are chosen specifically for the higher activity. Even though the process in not limited to the photoabsorbing materials, triple junction cells are required to provide enough photovoltage for the thermodynamic potential and overpotential of CO_2R.

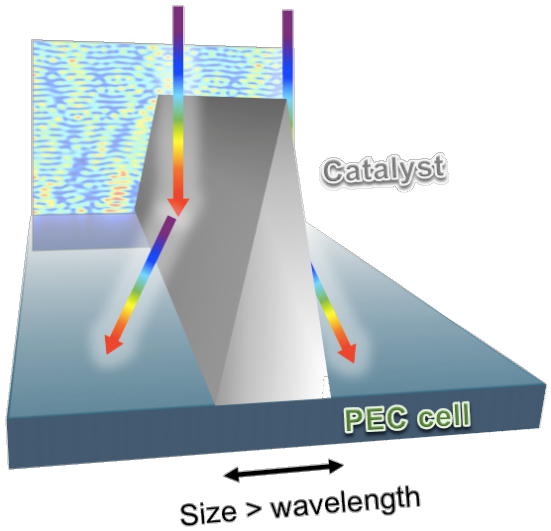

Figure 6.5: *Schematic illustration of light management with metal triangle catalyst on top of a semiconductor photoelectrochemical cell.*

The metal triangle catalysts are constructed to have heights (h) greater than the base width (w) of the triangles for enhancing actual catalytic surface area. The base to height ratio (w/h) of the triangle can range from about a 1:1 ratio to about 1:3. The base width of the triangle is supposed to be greater than the wavelength of incoming light, preventing coupling with the metal structure where optical loss can be introduced. For visible wavelength range, the base width of the triangle should be larger than 2 μm. Numerical calculations were used to investigate the optical response and determine the optimal geometry. In general, we would need larger geometric filling fraction of the metal catalysts on the electrode surface and therefore a high active catalyst area to help enhance the catalytic activity and reduce the overpotential. Figure 6.6 presents the simulated absorbance, reflectance, and transmittance spectra respectively of metal catalyst triangle coverage ranging from 0%, 10%, 25%, 50%, and 83% with base width of about 2.5 μm and a height of about 7 μm on GaAs substrate. The coverage can be defined as the occluded area by the metal triangle to the total surface area of the photoelectrochemical cell (w/p).

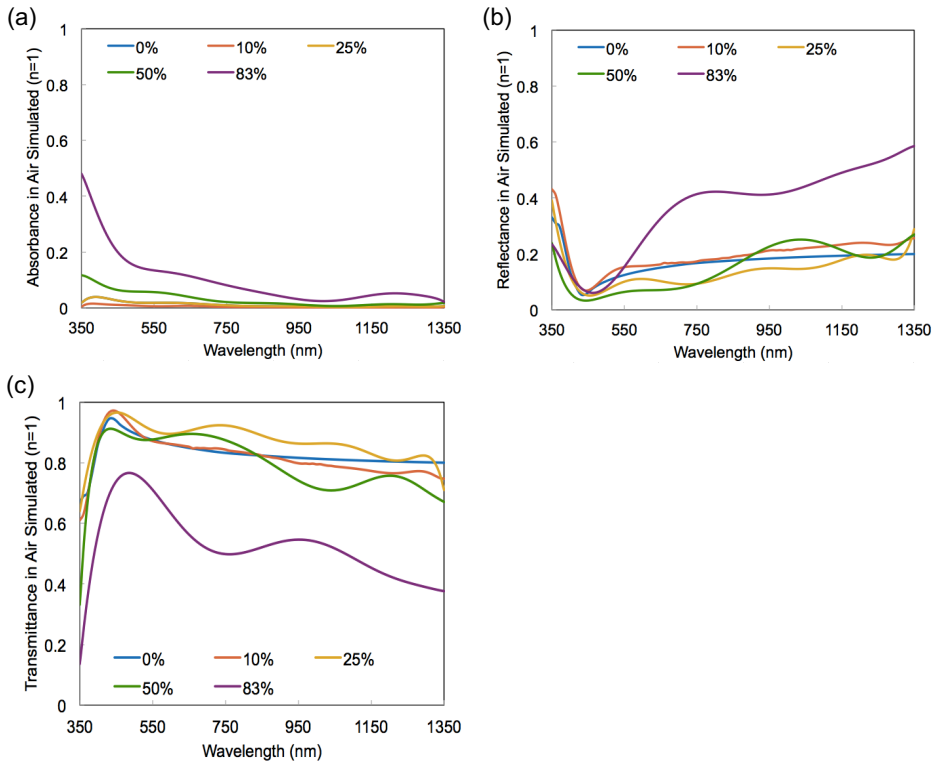

Figure 6.6: *Simulated (a) absorbance spectra, (b) reflectance spectra, and (c) transmittance spectra respectively of different Ag catalyst triangle coverages of 0%, 10%, 25%, 50%, and 85% with w = 2.5 μm and h = 7 μm on GaAs substrate.*

Table 6.1 lists the change of absorbance, reflectance, transmittance, and current of different metal catalyst triangle coverage ranging from 10%, 25%, 50%, to 83% as compared to 0% coverage. The catalyst surface area is defined as the sum of both the metal triangle slope surface area. While attaining high catalytic current, it is still required to maintain high transmission and high photocurrent. In the simulation, we found that a mesoscale Ag grid array with triangular cross-section lines, metal coverage of 50%, and catalyst surface area of 284.4% exhibits negligible additional reflection and absorption loss. Figure 6.7 exhibits the simulated field profile of a metal catalyst triangle with 50% coverage at λ = 500nm. The plane wave is reflected on the slope of the metal triangle and redirected to the wave to the photoelectrochemical cell. Metal catalyst grids with coverage ranging from 25% to 50% can be utilized as appropriate solution for balancing light management and catalytic current.

Table 6.1: *Change of absorbance, reflectance, and transmittance of of different Ag catalyst triangle coverages of 10%, 25%, 50%, and 85% with w = 2.5 μm and h = 7 μm on GaAs substrate related to 0% metal coverage.*

Metal coverage	Ave ΔR	Ave ΔA	Ave ΔT	Catalyst surface area
10%	0.027	0.005	-0.032	56.9%
25%	-0.030	0.012	0.018	142.2%
50%	-0.019	0.031	-0.012	284.4%
83%	0.194	0.098	-0.292	472.2%

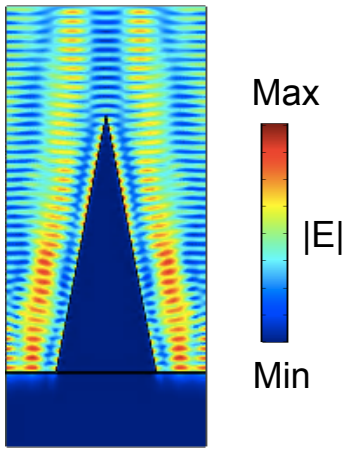

Figure 6.7: *Simulated field profile of a Ag catalyst triangle with w = 2.5 μm, h = 7 μm, and 50% coverages on GaAs substrate at λ=500nm.*

As proof of concept, Ag catalyst triangle catalysts with 2.5 μm width, 5 μm height (w/h = 1:2), and 35% coverage were fabricated with the printing process described in method section. The catalyst surface area of such a structure is calculated to be 144.3%. Additional catalyst layers including Au and Cu are selectively electrodeposited on the surface of the printed Ag triangle grids. Figure 6.8(a)-(c) shows elementary mapping through EDX (Energy-dispersive X-ray spectroscopy) of three types of metal catalyst triangle grid arrays on glass substrate, including Ag triangle, Au on Ag triangle, and Cu on Ag triangle. It is observed that after electrodeposition, the Ag catalysts are conformally covered by the other metal catalysts where signals from Ag are hindered. We note here that the catalysts are printed on an insulating glass substrate and later wire connected to the bottom PEC cell instead of directly printed on the PEC cell. It passivates the light absorber surface and reduces competing reactions of CO_2R reactions, hence improving the solar-to-fuel conversion efficiency.

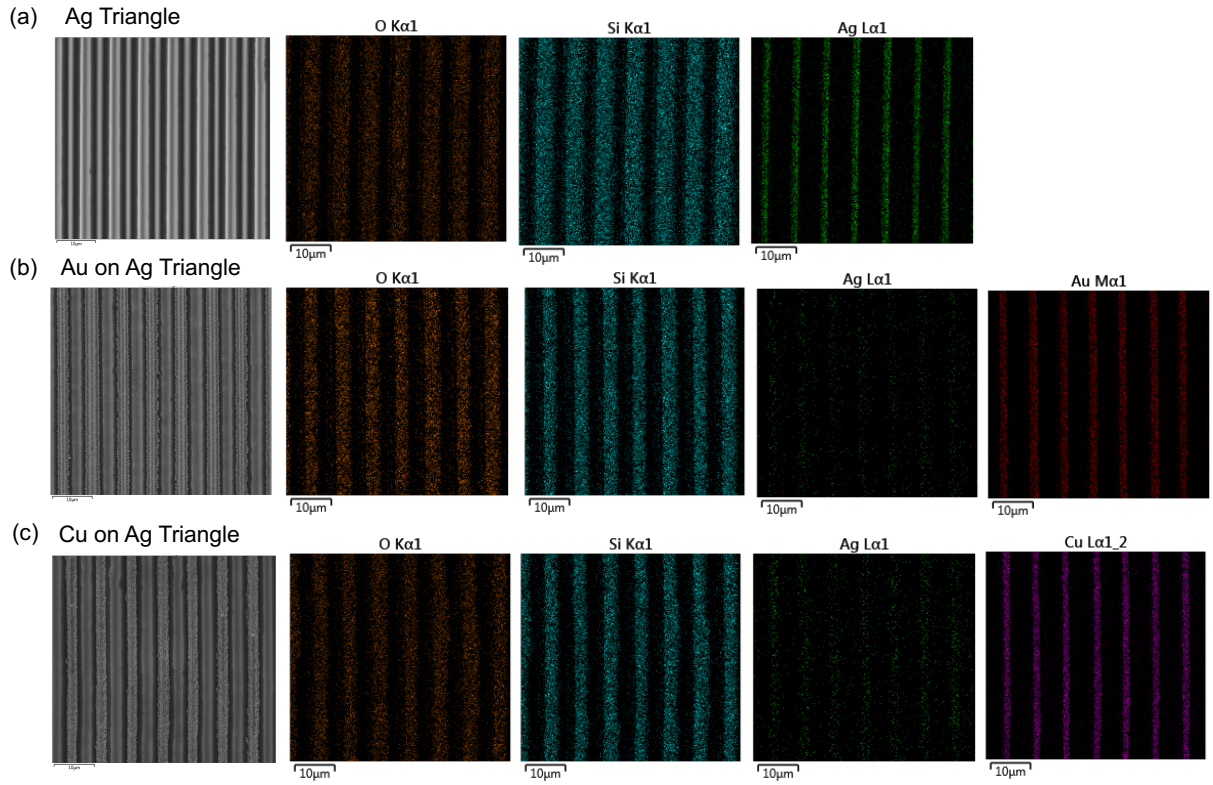

Figure 6.8: *EDS mappings of elements O, Si, Ag, Au, and Cu of the (a) Ag triangle (b) Au on Ag triangle (c) Cu on Ag triangle on glass substrate.*

Figure 6.9 includes the optical measurements in air with different wavelengths of light for the three types of metal catalyst triangle grid arrays on glass substrate with coverages of 35%. Near 10% reflection loss can be introduced with bare glass substrate. Figure 6.9(b) shows additional 10 % reflection loss from the 35% Ag triangle grids while the Au on Ag triangle and Cu on Ag triangle cases exhibit similar reflection loss at longer wavelengths but lower at shorter wavelengths. The overall reflections are higher than expected from the simulation, which can possibly be attributed to the non-ideal surface roughness. The morphology of the bare printed Ag triangle and after electrodeposition of Au and Cu are shown in SEM images of Figure 6.10. Even though rougher surfaces can be observed for both electrodeposited Cu and Au, the two samples do not show higher reflection loss due to the contribution of absorption loss, as shown in Figure 6.9(a). In particular, the needle structure Au catalysts exhibit the largest absorption loss. Figure 6.9(c) indicates the transmission spectra for the three metal catalyst triangle grids, where 35% Ag triangle grids show

the best transparency than the Cu on Ag triangle, with Au on Ag triangle being the worst. Although reflection and absorption loss are introduced from non-perfect geometry, the transmissions for the three samples are still higher than the calculated transmission spectrum for 200nm thick Ag film with 35% coverage, shown as the blue dashed line in Figure 6.9(c). While 35% Ag triangle maintained relatively higher transparency than the 35% Ag film, the catalyst surface area of 144.3% is 4 times larger, which is one of the critical benefits of the triangle grid design.

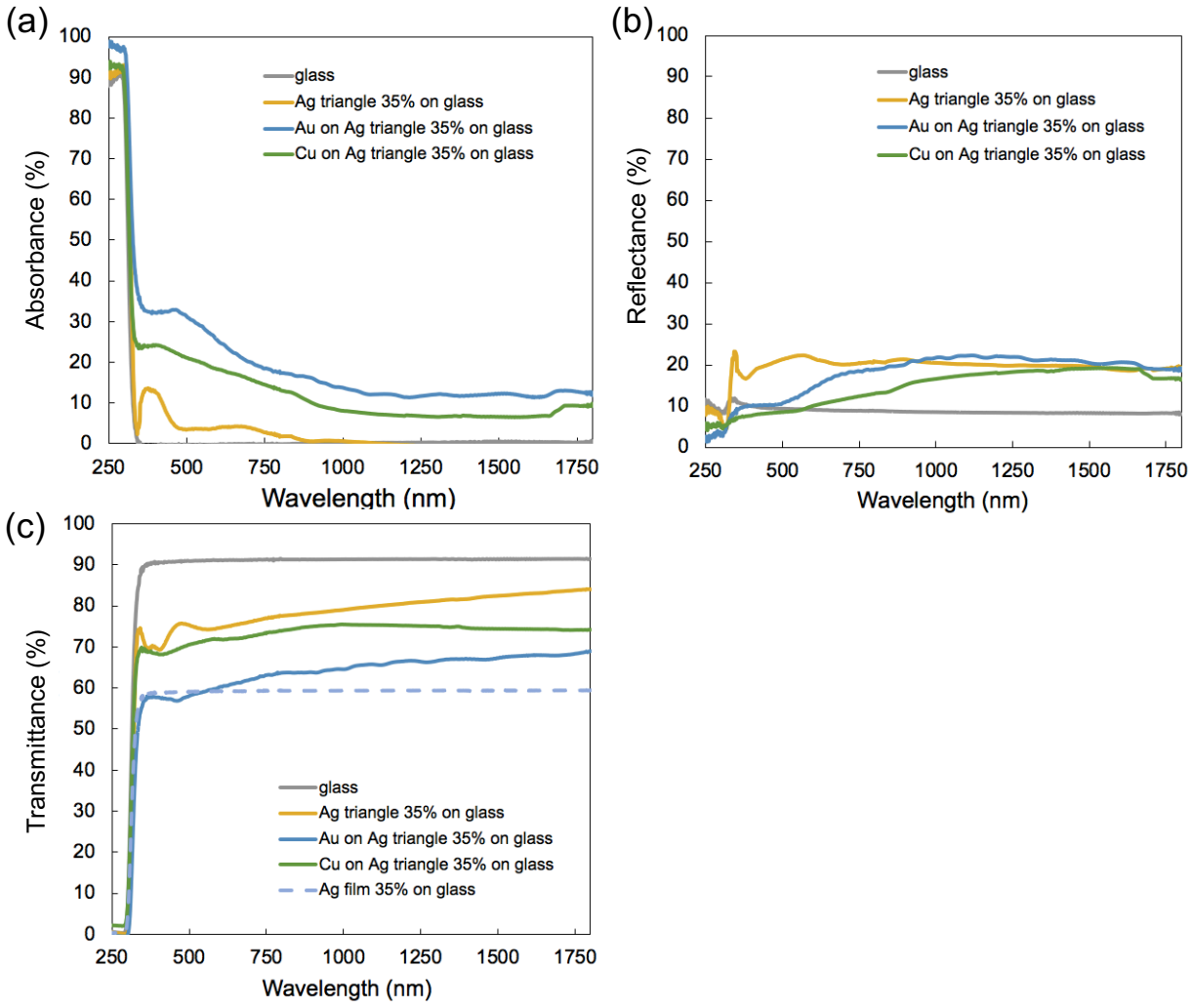

Figure 6.9: *Experimental measurements of (a) absorption spectra, (b) reflection spectra, and (c) transmission spectra respectively for different metal catalyst triangles with coverages of 35% on*

glass substrate. 0% coverage is shown as glass. Calculated transmission spectrum for 200nm thick Ag film with 35% coverage is included for comparison.

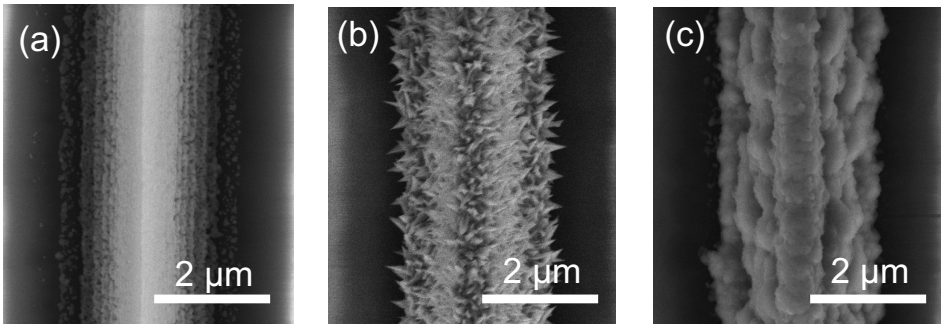

Figure 6.10: *SEM images of (a) Ag triangle, (b) Au on Ag triangle, and (c) Cu on Ag triangle on glass substrate with 35% coverage.*

To evaluate the catalytic behavior of the three different metal catalyst triangle grids, three-electrode measurements in CO_2 saturated 0.1 M $KHCO_3$ (bulk pH of 6.8) are conducted with results shown in Figure 6.11. For Ag triangle grids, both the Faradaic efficiency for CO and current density increased with increasing potential vs RHE with $f_{FE,CO}$ close to 90 % at -1.2 V vs. RHE, see Figure 6.11(a)(d). Comparable current density can be observed for both Au on Ag triangle grids (see Figure 6.11(b)) and Cu on Ag triangle grids (see Figure 6.11(c)) while Au on Ag triangle grids show higher current density at lower potential. The Au catalysts also shift the optimized faraday efficiency for CO to lower potential at -0.8V vs RHE though with lower $f_{FE,CO}$ of 65 %, see Figure 6.11(e). Higher value hydrocarbon products including acetate, ethylene, ethanol, and n-propanol can be generated with additional Cu catalysts as shown in Figure 6.11(f). At -1.4 V vs RHE, a total Faradaic efficiency for CO_2R can reach 90% with C_{2+} product over 50%. The product with highest Faradaic efficiency is ethanol with 32%. The selectivity is still a concern that effort for product separation would be required for practical application. In the later study, the better performing Ag triangle grids and Cu on Ag triangle grids are further evaluated.

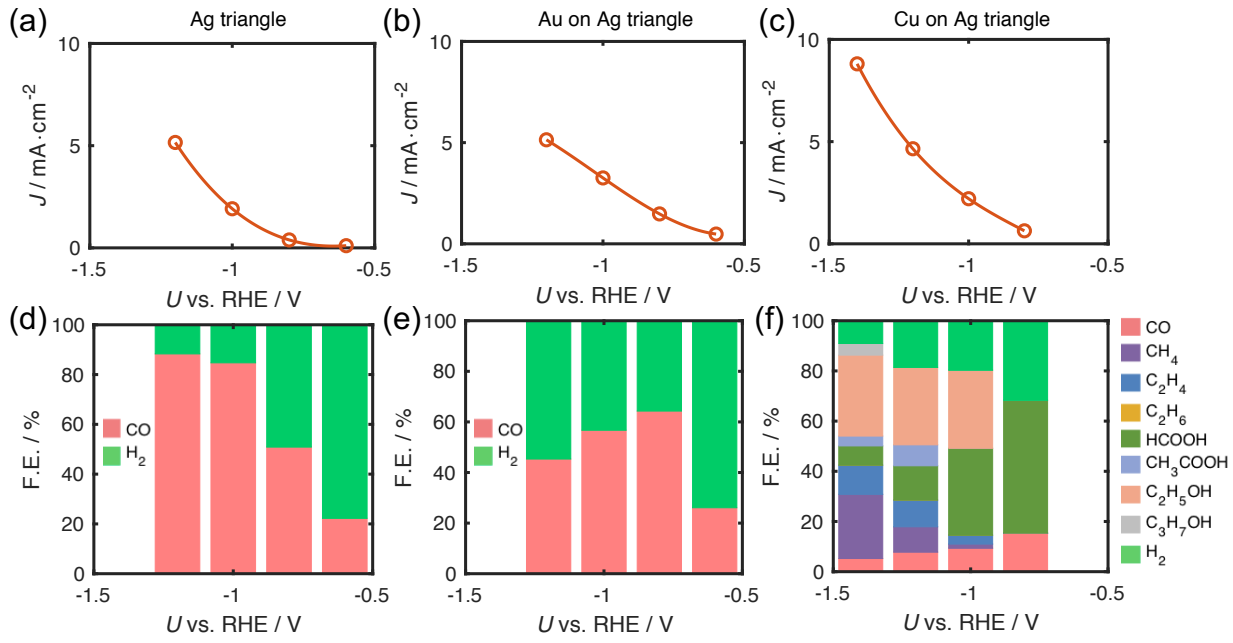

Figure 6.11: *Current density and product distribution at different potentials vs RHE for (a)(d) Ag triangle, (b)(e) Au on Ag triangle, and (c)(f) Cu on Ag triangle on glass substrate with 35% coverage.*

Two electrode measurements of metal triangular grid cathode and NiO_x mesh anode with a range of applying cell potentials were conducted for better understanding of full cell operation, and the resulting current density and product distribution are shown in Figure 6.12. For the case of Ag triangle grid cathode with NiO_x anode, see Figure 6.12(a), optimized faraday efficiency for CO can be achieved with cell voltage larger than 2.5 V. The high $f_{FE,CO}$ of 80 % can be extended to 2.9 V. For the case of Cu on Ag triangle grids cathode with NiO_x anode, see Figure 6.12(b), Faradaic efficiency of ethanol ~ 30% was achieved with cell voltage ranging from 2.5 V to 2.9 V. Other higher value hydrocarbon products start to generate with cell voltage larger than 2.7 V, realizing C_{2+} product over 50% and a total CO_2R Faradaic efficiency > 80%.

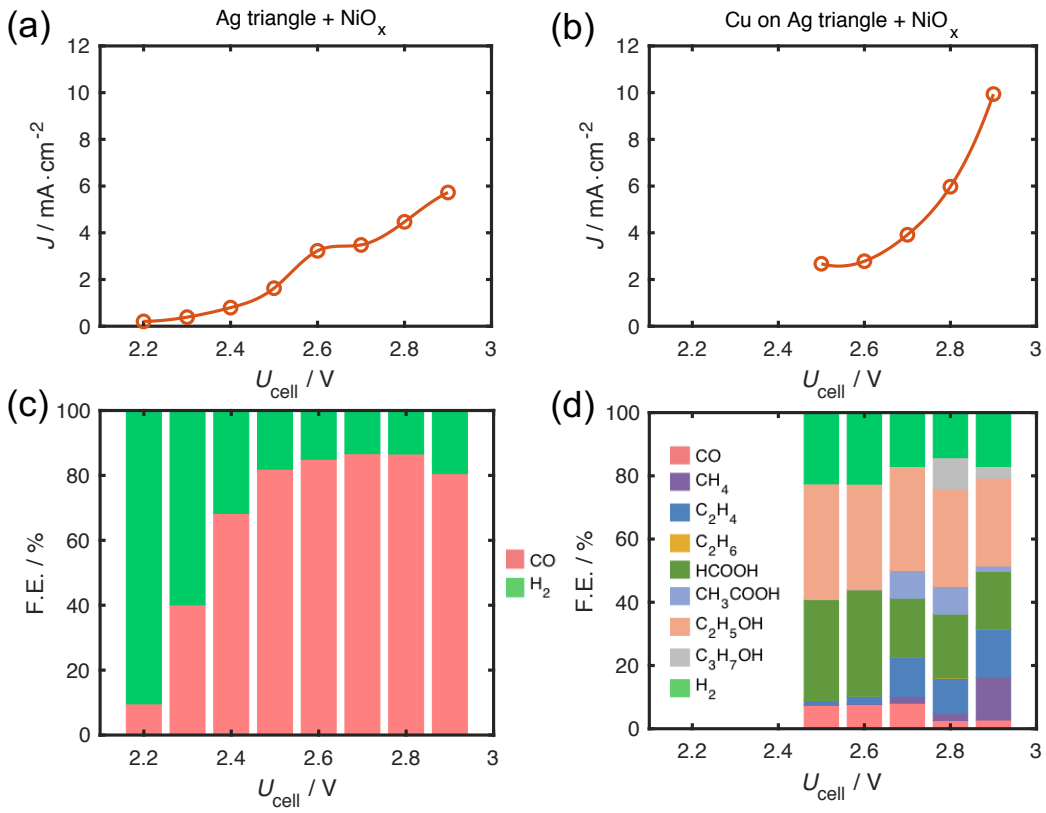

Figure 6.12: *Current density and product distribution at different cell potentials with NiO_x anode for (a)(c) Ag triangle, and (b)(d) Cu on Ag triangle on glass substrate with 35% coverage.*

For a fully integrated device with catalysts on the illuminated side of the light absorber, the optical response of the catalysts needs to be considered. We calculated the short circuit photocurrent of two different triple junction cells; one from Spectrolab with an open circuit voltage of 2.6 V and sub-cells of GaInP/GaInAs/Ge, the other from ISE with an open circuit voltage of 3.125 V and sub-cells of GaInP/GaAs/Si. By applying the transmission spectra of the two different metal triangle grids in conjunction with the external quantum efficiency (EQE, see Figure 6.13) of the two triple junction cells, the catalysts light blocking effect on each of the sub-cells can be evaluated. The short circuit photocurrent J_{sc} is then obtained from the minimum current density of the individual sub-cells. The calculation results are listed in Table 6.2. We found that the current limiting cell remains to be the middle cell for the Spectrolab 3J cell, and remains to be the bottom cell for ISE 3J cell no matter which catalyst is applied. The light limiting current density of the

Spectrolab 3J cell decreases from 14.83 mA/cm^2 to 11.46 mA/cm^2 for Ag triangle grids, to 10.93 mA/cm^2 for Cu on Ag triangle grids. Similarly, the light limiting current density of ISE 3J cell decrease from 11.66 mA/cm^2 to 9.15 mA/cm^2 for Ag triangle grids, to 8.73 mA/cm^2 for Cu on Ag triangle grids.

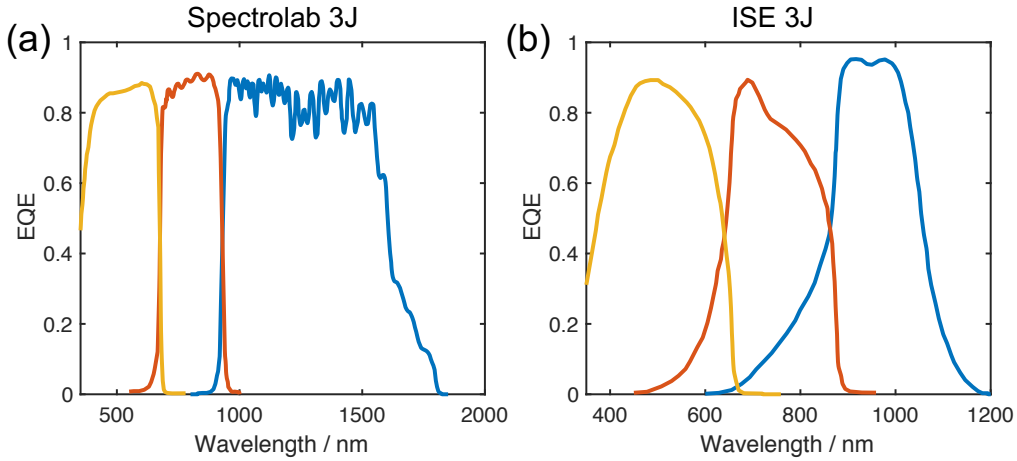

Figure 6.13: *External quantum efficiency of (a) Spectrolab GaInP/GaInAs/Ge triple junction cell, and (b) ISE GaInP/GaAs/Si triple junction cell.*

Table 6.2: *Current densities calculated for the individual sub-cells of the Spectrolab GaInP/GaInAs/Ge triple junction cell and ISE GaInP/GaAs/Si triple junction cell in conjunction with optical response of different catalysts under AM1.5G 1 sun illumination assuming the standard reference sunlight spectrum (AM1.5G ASTM G-173). The short circuit photocurrent J_{sc} is obtained from the minimum current density of the individual sub-cells.*

Device	Catalyst	J_{top} ($mA \cdot cm^{-2}$)	J_{middle} ($mA \cdot cm^{-2}$)	J_{bottom} ($mA \cdot cm^{-2}$)	J_{sc} ($mA \cdot cm^{-2}$)
Spectrolab 3J	none	15.56	14.83	18.53	14.83
	Ag triangle 35% on glass	11.57	11.46	14.93	11.46
	Cu on Ag triangle 35% on glass	11.02	10.93	13.90	10.93
ISE 3J	none	12.75	13.13	11.66	11.66
	Ag triangle 35% on glass	9.46	10.05	9.15	9.15
	Cu on Ag triangle 35% on glass	9.00	9.59	8.73	8.73

Figure 6.14 plots the J-V curves of the two 3J cells after modifying with catalyst transmission together with catalyst curve for the two metal triangle grid cathodes plus NiO_x anode. The intersect of the two curves defines the operation condition for the integrated ETC-PEC device. For Figure 6.14(a), Spectrolab 3J and Ag triangle/NiO_x curves intersect at 2.57 V and 2.7 mA/cm^2, so a solar-to-CO efficiency of 3.1 % can be expected. For Figure 6.14(b), Spectrolab 3J and Cu on Ag triangle/NiO_x curves intersect at a similar point 2.57 V and 2.7 mA/cm^2, and a total solar-to-fuel efficiency from CO_2R of 2.7 % and solar-to-C_{2+} efficiency of 1.1 % can be expected. For Figure 6.14(c), ISE 3J and Ag triangle/NiO_x curves can be interpreted to intersect at 3.0 V and 7.0 mA/cm^2, a solar-to-CO efficiency of 6.6 % can be estimated. For Figure 6.14(d), ISE 3J and Cu on Ag triangle/NiO_x curves intersect at 2.86 V and 8.6 mA/cm^2, a total solar-to-fuel efficiency from CO_2R of 8.7 % and solar-to-C_{2+} efficiency of 5.4 % can be expected.

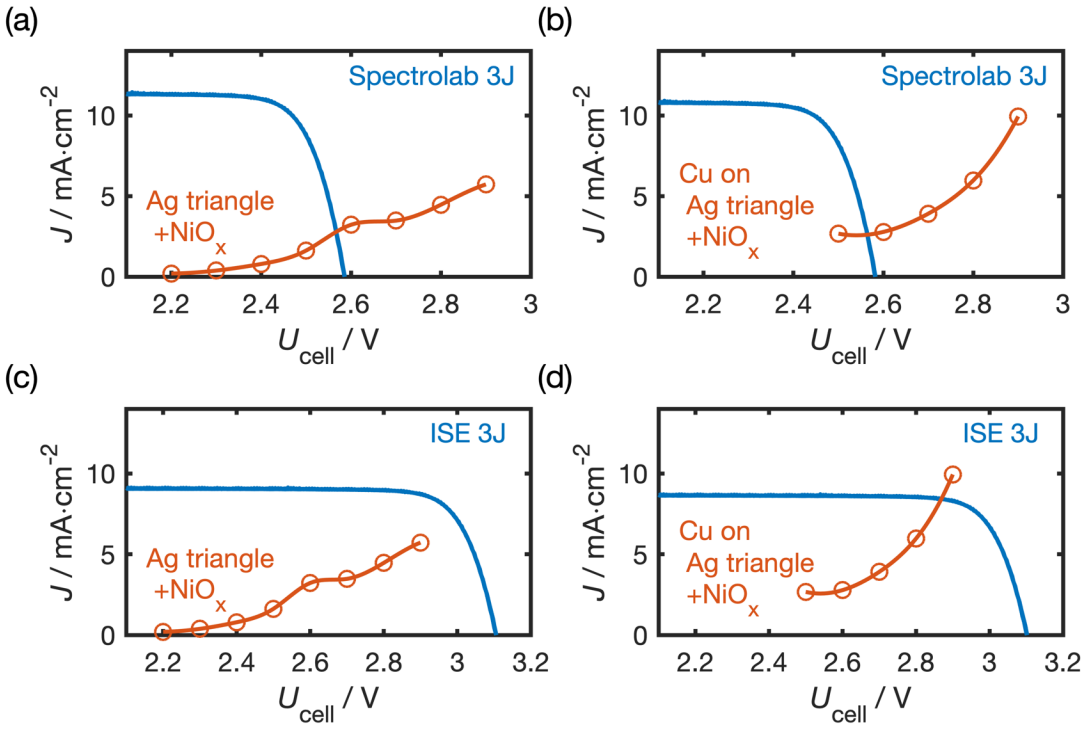

Figure 6.14: *Current density at different cell potentials of light absorber and cathode/anode catalysts defining the operation point for (a) Spectrolab 3J + Ag triangle/NiO_x, (b) Spectrolab 3J + Cu on Ag triangle/NiO_x, (c) ISE 3J + Ag triangle/NiO_x, and (d) ISE 3J + Cu on Ag triangle/NiO_x.*

We also experimentally realized the integrated ETC-PEC device with Spectrolab 3J cell and Ag triangle catalysts with 35% coverage. J-V characteristics and product distribution with three-electrode measurements performing CO_2RR in CO_2 saturated 0.1 M $KHCO_3$ under 1 Sun illuminations are shown in Figure 6.15. As comparison to bare Ag triangle catalysts, the integrated device with Ag triangular catalysts stacking on photovoltaic shows a positive shift of the J-V curve vs RHE. The trends of product distribution over applying potential are almost identical. No external bias operation can be achieved with 20 h stability as shown in Figure 6.16. Starting from ~3% solar-to-CO efficiency, the integrated device efficiency slowly drops to ~2% possibility due to the insufficient adhesion of the Ag triangle grids to the glass substrate during electrolysis.

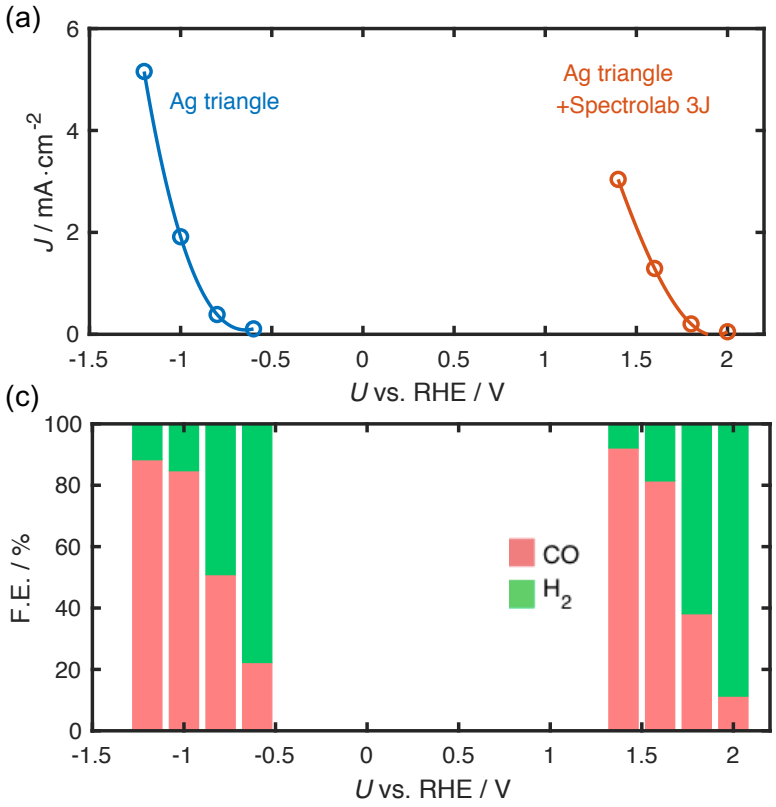

Figure 6.15: *(a) Current density and (b) product distribution at different potentials vs RHE for Ag triangle, and integrated ETC-PEC device with Spectrolab 3J plus Ag triangle on glass substrate with 35% coverage.*

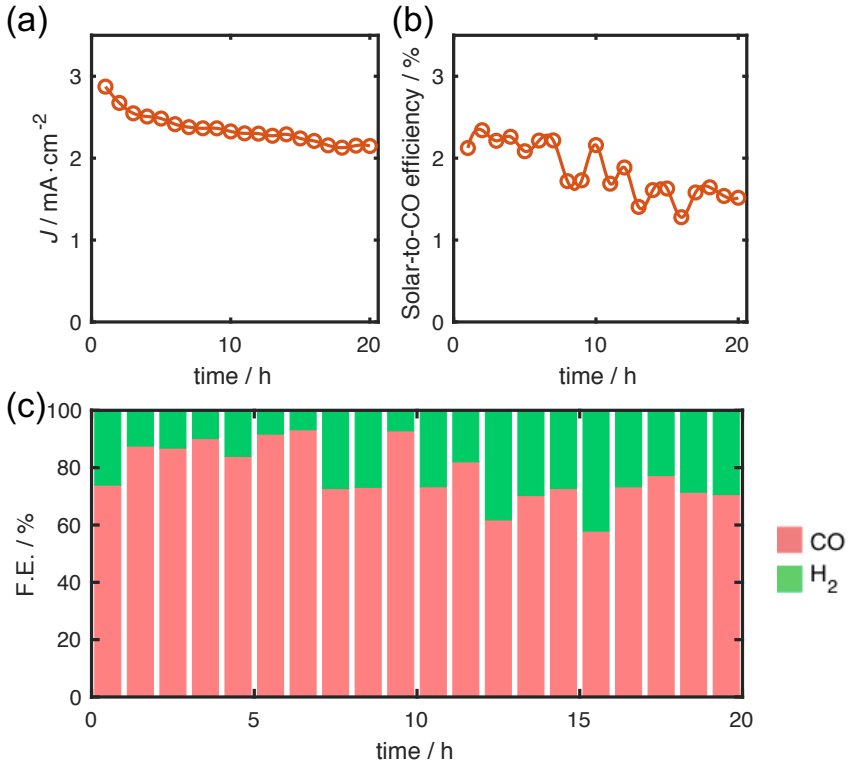

Figure 6.16: *(a) Current density, (b) solar to CO efficiency, and (c) product distribution at 0 V vs NiO_x counter electrode of the integrated ETC-PEC device with Spectrolab 3J + Ag triangle on glass substrate with 35% coverage over 20 h stability test.*

6.4 Conclusion and Outlook

A solar-driven photoelectrochemical device capable of reducing CO_2 without externally applied bias is achieved with ~3% solar-to-CO efficiency using Ag ETC-PEC. Over 6% solar-to-CO efficiency with Ag triangle catalysts or a total solar-to-fuel efficiency from CO_2R > 8 % and solar-to-C_{2+} efficiency > 5 % with Cu on Ag triangle catalysts can be expected with triple junction cell providing larger photovoltage. Our designs featuring photonic structures to enable high absorption light absorbers and effectively transparent catalyst layers for PEC cell are general approaches not limited to single reaction or specific photovoltaic system. Different metal catalysts can possibly be applied to reveal different chemical reactions and fuels. Together with the capability of scalable processes through ink printing and electroplating, it will be a critical step to advances in field of solar fuel generation and all other related optical applications.

Future directions involve extending device stability and new catalyst design for higher value product with high selectivity. The solar-to-fuel efficiency can be further increased with slightly higher metal coverage, and crossed grid structures with similar triangular cross section can also be considered. A new protection scheme allowing efficient passivation of the PEC cell from undesired competing reactions would be valuable for simpler integration devices.

CHAPTER 7
Interface Analysis of Catalysts and Protection Layer

7.1 Introduction

Band gap tailored dual junction light absorbers typically utilizing silicon and/or III-V semiconductors have the potential to provide the highest efficiency for unassisted water splitting in an integrated photoelectrochemical (PEC) device. [69] Depending on the desired product, similar devices optimized for CO_2 reduction consists of triple junction light absorbers [70,163] combined with catalysts needed for the desired reactions. However, these devices employ semiconductors, especially the widely used III-V compounds, that are typically unstable in aqueous media and will corrode and/or passivate unless protected by transparent, conducting, and chemically robust protective layers. [74,164,165] Amorphous defective TiO_2 (a-TiO_2) coatings have been found to yield protective layers that can pass charge from the semiconductor to the catalysts, are stable in highly basic solution, and can offer antireflective properties to PEC electrodes. The a-TiO_2 can be applied using atomic layer deposition (ALD) with tetrakis(dimethylamino)titanium (TDMAT) precursors at relatively low temperatures to yield protected photoanodes that facilitate the transport of holes.

It has been proposed that a gap states in the TDMAT a-TiO_2 protection layer is responsible for hole conduction. [74,166,167] Temperature dependent measurements showed a decreasing activation energy with decreasing temperature, which indicated that neither valence nor conduction band are the primary pathways of conduction. [167] The data was consistent with a hopping mechanism between Ti^{3+} and Ti^{4+} states and conductivity as well as size of the gap states correlated with the Ti^{3+} concentration. Solid liquid junctions of these protective a-TiO_2 coatings alone are shown not to be conductive and/or provide the necessary low overpotential for water oxidation. [74,166,167] However, in conjunction with the appropriate choice of metal catalyst, high catalytic exchange current densities and thus low overpotentials can be observed. Metals with a work function less than a-TiO_2 generally provided higher conductivities across the a-TiO_2/metal interface while high work function metals depleted the Ti^{3+} sites. [167] However, nickel as a high work function metal acted similar to low work function metals. It was suggested that properties other than the work function itself must contribute to the different conductivities.

This made nickel the material of choice for making TDMAT a-TiO_2 conductive and enabling water oxidation. However, a minimum thickness of nickel is required to observe significant catalytic current for water oxidation or when using a fast redox couple ($Fe(CN)_6^{3-/4-}$). [168] It has been shown in the past that ultrathin metal films and nanoparticles on oxide surfaces exhibit unique properties for catalytic systems. [169] For example, the deposition of thin reactive metal films Cr resulted in strong interaction with the interfacial TiO_2, leading to a change of the gap states in crystalline TiO_2 within the band gap at the metal interface. The ALD a-TiO_2 has a distorted octahedral symmetry (O_h) with a valence configuration of O $2p^6$ Ti $3d^0 4s^0$ which results in a pure O 2p derived valence band and pure Ti 3d and 4s derived conduction band. [170] The six oxygen ligands in O_h symmetry break the 3d-orbitals (d_{z^2}, $d_{x^2-y^2}$, d_{xy}, d_{xz}, d_{yz}) into e_g (pointing towards ligands) states and t_{2g} states (pointing between ligands). [170] The gap state in a-TiO_2 is a partial populated t_{2g} derived band (Ti^{3+}) which was originally unoccupied due to the d^0 character of TiO_2. [171] Successive dd transitions are possible after excitation of electrons from Ti 2p core level into e_g conduction band states followed by deexcitation from the t_{2g} valence band states into the core level hole, effectively creating an intermediate state with an electron in the e_g and a hole in the t_{2g} band (dd transition).

In this study we investigate the properties of an a-TiO_2/metal interface that controls the transfer of holes through the a-TiO_2 to Ni, Au and Ir contacts to understand why the observed catalytic currents of these systems differ. Resonant photoemission spectroscopy (resPES) and resonant inelastic X-ray scattering (RIXS) at the Ti 2p edge were used to investigate the a-TiO_2 gap state at the buried interface between the metal and the TiO_2. In resonance X-ray spectroscopy, the ground state is initially excited to an intermediate state, and in our case, this is a conduction band (CB) excited state. The lifetime of this CB excited state defines the full width at half maximum (FWHM) of the resonance. This intermediate state then decays by either emission of an Auger electron for resPES or of an X-Ray for RIXS. The final state is still an excited state (for RIXS and some decay channels for resPES) with a hole in the valence band, and its lifetime defines the FWHM of the valence band (VB) resonances. [172] Resonant X-ray spectroscopy is a two-dimensional technique using photoelectron/exciting photon energy in resonant photoelectron spectroscopy, resPES, or emitted X-Ray/exciting photon energy in resonant inelastic X-Ray scattering, RIXS. By this technique, the X-ray absorption spectrum (XAS) is split into individual

X-Ray photoelectron spectra or X-ray emission spectra for each excitation energy value. At the energy for a core level absorption of a particular element, the cross section for that element increases dramatically. It is several orders of magnitude higher than for any elements that have a different core level absorption energy. Due to the increased absorption cross section and the decay processes of the resonantly created core hole, the density of states of that element can be determined. Hence, valence bands measured by resonant X-ray spectroscopy give evidence of the partial density of valence band states (occupied states). For a complete set of VB spectra, the excitation energy is scanned over the core level absorption edges energies of the elements of interest. Scanning over the absorption edge an XAS spectrum can be recorded allowing to probe the CB states in addition, e.g. total electron yield (TEY) or total fluorescence yield (TFY).

7.2 Experimental Method

Films of a-TiO_2, prepared by atomic-layer deposition (ALD), [74,153,173,174] were deposited on degenerately doped p^+-type silicon (resistivity $\rho < 0.005$ Ω·cm) substrates. Si (100) wafers were first cleaned *via* an oxidizing etch by soaking of a 3:1 (volume ratio) "piranha" solution of concentrated H_2SO_4 (98 %) to 30 % H_2O_2 for 2 min, followed by a 10 s in a 10 % (by volume) solution of HF(aq). The wafers were then immediately etched in a 5:1:1 (volume ratio) solution of H_2O, 36 % hydrochloric acid, and 30 % hydrogen peroxide for 10 min at 75 °C before being moved into the ALD chamber. The a-TiO_2 was deposited from a tetrakis(dimethylamido)titanium (TDMAT) precursor in a Cambridge Nanotech Savannah ALD reactor. A 0.1 s pulse of TDMAT was followed by 15 s purge of N_2 at 20 sccm, followed by a 0.015 s pulse of H_2O before another 15 s purge with N_2. This process was repeated for 1500 cycles to reach ~ 70 nm in thickness. Metals were deposited via electron-beam evaporator (System 02520, Angstrom Engineering) with base pressure of $1x10^{-7}$ Torr at rate of 0.1 to 1 Å/s. Where desired, nickel was deposited at a RF sputtering power of 150 W for 20-300 s in an AJA-International sputtering system, at a rate of approximately 2 nm/min.

Resonant XPS experiments have been performed at BESSY II, Berlin at the soft X-ray beamline U49/2-PGM2. [175] The photon energy resolution used was around 30 meV. All spectra are corrected for the incoming photon flux. For measuring the resPES valence band spectra at the

Ti 2p, O 1s, and Ni 2p edge, the photon energy was varied over a wide range (452 eV – 475 eV; 525 eV – 550 eV; 845 eV – 865 eV, respectively) by sweeping the undulator gap and the monochromator in parallel. A SPECS Phoibos 150 was used as the electron analyzer and a 1D delay-line detector as the electron detector. The resolution of the spectrometer used was 70 meV. Together with the photon resolution, we have a resolution for XAS (CB) measurements of 30 meV and for PES (VB) of around 80 meV. To compensate for polarization dependence of the resonances a sample position with a magic incidence angle of 54.7 ° was chosen. [176] RIXS experiments were performed at the Advanced Light Source, Berkeley at beamline 8.0.1, using the iRIXS endstation equipped with two slit-less variable line-spacing (VLS) grating spectrographs. [177]

Laboratory XPS measurements were performed using a Kratos Axis Ultra system with a base pressure of < $1x10^{-9}$ Torr. A monochromatic AlKα (hν=1486.69 eV) source with a power of 150 W was used for all measurements. For ultraviolet photoelectron spectroscopy (UPS) a Helium gas discharge lamp was used to provide HeI excitation (hν=21.21 eV) for measurement of the material work function. Pure metal samples (99.99%) were sputter cleaned until no contamination or carbon was detectable prior to UPS measurement.

Electrochemical characterization was performed in a three-electrode configuration with a Ag/AgCl reference electrode and carbon counter electrode using a Biologic SP-200 potentiostat. To assess the conductivity of the samples, 50/350 mM $Fe(CN)_6^{3-/4-}$ was used as the electrolyte, which was vigorously stirred during the experiments. 1 M KOH was used as the electrolyte to determine the performance for the oxygen evolution reaction (OER). X-Ray diffraction (XRD) data was collected on a Bruker Discover D8 XRD with a micro-focus X-ray source (Cu) and VÅNTEC-500 large microgap detector. Scanning electron microscopy images were obtained with a FEI Nova NanoSEM 450 microscope.

7.3 Results and Discussion

Figure 7.1(a) shows the current voltage curves (*J-U*) in 1 M KOH for p^+-Si/a-TiO_2/Ni(20 nm) and p^+-Si/a-TiO_2/Ir(20 nm) samples. Redox peaks are observed prior to the onset to OER for the

p^+-Si/a-TiO_2/Ni sample at U = +1.44 V and +1.35 V vs. RHE corresponding to Ni(II)/Ni(III) oxidations and reductions, respectively. No redox peaks are observed for p^+-Si/a-TiO_2/Ir. Both OER catalyst iridium and nickel have comparable overpotentials in basic solution on inert conductive glassy carbon. [178] However, Figure 7.1(a) shows that p^+-Si/a-TiO_2/Ir(20 nm) had an overpotential 0.2 – 0.3 V higher than that of p^+-Si/a-TiO_2/Ni(20 nm) at a current density of 10 mA/cm^2. In contact with a fast one-electron redox couple, ferric ferrocyanide ($Fe(CN)_6^{3-/4-}$), Figure 7.1(b), p^+-Si/a-TiO_2/Ir(20 nm) showed slower kinetics than p^+-Si/a-TiO_2/Ni(20 nm). The current voltage plot for a p^+-Si/a-TiO_2/Au(20 nm) electrode also exhibited slow kinetics. It is noted that both gold and nickel have similar work functions, while the work function of iridium is larger. [178,179] Thus, the trend in conductivity observed was Ni>Ir>Au, and does not directly correlate with metal nobility or work function differences.

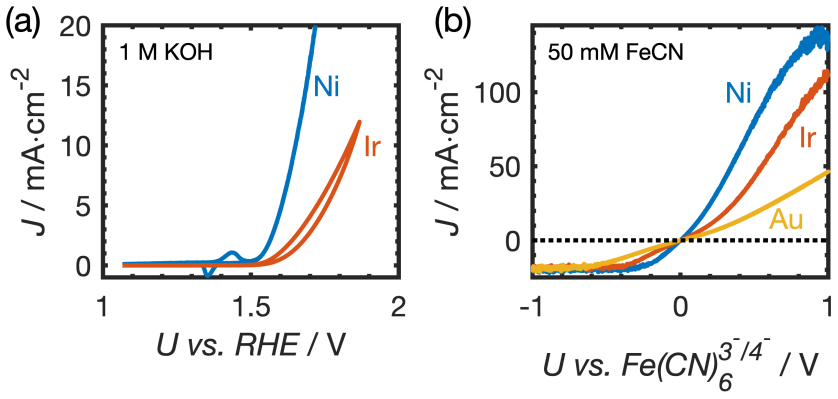

Figure 7.1: *(a) J-U measurements for p^+-Si/a-TiO_2/Ni and p^+-Si/a-TiO_2/Ir sample in 1.0 M KOH(aq). (b) J-U measurements for p^+-Si/a-TiO_2/M (M=nickel, iridium, gold) in 50/350 mM $Fe(CN)_6^{3-/4-}$(aq) solution.*

The dependence of the conductivity on metal thickness for p^+-Si/a-TiO_2/metal was also measured, as in Figure 7.2. Samples with thin nickel layers showed very little conductivity. A metal thickness of >2 nm was needed to produce significant conductivity. For Iridium, charge conduction was observed after a nominal metal thickness of 0.5 nm which gradually increased and saturated after 10 nm. For Gold, no hole conduction could be detected up to 5 nm, and only above

10 nm the a-TiO_2/Au layers were conductive. These results should be compared to the SEM images of the TiO_2/metal surfaces (Figure 7.3). Both nickel and iridium covered surfaces showed no distinctive surface morphology changes, indicating a smooth surface coverage of the thin metal layer. However, for gold deposition on TiO_2, the formation of nanoparticles could be observed up to a thickness of 5 nm. For 10 nm nominal gold layer thickness, these nanoparticles started to interconnect and form a continuous but still porous layer.

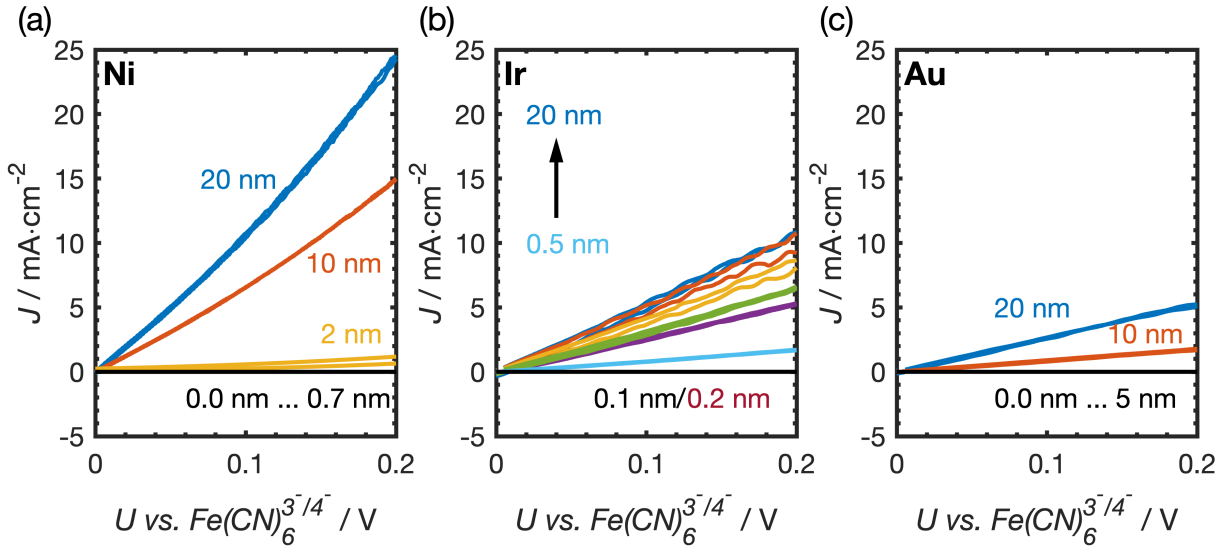

Figure 7.2: *J-U measurements for (a) p^+-Si/a-TiO_2/Ni, (b) p^+-Si/a-TiO_2/Ir, and (c) p^+-Si/a-TiO_2/Au in 50/350 mM $Fe(CN)_6^{3-/4-}$(aq) solution with different thicknesses of the metal layer.*

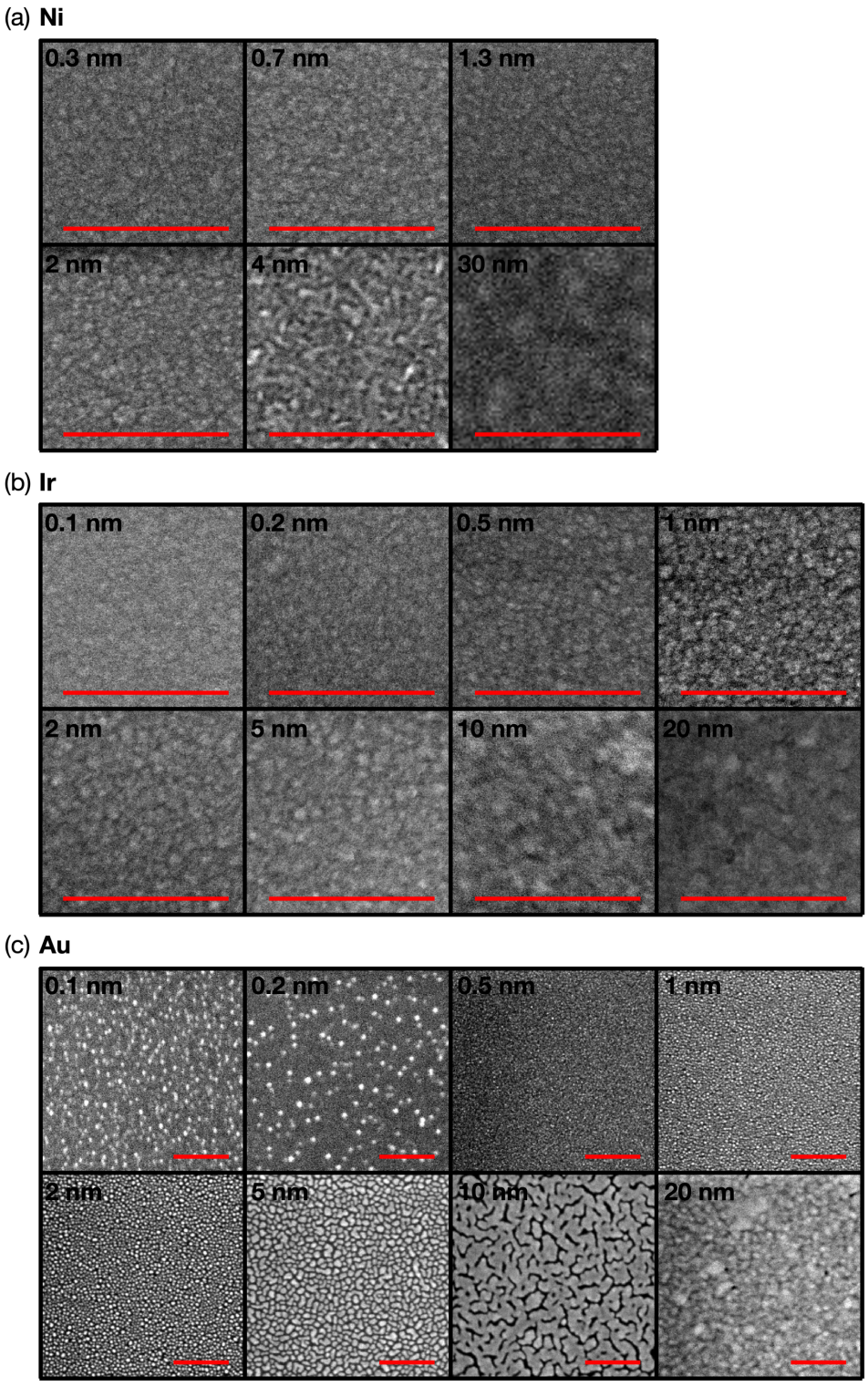

Figure 7.3: *Scanning electron microscopy images of a-TiO_2/M. M= (a) nickel, (b) iridium, and (c) gold for different metal thicknesses. The scale bar is 200 nm.*

Performance towards OER is a function of the effectiveness of the catalysts and the conductivity of the system. The conductivity is strongly dependent of the energetic alignment of the conduction and valence bands in the various materials. The energy band alignment between Si and-TiO_2 has been studied in detail previously [166], and we note that the p^+-Si/a-TiO_2 interface formed an ohmic contact as indicated by the absence of band bending in TiO_2 or p^+-Si after equilibration of the Fermi levels of both materials. Therefore, this interface should not significantly affect the conductivity from the Si to the metal catalyst, and thus we have focused on the a-TiO_2/metal interface.

Reference samples of TDMAT a-TiO_2 with and without metal contacts of nickel, iridium, and gold with metal thicknesses ranging from 0.1 Å to 200 Å were prepared. X-ray diffraction (XRD) spectra of these samples are shown in Figure 7.4. With increased metal layer thickness, the (111) metal diffraction peak becomes more pronounced for all metals with additional (200), (220), and (311) peaks for gold. No XRD signal could be observed for TDMAT a-TiO_2 on any of the samples.

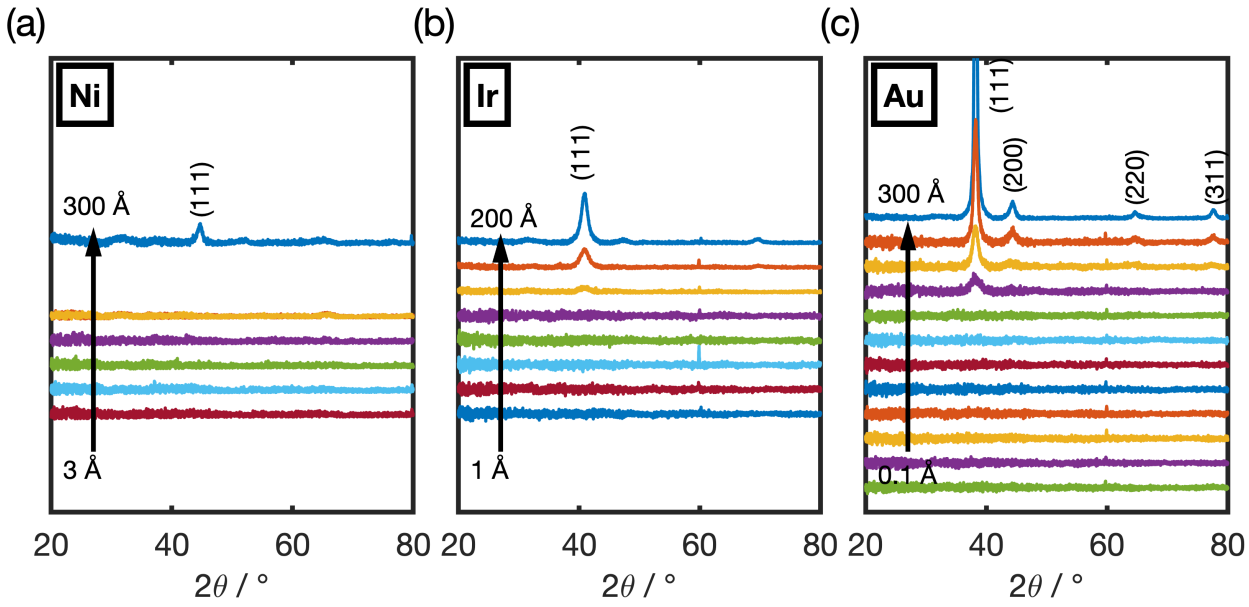

Figure 7.4: *XRD spectra for a-TiO_2/M (M=Ni, Ir, Au) for different metal layer thicknesses.*

Figure 7.5 shows high resolution XPS spectra of a-TiO_2/M devices for Ni 2p, Ir 4f, Au 4f, Ti 2p, and O 1s core levels with the valence band region. The valence band spectra for the bare

a-TiO_2 sample showed the characteristic gap state at a binding energy of ~1 eV, which shows no difference in intensity for bulk (Figure 7.6, $\theta = 0°$) or surface sensitive (Fig. S4, $\theta = 70°$) XPS. Upon deposition of less than one Å of metal, the gap state could not be detected by laboratory XPS due to the high intensity of the valence band states of the metal (Figure 7.5(d,l,h)). Thin layers of nickel and iridium showed metal oxide peaks for nickel (Figure 7.5(a)) and iridium (Figure 7.5(e)) as indicated by solid lines. Metallic peaks (dashed lines) at a lower binding energy were observed with increasing nickel and iridium thickness that did not obscure the metal oxide peaks, which indicated that the metal oxide was on the metal surface. Depth profiling of-TiO_2/Ni samples by changing the photon energy and thus the inelastic mean free path (IMFP) of the emitted electrons using synchrotron XPS revealed that the valence band nickel oxide peak decreased in intensity with decreasing surface sensitivity (increasing photon energy), supporting the conclusion that the metal oxide was on the surface of the metal layer. The opposite trend was observed for the metallic nickel contributions evident by states at the Fermi energy (E_F) (see Figure 7.7). Previous investigations using Ambient Pressure XPS also showed the presence of a metallic nickel phase for the samples in 1 M KOH under applied potential. [168] While no core level shifts for the metal peaks (Ni 2p, Ir 4f, Au 4f) were observed (only changes in oxidation state), binding energy shifts for the Ti 2p core level were observed for a-TiO_2/Ni and a-TiO_2/Ir samples. No shoulder or change in peak shape (FWHM) for the Ti 2p core level was evident in Figure 7.5(b,f,j), indicating that there was no oxidation state change for the a-TiO_2, i.e., and no transition from Ti^{4+} to Ti^{3+} or lower oxidation states. Thus, the single component for Ti $2p_{3/2}$ and Ti $2p_{1/2}$ core levels was assigned to Ti^{4+}, indicating that the shift in the Ti 2p core level was due to band bending and not to changes in oxidation state.

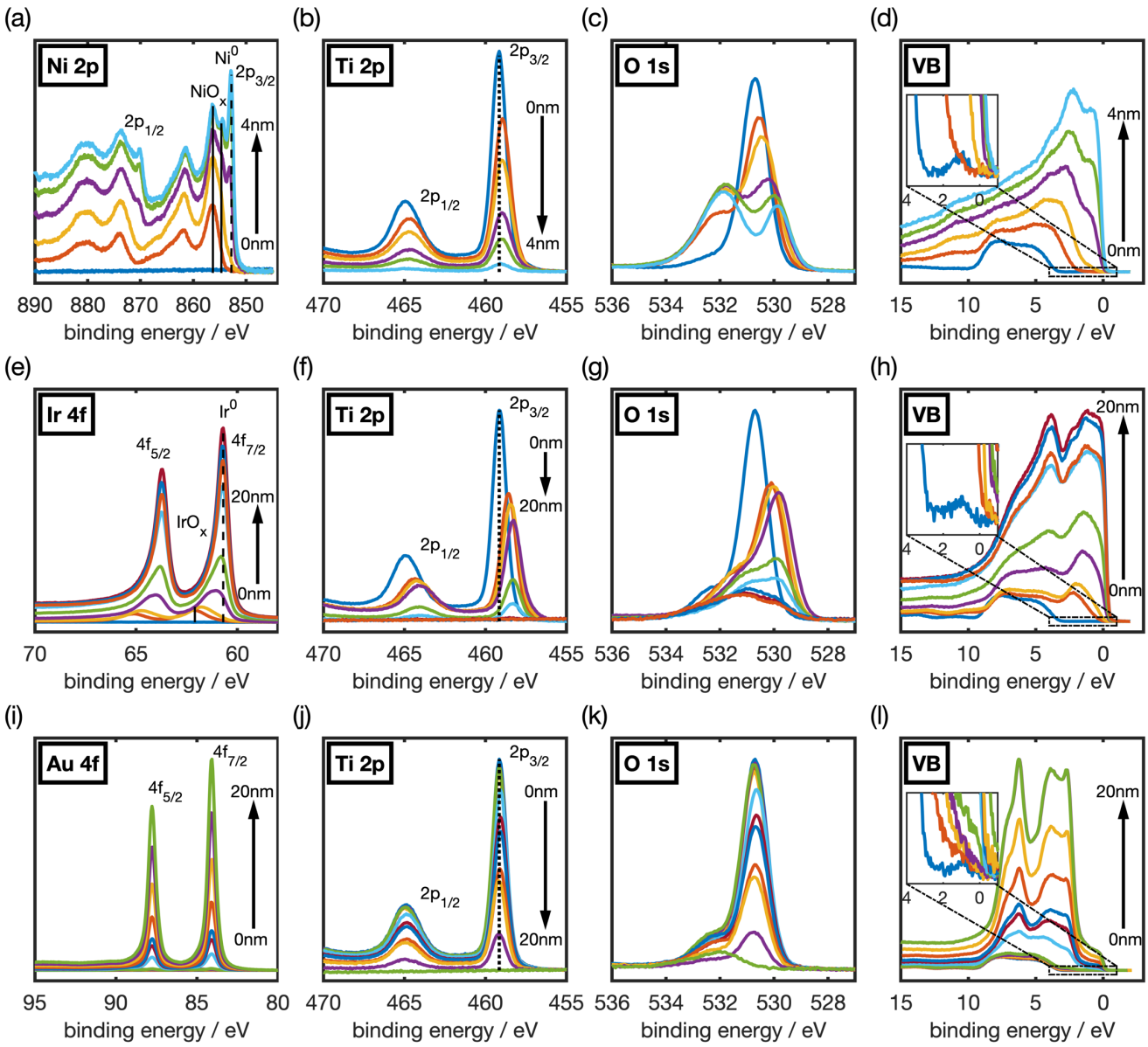

Figure 7.5: *XPS spectra for a-TiO_2/metal systems for (a-d) nickel, (e-h) iridium and (i-l) gold showing core level peaks for the metal, (a) Ni 2p, (e) Ir 4f, (i) Au 4f; (b, f, j) Ti 2p; (c, g, k) O 1s, and (d, h, l) of the valence band. The metal overlayer thicknesses are shown in the graph. The black dashed line shown in the Ti 2p core level plots indicates the position of bulk Ti $2p_{3/2}$ core level peaks, whereas the dashed and solid lines in (a) and (e) indicate the metallic and oxide peak position, respectively.*

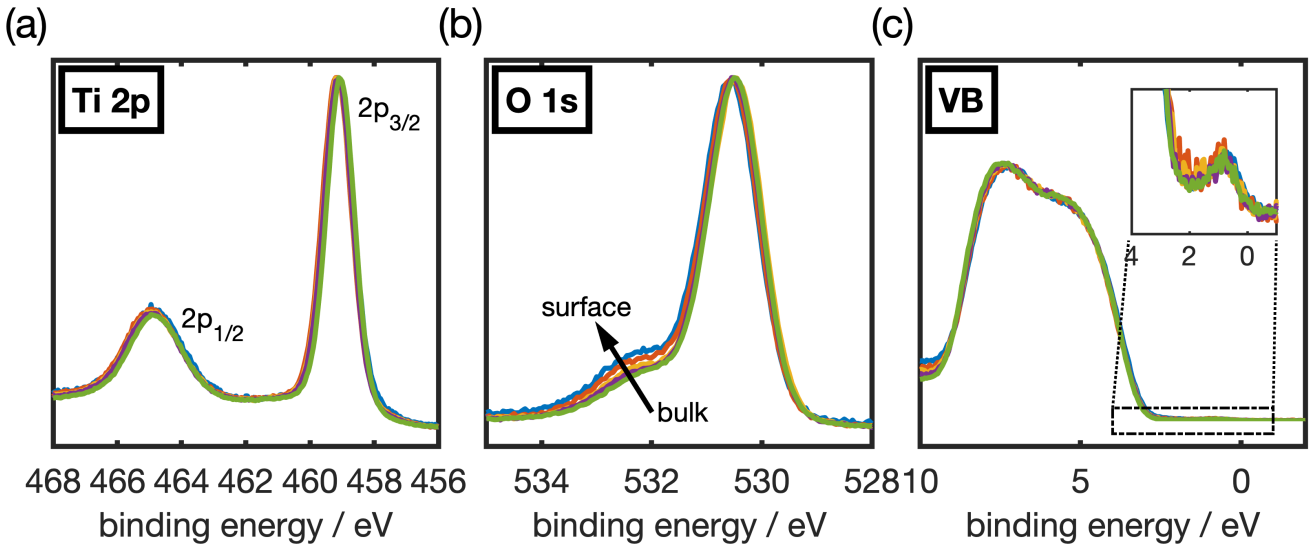

Figure 7.6: *XPS spectra for TDMAT ALD a-TiO_2 of the (a) Ti 2p and (b) O 1s core levels and (c) of the valence band for different emission angles from θ = 0° (bulk sensitive) to θ = 70° (surface sensitive) relative to the surface normal. With increased surface sensitivity (increased θ), an increase in the oxygen shoulder at 532.5 eV was observed.*

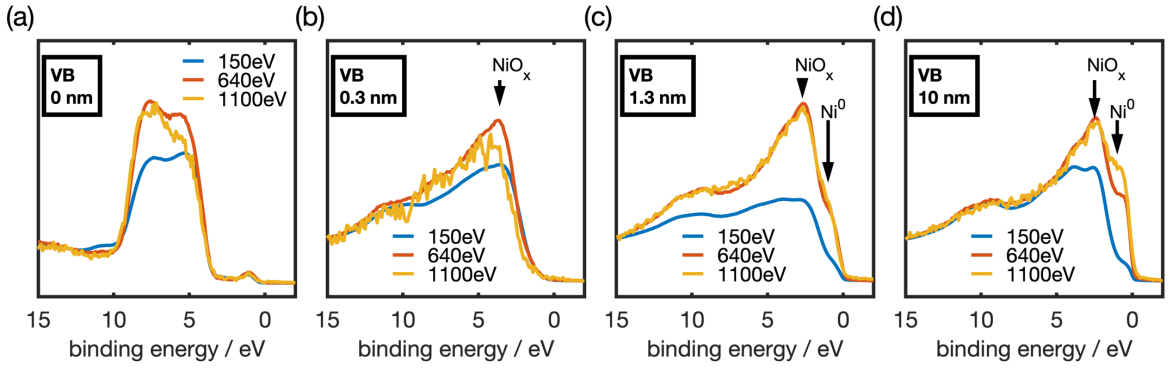

Figure 7.7: *Valence band spectra of for different nickel thicknesses: (a) 0 nm, (b) 0.3 nm, (c)1.3 nm, and (d) 10 nm. The spectra were recorded at three different photon energies: 150 eV, 640 eV, and 1100 eV corresponding also to the kinetic energy of electron from the upper valence band. Hence, the inelastic mean-free path (IMFP) of the photoelectrons corresponds to λ = 4.72 Å (Ni) to 6.28 Å (a-TiO_2) for E_K = 150 eV, λ = 11.19 Å (Ni) to 14.96 Å (a-TiO_2) for E_K = 640 eV, and λ = 16.64 Å (Ni) to 22.39 Å (a-TiO_2) for E_K = 1100 eV. Inelastic Mean-Free Path for elements under investigation for relevant photoelectron energies are calculated by IMFP-TPP2M.* [180]

For pristine TDMAT a-TiO_2 and each metal, the work function (Wf) was determined by ultraviolet photoelectron spectroscopy (UPS) using He I excitation (Figure 7.8(a)). The values were $Wf_{a\text{-}TiO2}$ = 4.7±0.10 eV, Wf_{Au} = 5.05±0.22 eV, Wf_{Ni} = 5.09±0.19 eV, Wf_{Ir} = 5.32±0.12 eV. The binding energy for the valence band minimum maximum for TDMAT a-TiO_2 was VBM = 2.94±0.10 eV .The band bending of the a-TiO_2 inferred from the changes in Ti $2p_{3/2}$ peak position shown in Figure 7.8(b) follows the trend of the differences in work functions between the a-TiO_2 and the metal, ΔWf. Differences between the magnitude of band bending and ΔWf were attributed to factors such as the interface dipole and fermi level pinning, and will be discussed later on.

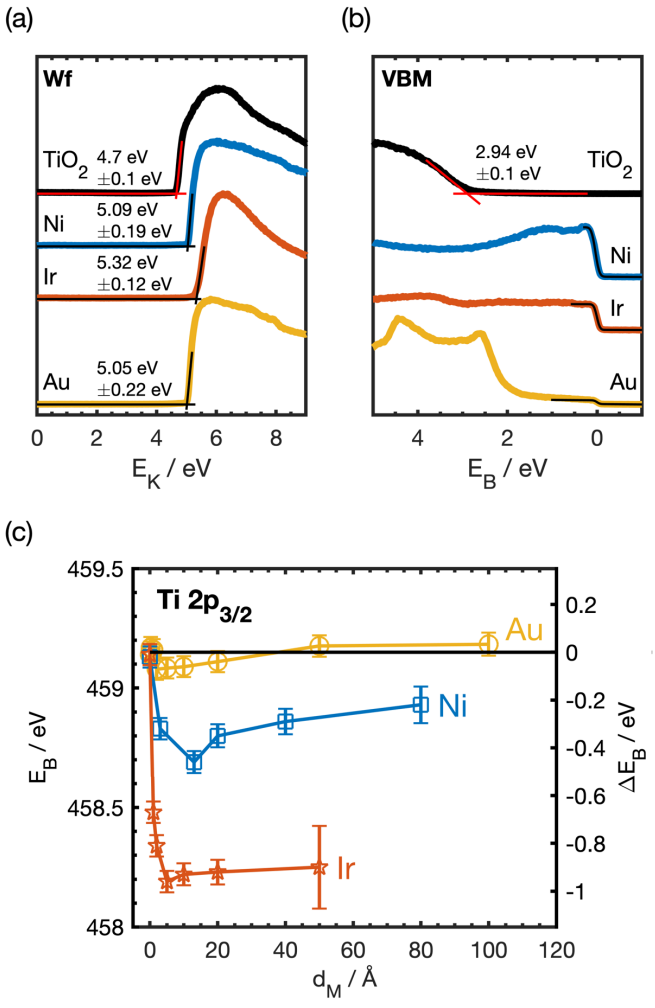

Figure 7.8: *He I ultraviolet photoelectron spectra (UPS) of TDMAT a-TiO_2/metal, with nickel, iridium, and gold showing (a) the work function and (b) valence band maximum. The metals were*

sputter-cleaned until no contamination or carbon was detectable. (c) Energy position of Ti $2p_{3/2}$ core level depending on contact metal and metal thickness. The values were extracted from Figure 7.5.

To further investigate the a-TiO_2/metal interface, resonant photoemission (resPES) and resonant inelastic X-ray scattering (RIXS) measurements were employed, which use an element-specific probe to look through the relatively thick metal layer and visualize changes in the valence band states of a-TiO_2. Standard X-ray photoelectron spectroscopy involves the measurement of core level (CL, Figure 7.9, process I) and valence band (VB) states (Figure 7.9, process II) of a specimen. Due to the distinguishable characteristic binding energies (E_B) between elements for core levels (binding energy difference is sufficiently large), different element and oxidations states can be identified without difficulty. However, for valence band spectroscopy, this is not the case, as every element has electronic states close to the fermi energy (E_F), making identification of different elemental contributions extremely challenging with standard laboratory X-ray spectroscopy. Instead, tunable synchrotron radiation makes it possible to excite valence band states in resonance and thus gives the possibility to distinguish between valence band states of different elements. With titanium as an example, these processes are described by equations below.

$$\text{Ti } 2p^6 + \hbar\omega'' \rightarrow \text{Ti } 2p^5 + e_{vac}^- \quad \text{(Equation 7.1)}$$

$$[VB]^n + \hbar\omega'' \rightarrow [VB]^{n-1} + e_{vac}^- \quad \text{(Equation 7.2)}$$

$$\text{Ti } 2p^6 + [VB]^n + [CB]^0 + \hbar\omega \rightarrow \text{Ti } 2p^5 + [VB]^n + [CB]^1 \quad \text{(Equation 7.3)}$$

$$\text{Ti } 2p^5 + [VB]^n + [CB]^1 \rightarrow \text{Ti } 2p^6 + [VB]^{n-1} + [CB]^0 + e_{vac}^- \quad \text{(Equation 7.4)}$$

$$\text{Ti } 2p^5 + [VB]^n + [CB]^1 \rightarrow \text{Ti } 2p^6 + [VB]^{n-1} + [CB]^1 + \hbar\omega' \quad \text{(Equation 7.5)}$$

For regular XPS with a fixed photon energy (e.g. monochromatic AlKα radiation of 1486.69 eV), Equation 7.1 depicts the excitation of a Ti 2p core level electron above the vacuum level (E_{vac}). Equation 7.2 shows the excitation of a valence band electron above E_{vac}. Since the photon energy is high enough to excite core levels above E_{vac} ($\hbar\omega$''>$E_{B,Ti\ 2p}$+Wf), two different final states can be found.

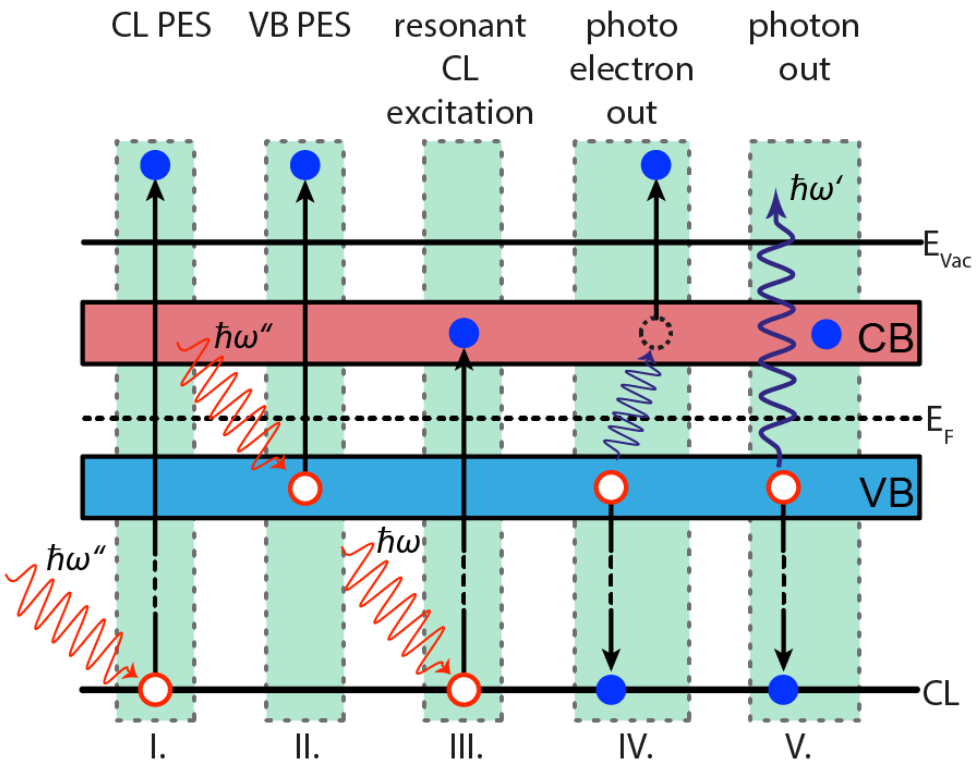

Figure 7.9: *Illustration of possible X-ray spectroscopy excitation and decay channels: I. Excitation of core level electron above the vacuum level (E_{Vac}); II. Excitation of valence band (VB) electron above the vacuum level; III. Resonant excitation of a core level electron into unoccupied states of the conduction band (CB); IV. After process III, an electron from the valence band refills the core hole transferring the energy to the initial excited core level electron thus exciting it above E_{Vac} (participator decay); V. After process III, an electron from the valence band refills the core hole with the emission of a photon.*

If we consider tunable photon energy with specific value of ħω that electron in CL can be excited into empty states of the conduction band, we will obtain an intermediate state shown in Figure 7.9 process III (resonant excitation). It has to be noted that this (optical) process is governed by dipole selection rules, indicating that all states (CL, VB and CB) need to be reached within the same atom. [175] High elemental sensitivity can thus be realized with this technique. The intermediate state can relax into different final states through several routes with only two discussed here (Figure 7.9, processes IV and V). Both have commonalities with the core hole (created through Figure 7.9 process III) refilled by a valence electron. The energy released can

either be transferred to the initial excited core electron in the conduction band so it can be excited above E_{vac} (Figure 7.9, process IV, participator Auger decay) or leave the atom as a photon with a characteristic energy. (Figure 7.9, process V)

It is evident that when the tunable photon energy is high enough ($\hbar\omega > E_{VB}+Wf$), Figure 7.9 process II also happens that the same final state for photoelectron spectroscopy channel can be reached as shown in Equation 7.2 and Equation 7.4. Though the initial excitation in Equation 7.3 is performed by resonant excitation, the valence band contribution from the corresponding element is thus enhanced. By directly subtracting the off-resonant valence band spectrum as a background from the on-resonant excitation, the valence band spectrum from single elemental species can be obtained. As comparison, the background subtraction is not necessary for the optical channel in Equation 7.5 as the emitted photons have a characteristic energy $\hbar\omega$' for each element.

Usually, the photon energy is scanned across the respective absorption edge (Ti $L_{2/3}$ edge for excitation from Ti 2p core levels) during X-ray absorption experiments. At each individual photon energy, a valence band or X-ray emission spectrum can be recorded, which results in resonant Photoelectron spectroscopy (resPES) or resonant inelastic X-ray spectroscopy (RIXS) maps. Traditionally, the photoelectron intensity is plotted versus the binding energy (or sometimes kinetic energy $E_K = \hbar\omega - E_B$), whereas in RIXS spectra, the photon yield is shown versus the loss energy ($E_{loss} = \hbar\omega - \hbar\omega'$) or emission energy $\hbar\omega$'.

The resPES color contour plot for-a-TiO_2 at the titanium $L_{2/3}$ edge for the a-TiO_2/Ni system is shown in Figure 7.10. It shows valence band XPS spectra recorded as a function of the exciting X-ray energy as scanned across the Ti 2p absorption edge. The ordinate is the binding energy of the initially formed excited valence state (-1 eV to 20 eV) and the abscissa reflects the excitation energy (452 eV – 475 eV). Off-resonant contributions to the spectra were subtracted using an off-resonant reference spectrum for the same sample at an excitation energy of 452 eV.

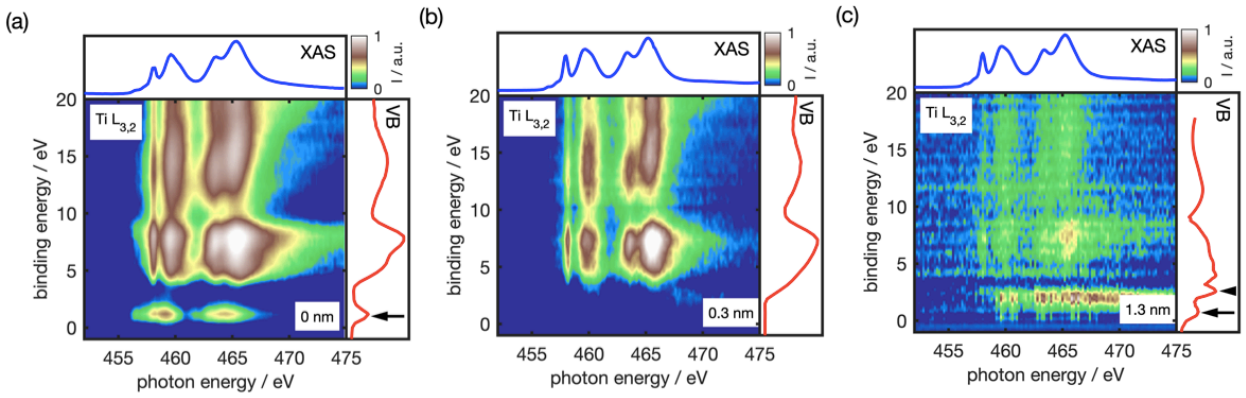

Figure 7.10: *Resonant photoemission maps at the Ti L3,2 edge of (a) p+-Si/a-TiO2, (b) p+-Si/a-TiO2/Ni(0.3 nm), and (c) p+-Si/a-TiO2/Ni(1.3 nm). The insets on the top show the total electron yield (TEY) mode XAS spectrum, and the inset on the right the valence band spectrum at 464 eV. In all spectra, the off-resonant contributions were subtracted using the off-resonant VB spectra at 452 eV. The black arrows on the right panel indicate the position of the gap state.*

Figure 7.10(a) shows the valence band resPES map for TDMAT a-TiO_2 at the Ti $L_{3,2}$ edges. The characteristic gap state is clearly evident in the resPES map at a binding energy of 1 eV for both the L_3 (459.6 eV photon energy) and L_2 edges (465.2 eV photon energy), as well as in the valence band spectra shown in the righthand side panel. The XPS of the pristine a-TiO_2 showed no difference between bulk and surface Ti 2p core and valence band levels (Figure 7.6), suggesting that the gap staes was the same throughout the bulk of the sample. After deposition of 0.3 nm of Nickel, no gap state was observable in the resPES map, Figure 7.10(b). When the nickel thickness was further increased to 1.3 nm, two gap states could now be observed with one peak at a slightly reduced binding energy of 0.7 eV and a second at 2.6 eV, as in Figure 7.10(c) righthand side panel. For this sample, the valence band on the right was measured separately with increased dwell time to improve signal to noise ratio of the spectra after recording of the initial map.

The resPES maps for the Oxygen K and Ni L_3 edges are shown in Figure 7.11and Figure 7.12. Figure 7.11(a) represents the Oxygen K edge map for pristine TDMAT a-TiO_2. The oxygen valence band states observed between binding energies of 5 and 10 eV and photon energies between 530 eV and 535 eV for the pristine a-TiO_2 were absent in the maps with increased nickel thickness. While for nickel layers <0.3 nm thick, the nickel was completely oxidized (Figure 7.5(a),

Figure 7.11(b)), and for thicker layers, the nickel was primarily metallic at the TiO_2 surface, with NiO_x at the nickel surface. Because of the limited information depth and element sensitivity of resPES, the oxide peaks observed for thicker layers should be attributed to oxygen of NiO_x rather than to oxygen in a-TiO_2. The corresponding Ni L_3 edge maps are shown in Figure 7.12. The two prominent features at photon energies of 853 and 854.7 eV were attributed to Ni^{2+} (NiO) and Ni^{3+} (NiOOH) states. [181,182] The valence band maximum shifted toward the Fermi energy with increasing nickel thickness from 0.3 nm to 1.3 nm.

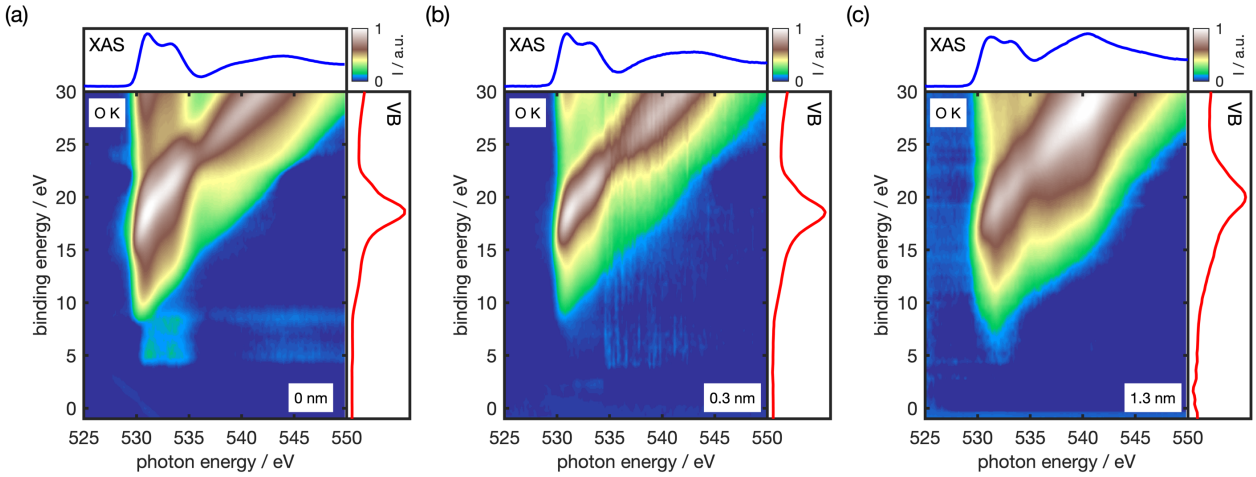

Figure 7.11: *Resonant photoemission maps at the Oxygen K edge of (a) p^+-Si/a-TiO_2, (b) p^+-Si/a-TiO_2/Ni(0.3 nm) and (c) p^+-Si/a-TiO_2/Ni(1.3 nm). The insets on the top show the TEY XAS spectrum and the inset on the left the valence band spectrum at 531 eV. In all spectra, the off-resonant contributions were subtracted using the off-resonant VB spectra at 525 eV.*

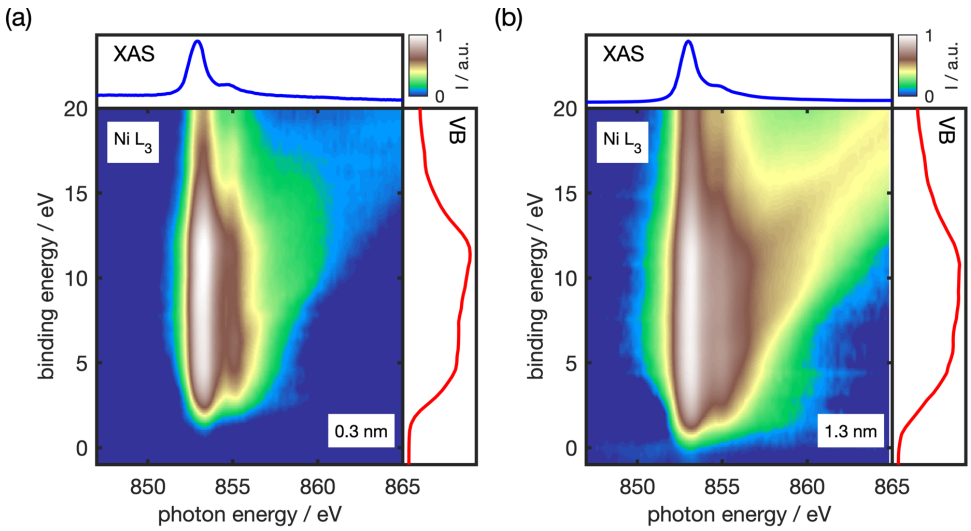

Figure 7.12: *Resonant photoemission maps at the Ni L_3 edge of (a) p^+-Si/a-TiO_2/Ni(0.3 nm) and (b) p^+-Si/a-TiO_2/Ni(1.3 nm). The insets on the top show the TEY XAS spectrum, and the insets on the left the valence band spectrum at 853 eV. In all spectra, the off-resonant contributions were subtracted using the off-resonant VB spectra at 846 eV.*

Oxygen vacancies in a-TiO_2 result in n doping. The localization of the mobile electron produces a partially populated t_{2g} band which is visible by XPS in the band gap at 1 eV binding energy. In RIXS, this is visible due to resonant excitation into the e_g band followed by de-excitation from the t_{2g} band resulting in a dd loss feature. [171] To illustrate the correlation between valence band gap state (XPS) and dd loss feature in RIXS, both measurements were performed on a sample with and without gap state. Figure 7.13 shows the valence band and RIXS spectra for pristine and annealed TDMAT a-TiO_2. For pristine a-TiO_2, the gap state is visible in the XPS valence band, and a dd transition peak can be observed in the RIXS spectrum. Upon annealing, the gap state in the XPS spectra disappeared and no dd transition in RIXS was visible.

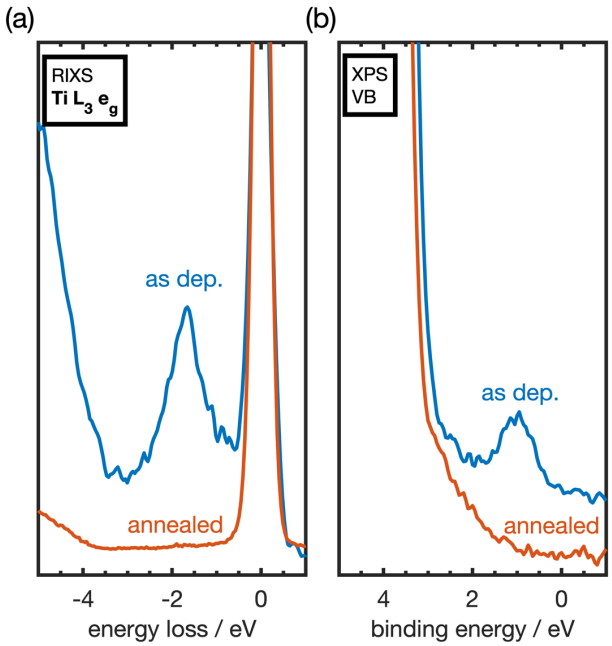

Figure 7.13: *(a) XPS valence band spectra and (b) RIXS spectra at the Ti L_3 e_g resonance for pristine and annealed a-TiO_2.*

For a-TiO_2/Ir and a-TiO_2/Au RIXS spectra (Figure 7.14(a-b)) the gap state was visible as a characteristic dd transition at an energy loss of 1.6 to 1.8 eV with the elastic X-ray scattering peak at 0 eV. To obtain a signal directly proportional to the intensity of the gap state, the intensity of the dd transition must be normalized to that of the elastic peak. In Figure 7.14(c), the normalized gap state intensity and its position are given as a function of metal coverage for both iridium and gold. No clear change was evident, suggesting that the gap state was unaffected by the deposition of iridium or gold.

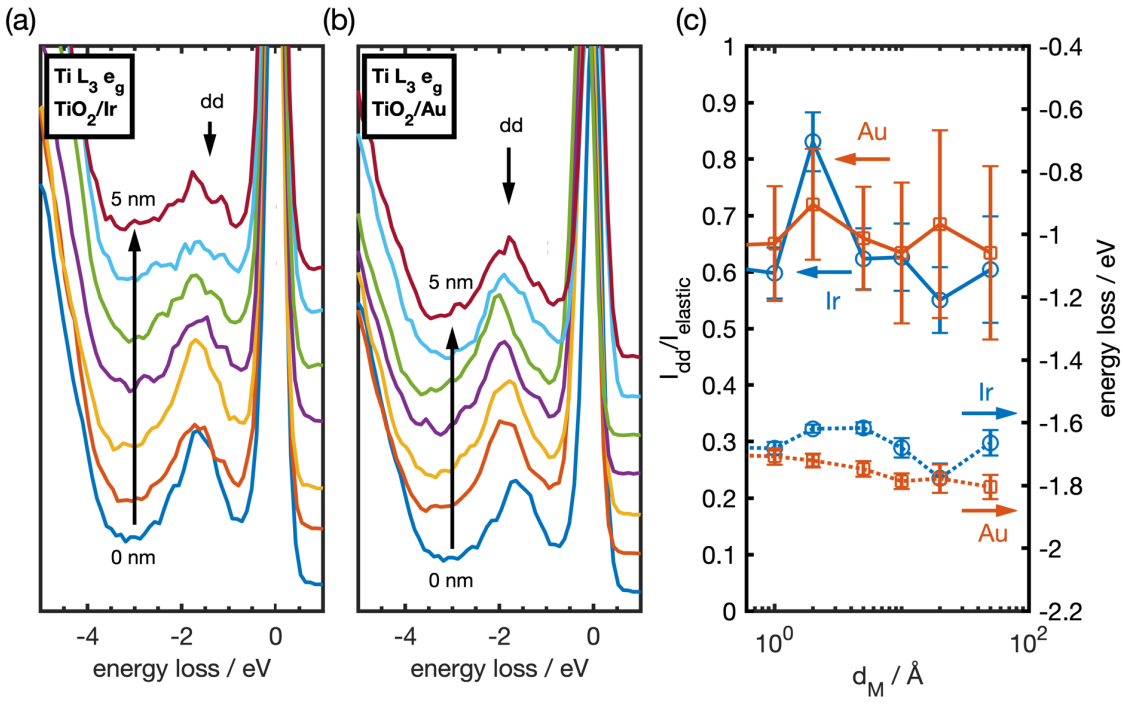

Figure 7.14: *RIXS spectra of (a) a-TiO_2/Ir and (b) a-TiO_2/Au at the Ti L_3 t_{2g} resonance. The position of the characteristic dd transition is indicated. (c) Intensity ratio of dd transition to elastic peak. A change in this normalized dd intensity gives evidence of changes in the gap state.*

The resPES results make it possible to determine the partial density of states for titanium, oxygen, and nickel of the valence band of TiO_2/Ni layer. Figure 7.15 summarized the density of states at valence band for the-TiO_2/Ni interface with varying nickel thickness. Pristine TDMAT a-TiO_2 shows a clear titanium derived gap state in the valence band at 1 eV (Figure 7.15(a)). The gap state of the pristine a-TiO_2 exhibits no change in intensity between the bulk and surface by XPS measurements (Figure 7.6(c)). Thus, the gap state extends throughout the bulk of the a-TiO_2. The resPES data showed that the gap state was not present at the TiO_2/Ni interface after deposition of a thin nickel layer (0.3 nm, Figure 7.15(b)), which was shown to be completely oxidized to NiO_x, as in Figure 7.5(a) and Figure 7.7(b). This change of the gap state upon nickel oxide deposition is attributed to a chemical change only at the a-TiO_2 surface. We propose that for thin layers of nickel, the NiO_x layer at the TiO_2 surface provides additional oxygen species to oxidize Ti interstitials (Ti^{3+}) in the a-TiO_2 at the surface and thus creates a thin interface layer of a-TiO_2 without the gap state. NiO_x also possesses a different work function than nickel which can be rather

large (6.7 eV) but also drops rapidly upon exposure to H_2O, O_2, and CO_2. [183] High work function materials can lead to a depletion of Ti^{3+} states and increase the junction resistance through band bending in a-TiO_2. [167] In a classical picture – for no reaction between metal and a-TiO_2 – a high work function of the contact material the Fermi energy would pass through the gap state in a-TiO_2 resulting in a reduction of charge carrier population of the gap state at the interface and reduction or complete blocking of hole conduction. The bulk properties of a-TiO_2 would not be affected. For thin layers of gold or iridium on a-TiO_2, no change in the gap state intensity was observed (Figure 7.14).

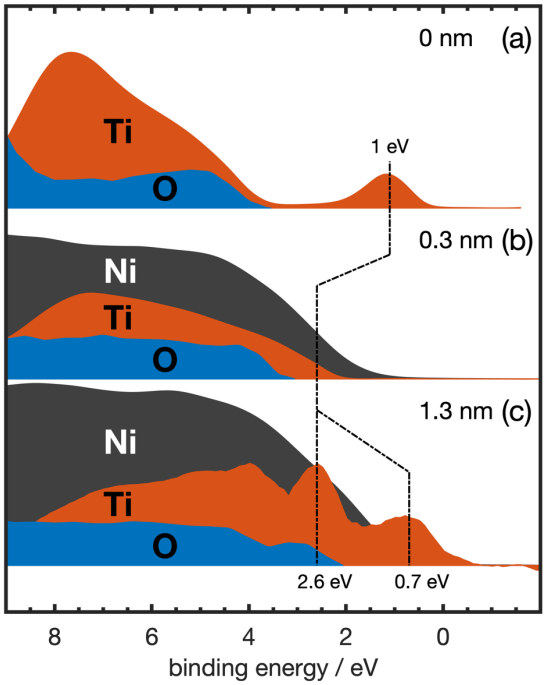

Figure 7.15: *Partial density of valence band states for titanium (red) and nickel (grey) derived states at the a-TiO_2-Ni interface for pristine (a) a-TiO_2, (b) a-TiO_2/Ni(0.3 nm), and (c) a-TiO_2/Ni(1.3 nm). The partial density of states (pDOS) is obtained by calculating the difference between on and off-resonance valence band spectra a the Ti 2p and Ni 2p X-ray absorption edge.*

For nickel thickness greater than 0.3 nm, the nickel at the a-TiO_2 interface becomes metallic. Depth profiling revealed the presence of this buried metallic nickel phase below the NiO_x surface layer. For this case, resPES showed the existence of two gap states at the a-TiO_2/Ni interface with binding energies of 2.6 eV and 0.7 eV (Figure 7.15(c)). We attribute the first gap state to be Ti

related and arise from partial reduction of the a-TiO_2 surface by Ni. The different binding energy can be related to possible change in Ti 3d density or change in local symmetry. Chemical reaction and hybridization of Ni with a-TiO_2 gives rise to the second gap state at 2.6 eV attributing it to Ni-Ti bond formation. Both gap states essentially fill the energy range from VBM to the Fermi energy. This effect was only observed for the a-TiO_2/metal interface, with the bulk a-TiO_2 unaffected. With the increase in the density of states in the band gap between VBM and Fermi energy, the a-TiO_2 will exhibit metallic character at the a-TiO_2/metal interface and thus enhance the conduction across the a-TiO_2/M interface. For a-TiO_2/Ir and a-TiO_2/Au, a similar behavior was not detected as the gap state showed no change over the range of metal deposition (Figure 7.14).

With the help of XPS and UPS, the band alignment between metal layer and TDMAT a-TiO_2 was also determined. Buried junctions are, in principle, accessible by XPS if they are not too remote from the top surface. At heterojunctions of semiconductors, thermodynamic equilibration of the electrochemical potentials of electrons in the semiconductors (Fermi level), ϕ, is established by the exchange of delocalized charges, inducing band bending due to non-compensated ionized doping atoms in the space charge regions, and/or by formation of an interface dipole δ at the interface. In general, the thermodynamic equilibration requires difference in electrochemical potential to be equal to the change in energy due to the band bending and surface dipole in the materials. The energy band relationships in semiconductor junctions can be determined from core level and valence band spectroscopy using X-ray photoelectron and the secondary electron emission cut-off (i.e. work function measurements) from ultraviolet photoemission spectroscopy. [184]

Because of the relatively small sampling depth of XPS, a general procedure for energy band profile determination is to measure the valence band maximum to core level binding energy differences [185,186] and then monitor variations of the well-defined substrate and adsorbate core level binding energy positions during step-by-step deposition of the contact material with typical thicknesses from 5 to 30 Å. [184,186] The individual band bending in a-TiO_2/metal was extracted from the core level shift of the Ti 2p core level and is summarized in Figure 7.8(b). The exact values which were extracted from XPS and UPS measurements (Figure 7.5, Figure 7.8) and resonant X-Ray spectroscopy (Figure 7.10, Figure 7.14) are consolidated in Table 7.1. Figure 7.16 shows the summary of band alignments for a-TiO_2/Ni (Figure 7.16(a)), a-TiO_2/Ir (Figure 7.16(b)), and

a-TiO_2/Au (Figure 7.16(c)). A detailed description on the calculation of the band-energy diagrams can be found in a previous study. [166] Both a-TiO_2/Ni and a-TiO_2/Ir show upward band bending in the a-TiO_2 close to the metal interface while a-TiO_2/Au shows no bending. In all three cases, the gap state in the a-TiO_2 extends to the TiO_2/M interface. No change in intensity was observed from bulk to surface for pristine a-TiO_2 without metal layer. In a previous study, it was shown that the band bending in the a-TiO_2 at the interface for a a-TiO_2/M device is fixed and independent from the applied potential in electrolyte. [168]

Table 7.1: *Parameters used for band-energy diagrams of a-TiO_2/M with M=nickel, M=iridium, and M=gold as shown in Figure 7.16. E_B is the binding energy. E_{BB} is the band bending at the interface. The band gap for TiO_2 was taken from previous studies.* [74,166]

Unit (eV)	**a-TiO_2/Ni**	**a-TiO_2/Ir**	**a-TiO_2/Au**
Φ_TiO_2	4.70	4.70	4.70
Φ_M	5.09	5.32	5.05
E_g_TiO_2	3.34*	3.34*	3.34*
E_B_Ti 2p, bulk	459.25	459.25	459.25
E_B_M, bulk	852.6	60.9	84
E_{BB}_TiO_2	0.19	0.92	0.05
δ (dipole)	0.20	-0.30	0.30
E_B_defect, bulk	1.0	1.0	1.0
FWHM_defect, bulk	0.88	0.88	0.88

E_B_defect, interface	0.7, 2.6	0.08	0.95
FWHM_defect, interface	1.4, 1.2	0.88	0.88

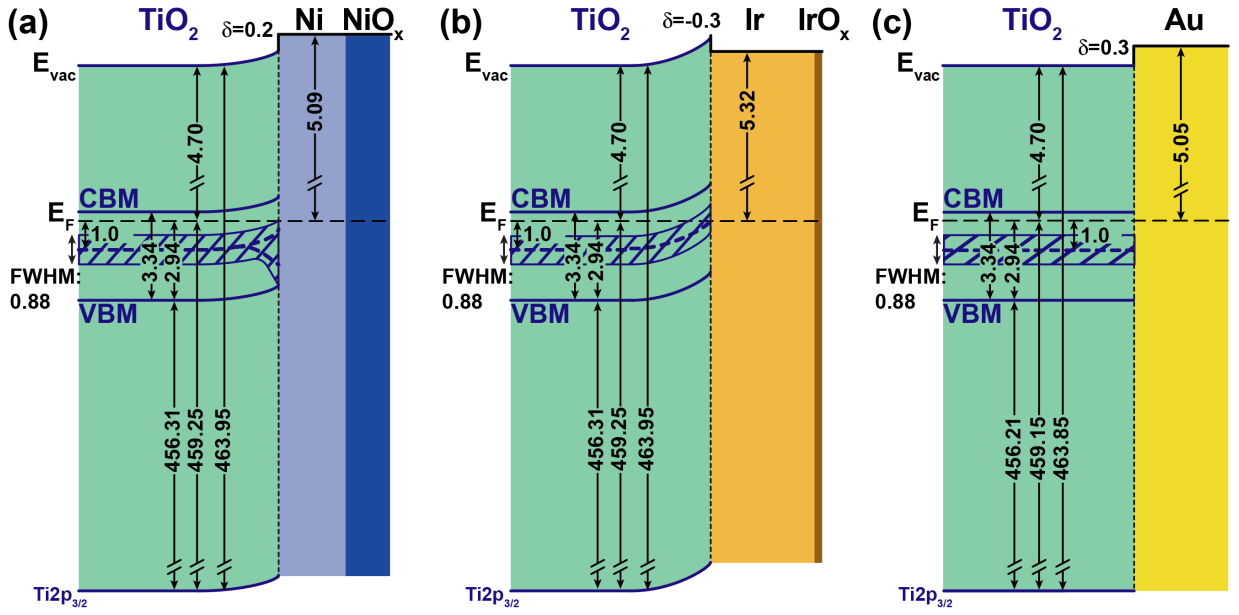

Figure 7.16: *Band-energy diagrams for a-TiO_2/M with M= (a) nickel, (b) iridium, and (c) gold. All numeric values are in eV. δ is the interface dipole energy difference between TDMAT a-TiO_2 and the metal. The hashed region between the VBM and CBM in the a-TiO_2 indicates the position of the gap state with the FWHM taken as its width. The values can also be found in Table 7.1.*

For a-TiO_2/Ni, the gap state is below the Fermi level with the gap between VBM and Fermi level completely filled with gap states at the TiO_2/Ni interface. This is shown in Figure 7.16(a) by extending the gap state (dashed region) to the VBM. For thin layers of nickel where the nickel was completely oxidized, no interfacial gap state was detected (Figure 7.15(b)), which results in a thin interfacial layer where the transport channel (the gap state) for holes from the substrate to the catalyst was not continuous. In agreement with this observation, conductivity measurements showed no conduction for a-TiO_2/NiO_x samples (Figure 7.2(a), up to 0.7 nm).

For the a-TiO_2/Ir, no change of the gap state at the interface was detected. Also, the Fermi energy passes through the top half of the gap state at the a-TiO_2/Ir interface, resulting in a thin layer where the gap state has reduced charge carrier population. Without the presence of the quasi-metallic channel and lower charge carrier density, the lower conducting behavior of a-TiO_2/Ir than a-TiO_2/Ni can be understood. The a-TiO_2/Au showed no significant change in binding energy of the Ti 2p core levels which signifies that there is no upward band bending. Thus, for a-TiO_2/Au, the band-energy diagram depicts a flat band condition for hole transport through the gap state to the metal (i.e. there is not an electric field that will propel holes through the a-TiO_2 toward the Au). This leads to the poorer performance of the a-TiO_2/Au system compared to the other two. Furthermore, it was observed that for thin layers of gold (up to 5 nm) in a-TiO_2/Au showed the presence of gold nanoparticles and no current was observed in these situations. This can be understood if in the a-TiO_2/Au system the gold nanoparticles exhibit a nonuniform barrier height contact to the electrolyte ("pinch-off") where the Au/electrolyte interface energetics are not determined by the work function of the gold but rather by the a-TiO_2. [187] This explanation is supported by the fact that for a uniform, but porous thin gold layer, the a-TiO_2/Au system then conducts current to the electrolyte, as in Figure 7.2. In the presence of gold nanoparticles, the contact behavior of the a-TiO_2/Au "pinch-off" system will be dominated the a-TiO_2/electrolyte interface and the observable current is dictated by the energetics imposed by the a-TiO_2/electrolyte junction. In our previous studies we have shown that for a-TiO_2/electrolyte systems an applied bias will be compensated by a-TiO_2 bend bending close to the electrolyte interface and will lead to the gap state getting pushed above the Fermi energy at the interface [168,188] This results in complete depopulation of the gap state at the interface and formation of a thin depletion region with hole-blocking properties. No current was observed under these conditions.

Although the difference in work function between a-TiO_2 and metal provided a general guideline for band alignment and conductivity evaluation for a-TiO_2/M interface, e.g. metals with a work function less than a TiO_2 provided higher conductivities, it cannot describe the difference in behavior for metals with similar work function. Here we showed that further effects have to be taken in account, i.e. reactivity of the metal and its ability to oxidize or reduce interfacial TiO_2 (in the presence or absence of additional oxygen sources) and local energy effects of nanoparticles.

7.4 Conclusion and Outlook

We investigated the conduction behavior between a "leaky" a-TiO_2 protection layer for photoanodes and metal catalysts (iridium, nickel, and gold). Resonant X-ray spectroscopy revealed a critical interfacial reaction between a-TiO_2 and nickel catalyst which can create either a non-conductive or a quasi-metallic surface layer on a-TiO_2 depending on the chemical state of the catalysts (nickel oxide or metallic nickel respectively). For a photoanode protection and catalyst layer system of a-TiO_2/Ni, it is required to have a minimum thickness of ~2 nm to prevent complete oxidation of the a-TiO_2 surface. Else a barrier for hole transport through the gap state will be created by elimination of the gap state at the surface of a-TiO_2. The superior performance of the a-TiO_2/Ni system over the a-TiO_2/Ir system is the result of the intrinsic formation of a quasi-metallic interface layer by gap steates between a-TiO_2 and nickel. It allows holes to conduct between the semiconductor through the thick but "leaky" a-TiO_2 protection layer to the nickel catalyst. This results in an ohmic contact between a-TiO_2/Ni. Non-reactive metals which form nanoparticles can even lead to complete loss of catalytic current due to "pinch-off" effect and hole barrier formation under anodic bias. This study suggests that a "reductive" metal on top of "leaky" a-TiO_2 is necessary for formation of quasi metallic interface layer between a-TiO_2 and catalyst.

Future direction involves applying the resPES and RiXS to understand the degradation mechanism when regular XPS cannot explain. Operando study is a powerful tool which would help to examine the surface chemistry during operation. With resonance, we can also distinguish the different valence and conduction band contributions (pDOS), as catalysis involves conduction and valence band for reduction and oxidation processes where regular XPS cannot distinguish. It would be valuable when a complicated catalyst with more than one kind of atom (for example, alloy, bimetallic, MoS_2...) or for OER (which involves oxides) that contribution from different atomic character can be examined.

CHAPTER 8

Summary

This thesis focuses on understanding comprehensive aspects from photonic design, interface study, to device integration. We first focused on enhancing absorption via nanophotonic design of a light absorber. III-V compound semiconductor nanowire arrays are promising candidates for energy harvesting due to their high volumetric absorption. Uniform nanowire arrays exhibit high absorption at certain wavelengths due to strong coupling into resonant waveguide modes. We have simulated and experimentally demonstrated near-unity, broadband absorption in sparse InP nanowire arrays (< 5% fill fraction) with multi-radii and tapered nanowire array designs, where incident visible light can be coupled into continuous waveguide modes in taper cone structures. For both designs, the polymer-embedded arrays achieved ~ 90% broadband absorption (λ = 400-900 nm) in less than 100 nm planar equivalence of InP. The addition of a silver back reflector increased this broadband absorption to ~ 95%.

To realize high solar-to-fuel efficiency in PEC devices, it is necessary to maintain a catalytic current density close to the light limiting photocurrent density for a solar-driven light absorber, which can be fulfilled when catalyst ensembles are highly transparent. We report a monolithic photocathode device architecture that exhibits significantly reduced surface reflectivity, minimizing parasitic light absorption and reflection losses. A tailored multifunctional crystalline titania interphase layer acts as a corrosion protection layer, with favorable band alignment between the semiconductor conduction band and the energy level for water reduction, facilitating electron transport at the cathode−electrolyte interface. It also provides a favorable substrate for adhesion of high-activity Rh catalyst nanoparticles. Under simulated AM 1.5G irradiation, solar-to-hydrogen efficiencies of 19.3 and 18.5% are obtained in acidic and neutral electrolytes, respectively. The system reaches a value of 0.85 of the theoretical limit for photoelectrochemical water splitting for the energy gap combination employed in the tandem-junction photoelectrode structure.

Solar-driven reduction of carbon dioxide represents a carbon neutral pathway for the synthesis of fuels and chemicals. We report here results for solar-driven CO_2 reduction using a gas diffusion electrode (GDE) directly powered by a photovoltaic cell. A GaInP/GaInAs/Ge triple junction photovoltaic cell was used to power a reverse-assembled gas diffusion electrode employing a Ag

nanoparticle catalyst layer. The device had a solar-to-CO energy conversion efficiency of 19.1 % under simulated AM 1.5G illumination at 1 Sun. The use of a reverse-assembled GDE prevented transition from a wetted to a flooded catalyst bed and allowed the device to operate stably for >150 h with no loss in efficiency. Outdoor measurements were performed under ambient solar illumination in Pasadena, CA, resulting in a peak solar-to-CO efficiency 18.7 % with a CO production rate of 47 $mg \cdot cm^{-2}$ per day and a diurnal-averaged solar to fuel conversion efficiency of 5.8 %. The high efficiency and stability of the system suggests that reverse-assembled GDEs are a promising path to producing chemical fuels from CO_2 and sunlight.

We further demonstrated light management strategies to create highly active and effectively transparent catalyst structures. Covering over 50% of the surface of a light absorber with an array of high-refractive-index TiO_2 nanocones imparted antireflective behavior (< 5% reflectance) to the surface and allowed > 85% transmission of broadband light to the underlying Si, even when thick metal contacts or opaque catalyst coatings were deposited on areas of the light-facing surface that were not directly beneath a nanocone. Three-dimensional full-field electromagnetic simulations for the 400 – 1100 nm spectral range showed that incident broadband illumination couples to multiple waveguide modes in the TiO_2 nanocones, reducing interactions of the light with the metal layer. A proof-of-concept experimental demonstration of light-driven water oxidation was performed using a p^+n-Si photoanode decorated with an array of TiO_2 nanocones additionally having a Ni catalyst layer electrodeposited onto the areas of the p^+n-Si surface left uncovered by the TiO_2 nanocones. This photoanode produced a light-limited photocurrent density of ~ 28 mA cm^{-2} under 100 mW cm^{-2} of simulated Air Mass 1.5 illumination, equivalent to the photocurrent density expected for a bare planar Si surface even though 54% of the front surface of the Si was covered by an ~ 70 nm thick Ni metal layer.

Another approach is developed with effectively transparent catalyst consisting of arrays of micron-scale triangular cross-sectional metal grid fingers. The capability of redirecting the incoming light to the open areas of the PEC cell reduces the overall shadow loss. Numerical calculations using full wave electromagnetic simulations were used to investigate the optical response and determine the optimal geometry and length scale. We found that a mesoscale Ag grid array with triangular cross-section lines and metal coverage of > 50% exhibits negligible additional reflection loss. Our designs feature photonic structures to enable high absorption light absorbers,

and effectively transparent catalyst layers for PEC cell are general approaches not limited to single reaction or specific photovoltaic system. Together with the capability of scalable processes through printing technology for catalysts using conductive inks and electroplating, it will be a critical step to advances in the field of solar fuel generation and all other related optical applications. It also opens up a new route for photoelectrochemical applications toward large-scale manufacturing.

Last but not least, the interfacial conduction mechanism between the commonly employed semiconductor protection layer titanium dioxide and metal catalysts is investigated. While iridium and nickel exhibit similar overpotential for oxygen evolution reaction in alkaline media, a-TiO_2/Ir requires higher overpotential than a-TiO_2/Ni to achieve the same current density. A combinatorial approach of electrochemistry, X-ray photoelectron spectroscopy, and resonant X-ray spectroscopy reveals the correlation between interfacial metal-TiO_2 properties and conduction. While both nickel and iridium metals impose band bending upon a-TiO_2, only nickel creates an interfacial quasi metallic a-TiO_2 surface due to creation of additional interface gap states. The use of noble metal catalysts (gold, iridium) will result in band bending or formation of a barrier while non-noble catalysts (nickel) create an ohmic contact after deposition of a minimum metal layer thickness.

For visualization, **Figure 8.1** summarizes the state-of-the-art solar fuel devices with contribution from this thesis for both water splitting and CO_2 reduction with four main categories of PV-Electrolyser, photoanode, photocathode, and PV plus photocathode.

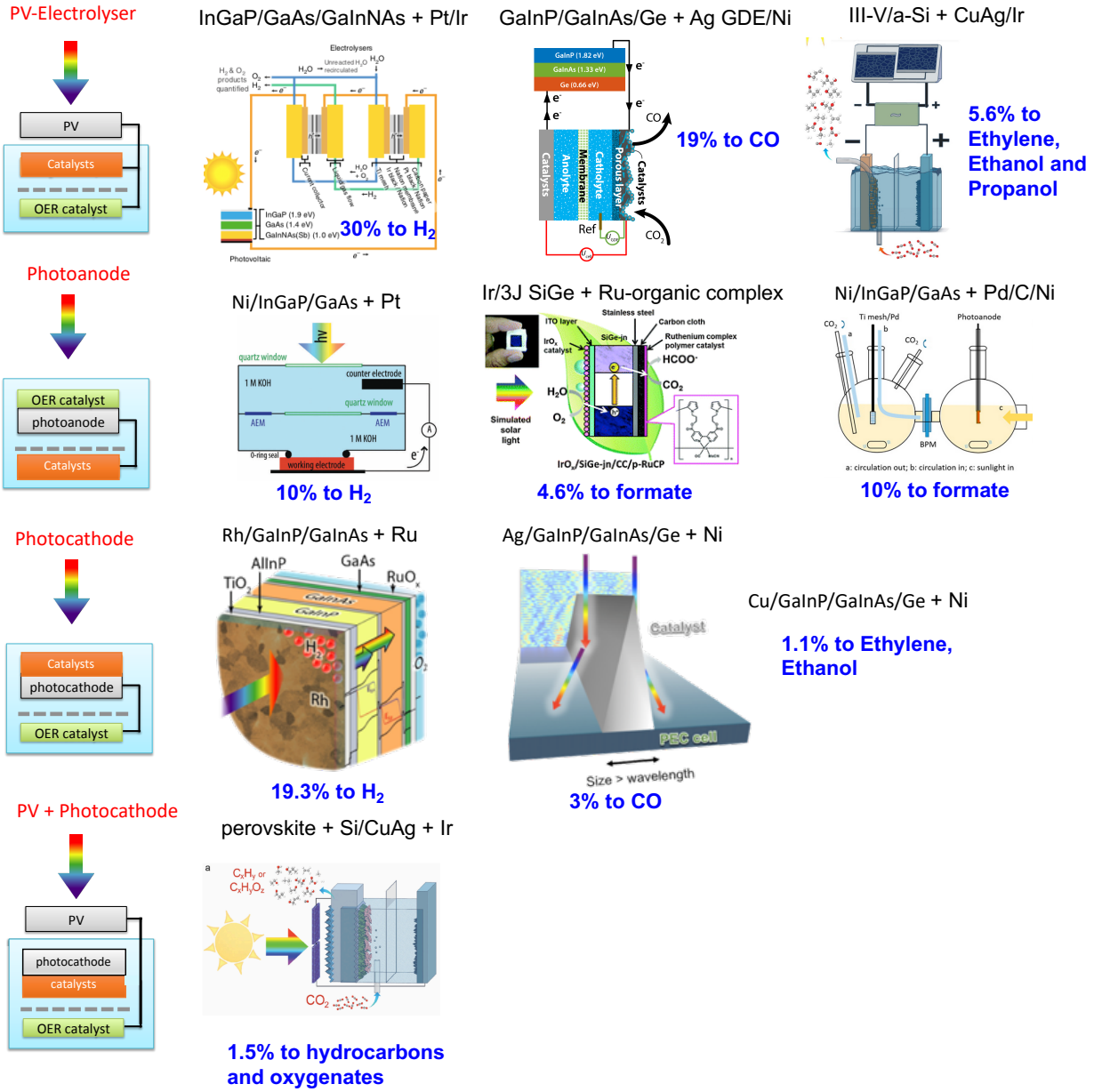

Figure 8.1: *State-of-the-art solar fuel device for water splitting and CO_2 reduction with category of PV-Electrolyser, photoanode, photocathode, and PV plus photocathode.*

References

[1] Davis, S. J.; Lewis, N. S.; Lewis, N. S.; Shaner, M. R.; Shaner, M.; Aggarwal, S.; Arent, D.; Azevedo, I. L.; Benson, S. M.; Bradley, T.; et al. Net-Zero Emissions Energy Systems. *Science* **2018**, *360* (6396), eaas9793.

[2] Armstrong, R. C.; Wolfram, C.; de Jong, K. P.; Gross, R.; Lewis, N. S.; Lewis, N. S.; Boardman, B.; Ragauskas, A. J.; Ehrhardt-Martinez, K.; Crabtree, G.; et al. The Frontiers of Energy. *Nat. Energy* **2016**, *1* (1), 15020.

[3] Lewis, N. S.; Lewis, N. S. Toward Cost-Effective Solar Energy Use. *Science* **2007**, *315* (5813), 798–801.

[4] Jia, J.; Seitz, L. C.; Benck, J. D.; Huo, Y.; Chen, Y.; Ng, J. W. D.; Bilir, T.; Harris, J. S.; Jaramillo, T. F. Solar Water Splitting by Photovoltaic-Electrolysis with a Solar-to-Hydrogen Efficiency Over 30%. *Nature Communications* **2016**, *7*, 13237.

[5] Young, J. L.; Steiner, M. A.; Döscher, H.; France, R. M.; Turner, J. A.; Deutsch, T. G. Direct Solar-to-Hydrogen Conversion via Inverted Metamorphic Multi-Junction Semiconductor Architectures. *Nat. Energy* **2017**, *2*, 17028.

[6] Cheng, W.-H.; Richter, M. H.; May, M. M.; Ohlmann, J.; Lackner, D.; Dimroth, F.; Hannappel, T.; Atwater, H. A.; Lewerenz, H.-J. Monolithic Photoelectrochemical Device for Direct Water Splitting with 19% Efficiency. *ACS Energy Lett.* **2018**, 1795–1800.

[7] Qiu, Y.; Liu, W.; Chen, W.; Zhou, G.; Hsu, P.-C.; Zhang, R.; Liang, Z.; Fan, S.; Zhang, Y.; Cui, Y. Efficient Solar-Driven Water Splitting by Nanocone BiVO4-Perovskite Tandem Cells. *Science Advances* **2016**, *2* (6), e1501764–e1506473.

[8] Huang, D.; Wang, K.; Yu, L.; Nguyen, T. H.; Ikeda, S.; Jiang, F. Over 1% Efficient Unbiased Stable Solar Water Splitting Based on a Sprayed Cu 2ZnSnS 4Photocathode Protected by a HfO 2Photocorrosion-Resistant Film. *ACS Energy Lett.* **2018**, 1875–1881.

[9] Reece, S. Y.; Hamel, J. A.; Sung, K.; Jarvi, T. D.; Esswein, A. J.; Pijpers, J. J. H.; Nocera, D. G. Wireless Solar Water Splitting Using Silicon-Based Semiconductors and Earth-Abundant Catalysts. *Science* **2011**, *334* (6056), 645–648.

[10] May, M. M.; Lewerenz, H.-J.; Lackner, D.; Dimroth, F.; Hannappel, T. Efficient Direct Solar-to-Hydrogen Conversion by in Situ Interface Transformation of a Tandem Structure. *Nature Communications* **2015**, *6*, 8286.

[11] Shaner, M. R.; Atwater, H. A.; Lewis, N. S.; McFarland, E. W. A Comparative Technoeconomic Analysis of Renewable Hydrogen Production Using Solar Energy. *Energy Environ. Sci.* **2016**, *9* (7), 2354–2371.

[12] Liu, J.; Liu, Y.; Liu, N.; Han, Y.; Zhang, X.; Huang, H.; Lifshitz, Y.; Lee, S.-T.; Zhong, J.; Kang, Z. Water Splitting. Metal-Free Efficient Photocatalyst for Stable Visible Water Splitting via a Two-Electron Pathway. - PubMed - NCBI. *Science* **2015**, *347* (6225), 970–974.

[13] Hisatomi, T.; Domen, K. Reaction Systems for Solar Hydrogen Production via Water Splitting with Particulate Semiconductor Photocatalysts. *Nature Catalysis 2018 1:8* **2019**, *2* (5), 387–399.

[14] Ra'di, Y.; Simovski, C. R.; Tretyakov, S. A. Thin Perfect Absorbers for Electromagnetic Waves: Theory, Design, and Realizations. *Phys. Rev. Applied* **2015**, *3* (3), 037001.

[15] Soukoulis, C. M.; Wegener, M. Past Achievements and Future Challenges in the Development of Three-Dimensional Photonic Metamaterials. *Nature Photonics* **2011**, *5* (9), 523–530.

[16] Landy, N. I.; Sajuyigbe, S.; Mock, J. J.; Smith, D. R.; Padilla, W. J. Perfect Metamaterial Absorber. *Phys. Rev. Lett.* **2008**, *100* (20), 207402.

[17] Sakr, E.; Dhaka, S.; Bermel, P. Asymmetric Angular-Selective Thermal Emission; 2016; Vol. 9743, pp 97431D–97431D–8.

[18] Argyropoulos, C.; Le, K. Q.; Mattiucci, N.; D'Aguanno, G.; Alu, A. Broadband Absorbers and Selective Emitters Based on Plasmonic Brewster Metasurfaces. *Phys. Rev. B* **2013**, *87* (20), 6.

[19] Liu, X. L.; Tyler, T.; Starr, T.; Starr, A. F.; Jokerst, N. M.; Padilla, W. J. Taming the Blackbody with Infrared Metamaterials as Selective Thermal Emitters. *Phys. Rev. Lett.* **2011**, *107* (4), 4.

[20] Khanikaev, A. B.; Wu, C. H.; Shvets, G. Fano-Resonant Metamaterials and Their Applications. *nanoph* **2013**, *2* (4), 247–264.

[21] Liu, N.; Mesch, M.; Weiss, T.; Hentschel, M.; Giessen, H. Infrared Perfect Absorber and Its Application as Plasmonic Sensor. *Nano Lett.* **2010**, *10* (7), 2342–2348.

[22] Zhu, J.; Yu, Z. F.; Burkhard, G. F.; Hsu, C. M.; Connor, S. T.; Xu, Y. Q.; Wang, Q.; McGehee, M.; Fan, S. H.; Cui, Y. Optical Absorption Enhancement in Amorphous Silicon Nanowire and Nanocone Arrays. *Nano Lett.* **2009**, *9* (1), 279–282.

[23] Fountaine, K. T.; Kendall, C. G.; Atwater, H. A. Near-Unity Broadband Absorption Designs for Semiconducting Nanowire Arrays via Localized Radial Mode Excitation. *Opt. Express* **2014**, *22* (S3), A930–A940.

[24] Salisbury, W. W. Absorbent Body for Electromagnetic Waves. **1952**.

[25] de Abajo, F. J. G. Colloquium: Light Scattering by Particle and Hole Arrays. *Rev. Mod. Phys.* **2007**, *79* (4), 1267–1290.

[26] Kats, M. A.; Capasso, F. Ultra-Thin Optical Interference Coatings on Rough and Flexible Substrates. *Applied Physics Letters* **2014**, *105* (13), 3.

[27] Laroche, M.; Albaladejo, S.; Gomez-Medina, R.; Saenz, J. J. Tuning the Optical Response of Nanocylinder Arrays: an Analytical Study. *Phys. Rev. B* **2006**, *74* (24), 5.

[28] Diedenhofen, S. L.; Grzela, G.; Haverkamp, E.; Bauhuis, G.; Schermer, J. J.; Rivas, J. G. Broadband and Omnidirectional Anti-Reflection Layer for III/v Multi-Junction Solar Cells. *Solar Energy Materials and Solar Cells* **2012**, *101*, 308–314.

[29] Basu, S.; Zhang, Z. M.; Fu, C. J. Review of Near-Field Thermal Radiation and Its Application to Energy Conversion. *Int. J. Energy Res.* **2009**, *33* (13), 1203–1232.

[30] Atwater, H.; Polman, A.; Kosten, E.; Callahan, D.; Spinelli, P.; Eisler, C.; Escarra, M.; Warmann, E.; Flowers, C. Nanophotonic Design Principles for Ultrahigh Efficiency Photovoltaics; Linke, H., Borgstrom, M., Pullerits, T., Samuelson, L., Sundstrom, V., Inganas, O., Eds.; Amer Inst Physics: Melville, 2013; Vol. 1519, pp 17–21.

[31] Callahan, D. M.; Munday, J. N.; Atwater, H. A. Solar Cell Light Trapping Beyond the Ray Optic Limit. *Nano Lett.* **2012**, *12* (1), 214–218.

[32] de Abajo, F. J. G. Graphene Plasmonics: Challenges and Opportunities. *ACS Photonics* **2014**, *1* (3), 135–152.

[33] Brar, V. W.; Jang, M. S.; Sherrott, M.; Lopez, J. J.; Atwater, H. A. Highly Confined Tunable Mid-Infrared Plasmonics in Graphene Nanoresonators. *Nano Lett.* **2013**, *13* (6), 2541–2547.

[34] Kats, M. A.; Sharma, D.; Lin, J.; Genevet, P.; Blanchard, R.; Yang, Z.; Qazilbash, M. M.; Basov, D. N.; Ramanathan, S.; Capasso, F. Ultra-Thin Perfect Absorber Employing a Tunable Phase Change Material. *Applied Physics Letters* **2012**, *101* (22), 5.

[35] Liu, X. L.; Starr, T.; Starr, A. F.; Padilla, W. J. Infrared Spatial and Frequency Selective Metamaterial with Near-Unity Absorbance. *Phys. Rev. Lett.* **2010**, *104* (20), 4.

[36] Chou, J. B.; Yeng, Y. X.; Lenert, A.; Rinnerbauer, V.; Celanovic, I.; Soljacic, M.; Wang, E. N.; Kim, S. G. Design of Wide-Angle Selective Absorbers/Emitters with Dielectric Filled Metallic Photonic Crystals for Energy Applications. *Opt. Express* **2014**, *22* (1), A144–A154.

[37] Gudiksen, M. S.; Lauhon, L. J.; Wang, J.; Smith, D. C.; Lieber, C. M. Growth of Nanowire Superlattice Structures for Nanoscale Photonics and Electronics. *Nature* **2002**, *415* (6872), 617–620.

[38] Park, H.; Dan, Y.; Seo, K.; Yu, Y. J.; Duane, P. K.; Wober, M.; Crozier, K. B. Filter-Free Image Sensor Pixels Comprising Silicon Nanowires with Selective Color Absorption. *Nano Lett.* **2014**, *14* (4), 1804–1809.

[39] Soci, C.; Zhang, A.; Bao, X. Y.; Kim, H.; Lo, Y.; Wang, D. L. Nanowire Photodetectors. *J. Nanosci. Nanotechnol.* **2010**, *10* (3), 1430–1449.

[40] Liu, X. L.; Wang, L. P.; Zhang, Z. M. Wideband Tunable Omnidirectional Infrared Absorbers Based on Doped-Silicon Nanowire Arrays. *J. Heat Transf.-Trans. ASME* **2013**, *135* (6), 8.

[41] Tilke, A. T.; Pescini, L.; Lorenz, H.; Blick, R. H. Fabrication and Transport Characterization of a Primary Thermometer Formed by Coulomb Islands in a Suspended Silicon Nanowire. *Applied Physics Letters* **2003**, *82* (21), 3773–3775.

[42] Anttu, N.; Xu, H. Q. Coupling of Light Into Nanowire Arrays and Subsequent Absorption. *J. Nanosci. Nanotechnol.* **2010**, *10* (11), 7183–7187.

[43] Garnett, E.; Yang, P. D. Light Trapping in Silicon Nanowire Solar Cells. *Nano Lett.* **2010**, *10* (3), 1082–1087.

[44] Cao, L.; Fan, P.; Vasudev, A. P.; White, J. S.; Yu, Z.; Cai, W.; Schuller, J. A.; Fan, S.; Brongersma, M. L. Semiconductor Nanowire Optical Antenna Solar Absorbers. *Nano Lett.* **2010**, *10* (2), 439–445.

[45] Hu, S.; Chi, C. Y.; Fountaine, K. T.; Yao, M. Q.; Atwater, H. A.; Dapkus, P. D.; Lewis, N. S.; Zhou, C. W. Optical, Electrical, and Solar Energy-Conversion Properties of Gallium Arsenide Nanowire-Array Photoanodes. *Energy Environ. Sci.* **2013**, *6* (6), 1879–1890.

[46] Liu, C.; Tang, J. Y.; Chen, H. M.; Liu, B.; Yang, P. D. A Fully Integrated Nanosystem of Semiconductor Nanowires for Direct Solar Water Splitting. *Nano Lett.* **2013**, *13* (6), 2989–2992.

[47] Woodhouse, M.; Goodrich, A. *Manufacturing Cost Analysis Relevant to Single-and Dual-Junction Photovoltaic Cells Fabricated with III-vs and III-vs Grown on Czochralski Silicon (Presentation)*; National Renewable Energy Laboratory (NREL), Golden, CO., 2014.

[48] Rosenwaks, Y.; Shapira, Y.; Huppert, D. Evidence for Low Intrinsic Surface-Recombination Velocity on P-Type InP. *Phys. Rev. B* **1991**, *44* (23), 13097–13100.

[49] Grzela, G.; Paniagua-Domínguez, R.; Barten, T.; Fontana, Y.; Sánchez-Gil, J. A.; Gómez Rivas, J. Nanowire Antenna Emission. *Nano Lett.* **2012**, *12* (11), 5481–5486.

[50] Muskens, O. L.; Rivas, J. G.; Algra, R. E.; Bakkers, E.; Lagendijk, A. Design of Light Scattering in Nanowire Materials for Photovoltaic Applications. *Nano Lett.* **2008**, *8* (9), 2638–2642.

[51] Fan, Z. Y.; Kapadia, R.; Leu, P. W.; Zhang, X. B.; Chueh, Y. L.; Takei, K.; Yu, K.; Jamshidi, A.; Rathore, A. A.; Ruebusch, D. J.; et al. Ordered Arrays of Dual-Diameter Nanopillars for Maximized Optical Absorption. *Nano Lett.* **2010**, *10* (10), 3823–3827.

[52] Lin, C. X.; Povinelli, M. L. Optical Absorption Enhancement in Silicon Nanowire Arrays with a Large Lattice Constant for Photovoltaic Applications. *Opt. Express* **2009**, *17* (22), 19371–19381.

[53] Abujetas, D. R.; Paniagua-Dominguez, R.; Sanchez-Gil, J. A. Unraveling the Janus Role of Mie Resonances and Leaky/Guided Modes in Semiconductor Nanowire Absorption for Enhanced Light Harvesting. *ACS Photonics* **2015**, *2* (7), 921–929.

[54] Seo, K.; Wober, M.; Steinvurzel, P.; Schonbrun, E.; Dan, Y. P.; Ellenbogen, T.; Crozier, K. B. Multicolored Vertical Silicon Nanowires. *Nano Lett.* **2011**, *11* (4), 1851–1856.

[55] Heiss, M.; Russo-Averchi, E.; Dalmau-Mallorqui, A.; Tutuncuoglu, G.; Matteini, F.; Ruffer, D.; Conesa-Boj, S.; Demichel, O.; Alarcon-Llado, E.; Morral, A. F. I. III-v Nanowire Arrays: Growth and Light Interaction. *Nanotechnology* **2014**, *25* (1), 9.

[56] Wallentin, J.; Anttu, N.; Asoli, D.; Huffman, M.; Åberg, I.; Magnusson, M. H.; Siefer, G.; Fuss-Kailuweit, P.; Dimroth, F.; Witzigmann, B.; et al. InP Nanowire Array Solar Cells

Achieving 13.8% Efficiency by Exceeding the Ray Optics Limit. *Science* **2013**, *339* (6123), 1057–1060.

[57] Diedenhofen, S. L.; Janssen, O. T. A.; Grzela, G.; Bakkers, E. P. A. M.; Gómez Rivas, J. Strong Geometrical Dependence of the Absorption of Light in Arrays of Semiconductor Nanowires. *ACS Nano* **2011**, *5* (3), 2316–2323.

[58] Deinega, A.; John, S. Solar Power Conversion Efficiency in Modulated Silicon Nanowire Photonic Crystals. *Journal of Applied Physics* **2012**, *112* (7), 7.

[59] Hong, L.; Rusli; Wang, X. C.; Zheng, H. Y.; Wang, H.; Yu, H. Y. Design Guidelines for Slanting Silicon Nanowire Arrays for Solar Cell Application. *Journal of Applied Physics* **2013**, *114* (8), 6.

[60] Cansizoglu, H.; Cansizoglu, M. F.; Finckenor, M.; Karabacak, T. Optical Absorption Properties of Semiconducting Nanostructures with Different Shapes. *Advanced Optical Materials* **2013**, *1* (2), 158–166.

[61] Lin, C. X.; Huang, N. F.; Povinelli, M. L. Effect of Aperiodicity on the Broadband Reflection of Silicon Nanorod Structures for Photovoltaics. *Opt. Express* **2012**, *20* (1), A125–A132.

[62] Vynck, K.; Burresi, M.; Riboli, F.; Wiersma, D. S. Photon Management in Two-Dimensional Disordered Media. *Nat Mater* **2012**, *11* (12), 1017–1022.

[63] Kelzenberg, M. *Silicon Microwire Photovoltaics*; California Institute of Technology, 2010.

[64] Snyder, A. W.; Love, J. *Optical Waveguide Theory*; Springer, 1983.

[65] Walter, M. G.; Warren, E. L.; McKone, J. R.; Boettcher, S. W.; Mi, Q.; Santori, E. A.; Lewis, N. S. Solar Water Splitting Cells. *Chem. Rev.* **2010**, *110* (11), 6446–6473.

[66] Khaselev, O.; Turner, J. A. A Monolithic Photovoltaic-Photoelectrochemical Device for Hydrogen Production via Water Splitting. *Science* **1998**, *280* (5362), 425–427.

[67] Lichterman, M. F.; Sun, K.; Hu, S.; Zhou, X.; McDowell, M. T.; Shaner, M. R.; Richter, M. H.; Crumlin, E. J.; Carim, A. I.; Saadi, F. H.; et al. Protection of Inorganic Semiconductors for Sustained, Efficient Photoelectrochemical Water Oxidation. *Catalysis Today* **2016**, *262*, 11–23.

[68] Bae, D.; Pedersen, T.; Seger, B.; Iandolo, B.; Hansen, O.; Vesborg, P. C. K.; Chorkendorff, I. Carrier-Selective P- and N-Contacts for Efficient and Stable Photocatalytic Water Reduction. *Catalysis Today* **2017**, *290*, 59–64.

[69] Fountaine, K. T.; Lewerenz, H.-J.; Atwater, H. A. Efficiency Limits for Photoelectrochemical Water-Splitting. *Nature Communications* **2016**, *7*, 13706.

[70] May, M. M.; Lackner, D.; Ohlmann, J.; Dimroth, F.; van de Krol, R.; Hannappel, T.; Schwarzburg, K. On the Benchmarking of Multi-Junction Photoelectrochemical Fuel Generating Devices. *Sustainable Energy Fuels* **2017**, *1*, 15010.

[71] Sathre, R.; Scown, C. D.; Morrow, W. R.; Stevens, J. C.; Sharp, I. D.; Ager, J. W., III; Walczak, K.; Houle, F. A.; Greenblatt, J. B. Life-Cycle Net Energy Assessment of Large-Scale Hydrogen Production via Photoelectrochemical Water Splitting. *Energy Environ. Sci.* **2014**, *7* (10), 3264–3278.

[72] Dimroth, F.; Beckert, R.; Meusel, M.; Schubert, U.; Bett, A. W. Metamorphic GayIn1−yP/Ga1−xInxAs Tandem Solar Cells for Space and for Terrestrial Concentrator Applications at C ≫ 1000 Suns. *Prog. Photovolt: Res. Appl.* **2001**, *9* (3), 165–178.

[73] Ohlmann, J.; Sanchez, J. F. M.; Lackner, D.; Förster, P.; Steiner, M.; Fallisch, A.; Dimroth, F. Recent Development in Direct Generation of Hydrogen Using Multi-Junction Solar Cells; Author(s), 2016; Vol. 1766, p 080004.

[74] Hu, S.; Shaner, M. R.; Beardslee, J. A.; Lichterman, M. F.; Brunschwig, B. S.; Lewis, N. S. Amorphous TiO_2 Coatings Stabilize Si, GaAs, and GaP Photoanodes for Efficient Water Oxidation. *Science* **2014**, *344* (6187), 1005–1009.

[75] Porter, J. D.; Heller, A.; Aspnes, D. E. Experiment and Theory of “Transparent” Metal Films. *Nature* **1985**, *313* (6004), 664–666.

[76] Sanz, J. M.; Ortiz, D.; Alcaraz de la Osa, R.; Saiz, J. M.; González, F.; Brown, A. S.; Losurdo, M.; Everitt, H. O.; Moreno, F. UV Plasmonic Behavior of Various Metal Nanoparticles in the Near- and Far-Field Regimes: Geometry and Substrate Effects. *J. Phys. Chem. C* **2013**, *117* (38), 19606–19615.

[77] Singh, M. R.; Clark, E. L.; Bell, A. T. Effects of Electrolyte, Catalyst, and Membrane Composition and Operating Conditions on the Performance of Solar-Driven Electrochemical Reduction of Carbon Dioxide. *Phys. Chem. Chem. Phys.* **2015**, *17* (29), 18924–18936.

[78] Verlage, E.; Hu, S.; Liu, R.; Jones, R. J. R.; Sun, K.; Xiang, C.; Lewis, N. S.; Atwater, H. A. A Monolithically Integrated, Intrinsically Safe, 10% Efficient, Solar-Driven Water-Splitting System Based on Active, Stable Earth-Abundant Electrocatalysts in Conjunction with Tandem III-v Light Absorbers Protected by Amorphous TiO2 Films. *Energy Environ. Sci.* **2015**, *8* (11), 3166–3172.

[79] Seh, Z. W.; Kibsgaard, J.; Dickens, C. F.; Chorkendorff, I.; Nørskov, J. K.; Jaramillo, T. F. Combining Theory and Experiment in Electrocatalysis: Insights Into Materials Design. *Science* **2017**, *355* (6321), eaad4998.

[80] Schreier, M.; Héroguel, F.; Steier, L.; Ahmad, S.; Luterbacher, J. S.; Mayer, M. T.; Luo, J.; Grätzel, M. Solar Conversion of CO₂ to CO Using Earth-Abundant Electrocatalysts Prepared by Atomic Layer Modification of CuO. *Nat. Energy* **2017**, *2*, nenergy201787.

[81] Gurudayal; Beeman, J. W.; Bullock, J.; Wang, H.; Eichhorn, J.; Towle, C.; Javey, A.; Toma, F. M.; Mathews, N.; Ager, J. W., III. Si Photocathode with Ag-Supported Dendritic Cu Catalyst for CO2 Reduction. *Energy Environ. Sci.* **2019**, *12* (3), 1068–1077.

[82] Zhou, X.; Liu, R.; Sun, K.; Chen, Y.; Verlage, E.; Francis, S. A.; Lewis, N. S.; Xiang, C. Solar-Driven Reduction of 1 Atm of CO_2 To Formate at 10% Energy-Conversion Efficiency by Use of a TiO_2-Protected III–v Tandem Photoanode in Conjunction with a Bipolar Membrane and a Pd/C Cathode. *ACS Energy Lett.* **2016**, *1* (4), 764–770.

[83] Zhou, X.; Xiang, C. Comparative Analysis of Solar-to-Fuel Conversion Efficiency: a Direct, One-Step Electrochemical CO 2Reduction Reactor Versus a Two-Step, Cascade Electrochemical CO 2Reduction Reactor. *ACS Energy Lett.* **2018**, 1892–1897.

[84] Delacourt, C.; Ridgway, P. L.; Kerr, J. B.; Newman, J. Design of an Electrochemical Cell Making Syngas (CO+H[Sub 2]) From CO[Sub 2] and H[Sub 2]O Reduction at Room Temperature. *J. Electrochem. Soc.* **2008**, *155* (1), B42–B49.

[85] Schulz, H. Short History and Present Trends of Fischer–Tropsch Synthesis. *Applied Catalysis A: General* **1999**, *186* (1-2), 3–12.

[86] Lum, Y.; Ager, J. W., III. Sequential Catalysis Controls Selectivity in Electrochemical CO 2reduction on Cu. *Energy Environ. Sci.* **2018**, *11* (10), 2935–2944.

[87] Welch, A. J.; DuChene, J. S.; Tagliabue, G.; Davoyan, A.; Cheng, W.-H.; Atwater, H. A.; Atwater, H. A. Nanoporous Gold as a Highly Selective and Active Carbon Dioxide Reduction Catalyst. *ACS Appl. Energy Mater.* **2018**, *2* (1), 164–170.

[88] Chen, Y.; Li, C. W.; Kanan, M. W. Aqueous CO_2 Reduction at Very Low Overpotential on Oxide-Derived Au Nanoparticles. *J. Am. Chem. Soc.* **2012**, *134* (49), 19969–19972.

[89] Hatsukade, T.; Kuhl, K. P.; Cave, E. R.; Abram, D. N.; Jaramillo, T. F. Insights Into the Electrocatalytic Reduction of CO2 on Metallic Silver Surfaces. *Phys. Chem. Chem. Phys.* **2014**, *16* (27), 13814–13819.

[90] Asadi, M.; Kim, K.; Liu, C.; Addepalli, A. V.; Abbasi, P.; Yasaei, P.; Phillips, P.; Behranginia, A.; Cerrato, J. M.; Haasch, R.; et al. Nanostructured Transition Metal Dichalcogenide Electrocatalysts for CO2 Reduction in Ionic Liquid. *Science* **2016**, *353* (6298), 467–470.

[91] Asadi, M.; Kumar, B.; Behranginia, A.; Rosen, B. A.; Baskin, A.; Repnin, N.; Pisasale, D.; Phillips, P.; Zhu, W.; Haasch, R.; et al. Robust Carbon Dioxide Reduction on Molybdenum Disulphide Edges. *Nature Communications* **2014**, *5* (1), 1330.

[92] Cheng, T.; Huang, Y.; Xiao, H.; Goddard, W. A., III. Predicted Structures of the Active Sites Responsible for the Improved Reduction of Carbon Dioxide by Gold Nanoparticles. *J. Phys. Chem. Lett.* **2017**, *8* (14), 3317–3320.

[93] Singh, M. R.; Kwon, Y.; Lum, Y.; Ager, J. W., III; Bell, A. T. Hydrolysis of Electrolyte Cations Enhances the Electrochemical Reduction of CO 2over Ag and Cu. *J. Am. Chem. Soc.* **2016**, *138* (39), 13006–13012.

[94] Liu, M.; Pang, Y.; Zhang, B.; De Luna, P.; Voznyy, O.; Xu, J.; Zheng, X.; Dinh, C. T.; Fan, F.; Cao, C.; et al. Enhanced Electrocatalytic CO₂ Reduction via Field-Induced Reagent Concentration. *Nature* **2016**, *537* (7620), 382–386.

[95] Varela, A. S.; Kroschel, M.; Reier, T.; Strasser, P. Controlling the Selectivity of CO2 Electroreduction on Copper: the Effect of the Electrolyte Concentration and the Importance of the Local pH. *Catalysis Today* **2016**, *260*, 8–13.

[96] Song, J. T.; Ryoo, H.; Cho, M.; Kim, J.; Kim, J.-G.; Chung, S.-Y.; Oh, J. Nanoporous Au Thin Films on Si Photoelectrodes for Selective and Efficient Photoelectrochemical CO2 Reduction. *Advanced Energy Materials* **2017**, *7* (3), 1601103.

[97] Li, J.; Chen, G.; Zhu, Y.; Liang, Z.; Pei, A.; Wu, C.-L.; Wang, H.; Lee, H. R.; Liu, K.; Chu, S.; et al. Efficient Electrocatalytic CO 2 Reduction on a Three-Phase Interface. *Nature Catalysis 2018 1:8* **2018**, *1* (8), 592–600.

[98] Verma, S.; Hamasaki, Y.; Kim, C.; Huang, W.; Lu, S.; Jhong, H.-R. M.; Gewirth, A. A.; Fujigaya, T.; Nakashima, N.; Kenis, P. J. A. Insights Into the Low Overpotential Electroreduction of CO 2to CO on a Supported Gold Catalyst in an Alkaline Flow Electrolyzer. *ACS Energy Lett.* **2017**, *3* (1), 193–198.

[99] Clark, E. L.; Resasco, J.; Landers, A.; Lin, J.; Chung, L.-T.; Walton, A.; Hahn, C.; Jaramillo, T. F.; Bell, A. T. Standards and Protocols for Data Acquisition and Reporting for Studies of the Electrochemical Reduction of Carbon Dioxide. *ACS Catal.* **2018**, 6560–6570.

[100] Kim, C.; Jeon, H. S.; Eom, T.; Jee, M. S.; Kim, H.; Friend, C. M.; Min, B. K.; Hwang, Y. J. Achieving Selective and Efficient Electrocatalytic Activity for CO_2 Reduction Using Immobilized Silver Nanoparticles. *J. Am. Chem. Soc.* **2015**, *137* (43), 13844–13850.

[101] Jiang, K.; Kharel, P.; Peng, Y.; Gangishetty, M. K.; Lin, H.-Y. G.; Stavitski, E.; Attenkofer, K.; Wang, H. Silver Nanoparticles with Surface-Bonded Oxygen for Highly Selective CO2 Reduction. *ACS Sustainable Chem. Eng.* **2017**, *5* (10), 8529–8534.

[102] Wang, Z.; Wu, L.; Sun, K.; Chen, T.; Jiang, Z.; Cheng, T.; William A Goddard, I. Surface Ligand Promotion of Carbon Dioxide Reduction Through Stabilizing Chemisorbed Reactive Intermediates. *J. Phys. Chem. Lett.* **2018**, *9* (11), 3057–3061.

[103] Hsieh, Y.-C.; Senanayake, S. D.; Zhang, Y.; Xu, W.; Polyansky, D. E. Effect of Chloride Anions on the Synthesis and Enhanced Catalytic Activity of Silver Nanocoral Electrodes for CO 2Electroreduction. *ACS Catal.* **2015**, *5* (9), 5349–5356.

[104] Lu, Q.; Rosen, J.; Zhou, Y.; Hutchings, G. S.; Kimmel, Y. C.; Chen, J. G.; Jiao, F. A Selective and Efficient Electrocatalyst for Carbon Dioxide Reduction. *Nature Communications* **2014**, *5* (1), 1–6.

[105] Dinh, C. T.; García de Arquer, F. P.; Sinton, D.; Sargent, E. H. High Rate, Selective, and Stable Electroreduction of CO 2to CO in Basic and Neutral Media. *ACS Energy Lett.* **2018**, *3* (11), 2835–2840.

[106] Tornow, C. E.; Thorson, M. R.; Ma, S.; Gewirth, A. A.; Kenis, P. J. A. Nitrogen-Based Catalysts for the Electrochemical Reduction of CO2 to CO. *J. Am. Chem. Soc.* **2012**, *134* (48), 19520–19523.

[107] Verma, S.; Lu, X.; Ma, S.; Masel, R. I.; Kenis, P. J. A. The Effect of Electrolyte Composition on the Electroreduction of CO2 to CO on Ag Based Gas Diffusion Electrodes. *Phys. Chem. Chem. Phys.* **2016**, *18* (10), 7075–7084.

[108] Higgins, D.; Hahn, C.; Xiang, C.; Jaramillo, T. F.; Weber, A. Z. Gas-Diffusion Electrodes for Carbon Dioxide Reduction: a New Paradigm. *ACS Energy Lett.* **2018**, *4* (1), 317–324.

[109] Singh, M. R.; Papadantonakis, K.; Xiang, C.; Lewis, N. S. An Electrochemical Engineering Assessment of the Operational Conditions and Constraints for Solar-Driven Water-Splitting Systems at Near-Neutral pH. *Energy Environ. Sci.* **2015**, *8* (9), 2760–2767.

[110] Lobaccaro, P.; Singh, M. R.; Clark, E. L.; Kwon, Y.; Bell, A. T.; Ager, J. W., III. Effects of Temperature and Gas–Liquid Mass Transfer on the Operation of Small Electrochemical Cells for the Quantitative Evaluation of CO2 Reduction Electrocatalysts. *Phys. Chem. Chem. Phys.* **2016**, *18* (38), 26777–26785.

[111] Song, J. T.; Song, H.; Kim, B.; Oh, J. Towards Higher Rate Electrochemical CO2 Conversion: From Liquid-Phase to Gas-Phase Systems. *Catalysts 2019, Vol. 9, Page 224* **2019**, *9* (3), 224.

[112] Weng, L.-C.; Bell, A. T.; Weber, A. Z. Modeling Gas-Diffusion Electrodes for CO 2 Reduction. *Phys. Chem. Chem. Phys.* **2018**, *20* (25), 16973–16984.

[113] Cook, R. L.; MacDuff, R. C.; Sammells, A. F. High Rate Gas Phase CO[Sub 2] Reduction to Ethylene and Methane Using Gas Diffusion Electrodes. *J. Electrochem. Soc.* **1990**, *137* (2), 607–608.

[114] Hori, Y.; Ito, H.; Okano, K.; Nagasu, K.; Sato, S. Silver-Coated Ion Exchange Membrane Electrode Applied to Electrochemical Reduction of Carbon Dioxide. *Electrochimica Acta* **2003**, *48* (18), 2651–2657.

[115] Dinh, C. T.; Burdyny, T.; Kibria, M. G.; Seifitokaldani, A.; Gabardo, C. M.; de Arquer, F. P. G.; Kiani, A.; Edwards, J. P.; De Luna, P.; Bushuyev, O. S.; et al. CO2electroreduction to Ethylene via Hydroxide-Mediated Copper Catalysis at an Abrupt Interface. *Science* **2018**, *360* (6390), 783–787.

[116] Li, Y. C.; Lee, G.; Yuan, T.; Wang, Y.; Nam, D.-H.; Wang, Z.; García de Arquer, F. P.; Lum, Y.; Dinh, C. T.; Voznyy, O.; et al. CO 2Electroreduction From Carbonate Electrolyte. *ACS Energy Lett.* **2019**, *4* (6), 1427–1431.

[117] Hossain, M. Z.; Rahim, N. A.; Selvaraj, J. A. L. Recent Progress and Development on Power DC-DC Converter Topology, Control, Design and Applications: a Review. *Renewable and Sustainable Energy Reviews* **2018**, *81*, 205–230.

[118] Holman, Z.; Boccard, M. Light Management in Silicon Solar Cells. In *Photovoltaic Solar Energy: From Fundamentals to Applications*; John Wiley & Sons, Ltd.: Hoboken, New Jersey, 2016; pp 136–149.

[119] Manzoor, S.; Yu, Z. J.; Ali, A.; Ali, W.; Bush, K. A.; Palmstrom, A. F.; Bent, S. F.; McGehee, M. D.; Holman, Z. C. Improved Light Management in Planar Silicon and Perovskite Solar Cells Using PDMS Scattering Layer. *Solar Energy Materials and Solar Cells* **2017**, *173*, 59–65.

[120] Haug, F. J.; Ballif, C. Light Management in Thin Film Silicon Solar Cells. *Energy Environ. Sci.* **2015**, *8* (3), 824–837.

[121] Schmid, M. Review on Light Management by Nanostructures in Chalcopyrite Solar Cells. *Semicond. Sci. Technol.* **2017**, *32* (4), 043003.

[122] Peer, A.; Biswas, R.; Park, J.-M.; Shinar, R.; Shinar, J. Light Management in Perovskite Solar Cells and Organic LEDs with Microlens Arrays. *Opt. Express* **2017**, *25* (9), 10704–10709.

[123] Hu, S.; Xiang, C.; Haussener, S.; Berger, A. D.; Lewis, N. S. An Analysis of the Optimal Band Gaps of Light Absorbers in Integrated Tandem Photoelectrochemical Water-Splitting Systems. *Energy Environ. Sci.* **2013**, *6* (10), 2984–2993.

[124] Raut, H. K.; Ganesh, V. A.; Nair, A. S.; Ramakrishna, S. Anti-Reflective Coatings: a Critical, in-Depth Review. *Energy Environ. Sci.* **2011**, *4* (10), 3779–3804.

[125] Krč, J.; Smole, F.; Topič, M. Potential of Light Trapping in Microcrystalline Silicon Solar Cells with Textured Substrates. *Prog. Photovoltaics: Res. Appl.* **2003**, *11* (7), 429–436.

[126] Campbell, P.; Green, M. A. Light Trapping Properties of Pyramidally Textured Surfaces. *J. Appl. Phys.* **1987**, *62* (1), 243–249.
[127] Yablonovitch, E.; Cody, G. D. Intensity Enhancement in Textured Optical Sheets for Solar Cells. *IEEE Trans. Electron Devices* **1982**, *29* (2), 300–305.
[128] Cho, S. J.; An, T.; Lim, G. Three-Dimensionally Designed Anti-Reflective Silicon Surfaces for Perfect Absorption of Light. *Chem. Commun.* **2014**, *50* (99), 15710–15713.
[129] Brongersma, M. L.; Cui, Y.; Fan, S. Light Management for Photovoltaics Using High-Index Nanostructures. *Nat Mater* **2014**, *13*, 451.
[130] Mokkapati, S.; Catchpole, K. R. Nanophotonic Light Trapping in Solar Cells. *J. Appl. Phys.* **2012**, *112* (10), 101101.
[131] Wilson, G. The Multi-TW Scale Future for Photovoltaics. *AIP Conf. Proc.* **2018**, *1924* (1), 020003.
[132] Sun, K.; Moreno-Hernandez, I. A.; Schmidt, W. C.; Zhou, X.; Crompton, J. C.; Liu, R.; Saadi, F. H.; Chen, Y.; Papadantonakis, K. M.; Lewis, N. S. A Comparison of the Chemical, Optical and Electrocatalytic Properties of Water-Oxidation Catalysts for Use in Integrated Solar-Fuel Generators. *Energy Environ. Sci.* **2017**, *10* (4), 987–1002.
[133] Yoshikawa, K.; Kawasaki, H.; Yoshida, W.; Irie, T.; Konishi, K.; Nakano, K.; Uto, T.; Adachi, D.; Kanematsu, M.; Uzu, H.; et al. Silicon Heterojunction Solar Cell with Interdigitated Back Contacts for a Photoconversion Efficiency Over 26%. *Nat. Energy* **2017**, *2*, 17032.
[134] Lammert, M. D.; Schwartz, R. J. The Interdigitated Back Contact Solar Cell: a Silicon Solar Cell for Use in Concentrated Sunlight. *IEEE Trans. Electron Devices* **1977**, *24* (4), 337–342.
[135] Spitzer, M. B.; Fan, J. C. C. Multijunction Cells for Space Applications. *Sol. Cells* **1990**, *29* (2), 183–203.
[136] Tian, B. Z.; Zheng, X. L.; Kempa, T. J.; Fang, Y.; Yu, N. F.; Yu, G. H.; Huang, J. L.; Lieber, C. M. Coaxial Silicon Nanowires as Solar Cells and Nanoelectronic Power Sources. *Nature* **2007**, *449* (7164), 885–U888.
[137] Mavrokefalos, A.; Han, S. E.; Yerci, S.; Branham, M. S.; Chen, G. Efficient Light Trapping in Inverted Nanopyramid Thin Crystalline Silicon Membranes for Solar Cell Applications. *Nano Lett.* **2012**, *12* (6), 2792–2796.
[138] Zhu, J.; Hsu, C. M.; Yu, Z. F.; Fan, S. H.; Cui, Y. Nanodome Solar Cells with Efficient Light Management and Self-Cleaning. *Nano Lett.* **2010**, *10* (6), 1979–1984.
[139] Yao, Y.; Yao, J.; Narasimhan, V. K.; Ruan, Z. C.; Xie, C.; Fan, S. H.; Cui, Y. Broadband Light Management Using Low-Q Whispering Gallery Modes in Spherical Nanoshells. *Nature Communications* **2012**, *3*.
[140] Kapadia, R.; Fan, Z. Y.; Takei, K.; Javey, A. Nanopillar Photovoltaics: Materials, Processes, and Devices. *Nano Energy* **2012**, *1* (1), 132–144.
[141] Narasimhan, V. K.; Hymel, T. M.; Lai, R. A.; Cui, Y. Hybrid Metal–Semiconductor Nanostructure for Ultrahigh Optical Absorption and Low Electrical Resistance at Optoelectronic Interfaces. *ACS Nano* **2015**, *9* (11), 10590–10597.
[142] Jeong, S.; Garnett, E. C.; Wang, S.; Yu, Z. G.; Fan, S. H.; Brongersma, M. L.; McGehee, M. D.; Cui, Y. Hybrid Silicon Nanocone-Polymer Solar Cells. *Nano Lett.* **2012**, *12* (6), 2971–2976.
[143] Yalamanchili, S.; Emmer, H. S.; Fountaine, K. T.; Chen, C. T.; Lewis, N. S.; Atwater, H. A. Enhanced Absorption and <1% Spectrum-and-Angle-Averaged Reflection in Tapered Microwire Arrays. *ACS Photonics* **2016**, *3* (10), 1854–1861.
[144] Fountaine, K. T.; Cheng, W.-H.; Bukowsky, C. R.; Atwater, H. A. Near-Unity Unselective Absorption in Sparse InP Nanowire Arrays. *ACS Photonics* **2016**, *3* (10), 1826–1832.
[145] Grandidier, J.; Callahan, D. M.; Munday, J. N.; Atwater, H. A. Light Absorption Enhancement in Thin-Film Solar Cells Using Whispering Gallery Modes in Dielectric Nanospheres. *Adv Mater* **2011**, *23* (10), 1272.

[146] Choy, J. T.; Bradley, J. D. B.; Deotare, P. B.; Burgess, I. B.; Evans, C. C.; Mazur, E.; Lončar, M. Integrated TiO2resonators for Visible Photonics. *Opt. Lett.* **2012**, *37* (4), 539–541.

[147] Evans, C. C.; Liu, C.; Suntivich, J. Low-Loss Titanium Dioxide Waveguides and Resonators Using a Dielectric Lift-Off Fabrication Process. *Opt. Express* **2015**, *23* (9), 11160–11169.

[148] Evans, C. C.; Shtyrkova, K.; Reshef, O.; Moebius, M.; Bradley, J. D. B.; Griesse-Nascimento, S.; Ippen, E.; Mazur, E. Multimode Phase-Matched Third-Harmonic Generation in Sub-Micrometer-Wide Anatase TiO2waveguides. *Opt. Express* **2015**, *23* (6), 7832–7841.

[149] Evans, C. C.; Shtyrkova, K.; Bradley, J. D. B.; Reshef, O.; Ippen, E.; Mazur, E. Spectral Broadening in Anatase Titanium Dioxide Waveguides at Telecommunication and Near-Visible Wavelengths. *Opt. Express* **2013**, *21* (15), 18582–18591.

[150] Guan, X.; Hu, H.; Oxenløwe, L. K.; Frandsen, L. H. Compact Titanium Dioxide Waveguides with High Nonlinearity at Telecommunication Wavelengths. *Opt. Express* **2018**, *26* (2), 1055–1063.

[151] Bradley, J. D. B.; Evans, C. C.; Choy, J. T.; Reshef, O.; Deotare, P. B.; Parsy, F.; Phillips, K. C.; Lončar, M.; Mazur, E. Submicrometer-Wide Amorphous and Polycrystalline Anatase TiO2waveguides for Microphotonic Devices. *Opt. Express* **2012**, *20* (21), 23821–23831.

[152] Sun, K.; Kuang, Y.; Verlage, E.; Brunschwig, B. S.; Tu, C. W.; Lewis, N. S. Sputtered NiO_X Films for Stabilization of P+N-InP Photoanodes for Solar-Driven Water Oxidation. *Advanced Energy Materials* **2015**, *5* (11), 1402276.

[153] Lichterman, M. F.; Carim, A. I.; McDowell, M. T.; Hu, S.; Gray, H. B.; Brunschwig, B. S.; Lewis, N. S. Stabilization of N-Cadmium Telluride Photoanodes for Water Oxidation to O2(G) in Aqueous Alkaline Electrolytes Using Amorphous TiO2films Formed by Atomic-Layer Deposition. *Energy Environ. Sci.* **2014**, *7* (10), 3334–3337.

[154] McDowell, M. T.; Lichterman, M. F.; Carim, A. I.; Liu, R.; Hu, S.; Brunschwig, B. S.; Lewis, N. S. The Influence of Structure and Processing on the Behavior of TiO_2 Protective Layers for Stabilization of N-Si/TiO_2/Ni Photoanodes for Water Oxidation. *ACS Appl. Mater. Interfaces* **2015**, *7* (28), 15189–15199.

[155] McDowell, M. T.; Lichterman, M. F.; Spurgeon, J. M.; Hu, S.; Sharp, I. D.; Brunschwig, B. S.; Lewis, N. S. Improved Stability of Polycrystalline Bismuth Vanadate Photoanodes by Use of Dual-Layer Thin TiO2/Ni Coatings. *J. Phys. Chem. C* **2014**, *118* (34), 19618–19624.

[156] Shaner, M. R.; Hu, S.; Sun, K.; Lewis, N. S. Stabilization of Si Microwire Arrays for Solar-Driven H2O Oxidation to O2(G) in 1.0 M KOH(Aq) Using Conformal Coatings of Amorphous TiO2. *Energy Environ. Sci.* **2015**, *8* (1), 203–207.

[157] Siklitsky, V. New Semiconductor Materials. Characteristics and Properties. *Available: http://www.ioffe.rssi.ru/SVA/NSM* **2001**.

[158] Kenney, M. J.; Gong, M.; Li, Y.; Wu, J. Z.; Feng, J.; Lanza, M.; Dai, H. High-Performance Silicon Photoanodes Passivated with Ultrathin Nickel Films for Water Oxidation. *Science* **2013**, *342* (6160), 836–840.

[159] Sun, K.; Ritzert, N. L.; John, J.; Tan, H.; Hale, W. G.; Jiang, J.; Moreno-Hernandez, I.; Papadantonakis, K. M.; Moffat, T. P.; Brunschwig, B. S.; et al. Performance and Failure Modes of Si Anodes Patterned with Thin-Film Ni Catalyst Islands for Water Oxidation. *Sustainable Energy Fuels* **2018**, *2* (5), 983–998.

[160] Chen, Y.; Sun, K.; Audesirk, H.; Xiang, C.; Lewis, N. S. A Quantitative Analysis of the Efficiency of Solar-Driven Water-Splitting Device Designs Based on Tandem Photoabsorbers Patterned with Islands of Metallic Electrocatalysts. *Energy Environ. Sci.* **2015**, *8* (6), 1736–1747.

[161] Choi, S. K.; Kang, U.; Lee, S.; Ham, D. J.; Ji, S. M.; Park, H. Sn-Coupled P-Si Nanowire Arrays for Solar Formate Production From CO2. *Advanced Energy Materials* **2014**, *4* (11), 1301614.

[162] Kong, Q.; Kim, D.; Liu, C.; Yu, Y.; Su, Y.; Li, Y.; Yang, P. Directed Assembly of Nanoparticle Catalysts on Nanowire Photoelectrodes for Photoelectrochemical CO 2Reduction. *Nano Lett.* **2016**, *16* (9), 5675–5680.

[163] Fountaine, K. T.; Lewerenz, H.-J. Efficiency Limits for Hydrogen and Formate Production via Fully-Integrated Photoelectrochemical Devices. *ECS Trans.* **2017**, *77* (4), 15–23.

[164] Sun, K.; Saadi, F. H.; Lichterman, M. F.; Hale, W. G.; Wang, H.-P.; Zhou, X.; Plymale, N. T.; Omelchenko, S. T.; He, J.-H.; Papadantonakis, K. M.; et al. Stable Solar-Driven Oxidation of Water by Semiconducting Photoanodes Protected by Transparent Catalytic Nickel Oxide Films. *PNAS* **2015**, *112* (12), 3612–3617.

[165] Bae, D.; Seger, B.; Vesborg, P. C. K.; Hansen, O.; Chorkendorff, I. Strategies for Stable Water Splitting via Protected Photoelectrodes. *Chem. Soc. Rev.* **2017**, *46* (7), 1933–1954.

[166] Hu, S.; Richter, M. H.; Lichterman, M. F.; Beardslee, J.; Mayer, T.; Brunschwig, B. S.; Lewis, N. S. Electrical, Photoelectrochemical, and Photoelectron Spectroscopic Investigation of the Interfacial Transport and Energetics of Amorphous TiO2/Si Heterojunctions. *J. Phys. Chem. C* **2016**, *120* (6), 3117–3129.

[167] Nunez, P.; Richter, M. H.; Piercy, B. D.; Roske, C. W.; Cabán-Acevedo, M.; Losego, M. D.; Konezny, S. J.; Fermin, D. J.; Hu, S.; Brunschwig, B. S.; et al. Characterization of Electronic Transport Through Amorphous TiO2 Produced by Atomic Layer Deposition. *J. Phys. Chem. C* **2019**, *123* (33), 20116–20129.

[168] Lichterman, M. F.; Richter, M. H.; Hu, S.; Crumlin, E. J.; Axnanda, S.; Favaro, M.; Drisdell, W.; Hussain, Z.; Brunschwig, B. S.; Lewis, N. S.; et al. An Electrochemical, Microtopographical and Ambient Pressure X-Ray Photoelectron Spectroscopic Investigation of Si/TiO_2/Ni/Electrolyte Interfaces. *J. Electrochem. Soc.* **2016**, *163* (2), H139–H146.

[169] Morales, F.; de Groot, F. M. F.; Glatzel, P.; Kleimenov, E.; Bluhm, H.; Hävecker, M.; Knop-Gericke, A.; Weckhuysen, B. M. In Situ X-Ray Absorption of Co/Mn/TiO 2Catalysts for Fischer−Tropsch Synthesis. *J. Phys. Chem. B* **2004**, *108* (41), 16201–16207.

[170] Diebold, U. The Surface Science of Titanium Dioxide. *Surface Science Reports* **2003**, *48* (5-8), 53–229.

[171] Moser, S.; Fatale, S.; Krüger, P.; Berger, H.; Bugnon, P.; Magrez, A.; Niwa, H.; Miyawaki, J.; Harada, Y.; Grioni, M. Electron-Phonon Coupling in the Bulk of Anatase <Span Class="Aps-Inline-Formula"><Math Xmlns="Http://Www.W3.org/1998/Math/MathML" Display="Inline"><Mrow><Msub><Mrow><Mi>TiO</Mi></Mrow><Mrow><Mn>2</Mn></Mrow></Msub></Mrow></Math></Span> Measured by Resonant Inelastic X-Ray Spectroscopy. *Phys. Rev. Lett.* **2015**, *115* (9), 096404.

[172] Glatzel, P.; Sikora, M.; Fernández-García, M. Resonant X-Ray Spectroscopy to Study K Absorption Pre-Edges in 3d Transition Metal Compounds. *Eur. Phys. J. Spec. Top.* **2009**, *169* (1), 207–214.

[173] Lichterman, M. F.; Richter, M. H.; Hu, S.; Crumlin, E. J.; Axnanda, S.; Favaro, M.; Drisdell, W.; Hussain, Z.; Mayer, T.; Brunschwig, B.; et al. Investigation of the Si/TiO2/Electrolyte Interface Using Operando Tender X-Ray Photoelectron Spectroscopy. *ECS Trans.* **2015**, *66* (6), 97–103.

[174] Richter, M. H.; Lichterman, M. F.; Hu, S.; Crumlin, E. J.; Mayer, T.; Axnanda, S.; Favaro, M.; Drisdell, W.; Hussain, Z.; Brunschwig, B.; et al. Measurement of the Energy-Band Relations of Stabilized Si Photoanodes Using Operando Ambient Pressure X-Ray Photoelectron Spectroscopy. *ECS Trans.* **2015**, *66* (6), 105–113.

[175] Schmeißer, D.; Hoffmann, P.; Beuckert, G. Electronic Properties of the Interface Formed by Pr_2O_3 Growth. In *Materials for Information Technology*; Springer: London, 2005; pp 449–460.

[176] Stöhr, J. *NEXAFS Spectroscopy*, 2nd ed.; Springer: Heidelberg, 2003; Vol. 25.

[177] Qiao, R.; Li, Q.; Zhuo, Z.; Sallis, S.; Fuchs, O.; Blum, M.; Weinhardt, L.; Heske, C.; Pepper, J.; Jones, M.; et al. High-Efficiency in Situ Resonant Inelastic X-Ray Scattering (iRIXS)

Endstation at the Advanced Light Source. *Review of Scientific Instruments* **2017**, *88* (3), 033106.

[178] McCrory, C. C. L.; Jung, S.; Ferrer, I. M.; Chatman, S. M.; Peters, J. C.; Jaramillo, T. F. Benchmarking Hydrogen Evolving Reaction and Oxygen Evolving Reaction Electrocatalysts for Solar Water Splitting Devices. *J. Am. Chem. Soc.* **2015**, *137* (13), 4347–4357.

[179] Michaelson, H. B. The Work Function of the Elements and Its Periodicity. *Journal of Applied Physics* **2008**, *48* (11), 4729–4733.

[180] Tanuma, S.; Powell, C. J.; Penn, D. R. Calculations of Electron Inelastic Mean Free Paths. v. Data for 14 Organic Compounds Over the 50–2000 eV Range. *Surface and Interface Analysis* **1994**, *21* (3), 165–176.

[181] Cho, D.-Y.; Song, S. J.; Kim, U. K.; Kim, K. M.; Lee, H.-K.; Hwang, C. S. Spectroscopic Investigation of the Hole States in Ni-Deficient NiO Films. *J. Mater. Chem. C* **2013**, *1* (28), 4334–4338.

[182] Mossanek, R. J. O.; Domínguez-Cañizares, G.; Gutiérrez, A.; Abbate, M.; Díaz-Fernández, D.; Soriano, L. Effects of Ni Vacancies and Crystallite Size on the O 1s and Ni 2p X-Ray Absorption Spectra of Nanocrystalline NiO. *J. Phys.: Condens. Matter* **2013**, *25* (49), 495506.

[183] Greiner, M. T.; Helander, M. G.; Wang, Z.-B.; Tang, W.-M.; Lu, Z.-H. Effects of Processing Conditions on the Work Function and Energy-Level Alignment of NiO Thin Films. *J. Phys. Chem. C* **2010**, *114* (46), 19777–19781.

[184] Mankel, E.; Hein, C.; Kühn, M.; Mayer, T. Electric Potential Distributions in Space Charge Regions of Molecular Organic Adsorbates Using a Simplified Distributed States Model. *physica status solidi (a)* **2014**, *211* (9), 2040–2048.

[185] Horn, K. Semiconductor Interface Studies Using Core and Valence Level Photoemission. *Appl. Phys. A* **1990**, *51* (4), 289–304.

[186] Franciosi, A.; Van de Walle, C. G. Heterojunction Band Offset Engineering. *Surface Science Reports* **1996**, *25* (1-4), 1–140.

[187] Rossi, R. C.; Lewis, N. S. Investigation of the Size-Scaling Behavior of Spatially Nonuniform Barrier Height Contacts to Semiconductor Surfaces Using Ordered Nanometer-Scale Nickel Arrays on Silicon Electrodes. *J. Phys. Chem. B* **2001**, *105* (49), 12303–12318.

[188] Lichterman, M. F.; Hu, S.; Richter, M. H.; Crumlin, E. J.; Axnanda, S.; Favaro, M.; Drisdell, W.; Hussain, Z.; Mayer, T.; Brunschwig, B. S.; et al. Direct Observation of the Energetics at a Semiconductor/Liquid Junction by Operando X-Ray Photoelectron Spectroscopy. *Energy Environ. Sci.* **2015**, *8* (8), 2409–2416.